Phase transitions within the lime cycle: Implications in heritage conservation

April, 2013

by
Krzysztof Kudłacz

University of Granada
Faculty of Science
Department of Mineralogy and Petrology

Editor: Editorial de la Universidad de Granada
Autor: Krzysztof Kudlacz
D.L.: GR 223-2014
ISBN: 978-84-9028-742-2

ACKNOWLEDGEMENTS

The work on this thesis was carried out in the Department of Mineralogy and Petrology at the University of Granada between May 2009 and November of 2012. The author would like to thank Prof. Carlos Rodriguez-Navarro and Prof. Alejandro Rodriguez-Navarro for the guidance and support they have offered throughout the duration of this thesis. I would like to thank Dr. Encarnación Ruiz-Agudo for assistance and comments. Financial support has been provided by the EU Marie Curie Initial Training Network Delta-Min (Mechanisms of Mineral Replacement Reactions) Grant PITN-GA-2008-215360 and through the P08-RNM-4169 grant (Proyecto de Excelencia, Junta de Andalucía).

ABSTRACT

This thesis deals with the study of three different processes within the lime cycle. These are: 1) thermal decomposition of dolomite ($CaMg(CO_3)_2$), 2) hydration of lime (CaO) and 3) carbonation of calcium hydroxide ($Ca(OH)_2$).

While the thermal decomposition of calcite, which represents the first step of the lime cycle, has been studied thoroughly, and its mechanism is now well established, this is not the case of the other relevant carbonate involved in the lime cycle, that is, dolomite. In fact, and despite over one hundred year studies, the thermal decomposition of dolomite is still a poorly understood process. In order to understand the ultimate mechanism(s) of such a reaction, dolomite single crystal were calcined in air at 500 ºC up to 1000 °C and in situ, in the TEM (high vacuum), following irradiation with the electron beam. In situ TEM shows that the decomposition involves the initial formation of a face centered cubic mixed oxide structure ($Ca_{0.5}Mg_{0.5}O$) with the following reactant/product orientation relationships: $[001]_{dolomite}//\langle 111\rangle_{oxide}$, $\langle\bar{4}41\rangle_{dolomite}//\langle 100\rangle_{oxide}$, $\{11\bar{2}0\}_{dolomite}//\{110\}_{oxide}$, $\{11\bar{2}8\}_{dolomite}//\{110\}_{oxide}$ and $\{10\bar{1}4\}_{dolomite}\wedge\{100\}_{oxide}\sim 12^{\circ}$. This phase undergoes de-mixing into oriented crystals of Mg-poor CaO and Ca-poor MgO solid solutions upon long term e-beam exposure. Ex situ TEM, XRD, 2D-XRD, and FESEM analyses show the formation of porous pseudomorphs made up of oxide nanocrystals with similar parent/product orientation relationships, but with limited Ca/Mg substitution (up to ~9-11 %) due to de-mixing (spinodal decomposition) of the metastable (Mg,Ca)O precursor. High ion diffusivity at $T > 500$ °C (ex situ experiments) favors the formation of pure CaO and MgO crystals during coarsening via oriented aggregation and sintering. These results show that the thermal decomposition of dolomite is topotactic (shear-transformation) and independent of pCO_2 (i.e., vacuum or air). Formation of Mg-calcite nanocrystals (up to ~8 mol % Mg) during the so-called "half decomposition" is observed at 650-750 ºC. This transient phase formed topotactically following the reaction of CaO nanocrystals (solid solution with ~9 mol % Mg) with CO_2 present in the air and/or released upon further dolomite decomposition. With increasing T, Mg-calcite transformed into calcite which underwent decomposition following the known topotactic relationship:

$\{10\bar{1}4\}_{calcite}//\{110\}_{CaO}$ and $<\bar{4}41>_{calcite}//<110>_{CaO}$. These observations solve the long standing controversy regarding the mechanism of the “two-stage” decomposition of dolomite which assumed the direct formation of calcite during the so-called “half-decomposition” of dolomite.

It has been hypothesized that hydration of lime, which represents the second step of the lime cycle, can take two different reaction pathways. The first one involves direct precipitation of calcium hydroxide from a supersaturated solution formed upon the dissolution of CaO in the slaking water. The second refers to the reaction between solid CaO and water vapor. Water is vaporized under the influence of heat released during hydration. The latter (i.e., vapor phase hydration) has received less attention in the literature. In order to shed some light on the mechanism(s) of vapor phase hydration as well as the crystallographic control in the advancement of the reaction CaO pseudomorphs (formed upon calcination in air at 700 °C up to 900 °C of calcite single crystals) were subjected to the effect of air de-voided of CO_2 at 50% RH. Crystallite size measurements (XRD) yielded equal values regardless the initial size of CaO crystals. FESEM analysis show the pseudomorphic character of hydration. This two observations are consistent with a coupled dissolution/precipitation reaction. Pole figure (2D-XRD) and HRTEM analyses point to the topotactic nature of the reaction with the following orientation relationships between lime and portlandite: $\{11\bar{2}0\}_{portlandite}//\{110\}_{lime}$ and $\{0001\}_{portlandite}//\{111\}_{lime}$. The topotactic nature of the reaction points to a solid state replacement of lime by portlandite. Most probably the selection of the ruling mechanism is controlled by RH and microstructural features, e.g., porosity, crystal size, which depend on the calcination *T* and retention time, and evolve as hydration progresses.

The reaction between calcium hydroxide (portlandite) and carbon dioxide, the so-called carbonation, which occurs via the reaction $Ca(OH)_2 + CO_2 \rightarrow CaCO_3 + H_2O$, results in the formation of precipitated calcium carbonate (PCC). This is the third, and the last stage of the lime cycle. Here, carbonation was performed in three different routes:

- precipitation at the water-air interface in solutions saturated with respect to $Ca(OH)_2$ (lime water) and exposed to air, with and without excess of solid $Ca(OH)_2$
- carbonation of portlandite single crystals placed in air at 93% RH for 4 moths

- carbonation of hydrated calcite pseudomorphs (HCP), calcined at *T* of 700-900 ºC, hydrated in CO_2-free atmosphere (50 %RH) and subsequently exposed to CO_2 ($10^{-3.5}$ atm)
- carbonation of two types of hydrated lime pastes (HLP) by exposition to air at 93% RH for 4 months

All experiments were performed at room temperature (20 ± 2 ºC) and pCO_2 ~$10^{-3.5}$ atm. Additionally to experiments, simulation of pore water chemistry in saturated calcium hydroxide solution in contact with air was performed using PHREEQC software.

The carbonation in lime water (pH ~12.4) results in early precipitation of unstable ACC, which subsequently undergoes transformation to calcite, with no metastable vaterite/aragonite. TEM-SEAD reveals that ACC is characterized by short range order (proto-calcite), which predetermines the formation of calcite. Under excess of solid $Ca(OH)_2$ in lime water, precipitation of scalenohedral calcite is favored. In the absence of additional $Ca(OH)_2$, calcite shows rhombohedral features.

Carbonation of portlandite single crystals results in pseudomorphs, that fully preserve the external hexagonal shape. 2D-XRD analysis discloses the epitactic nature of the process, showing the following crystallographic relationship: $<001>_{calcite}//<001>_{portlandite}$. This behavior is explained by considering the structure of hexagonal portlandite which is made up of alternating Ca^{2+} and OH^- layers piled up along the c-axis. Such a structure matches the calcite structure where alternating layer of Ca^{2+} and CO_3^{2-} pile up along the three-fold axis of this hexagonal phase. The crystallographic control in the advancement of the process along with the preservation of the external shape of the parent phase (pseudomorphism) point to a coupled dissolution/precipitation replacement of portlandite by calcite. Such a process progresses due to the contrasting molar volume of and solubility differences between parent and product phases which leads to porosity development and enables the advancement of the reaction front to the core of the replaced phase.

In-situ XRD analysis of solution with excess solid $Ca(OH)_2$ (portlandite) subjected to carbonation in air, along with field emission electron microscopy (FESEM) observations of carbonated portlandite single crystals, revealed that dissolution of portlandite is strongly anisotropic. Dissolution of portlandite prism faces progress faster than dissolution of basal planes. This is consistent with the features of portlandite crystal structure.

Carbonation of HCP and HLP involves two processes: precipitation of calcite from solution and direct replacement of portlandite crystals by calcite via coupled dissolution/precipitation reaction. Carbonated HCPs (independently of calcination *T*) show rhombohedral calcite crystals at the outer parts, and scalenohedral calcite in the deeper parts. Morphology and crystal size of calcite precipitated during carbonation of HLP are strongly affected by the surface area and pore size distribution of lime pastes, which also evolves while carbonation progresses.

The processes considered in this thesis have a great importance in many different fields: industrial, geochemical, pharmaceutical. In each of these areas, control over a process, leading to a product with desirable properties, is based on the understanding of its principles. The understanding of the mechanisms of the these reactions can shed some light on the problem of use of traditional lime based products in the field of cultural heritage conservation.

1. INTRODUCTION

This section introduces the idea and importance of the material, commonly known as lime. Its history of manufacturing and use will be shortly described. Later, three different processes, i.e., calcination, hydration and carbonation will be presented. Each of them will be placed in a broader context as parts of the so-called lime cycle. The summary of the current stage of knowledge, based on the literature review as well as main gaps in knowledge and unsolved problems will be discussed. Finally, the objectives of this PhD thesis will be outlined.

1.1. Mortars

A mortar constitutes a mixture of a binder, which fulfills the function of a glue, with an aggregate (e.g., sand) and water. Following its setting and hardening, mortar plays a structural, as well as decorative role like: masonry mortar between brick or stones, as finishing material for internal (plaster) and external (render) use, as a filler in walls cavities, as foundations flooring, as a decoration material etc (Lea, 1970; Elsen 2005). Throughout history, mankind has used various types of binders, with vast compositional diversity depending on both historical period and geographical location (Elsen, 2005). One of the oldest examples of binder used in building is mud (clay-rich earth materials) (Houben and Guillaud, 1994), that has been identified in the adobe walls of Jericho (Israel) dating back to 8300 BC (Allen and Tallon, 2011) or in the rammed earth structures in Çatalhöyük (Anatolia, Turkey) dating back to 7500-6000 BC (Mellart, 1967). However, this type of binder presents a low strength and a high susceptibility to weathering and damage. These dissatisfying properties are related to the lack of heat treatment (i.e., pyrotechnology) during their manufacturing. A new class of binders, superior in terms of strength, durability and application abilities, emerged with the advent of pyrotechnology ca. 12000 years ago (Kingery et al. 1988). Among them special place is taken by gypsum and lime used on a large scale from the Neolithic until the present days. In the following sections, attention will be paid on lime as the most significant building material.

1.2. Lime

The term lime is a collective description applied to the two types of limes, i.e., calcitic lime (calcium oxide: CaO) and dolomitic lime (mixture of CaO and magnesium oxide: MgO). These limes are products of calcination (i.e., thermally inducted decomposition) of two types of carbonate rocks. Calcitic lime is a product of calcite or aragonite (calcium carbonate: $CaCO_3$) calcination, whereas dolomitic lime is obtained by calcination of dolomite (calcium magnesium carbonate: $CaMg(CO_3)_2$). The same term is often applied to hydrated (slaked) forms of Ca and Mg oxides formed after calcination of carbonates.

Lime belongs to the family of the products having one of the most profound influence on human daily lives. It is used in building/construction, has a great importance in industrial processes like production of steel, food industry (as a source of calcium and magnesium), pharmacy, agriculture (Elsen 2006).

From a historical perspective, lime has been one of the most important material used in construction. The oldest example of its use, dating back to 12000 BC, was found in Palestine and Turkey (Kingery et al. 1988). Other archeological studies of ruins excavated in Çatalhüyück (Turkey), dating between 10000 and 5000 BC (Von Landsberg, 1992; Kingery et al., 1998) showed the use of lime in the construction of floors and pavings (Mellaart 1967). Lime was widely used as a binder by Romans, who were among the first that well understood the technical aspects of its manufacturing as well as the tailoring of its properties for many different purposes. Roman architect Vitruvius, in his “De architectura”, written ~30 BC, described the manufacture and criteria of making a good quality lime mortar. It is also worth mentioning, that other ancient civilizations like India, China and some pre-Columbian American cultures (e.g., Mayans, Aztecs) used lime as a construction material (Gárate Rojas, 1994).

Since the middle of the eighteen century traditional hydrated limes (aerial limes) started to phase out, being replaced by high performance hydraulic limes. This tendency intensified in the second half of the nineteen century with the invention of Portland cement, considered to be better in terms of hardening and setting time, especially in humid environments. However, the use of cement mortars in restoration of historical masonry, which is weaker and more porous than modern construction materials, has fostered deterioration. Conversely, the use of lime mortars in restoration and conservation can increase the long-term durability of old masonry due to their compatibility with traditional building materials (Elert et al, 2002). These desirable properties and compatibility are driving forces for the increasing interest observed in recent years for the use of lime based materials in the restoration of historic structures.

1.3. The lime cycle concept

Production of traditional lime mortars, as well as any lime-based product, requires a set of operations, starting with a carbonate (e.g., dolomite, calcite) as a raw material, and ending with carbonate as the binder or solid state product. These operations are a series of successive chemical reactions, leading from one component to another. All together yield in a concept called the lime cycle (Figure 1.1).

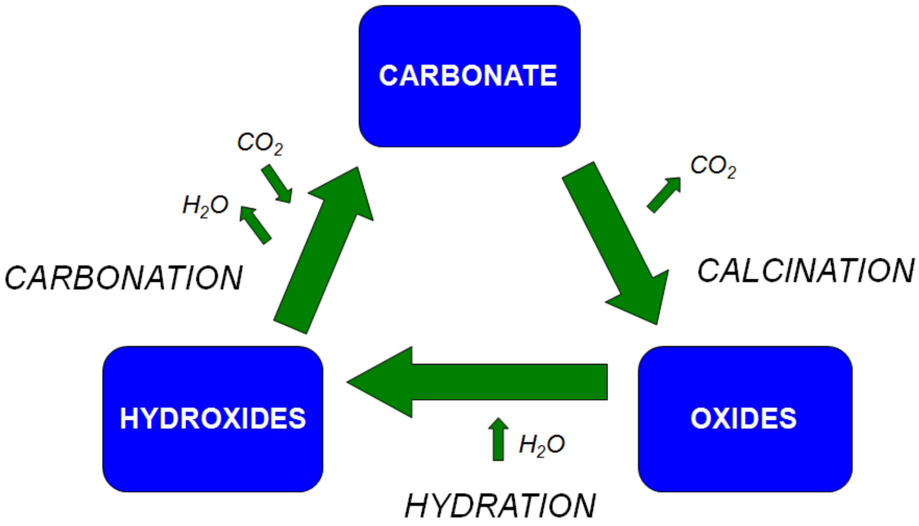

Figure 1.1. The lime cycle

The first step of the lime cycle, i.e., calcination, involves the thermal decomposition of carbonates (e.g., dolomite, calcite) into oxide(s) (e.g., quicklime) with the release of CO_2 (Rodriguez-Navarro et al., 2009, 2012). The next step of the lime cycle involves an hydration or slaking process. Water is added to quicklime, which turns into slaked lime (i.e., hydroxide(s)). The final stage of the lime cycle is carbonation. Hydroxide(s) in the presence of an aqueous phase, reacts with CO_2 (e.g., from the air), releasing water and transforming into carbonate(s), thus completing the cycle.

The conditions in which each step of the lime cycle is performed have a strong influence on the properties of the product, as well as its further development during subsequent steps (Gillott 1967). For instance, temperature and retention time during calcination control the size and reactivity of product oxide(s) (Rodriguez-Navarro et al., 2009, 2012). These parameters in turn control the kinetics of hydration and the properties of product hydroxide(s) (Wolter 2004; Ruiz-Agudo and Rodriguez-Navarro 2010). Finally, these features are expected to determine the properties of calcium carbonate formed upon carbonation of the hydrated product.

Different steps of the lime cycle, regarding both calcite and dolomite, have received various attention in the literature. For instance, thermal decomposition of calcite has been extensively studied and it is now well understood and known to be a topotactic reaction (Rodriguez-Navarro et al. 2009). In the case of dolomite thermal decomposition there is a lack of such consensus. Various models, often contradictory to each other, proposed in the literature show that such a reaction is still poorly understood. Moreover, the influence of pCO_2 on the reaction and on the selection on the mechanistic pathway (see sec. 1.4) is not well recognized (e.g., Haul and Markus 1952; Haul and Heystek 1952; Bandi and Krapf 1976; McIntosh et al. 1990; Dollimore et al. 1994). Also the crystallographic nature (epitactic/topotactic) of the reaction has not been established yet (Haul et al. 1951; Dasgupta 1967).

In the area of stone conservation, hydration of quicklime produced during calcination of dolomite (i.e., mixture of calcium oxide and magnesium oxide) and subsequent carbonation of hydrates is generally considered to be less important than hydration and carbonation of products based on calcium carbonate as a staring material (Elert et al., 2002). These processes are also more complicated from a technological and scientific point of view if compared to equivalent steps of calcitic lime cycle, including the problem of MgO reactivity (Carr 1976). These features, as well as the scope of the hydration and carbonation within the dolomitic lime cycle exclude these processes from the frame of this thesis.

Regarding hydration of calcium oxide there are two different routes described in the literature. The first one involves direct precipitation of calcium hydroxide from the solution formed upon slaked lime. The other one, known as vapor phase hydration, refers to the reaction between solid CaO and water vapor. Whereas direct precipitation of calcium hydroxide from solution has been thoroughly studied, including the problem of "aging" (Rodriguez-Navarro 1998; Ruiz-Agudo and Rodriguez-Navarro, 2010), the vapor phase hydration has attracted less attention and is still poorly understood. The mechanisms of such a reaction have not been well established yet (Ramachandran et al., 1964; Beruto et al., 1981; Wolter et al., 2004; Sato et al., 2007, Serris et al., 2011). Moreover, the problem of possible crystallographic control (epitaxy, topotaxy) in the advancement of the process is almost unnoticed (Beruto et al. 1981).

Carbonation of calcium hydroxide has received less attention than the other processes within the lime cycle. The majority of studies aimed at tailoring the size and physical properties of industrial precipitated calcium carbonate (PCC) (Uebo et al., 1992; Chen et al., 1997; Jung et al., 2000; García-Carmona et al., 2003; Doming et al., 2006). However, studies on industrial PCC production are not always directly applicable in the case of lime mortars carbonation. Other researchers have focused on the kinetics and effect of carbonation of portlandite in Portland cement (Johnstone and Glasser, 1992; Stepkowska, 2005; Glasser and Matschei, 2007). However the complex mineralogy and chemistry of this system precludes a direct application of these studies in the case of the carbonation of pure $Ca(OH)_2$. Despite some efforts (e.g., Rodriguez-Navarro et al., 2002; Cultrone et al., 2005; Cizer, 2009; Cizer et al., 2012), the study of phase and morphology evolution of calcium carbonate formed during carbonation of lime mortars is still an important need and there are several issues that remain obscure. For instance, the problem of a possible crystallographic control in the carbonation of calcium hydroxide is almost unnoticed (Gillot 1967; Stepkowska 2005).

From all the processes within the dolomitic lime cycle and the calcitic lime cycle three are considered in this thesis, i.e., 1) dolomite calcination, 2) calcium oxide hydration and 3) carbonation of calcium hydroxide. In the following section, an overview of these processes will be presented, including a literature review regarding the current stage and the main gaps in knowledge. Later on, the justification and aims of the study will be presented.

1.4. Dolomite calcination

It has been reported that depending on T and $p\mathrm{CO}_{2,}$ dolomite decomposes to final products in two different pathways: the so-called “one-step” (“one-stage”) or “full decomposition” and the “two-steps” (“two-stage”) or “half decomposition” routes. For this two reaction pathways different models, which sometimes contradict each other, have been proposed over the years, in particular regarding the “half decomposition”.

1.4.1. The one-step decomposition of dolomite

At low $p\mathrm{CO}_2$ pressure, i.e., at $p\mathrm{CO}_2$ below the equilibrium partial pressure for calcite decomposition at a given T, dolomite decomposition takes place in one step, or single stage decomposition, i.e., the so-called “full decomposition” (Haul and Heystek 1952; Haul and Markus 1952). There is however no agreement regarding the threshold $p\mathrm{CO}_2$ values at a given T. Different authors have proposed different $p\mathrm{CO}_2/T$ diagrams for this reaction (e.g., Graf and Goldsmith 1955; Powell and Searcy 1978) resulting in a high scattering of these values. For instance, Jacobs and Low (1974) reported a value of 12 Torr at 685 ºC; Powell and Searcy (1978) proposed a value of 50 Torr at 527 ºC; and Bandi and Krapf (1976) reported a higher value of 200 Torr for the decomposition of dolomite at 700 ºC. One of the possible explanation for such differences in threshold $p\mathrm{CO}_2$ may be related with experimental conditions, e.g., reaching of equilibrium, different decomposition runs including isothermal and non-isothermal ones and mass effect. This reaction is described by the following equation:

$$CaMg(CO_3)_2 \rightarrow CaO + MgO + 2CO_2 \quad (1.1)$$

This apparently straightforward reaction has been a source of a lot of controversy, in particular regarding the initial stages of the decomposition. Britton et al. (1951) proposed a model according to which dolomite decomposition results in the formation of a mixed oxide structure (Ca,Mg)O with its subsequent separation into lime (CaO) and periclase (MgO). A model proposed by Powell and Searcy (1978) assumed the formation of an amorphous mixed oxide. The model was an attempt to explain their kinetic study. Iwafuchi (1982) stated, that very low $p\mathrm{CO}_2$ facilitates the dissociation of carbonate ion (CO_3^{2-}) into O^{2-} and CO_2, what in turn leads to the formation of (Ca,Mg)O. The mixed oxide structure rapidly breaks down resulting in the formation of lime and periclase. The study on dolomite decomposition in vacuum by Spinolo and Anselmi-Tamburini (1989), reported on the formation of poorly crystalline stochiometric mixed oxide structure ($Mg_{0.5}Ca_{0.5}O$) which followed transformation into impure CaO and MgO. Cater and Buseck (1985) investigated dolomite decomposition in high vacuum, followed by its exposition to the electron-beam (in situ TEM). They showed that such a transition results in a mixed oxide with a face centered cubic structure (FCC). This initially stochiometric solution ($Mg_{0.5}Ca_{0.5}O$) underwent demixing into CaO and MgO upon long term exposure to the e-beam. Moreover, the authors stated that there is a well defined crystallographic orientation relationship between the dolomite precursor and the product solid solution. Most researchers (e.g., Engler et al. 1989) and particularly Haul´s group (Haul and Heystek 1952; Haul and Marcus 1952), concluded that dolomite decomposition at low $p\mathrm{CO}_2$ resulted in the direct formation of CaO and MgO.

1.4.2. The two-step decomposition of dolomite

At higher $p\mathrm{CO}_2$ (see above) dolomite decomposition is reported to occur via a “two-step” reaction. The first step (“half decomposition”) involves the decomposition of dolomite into calcite and periclase:

$$CaMg(CO_3)_2 \rightarrow CaCO_3 + MgO + CO_2 \quad (1.2)$$

followed by the decomposition of calcite at a *T* that depends on the experimental conditions (pCO_2, crystal size, sample mass and/or heating rate) (Lange and Roesky 1964; Milodowski et al. 1989; De Aza et al. 2002), as follows:

$$CaCO_3 \rightarrow CaO + CO_2 \quad (1.3)$$

While the mechanism of decomposition of $CaCO_3$ according to reaction 1.3 is well established and understood (Rodriguez-Navarro et al. 2009), the "half decomposition" of dolomite has been and still is a source of strong controversy. Several mutually excluding mechanistic models have been proposed for this reaction. All of them share some similarities, allowing to group them into the following models.

Model 1.

It has been proposed that dolomite decomposition takes place via its dissociation into pure calcium and magnesium carbonates, and successive decomposition of $MgCO_3$ (Schwob 1947; McIntosh et al. 1990)

$$CaMg(CO_3)_2 \rightarrow CaCO_3 + MgCO_3 \quad (1.4)$$

$$MgCO_3 \rightarrow MgO + CO_2 \quad (1.5)$$

This model however has been strongly criticized. Thermodynamic considerations performed by Spinolo and Beruto (1982) demonstrated that the thermal decomposition of dolomite does not involve the formation of $MgCO_3$. Their hypothesis has been conclusively confirmed by MacKenzie and Meinhold (1993) with the aid of ^{25}Mg solid state nuclear magnetic resonance (NMR), demonstrating that $MgCO_3$ does not occur at any stage of the decomposition. The authors suggested that dolomite should be seen as an independent mineral rather that a mixture of two carbonates (calcite and magnesite). They showed that periclase (MgO), which initially was not detectable by XRD (poorly crystalline or amorphous phase) formed at the early stages of decomposition. Despite these results, some more recent papers suggested that the half thermal decomposition of dolomite involves the dissociation into magnesite and calcite (e.g., Samtani et al. 2001).

Model 2.

Intermediate formation of a “mixed crystal” between calcite and magnesite (see Wilsdorf and Haul 1951; Hashimoto et al. 1980)

$$CaMg(CO_3)_2 \rightarrow CaCO_3(1\text{-}n)MgCO_3 + nMgO + nCO_2 \quad (1.6)$$

where *n* increases from 0 to 1 with time.

This models has been criticized for the lack of evidence for the formation of a mixed crystal solution with compositional variation between calcite and magnesite (Haul and Wilsdorf 1952). However, some authors (Hashimoto et al. 1980; Milodowski et al. 1989; Galai et al. 2007) proposed a variation of this model, with the formation of a metastable Mg-calcite solution

$$CaMg(CO_3)_2 \rightarrow CaMg_x(CO_3)_2 + (1 - x)MgO + (1 - x)CO_2 \quad (1.7)$$

where x decreases form 1 to 0 with time.

It has been shown that the 104 Bragg peak of calcite formed upon half decomposition of dolomite systematically shifts towards higher angles (smaller *d*-spacing values). This suggests some degree of substitution of Ca by Mg in the carbonate which decreases as the degree of transformation increases (Milodowski et al. 1989; Galai et al. 2007). The amount of Mg incorporated into calcite at *T* ranging 500-700 ºC is relatively small (about 6-10 mol% (Graf and Goldsmith 1955)) and increases up to 20 mol% for *T* higher than 900 ºC under very high pCO_2 (Goldsmith and Heard 1961).

Another variation of the “mixed crystal” model was proposed by Beruto et al. (2003). They suggested that dolomite “half decomposition” involves the formation of a metastable solid solution precursor, being a mixture of calcite and periclase:

$$CaMg(CO_3)_2 \rightarrow (1\text{-}x)CaCO_3(1\text{-}y)MgO + xCaCO_3 + yMgO + CO_2 \quad (1.8)$$

This model was based on the observation of Bragg peaks at 38.5, 43.5, 45 and 65 º2θ (Cu Kα radiation) which were assumed to correspond to a new phase, i.e., a solid solution of calcite and periclase. However, attempts to find a confirmation for the formation of this new phase in the literature failed. Moreover, the peaks overlap with the ones corresponding to dolomite and calcite.

Model 3.

The “recarbonation model”, which among others was suggested by Britton et al. (1952). This model states that the “half decomposition” results in the direct formation of CaO and MgO, according to Eq. 1.1 followed by the immediate recarbonation of highly reactive CaO crystals (Wiedemann and Bayer 1987), yielding the formation of calcite. This model was supported by researchers such as Lange and Roesky (1964) and Wiedemann and Bayer (1987). Moreover, Britton et al. (1952) proposed the formation of a metastable (Ca, Mg)O phase (mixed oxide solution) prior to the formation of CaO and MgO.

This model implies that the thermal decomposition of dolomite is independent of $p\text{CO}_2$, and that it does not affect the mechanisms of the reaction, which takes the same mechanistic pathways both at low $p\text{CO}_2$ (when the one-step decomposition takes place) and at high $p\text{CO}_2$ (when the “half decomposition” is assumed to occur). In other words, the so-called “half decomposition” must be an experimental effect without any influence on the mechanisms of the reaction. Despite its simplicity and straightforward explanation, this model has not received much attention in the literature.

Model 4.

The direct formation of calcite according to Eq. 1.2 appears to be the most widely accepted mechanism for the “half decomposition” of dolomite (Wilsdorf and Haul 1951; Haul and Markus 1952; Haul and Raal 1955; Bandi and Krapf 1976; Siegel et al. 1978; Engler et al. 1989; De Aza et al. 2002; Galai et al. 2007). In order to prove the correctness of this model, Haul et al. (1951) performed the thermal decomposition of dolomite in $^{13}\text{CO}_2$ enriched atmosphere. As a result they observed an enrichment of ^{13}C in the product calcite. Despite the fact that the most straightforward explanation for this result is the recarbonation of CaO with ^{13}C-enriched CO_2 present in the oven atmosphere, as discussed by Lange and Roesky (1964), Haul et al. (1951) pointed to a solid state exchange between carbonate groups in calcite and gaseous $^{13}\text{CO}_2$ that occurred due to a thermal (Hedvall) effect, thus supporting the direct formation of calcite from dolomite. Since 1951, most of published papers on the “half decomposition” followed Haul’s model without questioning the validity of the interpretation of $^{13}CO_2$ exchange experiment (e.g., Bandi and Krapf 1976; Siegel et al. 1978; Engler et al. 1989; Fazeli and Tareen 1992; De Aza et al. 2002; Maitra et al. 2005; Galai et al. 2007). Haul et al. (1951) also observed, using single crystal XRD, that calcination of dolomite results in a pseudomorph, where the product calcite shares the same crystallographic orientation with the precursor dolomite, concluding the topotactic nature of the process. On the other hand, no preferred orientation was observed in the case of MgO, in contrast to XRD analyses by Dasgupta (1967) and Hashimoto et al. (1980). However, there is still no consensus regarding the parent/product orientation relationships or the ultimate mechanism(s) of such a transformation.

Models summary

Apart from the different models for the thermal decomposition of dolomite proposed in the literature over the years, there is still ongoing debate on the role of pCO_2. It is not well recognized if it is a kinetic or a thermodynamic parameter and whether it is T-dependent or not. Some authors found no influence of pCO_2 on T for the “half decomposition” of dolomite (e.g., Haul and Markus 1952; Haul and Heystek 1952) while others reached an opposite conclusions (Bandi and Krapf 1976; McIntosh et al. 1990; Dollimore et al. 1994). Haul and Markus (1952) using thermogravimetric and differential thermal analyses showed that T for the “half decomposition” anomaly decreased with increasing pCO_2. They explained that phenomena as a change in the mechanism of dolomite thermal decomposition occurring when the pCO_2 threshold between the one-step and two-step decomposition is crossed. In contrast, Wiedemann and Bayer (1987) have shown that there is no such an anomalous behavior. They observed continuous increase in T of the endotherms corresponding to the first and the second stage of the decomposition, with increasing pCO_2, and concluded that the asymmetric shape of the first one (which may lead to an assumed decrease in T with increasing pCO_2) is the result of an overlapping recarbonation effect, i.e., weight gain in TG and/or exothermal effect in DTA following $CaO + CO_2 \rightarrow CaCO_3$.

The number of models, often contradicting each other, proposed for the one-step, and most significantly, for the two-step thermal decomposition of dolomite, shows forcibly that the mechanism(s) of such a reaction has not been established yet. One possible explanation for the persistent controversy regarding the ultimate mechanism(s) of the thermal decomposition of dolomite arises from the fact that many researchers derived their conclusions from a limited number of techniques such as TG/DTG and/or DTA, which can give only a partial view of the whole process. It seems that more suitable techniques for the identification of the intermediate and final products should be x-ray, electron, or neutron diffraction. Even when these techniques were applied, researchers have not been able to reach an agreement on the mechanisms of dolomite decomposition (see for instance Cater and Buseck 1985; Spinolo and Anselmi-Tamburini 1984a, 1984b, 1989; Engler et al. 1989; De Aza et al. 2002).

The presented overview shows that the main gaps in the knowledge regarding the thermal decomposition of dolomite can be reduced to three main problems. The first one is the lack of a valid model(s) of such a reaction. Another issue regards the influence of pCO_2 on the reaction and the selection of a mechanistic pathway. The last one is the problem of crystallographic control (epitactic/topotactic) during the reaction.

1.5. Hydration of lime (CaO)

The hydration of lime (also known as a slaking process), being the product of previously calcined calcium carbonate (i.e., calcite, aragonite) and often referred to as quicklime, is an exothermal reaction between CaO and water, resulting in calcium hydroxide:

$$CaO + H_2O = Ca(OH)_2 + 65\text{kj/mol} \quad (1.9)$$

Depending on the water/lime ratio, different types of final products are obtained. In the case of the stochiometric amount of reactants (“dry hydration”), the reaction results in a dry powder. This way of production of hydrated lime is often applied on the industrial scale. When the amount of water surpasses the amount of quicklime, an aqueous dispersion of hydroxide particles, commonly called lime paste or lime putty, is formed. Lime paste prepared in this way is also referred to as traditional slaked lime.

Numerous researches on the effect of oxide/water ratio, lime crystallite size, temperature, presence of additives and/or impurities, e.g.., alcohol, in the slaking water have been performed over the years (see Elert et al. 2002). Some efforts also have been made in order to elucidate the mechanisms of such a reaction (Ramachandran et al., 1964; Beruto et al., 1981; Wolter et al., 2004; Sato et al., 2007, Serris et al., 2011). It can be hypothesized, that the hydration may occur in two different routes. The first one involves direct precipitation of portlandite crystals from a supersaturated solution formed upon the dissolution of CaO in the slaking water. The other reaction pathway occurs as a solid state reaction between a considerable amount of CaO and water vapor. Water vaporizes under the influence of heat released during hydration (Wolter et al., 2004) and later on reacts with solid CaO. However, it is not clear how these two processes occur and what is their share in the overall reaction. There is almost no research approaching to the problem of crystallographic control (epitaxy, topotaxy) in the hydration process (Beruto et al., 1981).

Rodriguez-Navarro et al. (2005) have investigated traditional slaked limes (lime putties) and commercial hydrated lime (dry powder), showing that there are significant differences regarding their microtextural features, i.e., lime putties have a higher amount of particles with size below 1 µm. It appears that in the case of dry hydrated lime, the drying process led to two types of portlandite crystal aggregation: oriented (irreversible) and non-oriented (reversible). Oriented aggregation is responsible for an increase of the effective size of $Ca(OH)_2$ particles, i.e., aggregates, resulting in a significant reduction of parameters like surface area and reactivity, and a deterioration of rheological properties (viscosity, plasticity and workability) (Ruiz-Agudo and Rodriguez-Navarro, 2010). Conversely, the absence of drying during traditional lime slaking, leading to a lime putty, limits irreversible particle aggregation. This helps to explain why lime putties tend to have better rheological properties and are preferred in heritage conservation (Hansen at al. 2009)

Additionally, a wide range of phenomena takes place when lime putties are kept underwater for a long period of time after slaking. Such a treatment of the lime pastes is called “ageing” and involves periods of time in the order of months or years. It should be mentioned that ageing has been known and used since Roman times as a way of improving the properties of slaked lime (Cowper 1927; Ashurst 1990). This method, based on empirical observations, is commonly and successfully used in current times.

Despite the long history of this process, there was until recently an ongoing debate regarding whether or not ageing really results in any improvement of the properties of lime pastes, and if so, what are the origins and mechanisms of this phenomenon.

Rodriguez-Navarro et al. (1998) showed that ageing of lime pastes for 2 up to 10 months resulted in the reduction of the portlandite crystal size, and in an increase of the surface area of the paste. They showed that initial, most abundant portlandite crystals, with overdeveloped $\{10\bar{1}0\}$ forms underwent a preferred dissolution along (0001) planes, resulting in the increase of the amount of plate like crystals. Moreover, the secondary precipitation of planar portlandite crystals with sub-micrometer size was observed during ageing. These features, in turn, led to an increase in surface area, reactivity, dynamic viscosity and plasticity (Rodriguez-Navarro et al., 2009; Atzeni et al., 2004; Ruiz-Agudo and Rodriguez-Navarro 2010). Apart from ageing time, Ruiz-Agudo and Rodríguez-Navarro (2010) pointed to the influence of oxide precursor characteristics (hard vs. soft burnt lime) on the differences in the rheological evolution of slaked lime putties. Nevertheless, in all examined cases, an improvement of lime pastes properties was observed after long periods of ageing (a few months).

The previously hypothesized reaction between lime and water vapor (vapor phase hydration) has received much less attention than the precipitation of portlandite from lime water. Wolter (2004) proposed that such a reaction occurs when hard burnt lime contacts with liquid water, which evaporates under heat released during reaction. It should be noted that his investigations exemplified how previous steps of the lime cycle and their conditions (e.g., calcination *T*, soaking time) may influence on the selection of the hydration reaction pathways (solution mediated vs. vapor phase hydration). On the other hand, and as previously stated, the influence of the crystallographic structure of parent/product phases on the hydration reaction has remained almost unnoticed. Beruto et al. (1981) concluded that vapor-phase hydration of lime, which resulted in the formation of nanometer $Ca(OH)_2$ crystals, is a pseudomorphic reaction controlled by the structure of the reactant and product. They advanced the hypothesis that due to the structural similarities between $(111)_{lime}$ and $(001)_{portlandite}$ planes, the replacement of $O^{=}$ by two OH^{-} groups could easily occur, resulting in the topotactic formation of portlandite. If this hypothesis is correct, it would imply that microstructural characteristics of lime, like surface area, porosity and particle size, are inherited, at least partially, by the hydroxide. This mechanism could explain why and how, the different properties of quicklime influence the properties of slaked lime (Elert et al., 2002).

In summary, very limited studies on the vapor phase hydration of lime have not resulted in a model for this reaction. Moreover, there is no experimental evidence clearly showing the crystallographic relationship between lime and portlandite. In particular, there are no unambiguous results confirming or refuting the previously hypothesized topotactic nature of vapor phase hydration and its influence on the mechanism(s) of the reaction.

1.6. Carbonation of calcium hydroxide

1.6.1. An overview

Carbonation is the reaction between calcium hydroxide ($Ca(OH)_2$) and carbon dioxide (CO_2) taking place in the presence of an aqueous phase, which results in the formation of calcium carbonate ($CaCO_3$). This reaction is of great importance in industrial and geochemical areas (Doming et al., 2006). It is also a crucial process in the production of precipitated calcium carbonate (PCC), which finds applications as a filler in food, plastic, textile, paper, paint, cosmetic and pharmaceutical products (García-Carmona et al., 2003). The specific use and performance of PCC depend on its phase, morphology and physical properties (i.e., particle size, specific surface area). These parameters can be tailored by controlling the factors: reactants concentration, $[Ca^{2+}]/[CO_3^{2-}]$ ratio, dosing of additives and/or impurities (Uebo et al., 1992; Jung et al., 2000; García-Carmona et al., 2003; Doming et al., 2006 Montez-Hernandez et al., 2008). Carbonation is crucial in the hardening of traditional lime mortars, known since ancient times and used until the 19th century, when they were phased out by Portland cement (Cizer, 2009). As mentioned earlier, the use of lime based materials in restoration/conservation can increase the long-term durability of old masonry due to their compatibility with old building materials. Similar to the case of PCC production, it is necessary to determine which factors control the phase, morphology and physical properties of calcium carbonate formed upon carbonation of lime binders, in order to produce a material with desirable characteristics. The understanding of the mechanisms of calcium hydroxide carbonation is an important step in the design and application of binders to be used in the conservation of cultural heritage. Carbonation of calcium hydroxide is also an important reaction in Portland cement setting, and in its long-term performance (Johnstone and Glasser, 1992). Carbonation of portlandite, which constitutes ~20-25 wt% of hydrated cement, is known to be a process which reduces the highly alkaline pH of Portland cement. This in turn compromises the durability of cement, and is highly problematic in the case of steel-reinforced concrete (Johnstone and Glasser, 1992; Glasser and Matschei, 2007). Thus, understanding the mechanisms of portlandite carbonation in cement is a critical step for the designing of remediation strategies and for predicting its durability. Moreover, carbonation has a great potential in CO_2 sequestration (Lackner 2002; Regnault et al., 2009). The gained knowledge regarding $Ca(OH)_2$ carbonation can help in desining and optimizing new methods for capturing of such a greenhouse gas.

1.6.2. Carbonation of traditional lime mortars

Traditional lime mortars involve the mixture of calcium hydroxide with an aggregate (e.g., sand) and water. In such a system, where precipitated calcium carbonate works as a binder, the setting and hardening start with drying and shrinkage, and is followed by carbonation. The carbonation process occurs via a sequence of steps, which are (after Cizer et al., 2012):

1) diffusion of gaseous CO_2 through open pores.
2) dissolution of $Ca(OH)_2$ at the crystal surface in the pore water, followed by its dissociation as Ca^{2+} and OH^- ions, increasing the pH of the pore water up to ~12.4

$$Ca(OH)_2 \rightarrow Ca^{2+} + 2OH^- \quad (1.10)$$

3) absorption and dissolution of CO_2 in the alkaline pore water forming carbonic acid

$$CO_2 + H_2O \leftrightarrow H_2CO_3 \quad (1.11)$$

4) H_2CO_3 dissociation as bicarbonate (HCO_3^-) and bicarbonate dissociation as carbonate (CO_3^{2-}) ions

$$H_2CO_3 \leftrightarrow HCO_3^- + H^+ \quad (1.12)$$

$$HCO_3^- \leftrightarrow CO_3^{2-} + H^+ \quad (1.13)$$

5) finally, reaction between Ca^{2+} and CO_3^{2-} ions forming calcium carbonate through nucleation and subsequent crystal growth (Moorehead 1986; Van Balen and Van Gemert, 1994; Hansen et al., 2008) via the reaction:

$$Ca^{2+} + CO_3^{2-} \leftrightarrow CaCO_3 \quad (1.14)$$

The kinetics of all these interrelated processes and steps influence each other. The overall carbonation, which is an exothermic process, can be represented by the following equation:

$$Ca(OH)_2(s) + CO_2(g) \rightarrow CaCO_3(s) + H_2O(aq) + 74kJ/mol \quad (1.15)$$

In lime mortars, the carbonation reaction proceeds from the surface into the pore system at a rate controlled by drying, CO_2 diffusion, CO_2 and calcium hydroxide dissolution in the pore water, and calcium carbonate precipitation.

The pore structure and the pore water content play an important role in the progress of carbonation (Van Balen and Van Gemert, 1994; Papadakis et al., 1995; Van Balen et al., 1997; Cizer et al., 2012). The pore structure along with the pore water control the rate of CO_2 diffusion. The pore water also controls the reactants dissolution and concentration of Ca^{2+} and CO_3^{2-} ions, which latter on control the solution supersaturation and, in turn, the nucleation and growth rate of $CaCO_3$. Water evaporates upon drying leaving pores open. The overall porosity decreases with the precipitation of calcium carbonate crystals; i.e., the molar volume of $Ca(OH)_2$ is smaller than that of $CaCO_3$ (Cazalla et al. 2000), further affecting the kinetics of diffusion and dissolution processes, and the crystallization of $CaCO_3$. Ultimately, all these factors and processes will control the setting and carbonation of such a traditional lime binder. In turn, they will control the performance and durability of lime mortars which are gaining a prominent status as compatible materials for the conservation of the built heritage. Understanding how carbonation takes place and what is the ultimate mechanism of this important reaction is pivotal for the development and application of lime-based material in conservation interventions.

1.6.3. Calcium carbonate phase and morphology

One of the main problems regarding the carbonation of calcium hydroxide refers to the phase and morphology of precipitating calcium carbonate. Such a reaction results in precipitation of calcium carbonate as one of three polymorphs, i.e., calcite, aragonite or vaterite. Selection of precipitating phase depends on the reaction condition (i.e., temperature, pH and supersaturation) and on the presence of additives and/or impurities (Brečević and Nielsen, 1989; Rodriguez-Navarro et al., 2008). The most stable crystallite phase at ambient *T* and atmospheric pressure, i.e., calcite typically exhibits a $\{10\bar{1}4\}$ rhombohedral habit. Nevertheless, the $\{21\bar{3}4\}$ and $\{21\bar{3}1\}$ scalenohedra, $\{10\bar{1}0\}$ prism and $\{0001\}$ tabular habits as well as a $\{10\bar{1}1\}$ rhombohedral habit are also commonly found in nature. These morphologies are presented in Figure 1.2.

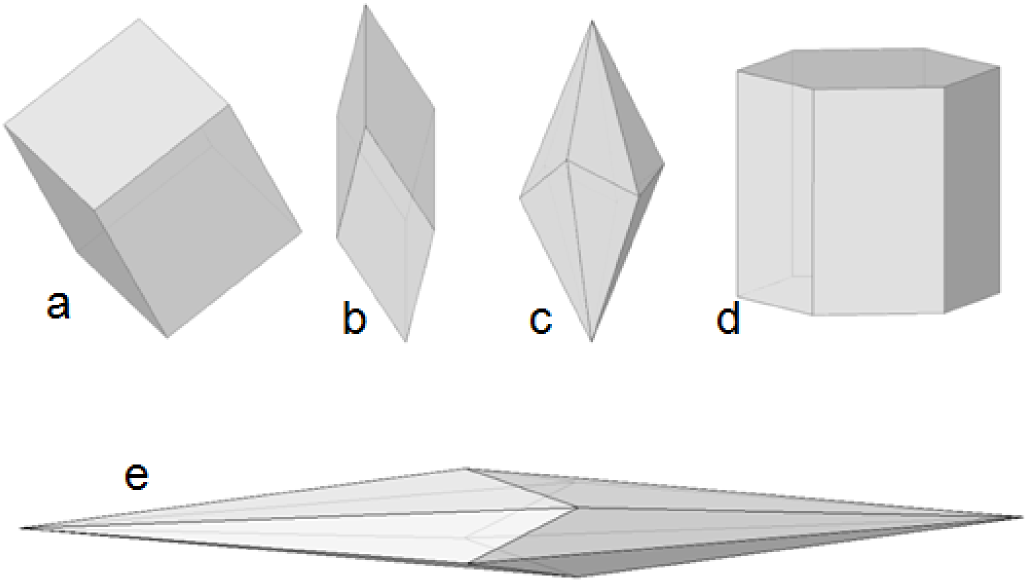

Figure 1.2. Different morphologies of calcite crystals: $\{10\bar{1}4\}$ rhombohedron (a), $\{10\bar{1}1\}$ rhombohedron (b), $\{21\bar{3}4\}$scalenohedron (c), $\{10\bar{1}0\}$prism and $\{0001\}$ pinacoid (d) and $\{21\bar{3}1\}$scalenohedron (e).

Aragonite and vaterite may play a role as a metastable precursor in the subsequent formation of stable calcite, following the so-called Ostwald rule of stages. Aragonite usually precipitates as crystals with needle like morphology, while vaterite tends to form polycrystalline spheres. Apart from crystalline phases, amorphous calcium carbonate

(ACC) may precipitate at the initial stages of carbonation, usually forming spheres with diameter smaller than 1 μm. ACC subsequently transforms into calcite as the carbonation progresses. This transformation may involve the formation of intermediate vaterite and/or aragonite according to the Ostwald's rule. The mechanism(s) of this transformation is not well understood. It has been proposed that such a transformation takes place via coupled dissolution/precipitation reaction (Aizenberg et al., 2002). Other researchers have proposed a solid state reaction following dehydration of ACC at room *T* (Radha et al., 2010).

1.7. The need for research and the aim of the study

Thermal decomposition of dolomite is of great importance in construction, steel industry, food production and pharmacy. Also, the use of dolomitic lime based binders, compositionally similar to those used in several historic structures, is gaining interest in the area of heritage conservation. Calcination of dolomite strongly influences the physicochemical properties of dolomite based products (e.g., dolomitic limes). However, despite being studied for more than a century, there is still no consensus regarding the ultimate mechanisms of thermally inducted decomposition of dolomite. There is also no agreement regarding the influence of $p\text{CO}_2$ on the reaction as well as the crystallographic nature (topotactic/epitactic) of the process.

As it has been stated earlier, hydration of calcium oxide may take two different reaction pathways. There is a lot of disproportion between published research on each of them. Whereas considerable amount of work has been dedicated to solution mediated hydration, the vapor phase hydration has been a subject of limited number of studies. The main reason for studying the hydration of lime is to complete the current knowledge regarding the possible mechanisms responsible for the transformation of lime into portlandite (dissolution/precipitation reaction, solid state reaction). It is also crucial to understand whether or not there is a crystallographic control (topotaxy/epitaxy) and its role in the advancement of the process.

Carbonation of calcium hydroxide has received less attention than other processes within the calcitic lime cycle. The majority of the research concentrated on tailoring the size and properties of industrial PCC. These result are not always directly applicable in the field of lime mortars carbonation. A lot of research aimed to study the kinetics and effects of carbonation in Portland cement. Unfortunately, the complex mineralogy and chemistry of these systems make impossible the application of these results in the case of carbonation of pure $Ca(OH)_2$. Despite some efforts (e.g., Rodriguez-Navarro et al. 2002; Cultrone et al. 2005; Cizer 2009), the phase and morphology evolution of calcium carbonate formed during carbonation of lime mortars still remains obscure. For instance, the problem of a crystallographic control in the advancement of the calcium hydroxide carbonation is almost unnoticed (Gillot 1967; Stepkowska 2005).

The aim of this study is to understand and contribute to the body of knowledge on the three different processes (i.e., calcination, hydration and carbonation) within the lime cycle and the understanding of the mechanisms of these processes (i.e., (1) dolomite thermal decomposition, (2) hydration of lime (CaO) and (3) carbonation of calcium hydroxide). All these processes are important from both scientific and technological point of view. The other goal of this thesis is also to outline possible application of the gained knowledge in the field of the conservation of cultural heritage.

2. DOLOMITE THERMAL DECOMPOSITION[*]

2.1. Introduction

Due to its scientific importance and technological relevance, the thermal decomposition of dolomite has been studied for over 100 year (Galwey and Brown 1999). Despite that fact, the reaction is still poorly understood. The various models, often contradicting each other, proposed for the “one step”, and more significantly for the “two step” routes, forcibly show that the mechanism(s) of thermally induced dolomite decomposition have not been established yet.

The goal of this part of the thesis is to understand and elucidate the ultimate mechanism(s) of thermally inducted decomposition of dolomite. In order to achieve that, textural and microstructural features of parent and product phases following calcination of dolomite, both in air (different heating conditions from flash decomposition to slow heating/long soaking time experiments), and in high vacuum (in the TEM) were studied. The crystallographic orientation relationship between the initial and final products was also examined in order to determine any possible crystallographic control in the advancement of the reaction (topotaxy/epitaxy).

2.2. Materials and Methods

2.2.1. Dolomite crystals

Dolomite crystals from Eugui, Pamplona (Spain) were used. Their high purity and quality were confirmed by powder X-ray diffraction (XRD) patterns revealing the presence of strong order (or superstructure) reflections (see Lipmann 1973). Prior to thermal treatment, crystals were cleaved using a blade in order to obtained millimeter-sized single crystals (ca 3x2x1). Prepared that way, two to three crystals with total mass ~170 mg were placed in cylindrically shaped ceramic crucibles (1.5 cm in diameter and 5

---

[*] The results presented and discussed in this chapter have been published in: Rodriguez-Navarro, C., Kudlacz, K., Ruiz-Agudo, E. (2012) The mechanisms of thermal decomposition of dolomite: New insights from 2D-XRD and TEM analyses. American Mineralogist 97, 38-51.

cm in height) and subjected to calcination in an air ventilated electric furnace (Select-Horn, Selecta). Two different calcination runs, here denoted as run A and run B, were performed. At least three repetitions of each run were made. During run A, after placing the samples inside, the oven was heated form 25 ºC up to the target *T* at a heating rate of 2 °C·min^{-1}. Once the target *T* was reached, a retention (soaking) time of 30 min was applied before reaching the next target *T*, at 50 ºC steps from 500 ºC up to 1000 ºC. In run B ("flash decomposition") the oven was heated form 25 ºC up to 400 ºC, and then samples were placed inside for one hour. The main purpose of this procedure was to release strain and avoid decrepitation of crystals during the following steps of thermal treatment, causing their jumping out of the crucible. This relatively low *T* did not result in decomposition of dolomite single crystals as confirmed by XRD and TEM analysis Subsequently, the oven was heated to the target *T* at a heating rate of 2 °C·min^{-1} (500-800 °C, 50 °C intervals). At each target *T*, samples were place inside the oven for 15 min. Moreover, two additional runs with a retention time of 5 and 10 min at 650 ºC and 700 ºC were performed in order to collect detailed information on calcium carbonate during the two-stage decomposition of dolomite. After soaking at each target *T* in both run A and run B, samples were collected, cooled down at room *T*, weighed, and introduced in tightly capped vials under dry N_2 atmosphere prior to further analysis.

Thermogravimetric (TG) analyses of the decomposition of dolomite single crystals were performed in flowing (100 cm^3·min^{-1}) air atmosphere on a Shimadzu TGA-50H analyzer equipped with a Mettler-Toledo AX26 Delta Range microbalance. For each TG run *T* was risen from 25 ºC up to 950 ºC at 2, 5, 10, and 15 ºC·min^{-1} heating rates. Dolomite single crystals with size of 2x2x1 mm (~10 mg) were placed into platinum crucibles. Such a small size of crystals was selected in order to minimize the mass effect which in turn leads to an increase of local (around and within crystal) $p\mathrm{CO}_2$. Weight loss of decomposed crystals was recorded at regular time intervals.

2.2.2. Mineralogical and textural analysis by XRD and 2D-XRD

Analysis of phase evolution during dolomite calcination at different *T* was performed using a Philips PW-1710 diffractometer with Cu Kα radiation (λ = 1.5405 Å). Data were collected from 20 to 70 °2θ at a counting rate of 0.03 °2θ s^{-1}. Prior to XRD patterns collection, samples were placed on zero-background silicon sample holder and then placed inside the diffractometer chamber. XRD analyses of calcined dolomite samples involved both the analysis of calcined dolomite single crystals (pseudomorphs) oriented with their $\{10\bar{1}4\}$ cleavage plane parallel to the sample holder and analysis of samples grinded in an agate mortar.

Pole figures describing the 3D orientation relationships between pseudomorphs and product crystals, i.e., between dolomite precursor and Ca and Mg oxides, were determined using an X-ray single crystal diffractometer equipped with an area detector (D8 SMART APEX, Bruker). For these 2D-XRD experiments, the working conditions were: Mo Kα (λ = 0.7093 Å), 50 kV and 30 mA, a pin-hole collimator of 0.5 mm in diameter, and an exposure time of 20 s per frame. Dolomite pseudomorphs were measured by reflection (diffractometer ω and 2θ angles were set at 10 and 20 degrees, respectively) resting flat on one of the cleavage rhombohedral faces. A set of frames (2D diffraction patterns) was registered while rotating the sample around φ angle (a frame every 5 degrees; a total of 36 frames). Pole densities for the strongest reflections of dolomite were calculated and displayed in stereographic projection using the XRD2DScan software (Rodriguez-Navarro 2006). Each pole figure displays the intensity variation of a given *hkl* reflection as a function of the sample orientation. From these plots, the 3D orientation of associated {*hkl*} faces was observed. Due to experimental constraints during 2D-XRD data collection, pole figures only represent planes with $\rho < 85°$ (where ρ is the angle between a given (*hkl*) face and the normal to the plane of projection). The evolution of crystallite size as a function of calcination *T* was performed with the aid of the XPowder software (Martin-Ramos 2004).

2.2.3. Electron microscopy analyses

The shape, morphology, size and structure of dolomite and products of calcination were examined with the aid of field emission scanning electron microscopy (FESEM), model Leo Gemini 1530 and transmission electron microscopy (TEM) using a Philips CM20, operated at a 200 kV acceleration voltage. Prior to TEM analyses samples were grinded in agate mortar, dispersed in ethanol, subjected to 60 second ultrasonic bath and finally deposited on Formbar-coated or carbon-coated copper grids. Bright field TEM observations were performed using a 40 µm objective aperture. Selected area electron diffraction (SAED) patterns were collected using a 10 µm aperture, which allowed collection of diffraction data from a circular area of 0.5 µm in diameter. In-situ decomposition of dolomite crystals (2-5 µm in size) following e-beam irradiation was also investigated using TEM (i.e., high vacuum conditions). The electron flux was maximized using a large (200 µm) condenser aperture and a focused beam spot size of ~200 nm, thus providing an estimated electron flux of ca. 50-70 $A\cdot cm^{-2}$. At this conditions full transformation was achieved after ~1-5 min of e-beam exposure. Prior to FESEM analysis, dolomite single crystal pseudomorphs, calcined at different *T* were placed onto carbon coated sticky stubs before carbon coating.

2.3. Results and discussion

2.3.1. Calcination and weight loss

Thermal decomposition of dolomite single crystals (runs A and B) resulted in pseudomorphs that fully preserved the external shape of the $\{10\bar{1}4\}$ rhombohedron. The cross-cut section of the partially decomposed pseudomorphs showed a transparent rhombohedron core surrounded by a brownish external shell. This observation points to a strong crystallographic control in the advancement of the reactant-product interface while the reaction progresses towards the core of the sample. It should be mentioned, that very similar observation were made in the case of thermally induced decomposition of other rhombohedral carbonates, like calcite (Rodriguez-Navarro et al., 2009).

Dolomite single crystals weight loss as a function of *T* for calcination in the TG at a heating rate of 10 $^{\circ}C\cdot min^{-1}$ is presented in Figure 2.1. TG results obtained at heating rates 2, 5 and 15 $^{\circ}C\cdot min^{-1}$ showed sudden and significant weight loss in the *T* range 285-500 ºC making impossible to consider the data as reliable ones. This effect can be associated with decrepitation of dolomite crystals (McCauley and Johnson 1991; Dollimore et al. 1994). TG results show that the decomposition of dolomite single crystals in air takes place via a one step route (e.g., Bandi and Krapf 1976). Decomposition starts at ~500 ºC, progressing at a relatively slow rate up to 750 ºC, when a higher, almost constant decomposition rate was observed up to ~900 ºC, i.e., up to the full decomposition. On the other hand, a two stage weight loss was observed in the decomposition performed in the electric furnace under air atmosphere and at a heating rate of 2 ºC·min^{-1} (run **A**) (Figure 2.1). The transition between the first and the second step of the decomposition occurred within a short range of *T* (650-750 ºC). This tendency is in agreement with other studies reporting a two stage decomposition in air (Lange and Roesky 1964; Engler et al. 1989), and has been observed when $p\text{CO}_2$ was close to the transition between a one-step and a two-step decomposition mechanism (Haul and Marcus 1955; Bandi and Krapf 1976; Wiedemann and Bayer 1987). Factors like static atmosphere and differences in sample mass seem to have a strong influence on the weight loss trends observed in TG and furnace experiments (run **A**). In particular, mass effect influences a self-generated CO_2 atmosphere, which induces a two-stage decomposition process above a critical threshold mass value (Sharp et al. 1990; Samtani et al. 2001). Final weight loss ranged from 44.6-45.6 wt % in the case of TG, and up to 47.1 wt % in run A. These values are in agreement with the theoretical prediction of weight loss for pure, stochiometric dolomite which amounts to 47.7 wt % (Powell and Searcy 1978).

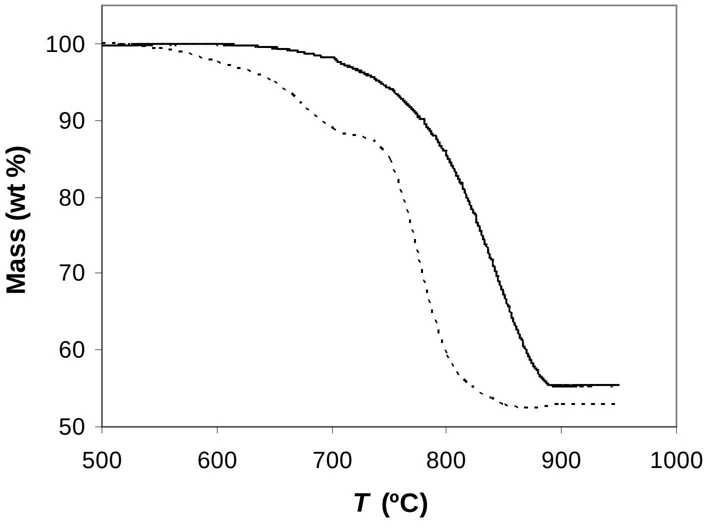

Figure 2.1. Weight loss of dolomite single crystals as a function of *T* calcined (in air) in the TG at a heating rate of 10 ºC/min (solid line) and in the electric furnace at a heating rate of 2 ºC/min (dashed line).

2.3.2. Powder XRD

Powder XRD analysis of grinded dolomite pseudomorphs from run A, showed the presence of dolomite Bragg peaks up to 800-850 ºC (Figure 2.2). This suggests that there is no significant thermally induced changes in dolomite structure prior to the decomposition. Also, reflections corresponding to magnesite were not observed at any stage of the calcination. These results contradicts previous models assuming the decomposition of dolomite into two carbonates (Model 1), i.e., calcite ($CaCO_3$) and magnesite ($MgCO_3$), and those proposing the formation of Ca-rich and Mg-rich carbonate precursors prior to the formation of pure oxide products (Model 2). At 600 ºC, Bragg peaks of 200_{MgO} and 200_{CaO} appeared (Figure 2.2), confirming the presence of calcium and magnesium oxide. However, resolving of these peaks was difficult due to their profile features, i.e., 200_{MgO} was broad and small, while the more intense 200_{CaO} overlapped with the $110_{dolomite}$ peak. At this T the degree of conversion α was 0.05 ($\alpha = M_0 - M_T/M_F$, where M_0 is the mass of dolomite at the beginning of the experiment, M_T is the mass at a given T, and M_F is the mass at the end of the full decomposition). No oxide product was detected at lower T (i.e., at $\alpha < 0.05$). Possible explanations for this situation may be related with the dilution of oxides in the grinded sample, as well as with poor crystallinity or even amorphous character of the oxides at the initial stage of their formation (Britton et al. 1952; Powell and Searcy 1978). The observed evolution of lime and periclase Bragg peaks along with already published results seem to support this idea. CaO and MgO Bragg peaks initially occur as small and broad, transforming into high and sharp with increasing T (Figure 2.2). Moreover, Engler et al. (1989) reported the XRD detection of lime and periclase at a T about 100-200 ºC higher than that corresponding to the beginning of decomposition determined by TG and/or DTA. The in-situ XRD study by Readman and Blom (2005) also showed a reduction in the intensity of dolomite peaks at T ~200 ºC lower than that corresponding to the appearance of first oxides peaks.

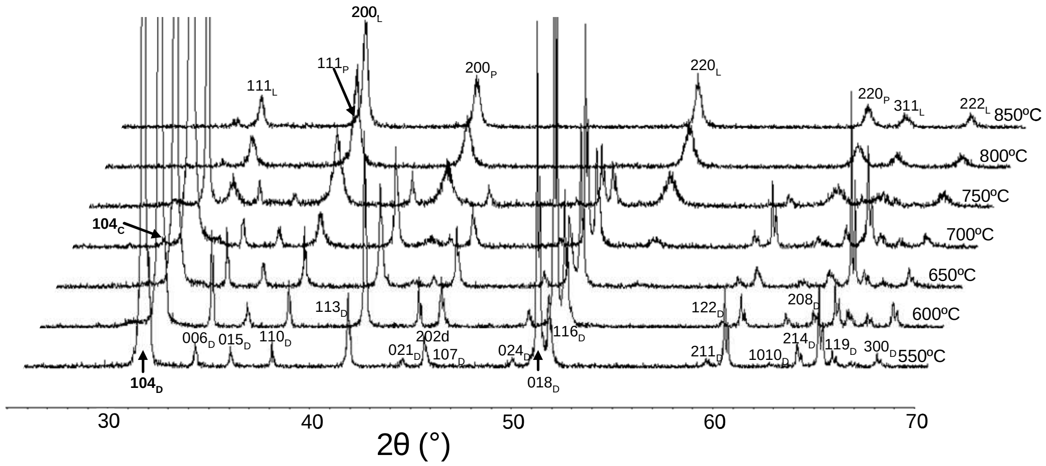

Figure 2.2. Powder XRD patterns of grinded dolomite pseudomorphs calcined at different *T* in run A. Indicated phases: D-dolomite, C-Mg-calcite, L-lime, P-periclase.

Powder XRD patterns in the *T* range 650-750 ºC showed broad, low intensity peak, whose *d*-spacing varied from 3.005 Å (at the lowest *T*) up to 3.03 Å (when *T* reached 750 ºC). This peak corresponds to $104_{\text{Mg-Calcite}}$, initially containing ~9 mol % Mg (Goldsmith and Graf 1958) which releases Mg with increasing *T*. Better resolution of this peak was obtained in single crystal pseudomorphs which were not subjected to grinding (see below). The formation of Mg-calcite is associated with a mass effect leading to the increase of local $p\text{CO}_2$ (i.e., around the calcined crystal), sufficient to trigger the “half decomposition” in air and resulting in the two-stage weight loss (Figure 2.1). There are other studies reporting the formation of Mg-calcite during the “half decomposition”. However no agreement on how this phase is formed was reached. Lange and Roesky (1964) stated that Mg-calcite formed along with MgO and CaO, was a product of recarbonation of impure CaO (i.e., Model 3). The presence of a CaO fraction, which did not underwent a recarbonation was an effect of insufficient $p\text{CO}_2$. Hashimoto et al. (1980) suggested that Mg-calcite is formed directly from dolomite during its half decomposition under CO_2 atmosphere (Model 2). Milodowski et al. (1989) concluded that the first stage of dolomite decomposition in a CO_2 atmosphere results in a direct formation of Mg-calcite (with 5-10 mol% Mg) which tends to release Mg out of its structure with progressing decomposition (increasing *T*) (Model 4). Their mechanistic model for dolomite decomposition into Mg-calcite is derived from the high-T, high-pCO_2 dolomite-magnesium calcite phase diagram proposed by Graf and Goldsmith (1955), based on equilibrium thermodynamics. However, dolomite decomposition is a non-isothermal process, far from equilibrium, ruled by kinetics rather than by thermodynamics (Haul and Markus 1952). Fazeli and Tareen (1992) showed that calcite with 10 mol % Mg is formed during dolomite half decomposition in CO_2 atmosphere as well as in air. The formation of Mg-calcite in air was also confirmed by De Aza et al. (2002) in their neutron diffraction study. In both cases the authors agreed that this phase is formed directly after dolomite (Model 4). Other authors also consented that Mg-calcite is formed after dolomite during the “half decomposition” and becomes less Mg-rich as the reaction progresses with increasing T (Maitra et al. 2005; Galai et al. 2007). Results presented here confirm that Mg-calcite is a phase produced after the “half decomposition” of dolomite and decreases in Mg content with increasing T. The decreasing Mg content within its structure can be explained by thermally induced Mg ions diffusion (whose diameter is smaller than Ca ions) out of the carbonate structure (Milodowski et al. 1989; Readman and Blom 2005). However, the direct formation of Mg-calcite is not consistent with results presented here, as will be discussed later on.

2.3.3. XRD of single crystal pseudomorphs

XRD analysis of single crystal pseudomorphs (run A) show no product phases at T below 550 ºC. Similar to the case of grinded samples, small and broad Bragg peaks of lime and periclase were initially detected at 600 ºC (Figure 2.3). Due to pseudomorphs orientation, i.e., orientation along dolomite precursor cleavage plane, only 104_{dolomite} and 208_{dolomite} reflections were observed, showing significantly lower intensity if compared to grinded samples. This feature facilitated the unambiguous identification and resolving of 200_{CaO} peak, which overlapped with the 110_{dolomite} in the previous case (Figure 2.2). As the transformation progressed with increasing T, CaO and MgO peaks intensity increased and these peaks became better defined. At 650 ºC, the 104_{dolomite} peak continued decreasing in intensity. Moreover, a new reflection at d-spacing of 3.01 Å corresponding to Mg-calcite with ~8 mol % Mg appeared. Despite being relatively broad, it revealed a better definition and a higher intensity than that of grinded samples (Figure 2.2). At 750 ºC and above, neither Mg-calcite nor calcite peaks were present in calcined pseudomorphs. Dolomite 104 Bragg peak decreased in intensity, as opposed to lime and periclase Bragg peaks which became higher and sharper, and fully disappeared at 800 ºC. These observations suggest that Mg-calcite was an intermediate phase developing on the pseudomorph surface, which with increasing *T* transformed into calcite, and finally decomposed into CaO and CO_2 (Figure 2.3)

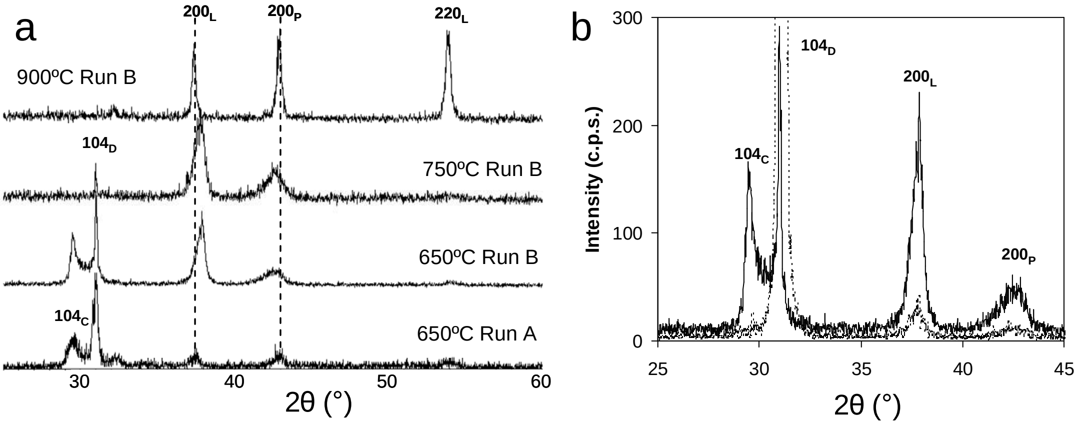

Figure 2.3. XRD patterns of dolomite single crystal pseudomorphs calcined at different *T* in runs A and B. Note the shifting of 200_{oxide} peaks of run B pseudomorphs from their theoretical position (dashed vertical lines) (a). Details of single crystal pseudomorphs (run B) calcined for 5 min (dotted line pattern) and 15 min (solid line pattern) (b). Mg-calcite 104 Bragg peak appears after 15 min calcination, while oxide 200 peaks are already present after 5 min calcination time.

Crystallite size evolution of CaO and MgO products as a function of *T* is presented in Figure 2.4. Due to the small peak size, the calculation of crystallite size was performed for samples calcined in the *T* range 750-1000 ºC. The crystallite size increased from 15-19 nm (750 ºC) up to 36-44 nm (1000 ºC), and from 12-16 nm (750 ºC) up to 38-44 nm (1000 ºC) in the case of CaO and MgO, respectively (Figure 2.4). It appears that nascent CaO and MgO nanocrystals coarsened due to oriented aggregation and sintering. Similar formation of CaO nanocrystals has been described in the case of the thermal decomposition of calcite (Rodriguez-Navarro et al. 2009). These results also reveal similarities in CaO and MgO crystallite size. A similar trend in the evolution of crystallite size with *T* was reported by Haul and Raal (1955). However, in the case of their study, the crystallite size varies from 9 nm (MgO) and 12 nm (CaO) at 750 ºC, up to 100 nm at 1000 ºC, what could be associated with enhanced sintering in a CO_2 atmosphere (Beruto et al. 2003a, 2003b). Spinolo and Anselmi-Tamburini (1984b) have shown that during the initial stages of the decomposition in vacuum, when no sintering occurs, the crystalline size remains constant, with size of ~5 nm and ~30 nm for CaO and MgO. The reported values are lower and higher, respectively, than crystallite sizes measured here at 750 ºC.

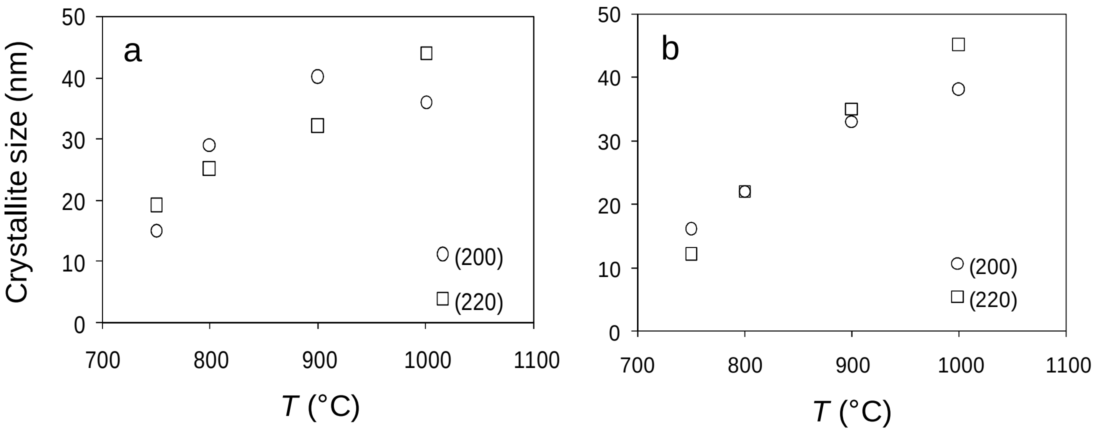

Figure 2.4. Crystallite size evolution with *T* of (a) lime and (b) periclase, calculated from broadening of 200 and 220 Bragg peaks.

In the case of run B, first CaO and MgO Bragg peaks appeared at 650 ºC. Their appearance at *T* 50 ºC higher in the case of run B (here also denoted as "flash" decomposition), is associated with a shorter soaking time, if compared to run A. In all runs performed, dolomite was present at *T* ranging from 500 ºC up to 750 ºC, and disappeared at 800 ºC (Figure 2.3a). At 650 ºC, $104_{\text{Mg-Calcite}}$ (~5-7 mol% Mg) was recorded along with CaO and MgO Bragg peaks, and was not observed at higher *T*. In comparison, in grinded samples (run A) the peak was present up to 750 ºC. These results indicate that after the carbonate was formed on the sample surface it underwent a fast decomposition and its reaction front progressed towards the sample core, as it has been described in the case of calcite (Rodriguez-Navarro et al., 2009). Britton et al. (1952)

observed that the calcite layer formed during thermal decomposition of dolomite lags the dolomite reaction front. It should mentioned that when Cu Kα radiation is used, only the outer surface of ~100 nm thickness effectively contributes to XRD. Flash decomposition with 5 and 10 min time performed at 650 ºC did not show the presence of Mg-calcite, or revealed small $104_{\text{Mg-calcite}}$ Bragg peak along with small and broad 200_{CaO} and 200_{MgO} respectively. The $104_{\text{Mg-calcite}}$ peak intensity, as well as the intensities of 200_{CaO} and 200_{MgO} peaks, increased significantly after 15 min soaking time. These results show that Mg-calcite formation is favored under longer retention times at constant T, i.e., when a higher degree of decomposition is reached, and that the formation of Mg-calcite is preceded by the formation of oxides product (CaO and MgO). It appears, that the formation of Mg-calcite is the result of recarbonation of nascent CaO and MgO mixed crystals (i.e., forming (Ca,Mg)O).

Pseudomorphs calcined at 550-800 ºC (Figure 2.3a) showed a systematic shifting of the Bragg peaks of CaO and MgO towards higher and lower 2θ angles, respectively. The shift was more noticeable in the case of run B than in the case of run A. This is clearly seen when XRD patterns of run A and run B samples calcined at T 650-750 ºC are directly compared (Figure 2.3a). These results point to the existence of a (partial) solid solution of CaO and MgO (Spinolo and Anselmi-Tamburini 1984). It should be mentioned that the thermal decomposition of mixed metal carbonates has been proposed as an efficient synthesis pathway for complex metal oxides with a broad range of solid solution compositions (Rao and Gopalakrishnan 1987).

The mol percentage of each oxide in the solid solution was calculated using the following equation:

$$C_{ss} = 100 \frac{\left| X_{theor} - X_{\exp} \right|}{\Delta d_{hkl}} \qquad (2.1)$$

where X_{theor} and X_{exp} are the theoretical and experimental d_{hkl}-spacing (in Å), respectively, of a given hkl_{CaO} or hkl_{MgO} peak and Δd_{hkl} the difference between the theoretical d_{hkl}-spacing of a given hkl_{CaO} and the corresponding hkl_{MgO}. Despite some irregularities in the peak profile evolution (broadness, asymmetry) with T, which in turn lead to data scattering, a clear tendency for each oxide to become purer with increasing T was observed in both runs A and B (Figure 2.5). Similar results were obtained by

Readman and Blom (2005). The strong dependence of this effect on the calcination *T* as well as on the soaking time at a given *T*, what is illustrated by the different degree of ion substitution in run A and run B calcined at the same *T*, can be explained considering that higher *T* and/or longer soaking time favor de-mixing of the initial mixed oxide structure via counter diffusion of Ca and Mg ions leading to pure CaO and MgO. These findings are fully consistent with results obtained from flash decomposition with 5 min soaking time at *T* 650 – 750 ºC, showing the highest values of cation substitution: 9.5-11 mol% Mg in CaO and 5-7 mol% Ca in MgO. The different kinetics of Ca and Mg diffusion out of mixed oxide solid solutions is explained by the differences in radius of Ca (0.99 Å) and Mg (0.66 Å) (Fisler and Cygan, 1999). The diffusion of smaller Mg ions out of Mg-calcite structure is faster than Ca, leading to the higher initial amount of Ca in MgO, whereas the initial amount of Mg in CaO is fully lost at the same *T*.

The formation and evolution with *T* of the mixed oxide structure can be explained with the aid of the model of dolomite thermal decomposition in vacuum proposed by Spinolo and Anselmi-Tamburini (1989). The authors showed that the initial stage of the decomposition involved the formation of a face centered cubic mixed oxide structure $Mg_{0.5}Ca_{0.5}O$, which rapidly follows de-mixing via spinodal decomposition leading to CaO and MgO with certain degree of substitution by Mg and Ca ions, respectively (denoted here as CaOss and MgOss, ss-solid solution). The degree of substitution between oxides is described by the spinodal curve in the CaO-MgO phase diagram, where the maximal amount of Mg in CaO and Ca in MgO at *T* 650-750 ºC equals 17 mol% and 9 mol%, respectively (Spinolo and Anselmi-Tamburini 1989), and which are similar to those presented here. XRD analysis failed to detect the initial $Mg_{0.5}Ca_{0.5}O$ phase reported by Spinolo and Anselmi-Tamburini (1985) and by Cater and Busek (1985) in their high vacuum, in-situ TEM observations. It appears that during dolomite decomposition in air or in a CO_2 atmosphere, where the decomposition occurs at higher *T* comparing to vacuum, the higher mobility of Ca and Mg ions may cause the fast transformation of the mixed oxide structure into impure CaO and MgO solid solutions. The problems associated with the observation of such a metastable phase may explain why there is no study reporting the formation $Mg_{0.5}Ca_{0.5}O$ during dolomite decomposition in air or in CO_2 atmosphere.

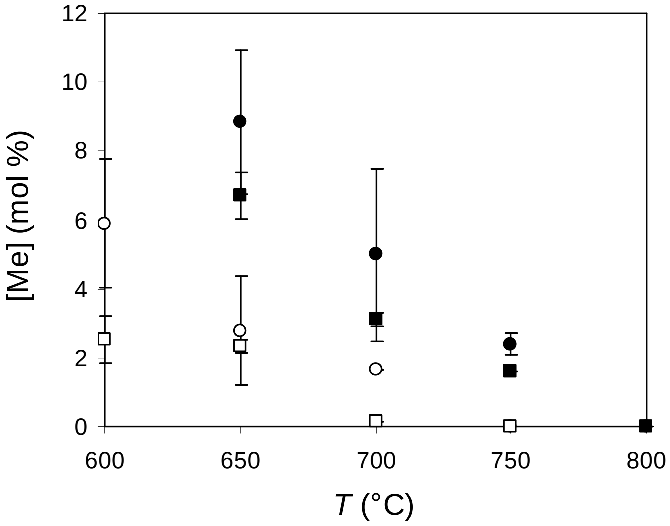

Figure 2.5. Variation of Me (Me = Mg or Ca) concentration in the product oxide solid solution with calcination *T*. Legend: solid symbols (Run B), empty symbols (Run A); circle = Mg in CaO; square = Ca in MgO.

2.3.4. Orientation relationships: 2D-XRD results

The low degree of conversion at *T* below 750 ºC prevented the identification of any preferred orientation of the oxide products in the calcined pseudomorphs. On the other hand, pole figures of pseudomorphs calcined at a higher *T*, both in run A and B, reveal strong preferred orientation of CaO and MgO crystals (Figure 2.6). Two sets of $\{100\}_{CaO}$ and $\{100\}_{MgO}$ planes were oriented nearly parallel (~12º) to $\{10\bar{1}4\}_{dolomite}$ ($(10\bar{1}4)_{dolomite}$ is the projection plane (Figure 2.6)). Set 1 (Figure 2.6 b and d) shows that $[100]_{CaO}$ and $[100]_{MgO}$ were parallel to $[841]_{dolomite}$ (being one of the $<\bar{4}41>_{dolomite}$ equivalent directions). Set 2 (Figure 2.6 b and d) defined in the case of MgO, was located at 180º rotating along the normal to the projection plane. It displays the same crystallographic parent/product orientation relationship like Set 1, but with respect to a dolomite precursor twinned along $(10\bar{1}\bar{2})$ plane following the dolomite $\{10\bar{1}\bar{2}\}$ twin law (scheme in Figure 2.6a). The dolomite twinning is favored at high *T* (Barber and Wenk 1979), and most probably was associated with stress release during decrepitation. It resulted in two sets of dolomite precursors with the $[841]_{dolomite}$ directions forming an angle of ~30º with respect to each other. The pole figures of $\{220\}_{CaO}$, $\{222\}_{CaO}$, $\{220\}_{MgO}$ and $\{222\}_{MgO}$ pointed to the presence of two sets of CaO and MgO crystals, oriented with their [100] poles at ~ 30º with respect to each other. The pole figure of $\{220\}_{CaO}$ (Figure 2.6b), as well as that of $\{220\}_{MgO}$, showed the following parent/product orientation relationships: $\{11\bar{2}0\}_{dolomite}//\{110\}_{oxide}$, $\{11\bar{2}8\}_{dolomite}//\{110\}_{oxide}$. The observed orientation of Set 1 of oxide product(s) with respect to the dolomite precursor is presented in Figure 2.6. A 180º rotation of Set 1 around a direction normal to the projection plane leads to the orientation of Set 2. At 750 ºC a clear preferred orientation of Mg-calcite with respect to the dolomite precursor was also observed (Figure 2.6f), with the following orientation relationships: a) $(10\bar{1}4)_{dolomite}$ nearly parallel to $(10\bar{1}4)_{Mg\text{-}calcite}$ and b) $(11\bar{2}0)_{dolomite}//(11\bar{2}0)_{Mg\text{-}calcite}$. The Mg-calcite orientation corresponded to the orientation of the second subset of twinned dolomite, i.e., this orientation being the result of a 180º rotation of the dolomite crystal presented in the Figure 2.6. around a direction normal to the projection plane. This suggests that the poorly defined orientation of $(200)_{CaO}$ of Set 2 (Figure 2.6a) is the result of a reduction in intensity of the 200 Bragg peak corresponding to this set of CaO crystals, after they underwent a partial recarbonation leading to Mg-calcite preserving the orientation of oxide precursor.

Pole figures of pseudomorphs calcined at 800, 900 and 1000 ºC compared to those from pseudomorphs calcined at 750 ºC showed the same sets of crystals, with additional, well defined maxima of $(200)_{CaO}$. These spots correspond to two sets of crystals, oriented with respect to each other at 90º, and at an angle of 30º (Set 3) and 60º (Set 4) with respect to the $(10\bar{1}4)_{dolomite}$ pole (Figure 2.6g). These orientation relationships were also present in pseudomorphs calcined at 750 ºC but were not that well defined (Figure 2.6b). Similar orientation features were observed in the case of calcite thermal decomposition (Rodriguez-Navarro et al. 2009) and are in agreement with XRD results of pseudomorphs calcined at $T \geq 800$ ºC. It appears that the orientation relationships of Set 1 and Set 2 are developed at the initial stages of the dolomite decomposition, whereas the orientation relationships of Set 3 and Set 4 correspond to the decomposition of Mg-calcite formed during the “half decomposition” of dolomite.

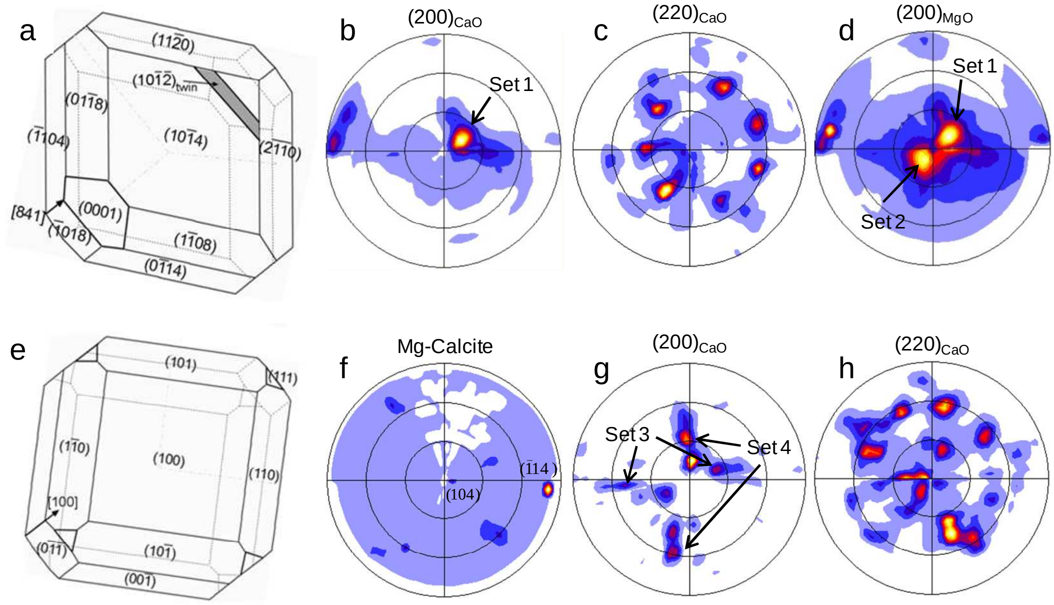

Figure 2.6. Pole figures of dolomite single crystals decomposition products: (a) scheme of a dolomite rhombohedron resting flat on its $(10\bar{1}4)$ face (relevant crystal faces are depicted, as well as a slab–shaded- corresponding to the $(10\bar{1}\bar{2})$ twin plane); (b) (200) and (c) (220) pole figures of CaO; (d) (200) pole figure of MgO. Note the existence of two sets (Sets 1 and 2) of CaO and MgO crystals with (100) planes forming an angle of ca. 12º with $(10\bar{1}4)_{dolomite}$ and with their poles rotated 180 º with respect to each other, thus resulting in the two maxima in the (200) pole figures, best observed in (d). Set 1 displays the following orientation relationship: $[841]_{dolomite}//[100]_{oxide}$ and $\{11\bar{2}0\}_{dolomite}//(110)_{oxide}$ as it is graphically displayed in the scheme of the oxide product (e). Set 2 displays an identical orientation relationship with respect to the twined slab depicted in (a); (f) (104) pole figure of Mg-calcite present at 750 ºC, showing that the twined slab in (a) shares the same orientation. At 1000 ºC, the (200) pole figure of CaO (g) shows additional maxima corresponding to two sets of CaO crystals with (100) planes rotated ca. 90 º (Sets 3 and 4) and forming and angle of 30º and 60º with respect to the $(10\bar{1}4)$ pole of dolomite. The corresponding (220) pole figure of CaO (h) shows a maximum parallel to the $(10\bar{1}4)$ pole figure of the former Mg-calcite.

2.3.5. FESEM analysis of pseudomorphs

FESEM observations of the microtextural characteristics of the pseudomorphs from run A generally offered a better insight into dolomite calcination and its evolution with *T*, if compared with those from run B. Therefore, the following section will be concentrated on the presentation and discussion of the results obtained from the analysis of run A samples.

Thermally induced microstructural changes were first observed in samples calcined at 600 ºC. Close examination of the dolomite $(10\bar{1}4)$ plane revealed the formation of a highly porous anhedral texture composed of crystal aggregates with nanometer size (~20-90 nm). (Figure 2.7a). The same textural features were observed in pseudomorphs calcined at 700 ºC. Figure 2.7b shows the development of cross-cutting cracks and growth of a subset of crystals, with size ranging from 100 up to 400 nm and with better defined crystal faces (inset in Figure 2.7b), on the surface of the pseudomorphs. These larger crystals were more abundant under the surface layer, and displayed a highly oriented arrangement (Figure 2.7c). They were lined by the nanocrystals shown in the inset of Figure 2.7a (i.e., MgO and CaO nanocrystals). These observations imply that: (i) either these larger crystals are CaO or MgO that underwent a very rapid oriented aggregation and coarsening (sintering) or (ii) they are Mg-$CaCO_3$ crystals formed after the carbonation of (impure) CaO nanocrystals due to the build up of CO_2 pressure as the calcination front moved towards the core of the dolomite crystal. The first hypothesis contradicts the XRD crystallite size measurements, which show similar sizes of CaO and MgO crystallites at each stage of calcination. In contrast, the second hypothesis is in agreement with XRD results revealing the formation of Mg-calcite in samples calcined at 650-700 ºC. At 750-800 ºC, the development of highly oriented cracks was observed (Figure 2.7d), with the transformed rims located underneath, made up of highly oriented, elongated, blade-shaped crystals (Figure 2.7e). The formation of these cracks is most probably the result of stress release, which occurs when a decomposed layer, formed on the untransformed dolomite core, reaches a critical thickness (~50 μm). Accumulation of stress is due to the differences in molar volume between dolomite and product phases (Beruto et al. 2004). Stress release contributes to the difusionless coarsening of oxide nanocrystals via an oriented attachment. Thus, it should be considered as an important driving force in dolomite, as well as other carbonate (e.g., calcite), thermally induced decomposition (Rodriguez-Navarro et al. 2009). As a result of such an oriented attachment, the cracks also present a high degree of orientation. The crystallographic relationships between dolomite precursor and product oxides derived from the analysis of the pole figures, i.e., $\{11\bar{2}0\}_{dolomite}//\{110\}_{oxide}$ and $\{11\bar{2}8\}_{dolomite}//\{110\}_{oxide}$ indicate that the oxide crystal blades, shown in Figure 2.7e are parallel to the cracks lips, which means that they are oriented with $[110]_{oxide}$ parallel to either $[010]_{dolomite}$ or $[2\bar{2}1]_{dolomite}$.

At 750 ºC, the pseudomorph surface showed an homogenous texture made up of crystals ~50-100 nm in size, with no further transformation in deeper layer. XRD results showed the disappearance of Mg-calcite at the pseudomorph surface at 700-750 ºC. Therefore, the origin of these textural changes seems to be the result of the decomposition of Mg-calcite precursor on the outer layer. At 800 ºC the reaction front depth was ~100 µm. At 850 ºC the surface cracks were still observed and disappearance of larger crystals lined by nanocrystals observed on the pseudomorph surface at 650-700 ºC occurred in deeper parts. In their place, highly porous and homogenous aggregate of anhedral nanocrystals ~50-100 nm in size developed, both on the surface as well as in deeper parts of the pseudomorph (Figure 2.7f). As mentioned earlier, this texture developed as a result of Mg-calcite decomposition. These observations are in agreement with XRD and weight loss measurements, showing that the plateau in the mass% vs. T corresponding to the formation of Mg-calcite, expanded from 650 ºC up to ~800ºC. At 900 ºC the first symptoms of intensive sintering were observed (Figure 2.8a). Sintered crystals, as confirmed by 2D-XRD results, did not undergo any changing in crystallographic orientation. At 1000 ºC sintering reached a higher degree leading to the creation of CaO and MgO crystal aggregates of micrometer size (Figure 2.8b). It should be noted, that such a coarsening has been reported by other authors (e.g., Fonseca et al. 1998).

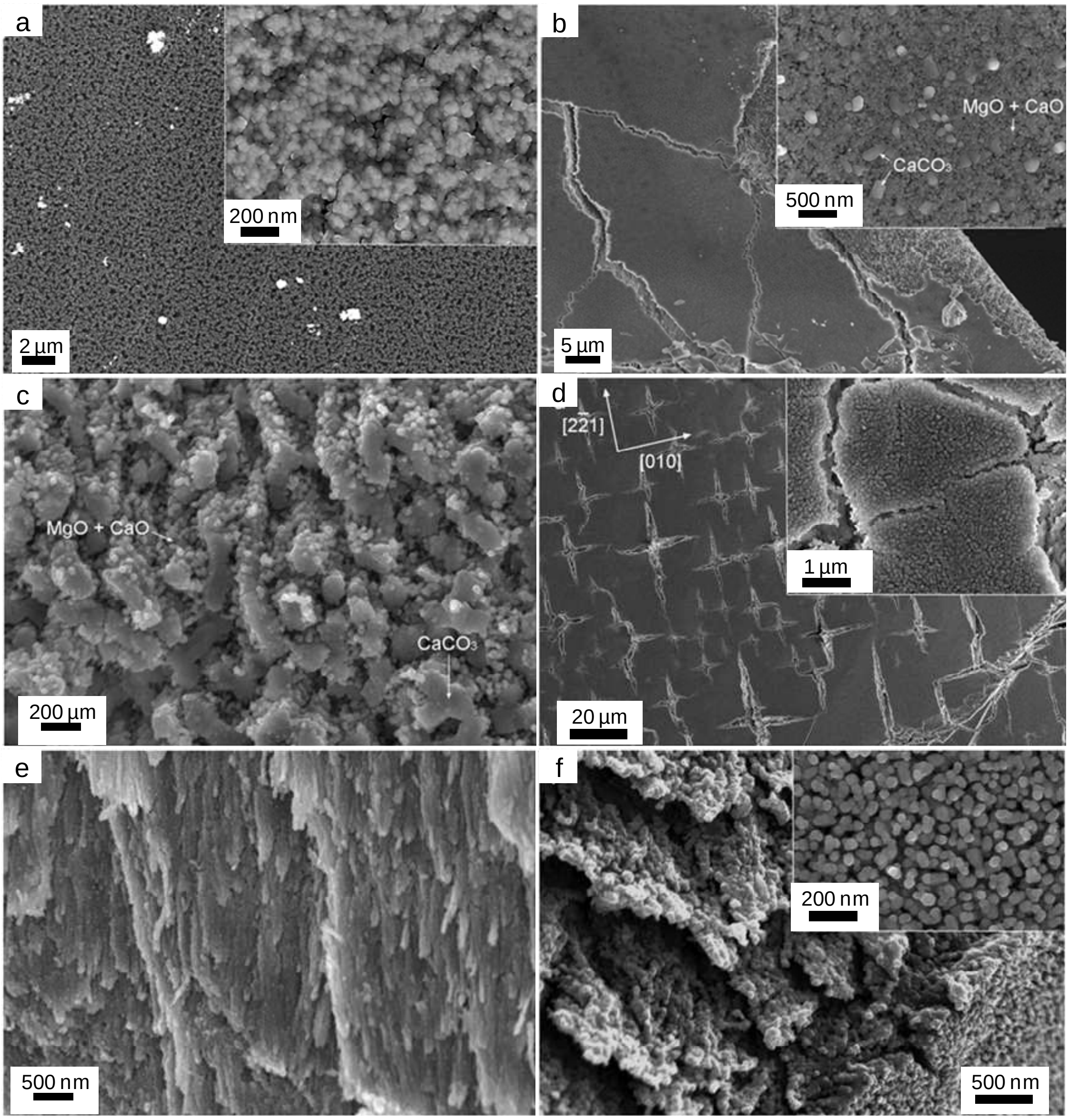

Figure 2.7. FESEM images of calcined dolomite pseudomorphs: a) porous aggregate of oxide nanocrystals (details in inset) formed at 600 ºC; b) initial development of cross-cutting cracks at 700 ºC and growth of a randomly distributed subset of Mg-calcite crystals (up to 100-400 nm in size) with better defined crystal faces (inset) than the oxide nanocrystals; c) detail of larger (0.2-1 µm in size), oriented calcite crystals surrounded by oxide nanocrystals underneath the surface of the pseudomorph calcined at 700 ºC; d) oriented, star-shaped cracks formed at 750 ºC (see detail in inset); e) blade-shaped oriented crystals growing at 750 ºC in a section normal to the dolomite pseudomorph

cleavage plane; f) porous aggregate of oxide nanocrystals formed at 850 ºC after the decomposition of the carbonate (see detail in inset).

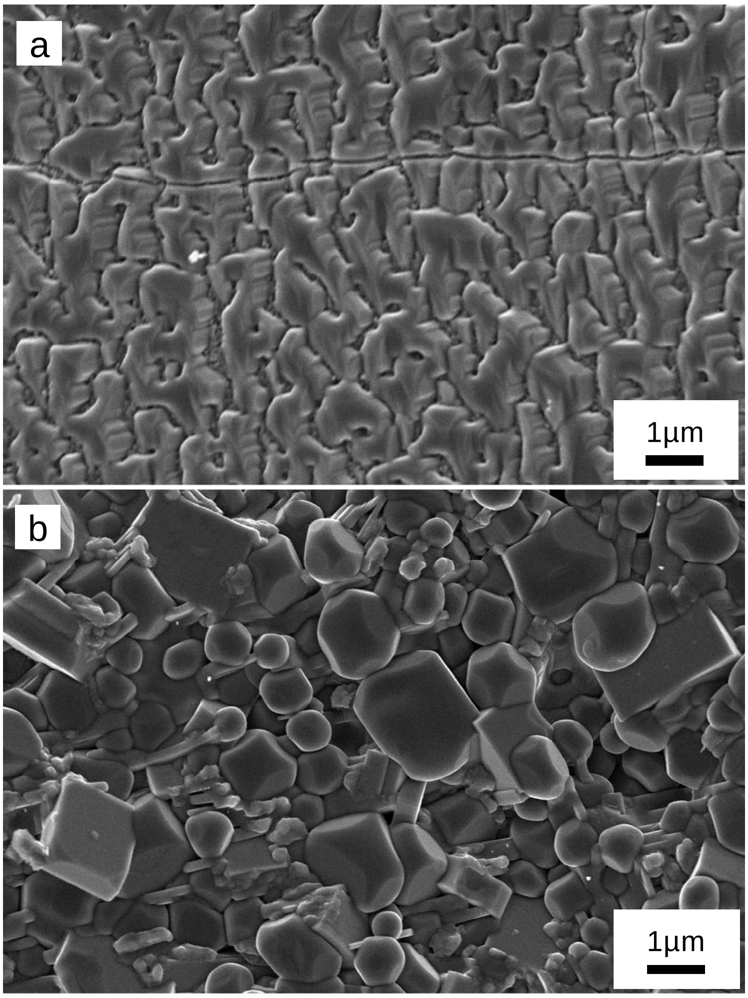

Figure 2.8. FESEM of dolomite pseudomorphs calcined in air: a) oriented aggregate of oxide products showing sintering at 900 ºC; b) oxide crystals sintered at 1000 ºC.

2.3.6. TEM analysis of the pseudomorphs

Ex situ TEM analyses did not revealed any oxide products in pseudomorphs calcined below 600 ºC (run A). The most probable explanation is that due to the small degree of conversion ($\alpha \leq 0.02$) the probability of spotting the partially transformed area was very low. At 600 ºC, the formation of scattered aggregates made of oriented oxide nanocrystals (~5-10 nm) usually at grain edges or lining fractures, was observed (Figure 2.9a). SAED patterns showed only the spots of twinned dolomite (i.e., two sets of 110* and 018* reciprocal vectors (Figure 2.9b)) and a few diffuse and weak rings corresponding to an unidentified, amorphous or poorly crystalline product(s) phase. At 650 ºC, the formation of thin and porous rims, made of nanometric oxide crystals, surrounding the undecomposed dolomite core was observed (Figure 2.9c and Figure 2.9d). Figure 2.9e presents a SAED pattern along $[1\bar{1}0]_{dolomite}$ showing dolomite spots and diffuse spots of $200_{(Mg,Ca)O}$. The presence of spots corresponding to oxide products indicates their preferred orientation. The oxide product d_{200}-spacing equals 2.15 Å, what according to Eq. 2.1. yields a mixed oxide structure with formula $Mg_{0.86}Ca_{0.14}O$. This observed mixing degree of MgO and CaO solid solution, which corresponds to the early stage of the dolomite decomposition is higher than that observed at higher *T* with the aid of XRD. Other spots, with *d*-spacing of 2.98 Å, which do not correspond to dolomite or the oxide product, were also observed. This *d*-spacing value corresponds to the 104 Bragg peak of Mg-calcite with 16.8 mol% Mg. Such a value, however, is higher than the value established from XRD measurements. These differences may come as a result of *d*-spacing measurement error (from SAED pattern). It is also possible that at relatively low *T*, during the initial stages of the decomposition, Mg-calcite contains more Mg, which diffuses out of the calcite structure with increasing *T* and soaking time. The overlapping of two sets of $[1\bar{1}0]_{dolomite}$ zone-axis SAED patterns was observed (reciprocal lattice vectors marked as 1* and 2* in Figure 2.9e). The source of this phenomena is related with twinning deformation following the$\{01\bar{1}2\}$ twin law, most probably induced by the *T* increase. Like in the case of the thermal decomposition of calcite (Rodriguez-Navarro et al. 2009), the development of twin crystals partially masked the orientation relationship(s) between parent and product phases. However, the occurrence of twinning deformation explains the development of two sets of oriented oxide product crystals observed using 2D-XRD (Figure 2.6).

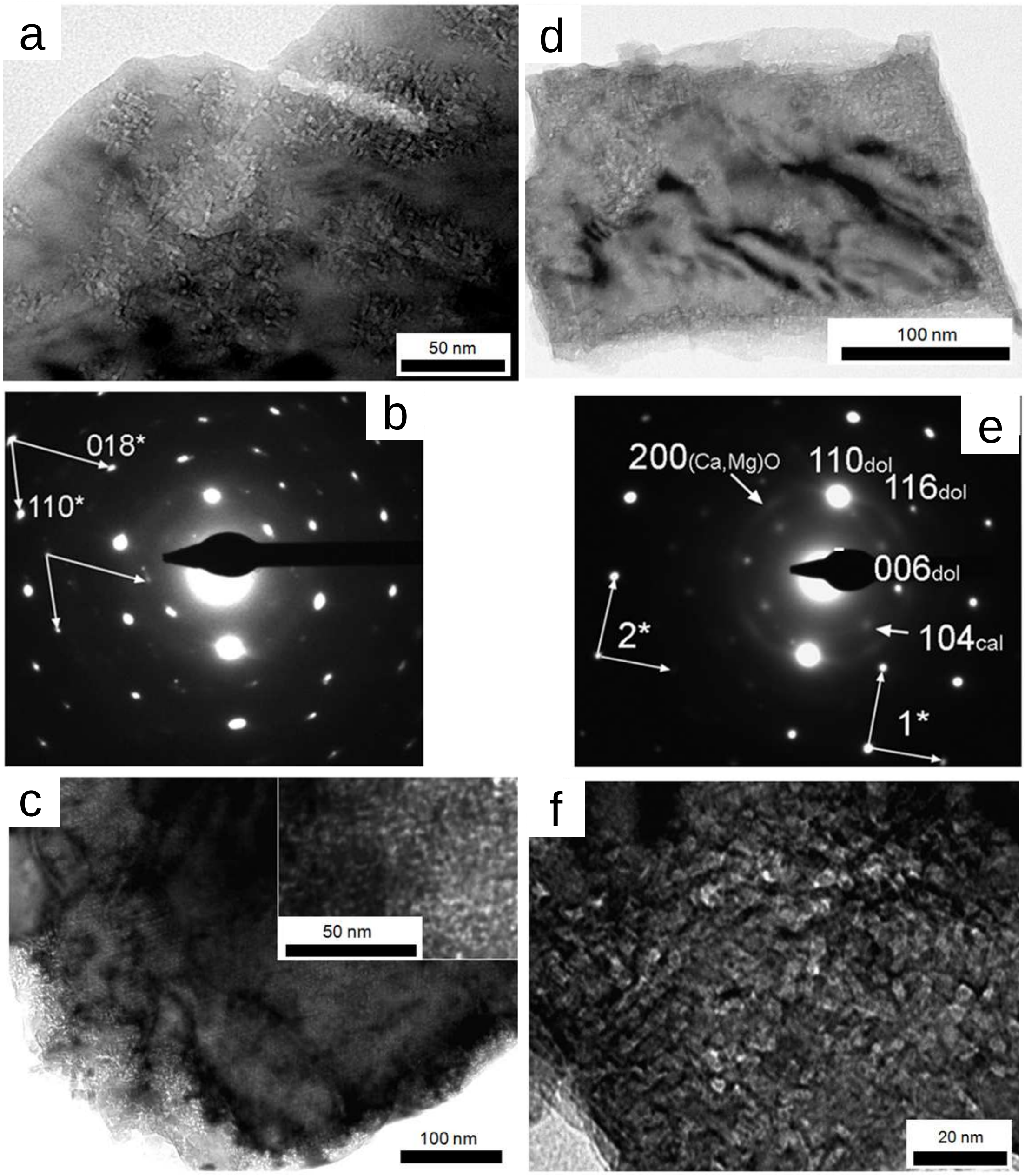

Figure 2.9. TEM images of dolomite pseudomorphs calcined in air. Initial decomposition at 600 ºC resulting in the formation of oriented nanocrystals lining fractures (a) and corresponding SAED pattern along $[8\bar{8}1]$ zone axis (b) showing two reciprocal lattices corresponding to twinned dolomite. Formation of porous pseudomorph at 650 ºC where oxide product nanocrystals formed at the grain edges (details in inset) (c). Pseudomorph partially transformed at the edges (calcined at 650 ºC) (d) and corresponding SAED

pattern (e) showing the twinned dolomite (reciprocal vectors of two lattices, 1* and 2*) and diffraction spots corresponding to oriented (Ca,Mg)O and Mg-calcite. Details of oriented nanocrystals (f) formed at the transformed edge of the pseudomorph shown in (d).

Pseudomorphs calcined at 850 - 950 ºC show well oriented, larger CaO and smaller MgO crystals. In some cases, CaO crystals surrounded MgO ones (Figure 2.10a), which has been reported as a typical feature of sintered doloma (Fonseca et al. 1998). As calcination *T* increases, the oriented aggregates of CaO and MgO nanocrystals tend to grow (Figure 2.10b). These is in agreement with 2D-XRD and FESEM observation regarding crystal coarsening via oriented aggregation and sintering.

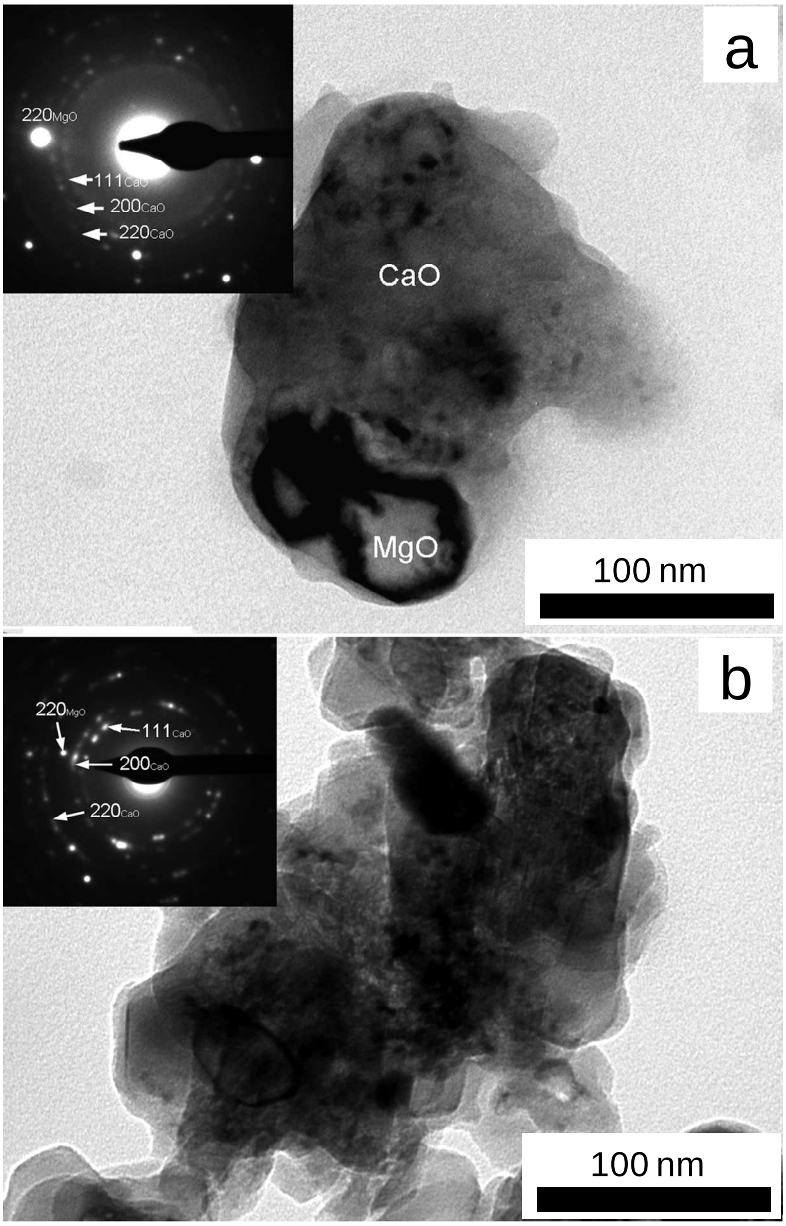

Figure 2.10. TEM images of pseudomorphs calcined in air: a) MgO crystals surrounded by CaO crystals (SAED in inset) formed at 850°C; b) oriented aggregates of CaO and MgO nanocrystals (SAED in inset) formed at 950 °C.

2.3.7. In-situ TEM decomposition

Decomposition of dolomite crystals (~2–5 µm in size) was induced by e-beam exposure for 2-5 min, using a large 200 µm condenser aperture. The use of a smaller 100 µm condenser aperture did not result in decomposition of dolomite within 30 min exposure time. Cater and Buseck (1985) suggested that the e-beam induced decomposition of dolomite occurs due to direct bond breaking (radiolysis), which is expected to be independent of condenser aperture size. This is not supported by the experimental evidence, showing a strong correlation between condenser size and the appearance of an effect. The e-beam decomposition of dolomite seems to be a thermal phenomenon (Egerton and Malack 2004).

Nanostructural changes of pseudomorphs at the initial stages of decomposition (Figure 2.11a) involved the formation of a mottled structure (Wenk et al. 1983). The full decomposition resulted in highly porous aggregates made up of two sets of nanocrystals, crosscutting at ~90°, with sizes between 1 and 5 nm (Figure 2.11b).

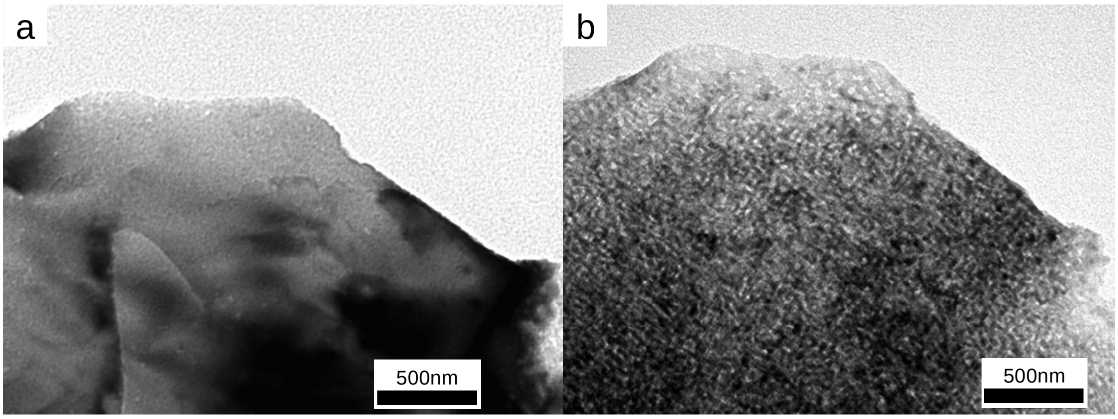

Figure 2.11. TEM images of dolomite crystal decomposed in-situ: the beginning of e-beam irradiation (a) and full decomposition achieved after 5 min, resulting in the formation of a porous pseudomorph made up of oriented oxide product nanocrystals (b)

SAED patterns of the pseudomorphs after full decomposition (Figure 2.12 and Figure 2.13) correspond to a single oxide phase with FCC structure (Cater and Buseck, 1985). The elliptical shape of the diffraction spots points to a poorly crystalline and highly oriented aggregate. Measured oxide d_{hkl}-spacings are as follows: d_{111} = 2.63 Å;

d_{200} = 2.21 Å, and d_{220} = 1.58 Å. These values are intermediate to d_{hkl}-spacings of CaO (d_{111} = 2.77 Å; d_{200} = 2.40 Å, d_{220} = 1.70 Å) and MgO (d_{111} = 2.43 Å; d_{200} = 2.10 Å, d_{220} = 1.49 Å) and correspond to the FCC mixed oxide structure, described by the formula $Mg_{0.5}Ca_{0.5}O$. During one of the decomposition runs, demixing of oxide into oxides (CaOss and MgOss) upon long e-beam exposure was observed, leading to the separation of each elliptical spots in the SAED pattern into two parallel elliptical spots (Figure 2.14). Measured d_{hkl}-spacings corresponds to oxides with $Ca_{0.75}Mg_{0.25}O$ and $Ca_{0.15}Mg_{0.85}O$ formulas. These compositions are in agreement with the results obtained for the pseudomorphs calcined in air at 650 ºC, and are consistent with those defined for the coherent spinodal curve in the CaO-MgO system (Spinolo and Anselmi-Tamburini 1989).

The two main orientation relationships between dolomite precursor and mixed oxide product revealed by SAED patterns are the following: (1) $[\bar{4}41]_{dolomite}//[100]_{oxide}$, with $(11\bar{2}0)_{dolomite}//(011)_{oxide}$, $(11\bar{2}8)_{dolomite}//(01\bar{1})_{oxide}$, and $(10\bar{1}4)_{dolomite} \wedge (010)_{oxide}$ ~12º (Figure 2.12); and b) $[001]_{dolomite}//[111]_{oxide}$ with $\{11\bar{2}0\}_{dolomite}//\{110\}_{oxide}$ (Figure 2.13). These crystallographic orientation relationships are fully consistent with those determined by 2D-XRD analysis of the pseudomorphs calcined in air. The second orientation relationship was also reported by Cater and Buseck (1985).

It should be mentioned that e-beam irradiation of dolomite can result in twinning as well as in its deformation. This in turn can lead to the formation of dolomite crystallites with different orientation. This situation is depicted in Figure 2.13b, where the development of cracks introduces some degree of misorientation into the product oxide crystals resulting in additional and weak 111 and 200 Debye rings. A similar phenomenon is presented in Figure 2.14b, where the $[001]_{\text{dolomite}}$ zone axis SAED pattern shows extra reflections. As a consequence, the SAED patterns of nanocrystals oxide product show intense spots corresponding to the $[111]_{\text{oxide}}$ zone axis, along with additional and less intense spots corresponding to 111 and 200 oxide reflections. As it has been shown in the case of calcite thermal decomposition, this effect may be responsible for masking the orientation relationship between parent and product phase (Rodriguez-Navarro et al., 2009).

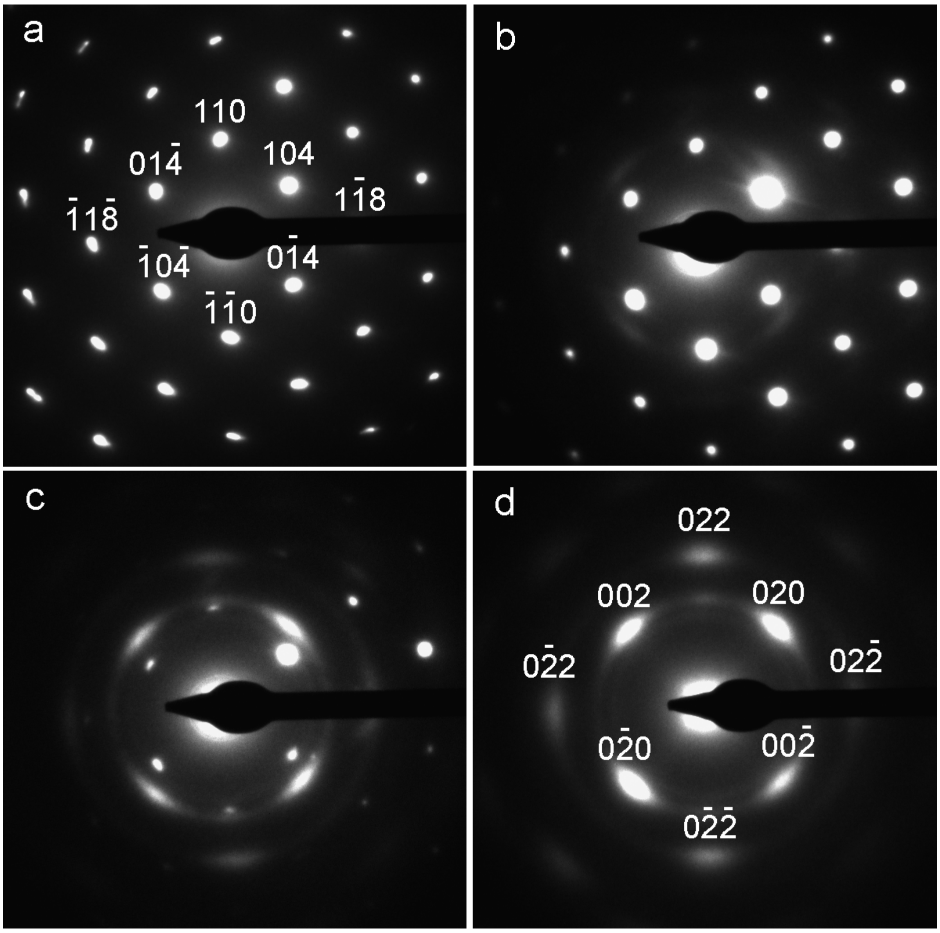

Figure 2.12. SAED sequence of in-situ (e-beam induced) dolomite decomposition resulting in the formation of (Ca,Mg)O. a) dolomite $[\bar{4}41]$ zone axis pattern before decomposition; b) initial decomposition shown by the appearance of elliptical spots of the oxide; c) further decomposition and d) complete transformation into oriented oxide crystals with their [100] zone axis parallel to dolomite $[\bar{4}41]$.

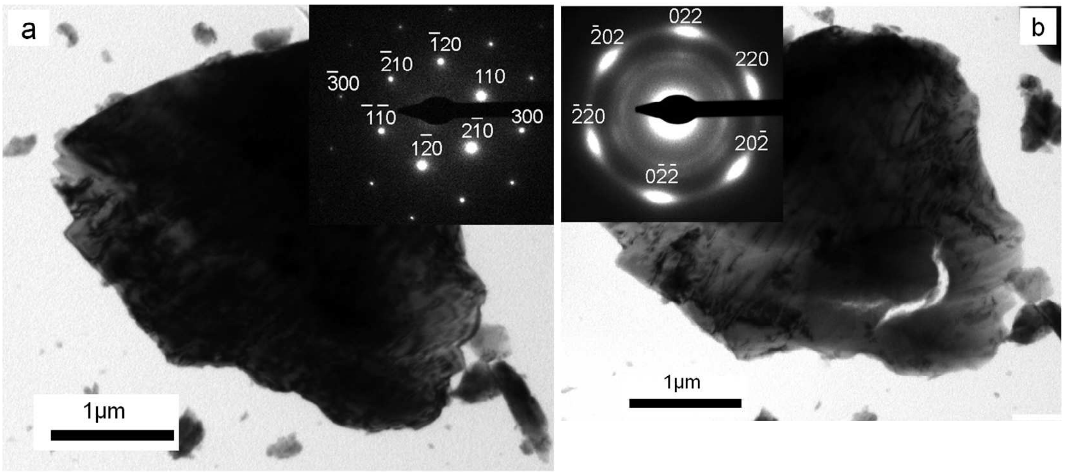

Figure 2.13. TEM images of dolomite crystal: a) before e-beam decomposition. The [001] zone axis SAED pattern of dolomite is shown in inset; and b) after 5 min e-beam irradiation, resulting in full decomposition into a porous pseudomorph made up of oriented oxide nanocrystals. The [111] zone axis SAED pattern of the oxide is shown in inset. Additional weak Debye rings corresponding 111 and 200 oxide reflections are also observed.

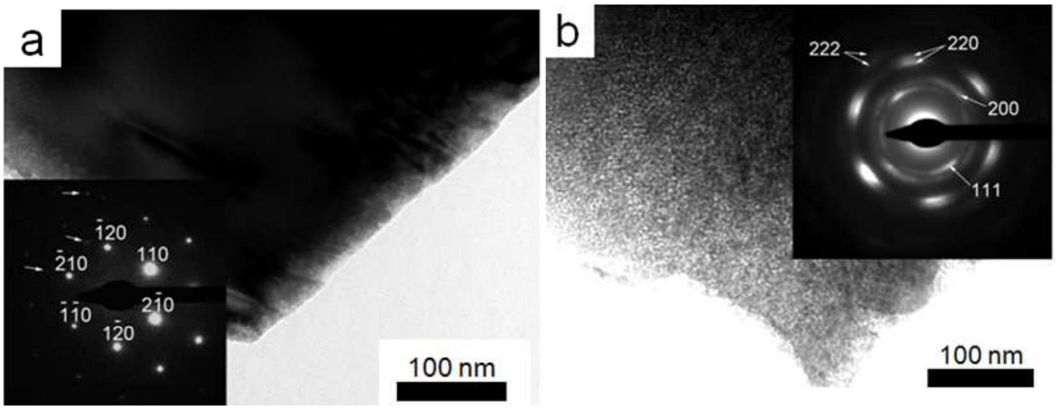

Figure 2.14. TEM images of dolomite crystal: a) right at the beginning of e-beam irradiation. The [001] dolomite zone axis SAED pattern (inset) shows extra spots (arrows) corresponding to the reciprocal lattice of a twined section; and b) after 5 min irradiation, resulting in full decomposition into a porous pseudomorph made up of oriented oxide nanocrystals. The [111] oxide zone axis SAED pattern shows splitted spots due to demixing of (Ca,Mg)O. Additional 111 and 200 oxide reflections (showing splitting) are observed.

2.3.8. The mechanism of thermal decomposition of dolomite.

In-situ TEM results showing the formation of metastable mixed-oxide phase ($Mg_{0.5}Ca_{0.5}O$) with FCC structure during dolomite decomposition in vacuum are in agreement with findings presented by Cater and Buseck (1985) and Spinolo and Anselmi-Tamburini (1989), as well as with the hypothesis on the formation of such a precursor of CaO and MgO, proposed by Britton et al. (1952) and Powell and Searcy (1978). As it has been shown by Spinolo and Anselmi-Tamburini (1989), this mixed-oxide structure undergoes spinodal decomposition into impure calcium and magnesium oxides. This was also observed here, both following decomposition in vacuum (TEM) and in air. Cater and Buseck (1985) observed the formation of CaO and MgO from mixed oxide precursor, upon long time exposure to the e-beam, via an intermediated amorphous phase. A possible explanation for this phenomenon could be related to the features of the dolomite sample used by these authors, i.e., synthetic crystals of 0.1 to 20 µm size. The unusual decomposition pathway of disordered, microcrystalline dolomite was reported by other researchers (Navrotsky et al., 1999). Continuous preservation of the preferred parent/product orientation relationship was observed at every stage of the transition, including the formation of mixed oxide structure, and its subsequent transformation into CaO and MgO. Therefore the formation of an intermediate amorphous phase, at any stage of the process, seems to be rather improbable. Otherwise, the loss of the crystallographic information following the formation of an amorphous phase would be expected. This, however, does not preclude the possibility of the formation of a poorly crystalline intermediate phase with short range order. Such a metastable phase may very likely transform into crystalline, highly oriented product oxide(s), that can coarsen via an oriented aggregation mechanism (Penn and Banfield, 1998). For instance, the transformation of an amorphous phase, characterized by short-range order into a crystalline one, of which both bear a strong structural resemblances, has been reported in the case of the transformation of amorphous calcium carbonate (ACC) into a specific calcium carbonate polymorph (Lam et al. 2007).

As shown by XRD analyses, the decomposition in air results in the formation of impure CaO (with up to 12 mol% Mg) and MgO (with up to 8 mol% Ca). On the other hand, TEM-SAED examinations of pseudomorphs calcined at 650 ºC indicate higher degree of ion substitution in the mixed oxide structure. These observations suggest, that the initial stages of the decomposition in air should involve the formation of a mixed oxide precursor with stochiometry similar to that observed during in-situ TEM decomposition. However, the rapid spinodal decomposition of such a mixed oxide prevents its detection. It can be suggested, that soaking time and increasing *T* are main factors responsible for the demixing process and subsequent formation of pure CaO and MgO via diffusion out of their structures of Mg and Ca ions, respectively. The fact that the nascent mixed oxide structure presents poor crystallinity may be the reason why it was not detected by XRD at a *T* range 500-600 ºC. Moreover, despite the fact that the degree of transformation at this *T* range reached up to 5% no oxide products were recorded. This problem has also been noticed by several authors. McKenzie and Meinhold (1993) in their NMR study, showed the development of MgO with no simultaneous detection of any oxide product by XRD, concluding the formation of poorly crystalline or amorphous MgO. The authors did not take into account the CaO and its role in the process. Nevertheless, their findings along with those presented here suggest that the initial oxide should contain stochiometric amounts of Ca and Mg ions. After spinodal demixing occurs, resulting in the formation of CaOss and MgOss, these products could be detected by XRD. Further increase in *T* with time leads to purification of lime and periclase, as indicated by XRD results.

Decomposition of dolomite, both in vacuum (in-situ TEM) and in air, results in oxide products exhibiting preferred crystallographic orientation with respect to the dolomite precursor. Regardless of decomposition pathway (in air or in vacuum), the orientation relationship remains identical in each case. The orientation of oxides with respect to dolomite shows a three dimensional relationship, indicating the topotactic nature of the process. A comparison between dolomite and FCC oxide (lime, periclase or mixed oxide) structures shows good matching between dolomite alternating layers of metal and carbonate ions along the c-axis of the hexagonal unit cell ($a = 4.8079$ Å, $c = 16.010$ Å, space group $R\bar{3}$) and the alternating layers of metal and oxygen along <111> direction of FCC oxide (Figure 2.15). The thermally induced decomposition of dolomite, as in the case of calcite (Rodriguez-Navarro et al. 2009), occurs via dissociation of the carbonate group (CO_3^{2-}), which results in the release of CO_2 in gaseous form. After that O^{2-} is left which bonds to Ca or Mg ions. This transformation results in shrinking of the former dolomite structure along the c-axis. 2D-XRD and SAED analyses show that such a shrinkage leads to a ~12° tilting of former $\{10\bar{1}4\}_{dolomite}$ planes to form $\{100\}_{oxide}$ planes. The structural similarities between these two planes and the origin of such a tilting becomes more vivid, when these two planes are directly compared, as depicted in Figure 2.15. The release of CO_2 from carbonate groups followed by decreasing bond length, show that the $(10\bar{1}4)$ dolomite plane can easily transform into the (100) oxide plane. This transition occurs by difusionless, limited and cooperative ion displacement (Bertrand 1978). The difference in bond length between dolomite precursor and product phase causes discontinuities in the crystal structure. This in turn leads to the formation of highly oriented and porous aggregates of nanocrystals, what was observed in pseudomorphs calcined in air and in vacuum (in-situ TEM). Due to the relatively low *T* (~500 ºC) of the initial stages of dolomite decomposition in air, and even lower in case of the decomposition in vacuum, Ca and Mg ions diffusion is limited. As an effect of diffusion limitation, the alternating layers of Ca and Mg are preserved, while CO_2 is released, forming a new mixed oxide structure. Further heating results in demixing (spinodal decomposition) of this structure, and purification of each oxide via diffusion of ions out of their structures with rising *T*. Nevertheless, the topotactic relationship between dolomite and each oxide product was observed at every stage of the transformation, both in air and in vacuum. In contrast to conclusions withdrawn by Haul's group, and commonly accepted by other authors (see Model 4), these results show that the thermal decomposition of dolomite takes the same mechanistic path, independently of $p\text{CO}_2$ value.

The thermal decomposition of other carbonates like calcite (Rodriguez-Navarro et al. 2009), siderite $FeCO_3$ (Dasgupta 1961), magnesite $MgCO_3$ (Dasgupta 1964; Singh Dev 1972; Kim et al. 1987) and otavite $CdCO_3$ (Floquet and Niepce 1978) also indicates the topotactic nature of the process. However, the developed parent/product orientation relationship in the case of dolomite decomposition is simpler than in other carbonates. This phenomenon may be explained by taking into account the lattices of these carbonates. Calcite-type carbonates belong to the $R\bar{3}c$ space group, whereas the presence of alternating layers of Ca and Mg in the dolomite structure, along with a rotation of the carbonate groups around the *c*-axis, reduces the symmetry to a $R\bar{3}$ space group. This in turn leads to the disappearance of the gliding planes parallel to the *c*-axis and reduces the number of symmetrically equivalent directions along which the product can be formed during a topotactic reaction.

The formation of oriented Mg-calcite nanocrystals is another interesting observation. Mg-calcite tends to release Mg ions out of its structure with rising *T*, transforming into calcite. Obtained results show, that during “half decomposition” in air, the formation of oriented Mg-calcite nanocrystals is always preceded by the formation of CaOss and MgOss nanocrystals. This suggests, that Mg-calcite is formed via solid state reaction between nascent CaOss nanocrystals and CO_2. This reaction preserved the initial orientation of CaOss nanocrystals and led to the incorporation of Mg ions (present in CaOss structure) into Mg-calcite structure. The solid state recarbonation of CaO at the *T* range considered here has been reported (Agrinier et al., 2011). On the other hand, the recarbonation of MgO during thermal decomposition of dolomite and magnesite was not observed (Agrinier et al., 2011), which fully agrees with results presented here. Calcite, formed after diffusion of Mg ions out of Mg-calcite structure, decomposes at $T > 750$ ºC into CaO and CO_2. The orientation relationship between CaO and calcite shows that the decomposition is topotactic in nature as shown by Rodriguez-Navarro et al. (2009).

These results indicate, that the so-called “half decomposition” or ”half calcination” is meaningless from a mechanistic point of view. Moreover, this term implies the occurrence of hypothetical phases during calcination of dolomite in air or in CO_2 atmosphere, e.g., magnesite along with calcite (Model 1). It should be emphasized that the use of such a terminology is confusing, since “half decomposition” or “half calcination” is not a real process, but an effect of recarbonation of CaO crystals resulting in calcite, where CaO along with MgO are the products of direct decomposition of dolomite.

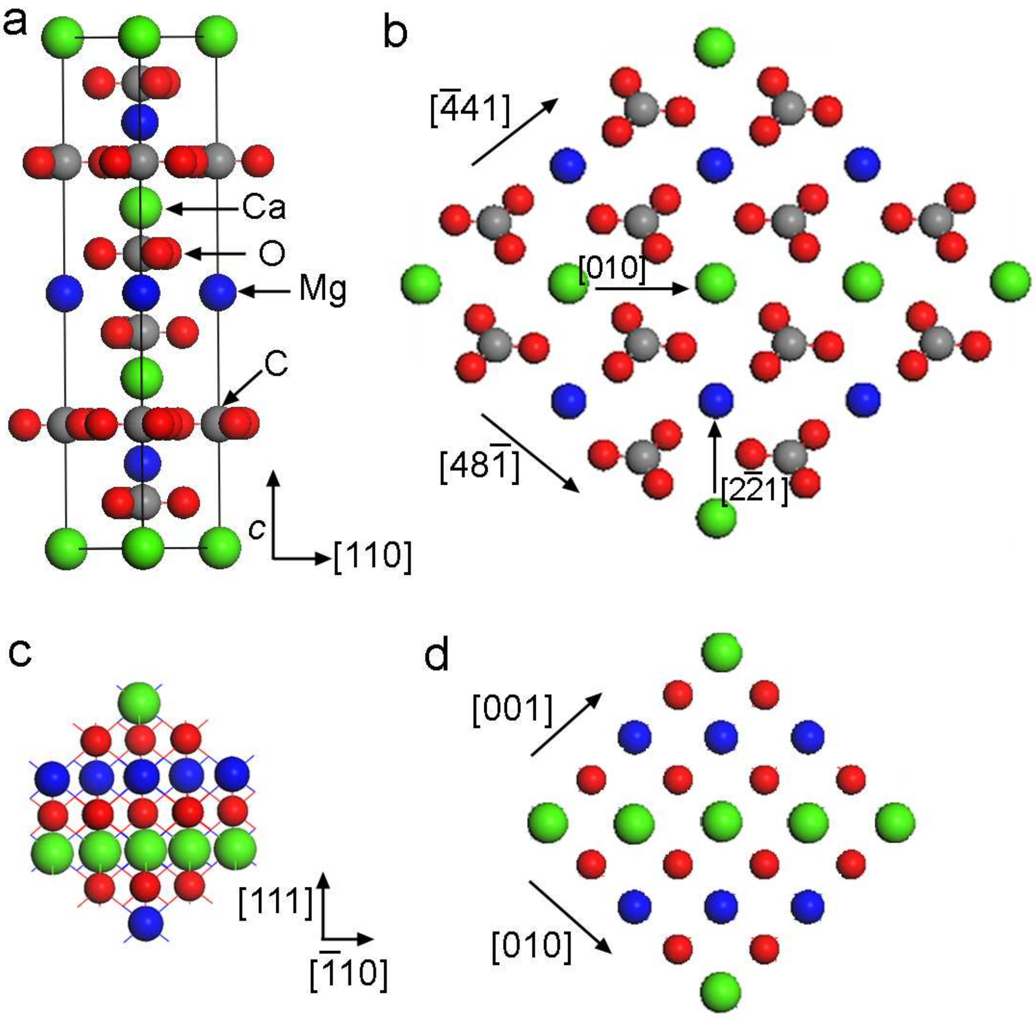

Figure 2.15. Scheme representing the structure of dolomite hexagonal unit cell (a), the dolomite (10$\bar{1}$4) plane (b), the structure of $CaMgO_2$ viewed along [$\bar{1}\bar{1}$2] direction (c), and the projection of the mixed oxide structure along [100] (d).

3. HYDRATION OF LIME

3.1. Introduction

Based on the literature study, it could be hypothesized that hydration of lime can take two different reaction pathways. The first one (i.e., solution mediated hydration) occurs via direct precipitation of portlandite crystal from a supersaturated solution formed upon dissolution of CaO in the slaking water. The other hydration pathway involves a reaction between solid CaO and water vapor, and is referred to as the vapor phase hydration. Whereas solution mediated hydration has been thoroughly studied, including the problem of "aging" (Rodriguez-Navarro 1998; Ruiz-Agudo and Rodriguez-Navarro, 2010), the vapor phase hydration has attracted less attention and is still poorly understood. The mechanisms of such a reaction have not been well established yet. Moreover, the problem of possible crystallographic control (epitaxy, topotaxy) in the advancement of the process is almost unnoticed (Beruto et al. 1981).

In an attempt to elucidate the mechanism(s) and possible crystallographic control (topotaxy/epitaxy) of lime hydration, CaO pseudomorphs (being the product of calcite calcination in air at 700 ºC up to 900 °C) were subjected to the effect of air de-voided of CO_2 at 50 % RH. Hydrated pseudomorphs were analyzed with various techniques in order to examine the structural evolution at micro and nano scale, as well as the parent/product orientation relationship.

3.2. Materials and Methods

3.2.1. Calcination of calcite and hydration of its pseudomorph

Optical quality calcite crystals (from Santorini, Greece) were cleaved using a knife blade to obtain millimeter sized single crystal (ca 3x2x1). Subsequently, cut out single crystals were placed (2-3 crystals) in cylindrically shaped ceramic crucibles (1.5 cm in diameter and 5 cm in height) and subjected to calcination in an air-ventilated electric furnace (mode Select-Horn, Selecta). The samples were placed inside the oven, which afterwards was heated form 18 °C up to the target *T* at a rate of 2 °C/min. Once each target *T* was reached, a retention (soaking) time of 30 min was applied before reaching the next target *T*, staring from 800 °C up to 1000 °C with 100 °C interval. After 30 min soaking time at each target *T*, samples were collected, cooled down at room *T*, weighed and introduced in tightly capped vials under dry N_2 atmosphere prior to further analysis. For each target *T* three calcination runs were performed. The averaged weight loss percent (wt%) at target *T* (α) was calculated using the following:

$$\alpha = 100(\frac{m_i - m_f}{m_i}) \quad (3.1)$$

where:

m_i – initial mass before calcination

m_f – final mass after calcination at a particular *T*

Following calcination, calcite single crystal pseudomorphs were place in a air tight plastic container with atmosphere devoid of CO_2 at 20 °C and ~50% RH for 24, 48 and 72 h in order to subject them to vapor phase hydration. The CO_2 free atmosphere was achieved by placing a sodium hydroxide solution inside the container, which absorbed CO_2 molecules. This procedure was necessary in order to prevent carbonation of nascent portlandite crystals, thus precluding the possibility of lime/portlandite orientation relationships measurement. A constant RH of ~50 %, necessary for the progress of the reaction over time, was achieved using a potassium chloride saturated solution placed inside the container.

3.2.2. Mineralogical and textural analysis with XRD and 2D-XRD

Analysis of phase evolution during hydration of calcined calcite pseudomorphs decomposed at different *T* was performed using a Philips PW-1710 diffractometer with Cu Kα radiation (λ = 1.5405 Å). Data were collected from 15 to 40 °2θ at a counting rate of 0.03 °2θ s^{-1}. Samples were placed on zero-background silicon sample holder oriented with the $\{10\bar{1}4\}$ cleavage plane of calcite pseudomorph parallel to the sample holder, and then placed inside the diffractometer chamber. The evolution of the product phase crystallite size as a function of calcination *T* was performed with the aid of the XPowder software (Martin-Ramos 2004).

Pole figures describing the 3D orientation relationship between CaO reactant (being the product of calcite thermal decomposition) and calcium hydroxide product (portlandite) were determined using an X-ray single crystal diffractometer equipped with an area detector (D8 SMART APEX, Bruker). For these 2D-XRD experiments, the working conditions were: Mo Kα (λ = 0.7093 Å), 50 kV and 30 mA, a pin-hole collimator of 0.5 mm in diameter, and an exposure time of 20 s per frame. Samples were measured by reflection (diffractometer ω and 2θ angles were set at 10 and 20 degrees, respectively) resting flat on one of the cleavage rhombohedral faces of the pseudomorph. A set of frames (2D diffraction patterns) was registered while rotating the sample around φ angle (a frame every 5 degrees; a total of 36 frames). Pole densities for the reflections of portlandite and lime were calculated and displayed in stereographic projection using the XRD2DScan software (Rodriguez-Navarro 2006).

3.2.3. Electron microscopy analysis

The shape, size morphology and structure of the hydrated calcite pseudomorphs were analyzed using transmission electron microscopy (TEM) and field emission scanning electron microscopy (FESEM). TEM analysis involved bright field, SAED and HRTEM observation using a Tecnai G2 F20, operating at 200 kV acceleration voltage. Prior to TEM analyses samples were gently grinded in agate mortar, dispersed in ethanol, subjected to 120s ultrasonic bath and finally deposited on Formbar-coated or carbon-coated copper grids. Prior to FESEM analysis, hydrated calcite single crystal pseudomorphs, calcined at different *T* were placed onto carbon coated sticky stubs before carbon coating.

3.3. Results

3.3.1. Calcination and hydration

The thermal decomposition of calcite resulted in pseudomorph, preserving the external shape of rhombohedra. It is now well known that thermally induced transformation of calcite into CaO is a topotactic reaction (Rodriguez-Navarro et al., 2009). Depending on the temperature and time of calcination, different degrees of transformation are observed. Figure 3.1 shows the average wt% loss during calcite calcination calculated from nine runs, according to equation 3.1. Single crystal calcite pseudomorphs calcined at 700 ºC show relatively small weight lost ~ 10 wt%, which corresponds to ~5 % transformation of calcite into CaO. In the case of crystals calcined at 800 ºC and 900 ºC weight loss amounts to ~42 and ~48 % respectively. The later values correspond (within standard error) to stochiometric loss of CO_2 from $CaCO_3$ (~44 %), indicating the full transformation of calcite into CaO.

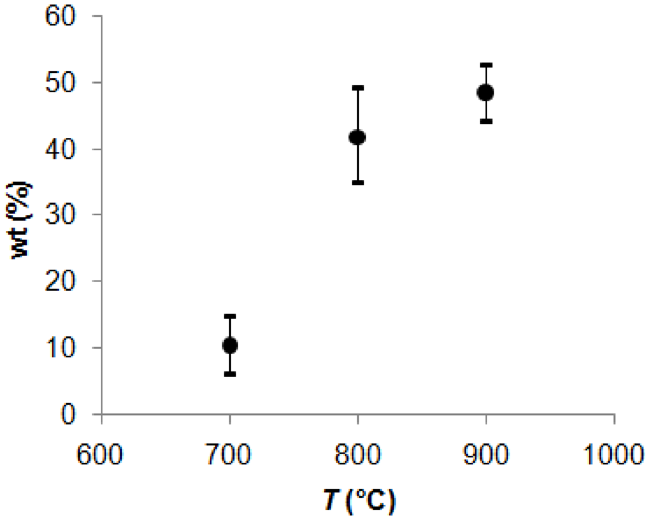

Figure 3.1. Weight loss (wt) vs. *T* during calcination upon 30 min retention time

Calcite pseudomorphs placed in a tight container with air devoid of CO_2, and subjected to the effect of water vapor (RH ~50 %), tend to disintegrate into crystals with millimeter and sub-millimeter size along with loose, powder-like material. A similar behavior of calcite pseudomorphs subjected to hydration was observed by other researchers (Ramachandran et al., 1964). This tendency was first observed after ~ 6 hours from the beginning of the hydration. However, in order to assure the maximal degree of hydration, the crystals were subjected to hydration for a longer period of time, i.e., 24, 48 and 72 hours prior to different types of analysis. The degree and features of pseudomorphs disintegration did reveal no observable relationship with calcination *T*, showing similar characteristics in all cases. The only difference was noticed in the case of the pseudomorphs calcined at 700 °C. As hydration progressed and outer parts of the pseudomorphs detached, the untransformed calcite core was exposed. The presence of residual calcite is related to the relatively low degree of transformation (~5%).

3.3.2. Phase evolution: XRD and 2D-XRD

Due to the characteristics of hydrated samples, most of the XRD analyses yielded data with poor quality. The low reliability of XRD patterns is related to disintegration of initial pseudomorphs into small fractions with different sizes and shapes, and creation of loose (powder like) material. These features, after placing hydrates on the XRD holder, leaded to random scattering of X-rays (e.g., fractions of pseudomorphs non parallel to holder plane) and shadowing (differences in heights among pseudomorph fractions). The poor quality of collected XRD patterns prevented reliable peak profile analysis (i.e., crystallite size measurement). XRD patterns with quality enabling crystallite size determination were obtained from pseudomorphs hydrated for 72 h (Figure 3.2). In addition to the limited number of reliable XRD results, 2-theta scans, which can be viewed as equivalents of XRD patters, were calculated from 2D-XRD diffraction patterns using XRD2DScan software (Rodriguez-Navarro 2005) (Figure 3.3 and Figure 3.4). It should be mentioned in this context, that the advantage of 2D-XRD analysis, if compared to traditional XRD, was the possibility of analyzing smaller fractions of the samples and their precise placing on the trajectory of incident X-ray beam. The main limitation, however, of 2-theta scans if compared with XRD patterns, was the inability to perform crystal size measurements due to the significant instrumental peak broadening.

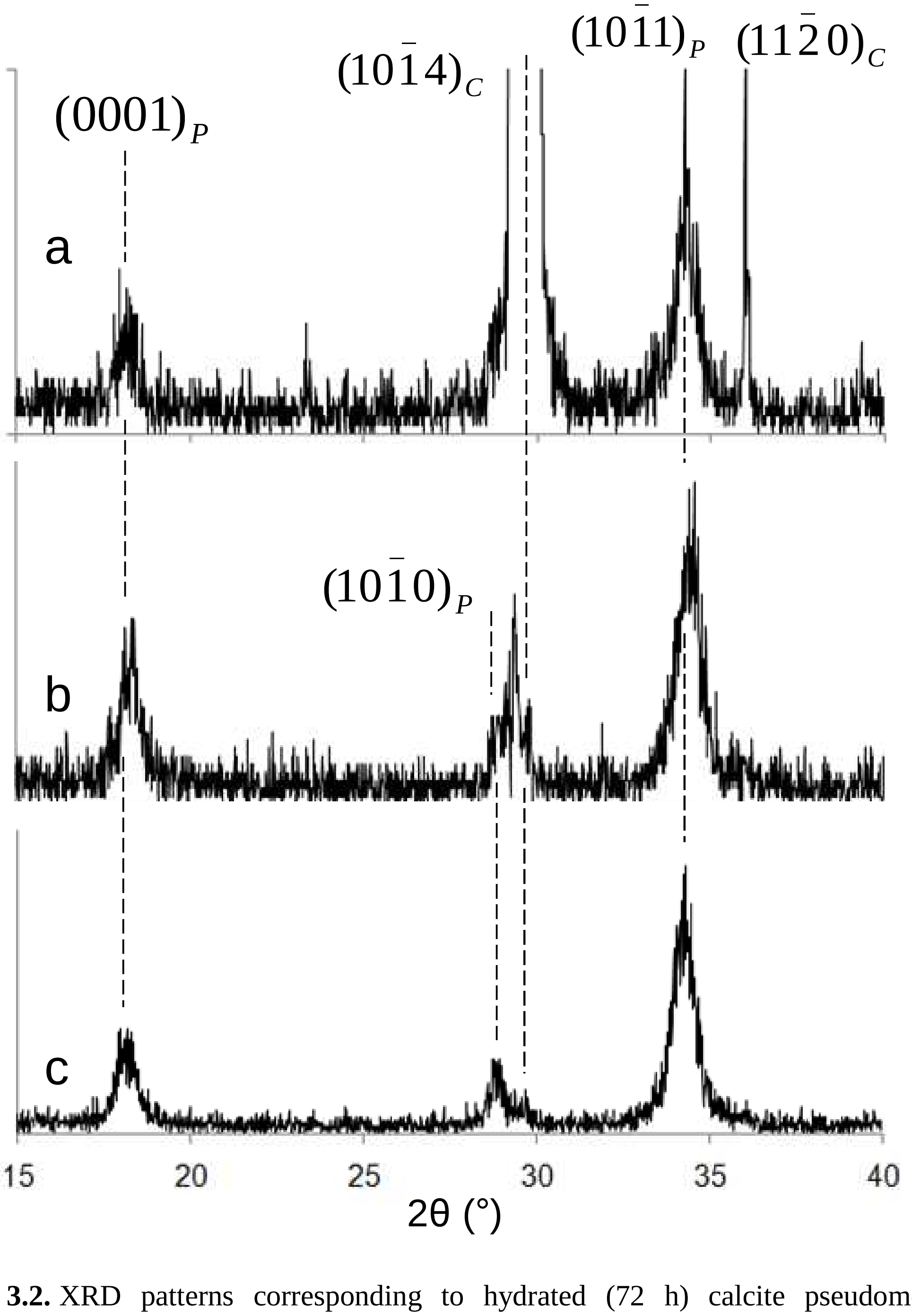

Figure 3.2. XRD patterns corresponding to hydrated (72 h) calcite pseudomorphs calcined at 700 (a), 800 (b) and 900 ºC (c). Note the presence of calcite (C) and portlandite (P) in each sample.

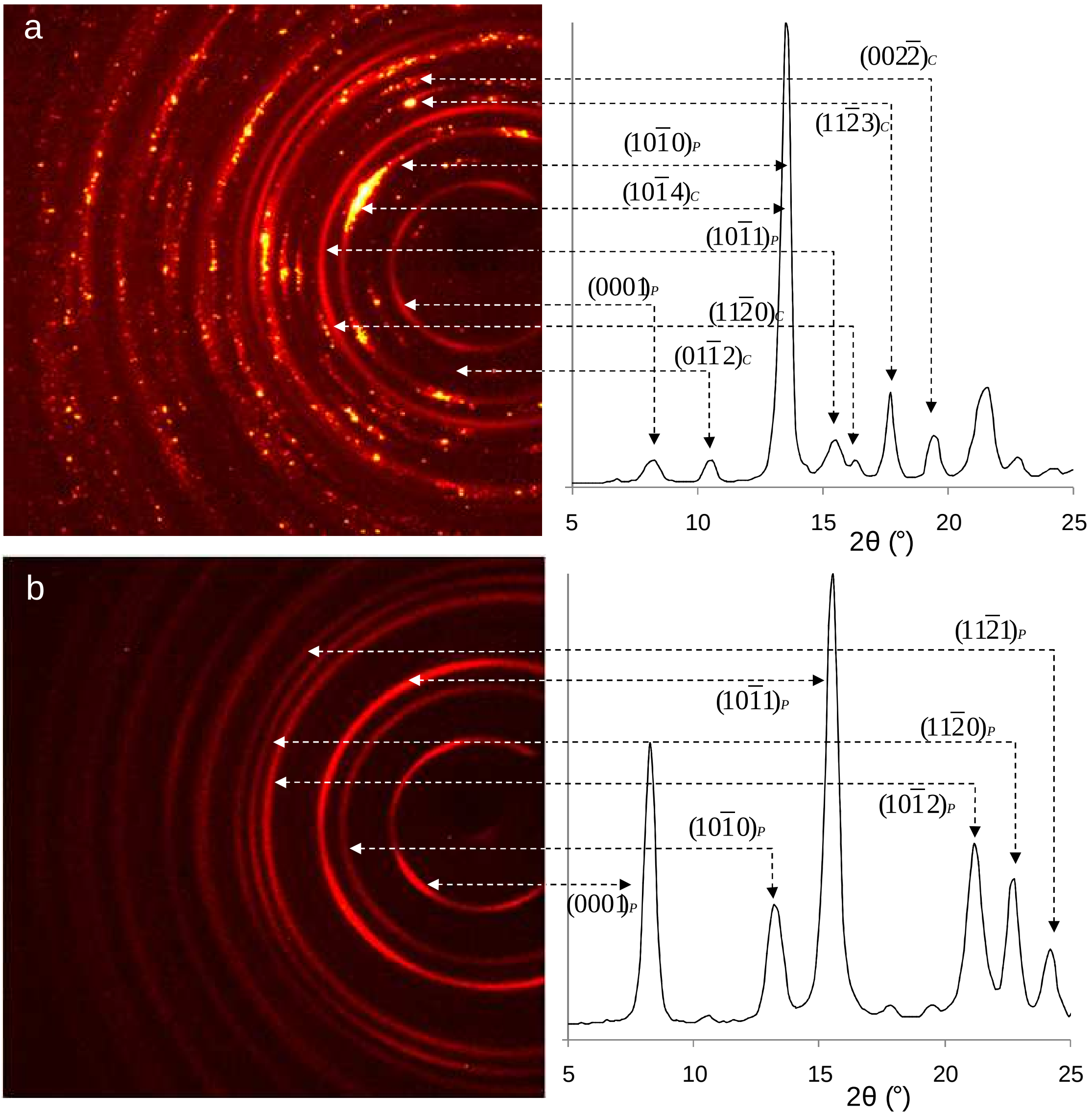

Figure 3.3. 2D-XRD patterns and 2-theta scans corresponding to pseudomorphs hydrated for 72 h, calcined at 700 °C (a) and 900 °C (b). Note the presence of non decomposed calcite in the case of the sample calcined at 700 °C.

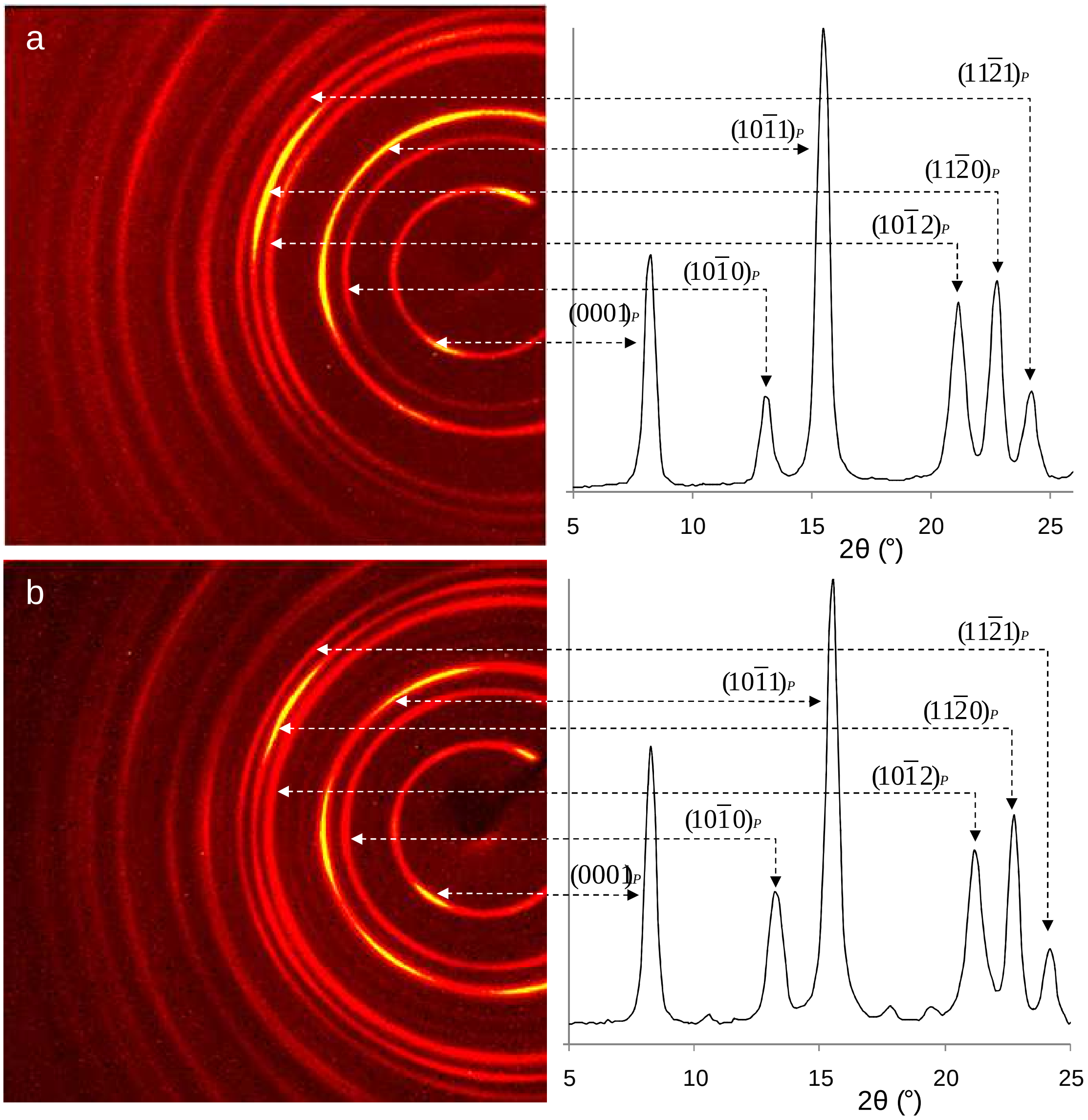

Figure 3.4. 2D-XRD patterns and 2-theta scans of pseudomorph calcined at 800 °C and subsequently hydrated for 24 h (a) and 72 h (b). Note that full transformation of lime into portlandite took place just after 24 hours.

Figure 3.2 shows XRD patterns of calcite pseudomorphs calcined at different *T* and subjected to the effect of water vapor for 72 h. None of the patterns revealed the presence of CaO Bragg peaks, what was also confirmed by 2D-XRD analysis (Figure 3.3 and Figure 3.4), indicating the full transformation of lime into portlandite. On the other hand, FESEM and HRTEM observations revealed the presence of CaO in deeper parts of some pseudomorphs. The lack of CaO Bragg peaks in the XRD patterns and 2D-XRD images, could be related to the limited penetration of X-rays. Each of the XRD patterns show the presence of calcite 104 Bragg peaks, which tend to decrease with increasing *T*, i.e., with increasing degree of calcination. In contrast, integrated 2D-XRD 2-theta scans of small (millimeter and sub-millimeter size) calcite pseudomorphs, after 72 hour exposure to water vapor, show the presence of calcite only in pseudomorph calcined at 700 ºC (Figure 3.3), what can be explained by the relatively small degree of calcination at this *T*. Thus, the origin of calcite reflections should be related with the untransformed calcite core of the pseudomorph, which is uncovered when the transformed shell fell off during hydration, rather than with carbonation of $Ca(OH)_2$.

Figure 3.5 shows portlandite crystallite sizes, developed after 72 h of hydration of calcite pseudomorphs calcined at different *T*. Interestingly, crystallite sizes do not show significant differences. Moreover, 2-theta scans of pseudomorphs calcined 800 ºC, show the same FWHM values for all Bragg peaks after 24 h and 72 h hydration (e.g., $101_{portlandite}$ with FWHM ~5º), indicating that no significant changes in the crystallite size evolution took place after the hydration was completed. Rodriguez-Navarro et al. (2009) report that the crystallite size of CaO is ~27 nm and ~57 nm at 800 and 900 ºC, respectively. As a first approximation, it could be expected that this increasing trend could be inherited by nascent portlandite crystals, if a topotactic, solid-state hydration mechanism would be at work. Since it was not observed here, it could be hypothesized, that the mechanism(s) via which hydration took place did not preserve a relevant textural information such as the crystallite size.

Calcite pseudomorphs are highly porous (up to 54.2 %) (Beruto et al. 2004) and display a large amount of mesopores and micropores (Rodriguez-Navarro et al. 2009). These features are expected to facilitate capillary condensation of water at relatively low RH (~50 %), due to the Kelvin effect (Beruto et al. 1981) followed by dissolution of CaO and precipitation of $Ca(OH)_2$. This mechanism would led to the occurrence of portlandite crystals with approximately the same size regardless the initial size of CaO crystals. Such a dissolution/precipitation process would be kinetically much faster than a solid state reaction (Putnis 2009), and could explain full (or almost full) transformation of CaO into $Ca(OH)_2$ within such a short time (~24 h) at room *T*. On the other hand, as shown in the next section, a strong crystallographic control in the advancement of the hydration is observed. This implies, that the hypothesized dissolution of Cao and subsequent precipitation of $Ca(OH)_2$ has to take place on a sufficiently thin interface as to allow the preservation of crystallographic orientation information (Putnis 2009).

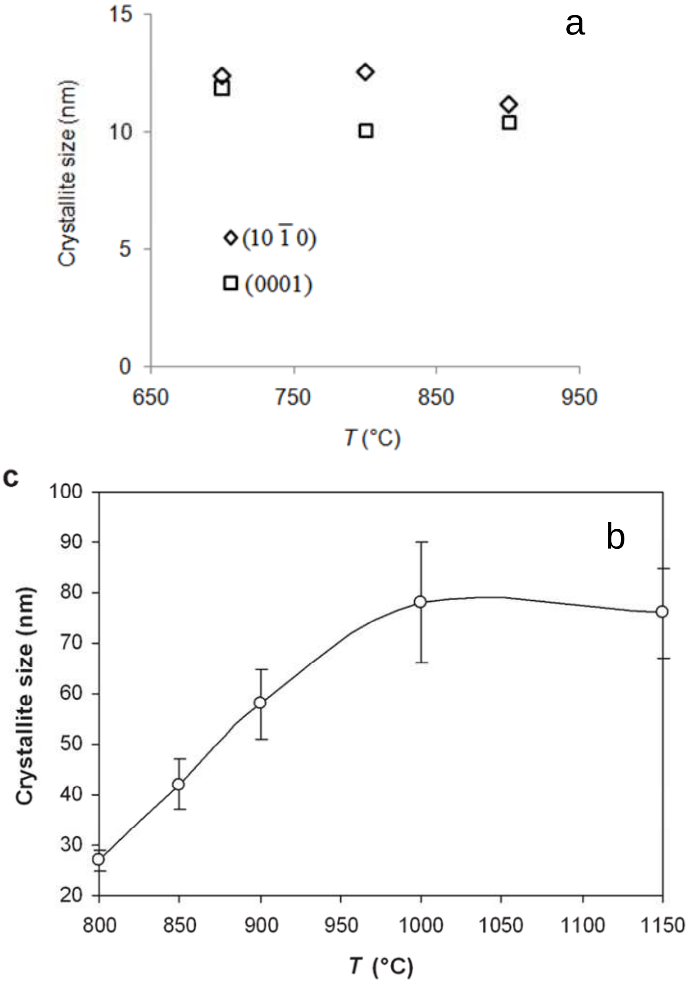

Figure 3.5. (a) Portlandite crystallite size developed on the calcite pseudomorph as a function of calcination *T* and (b) evolution of CaO crystallite size in calcined pseudomorphs (from Rodriguez-Navarro et al. 2009).

3.3.3. *Orientation relationships*

Pole figures of $(11\bar{2}0)$ and (0001) planes of portlandite, obtained from 2D-XRD analysis of hydrated pseudomorphs, confirmed a strong preferred orientation of portlandite crystals. Best quality pole figures were obtained from pseudomorphs calcined at 800 ºC (Figure 3.6). As shown by Rodriguez-Navarro et al. (2009), during calcination, CaO develops on the calcite lattice with $\{110\}_{CaO}$ planes oriented nearly parallel (~15º) to $\{10\bar{1}4\}_{calcite}$ ($(10\bar{1}4)_{calcite}$ is the pole figure projection plane), this was also observed here (Figure 3.6a). Moreover, pole figures of $\{110\}_{CaO}$ and $\{111\}_{CaO}$ show the existence of two sets of crystals (Figure 3.6a and Figure 3.6b) rotated with respect to each other around the normal to the projection plane at an angle of ~75º. Rodriguez-Navarro et al. (2009) have reported on the existence of such a set of crystals at an angle of either ~75º or ~90º. The existence of the latter was not observed here.

Figure 3.6c presents the pole figure of $(11\bar{2}0)_{portlandite}$ showing two sets of portlandite crystals with their $(11\bar{2}0)$ planes oriented nearly parallel to the pole figure projection plane. These two sets of portlandite crystal are rotated with respect to each other around the normal to the projection plane at an angle ~75º. These features indicate that portlandite developed with $\{11\bar{2}0\}$ planes parallel to {110} planes of former CaO. This situation should unambiguously impose parallelism between $\{0001\}_{portlandite}$ and $\{111\}_{CaO}$ planes. This is confirmed by the pole figure of $(0001)_{portlandite}$ (Figure 3.6d). The distribution of $\{0001\}_{portlandite}$ spots matches that corresponding to $\{111\}_{CaO}$, resulting in four sets of portlandite crystals. The crystallographic orientation relationships did not change in the studied calcination *T* range.

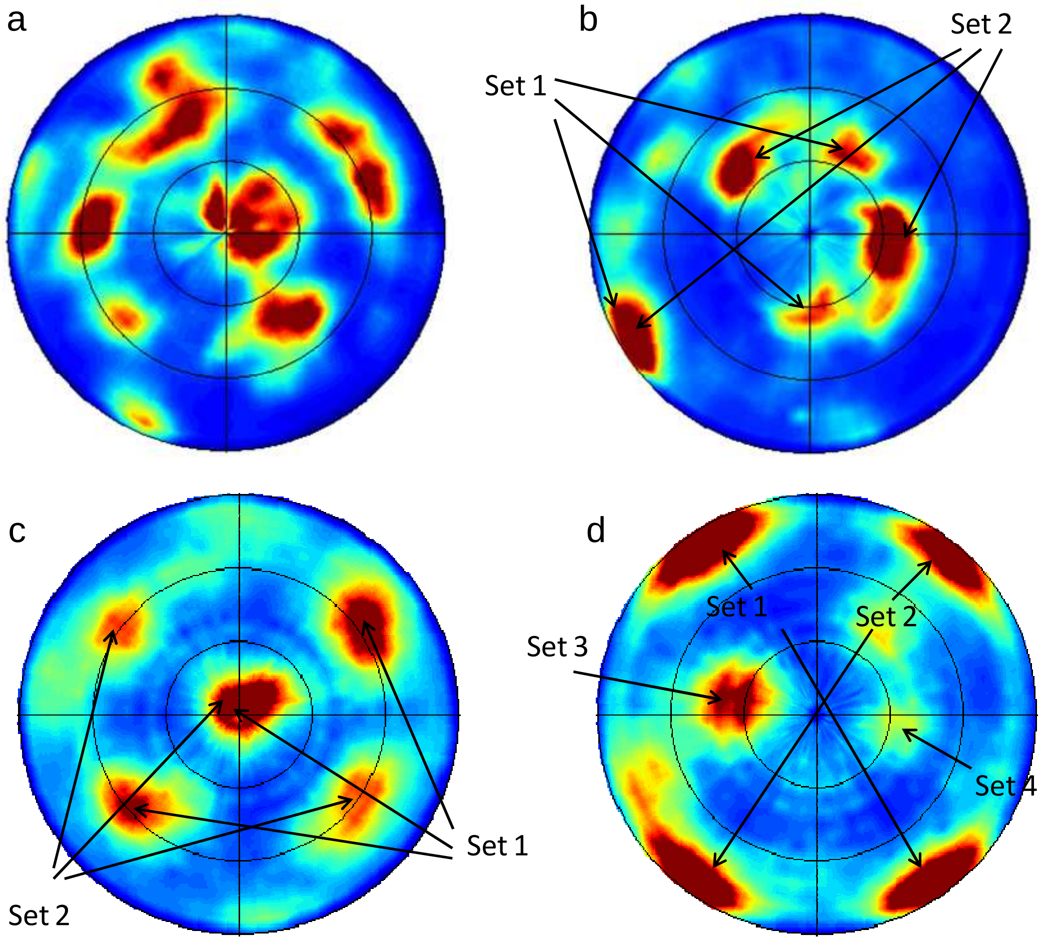

Figure 3.6. Pole figures of lime developed on the surface of calcite pseudomorphs: (a) (220) and (b) (111) and portlandite after hydration in air de-voided of CO_2 at RH 50%: (c) $(11\bar{2}0)$ and (d) (0001).

3.3.4. FESEM analysis

FESEM observations confirmed that CaO hydration can take place preserving the external shape of the rhombohedral pseudomorph (Figure 3.7). Such a reaction is thus pseudomorphic. In agreement with XRD and 2D-XRD analyses, FESEM observations of hydrated pseudomorph, calcined at 700 ºC (Figure 3.8), confirmed the presence of an untransformed calcite core, surrounded by an external shell of portlandite. The formation of cracks following $\{10\bar{1}4\}$ cleavage plane was observed. This led to the breakdown of the calcite single crystal into different pieces ~1-5 µm in size. It has been stated that the formation of cracks precedes the thermal decomposition of calcite (Boynton, 1980; Spinolo and Anselmi-Tamburini, 1989). 2D-XRD analyses of calcined pseudomorphs show a strong preferred orientation of developed CaO crystals. The development of such a crystallographic texture during calcination, which is now well understood (Rodriguez-Navarro et al., 2009) is expected to have a profound influence on the progress of subsequential processes within the lime cycle (i.e., hydration and subsequent carbonation of calcium hydroxide). Crystallographic texture may control the advancement of the subsequential processes and the properties (e.g., physical, mechanical) of the sample related with anisotropy.

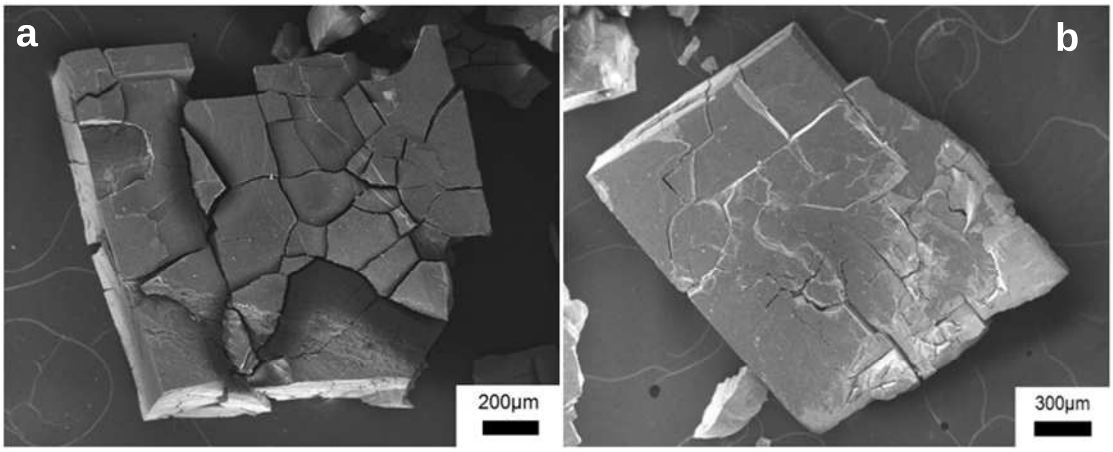

Figure 3.7. Calcite pseudomorphs calcined at 800 ºC (a) and at 900 ºC (b) subjected to hydration in air atmosphere RH 50% for 72 h. Note the preservation of original rhombohedral shape of calcite single crystal, cracking and fracturing due to increase in the molar volume during hydration.

At T ≥ 800 ºC, hydrated pseudomorphs showed the formation of cracks responsible for the development of a fragile hydrate shell, its disintegration and surface detachment as packages ~10-200 µm in size (Figure 3.7). As mentioned earlier, this complicated proper XRD analysis of the parent/product textural relationships. The cracking occurs as a result of the significant differences in molar volume (~34 %) between product (portlandite) and parent (lime) phases (Beruto et al., 1981). Moreover, the formation of smaller cracks affecting smaller volumes was observed at higher magnification (Figure 3.9). The mechanisms of their formation is most probably similar to that described for the previous case. It should be mentioned, that the formation of cracking can facilitate the hydration process by providing pathways throughout which liquid/gas phases can reach deeper parts of the pseudomorph (Wolter, 2004). On the other hand, the volume increase associated with the replacement of lime by portlandite, led to a significant reduction in porosity. It has been proposed that such a tight closing of pore space may hinder the progress of the hydration process (Wolter, 2004; Serris, 2011), preventing the water vapor from penetrating deeper parts of the pseudomorph. Figure 3.10 shows the interface between parent/product phases observed in the case of pseudomorphs calcined at 900 ºC. The most significant textural feature is a difference in porosity between lime and newly-formed portlandite. The original highly porous texture is build up of rod shaped crystals with ~600 nm size, whereas the product phase shows a very homogenous structure with no well defined crystal morphology and no porosity. This helps explain why a self-limited hydration process has been described for the core of CaO hydration (Wolter 2000). However, the presence of cracks seems to overrule this effect, as shown here by XRD results indicating full transformation of CaO into $Ca(OH)_2$ in all cases.

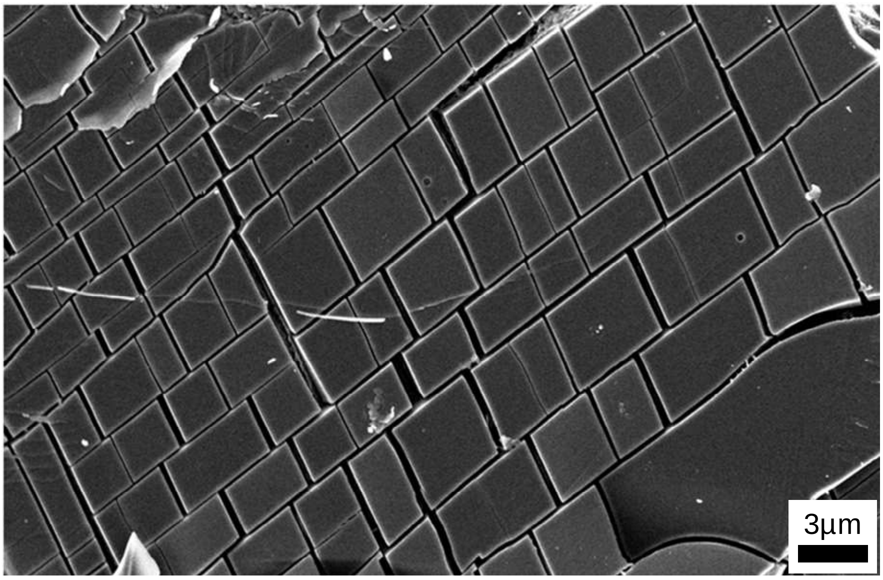

Figure 3.8. Formation of cracks and break down into small rhombohedral crystal on the surface of a single calcite crystal, preceding the thermal decomposition of calcite observed at 700 ºC.

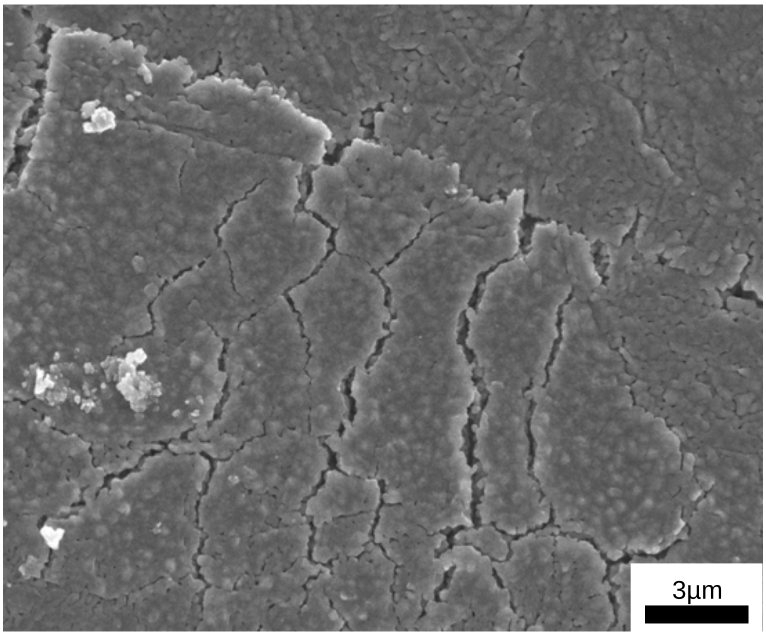

Figure 3.9. Cracks formed after 72 h hydration on the surface of the pseudomorph (calcined at 900 ºC) as a result of an increase in molar volume between parent (lime) and product phase (portlandite).

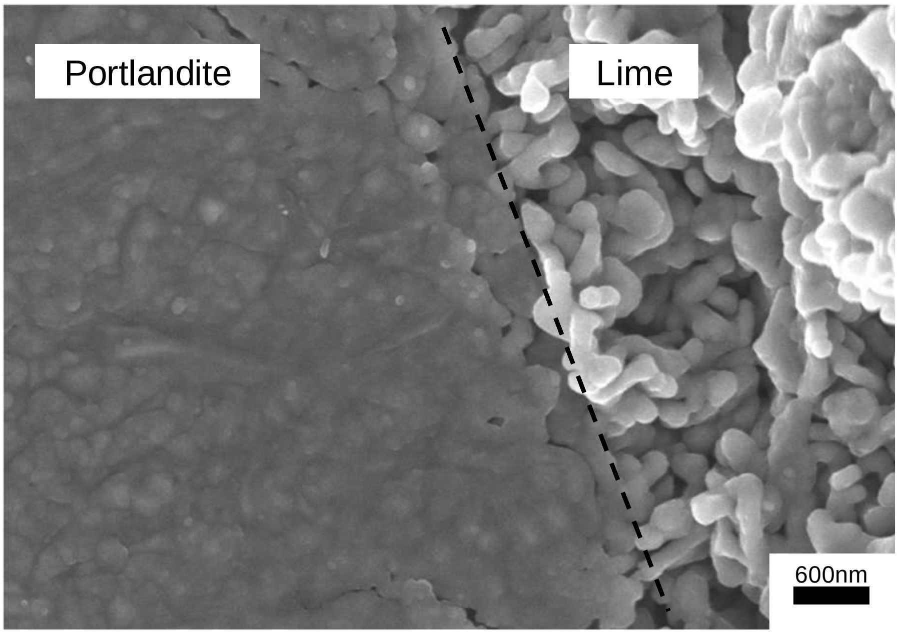

Figure 3.10. Partially hydrated calcite pseudomorph (calcined at 900 ºC) showing the border between parent (lime) and product (portlandite) phases (visible in deep parts of the sample). Precipitating portlandite presents almost no porosity and no distinct crystal morphology, while CaO forms a highly porous structure made up of nano-sized particles.

3.3.5. TEM observation

Figure 3.11 shows the formation of a randomly oriented aggregate of portlandite crystals observed under TEM. Interestingly, crystals do not show any distinct morphology. Similar features were observed with FESEM on the surface of hydrated pseudomorphs. The corresponding SAED pattern is presented in Figure 3.11 (inset). The second, fourth, sixth and seventh diffraction rings have corresponding *d*-spacing values of 3.16 Å, 1.83 Å, 1,41 Å and 1.28 Å. By comparison with theoretical positions, it can be assumed that these values correspond to portlandite 100, 110, $20\bar{1}$ and 113 Bragg peaks. As revealed by previous results (XRD, 2D-XRD and FESEM), in the considered sample three phases could be expected, i.e., calcite (due to limited conversion), lime and portlandite. Nevertheless, the positions of other rings cannot be easily assigned to any of these phases. Interestingly, the position of the first diffraction rings (*d*-spacing 3.6 Å) matches to 110_{vaterite}. However, the existence of vaterite was not confirmed by any other studies performed here. It could be hypothesized, that the presence of this diffraction ring, as well as those un-assigned to any phase, points to the formation of an intermediate phase during lime to portlandite transformation. The existence of such a phase could be the result of some structural changes. As indicated by the pole figure analysis, and will be discussed later, a possible route for the topotactic transformation of lime into portlandite requires the expansion of $\{111\}_{lime}$ planes from 2.77 Å up to 4.91 Å in order to form $\{0001\}_{portlandite}$.

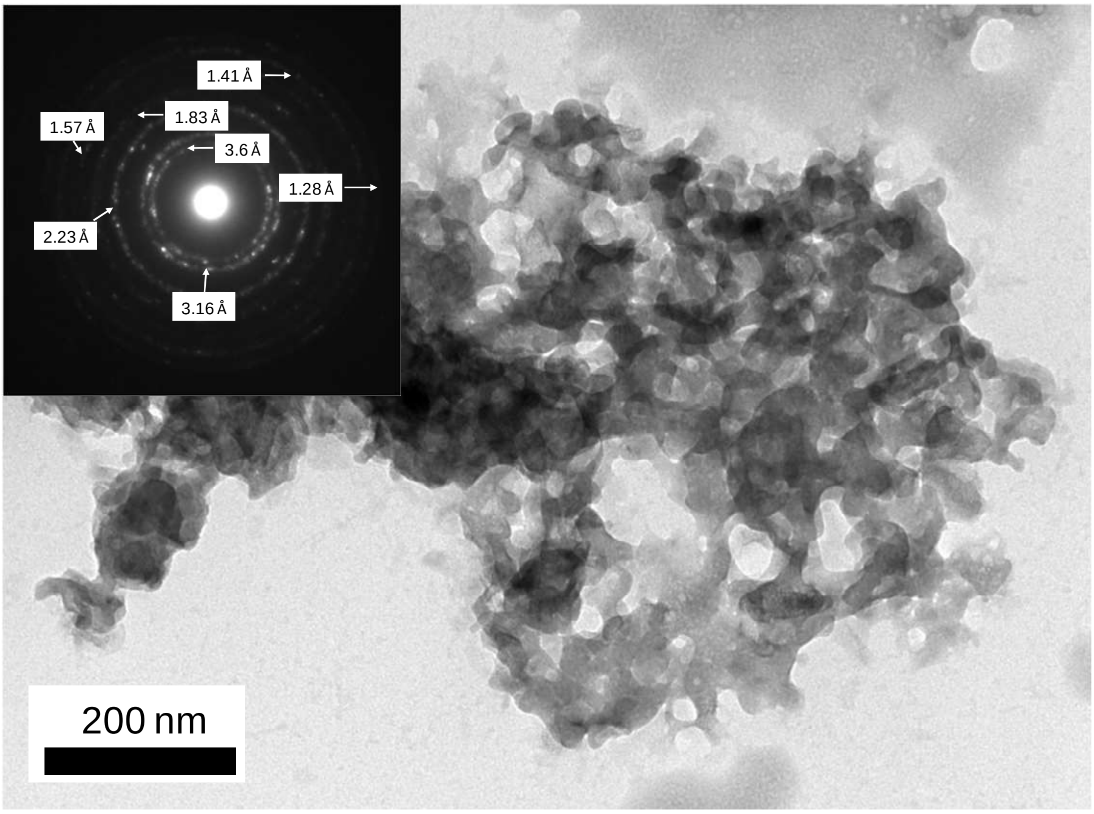

Figure 3.11. Random aggregation of crystals produced by hydration of calcite pseudomorphs calcined at 900 ° and corresponding SAED pattern (inset).

Figure 3.12a shows a high resolution transmission electron microscopy (HRTEM) image of hydrated lime. The corresponding fast Fourier transformation (FFT) of this image is presented in Figure 3.12b. Interestingly, measured *d*-spacing values and reciprocal lattice characteristics (i.e., FFT image which is equivalent to the SAED pattern) show that the present phase is neither lime, nor portlandite. It should be expected that this structural changes occur as a result of incorporation of water into the lime structure (i.e., substitution of oxygen (O^{2-}) by two hydroxyl (OH^{-}) groups) and point to the existence of an intermediate phase between lime and portlandite. There is however the question how this intermediate phase grows from the parent (lime) phase. This intermediate structure may be easily obtained from the lime structure by expanding along [110] direction from the initial ~3.4 Å up to ~4.5 Å. This [110] distance change results in a d_{111} increase form ~2.77 Å to ~3.6 Å (Figure 3.13). Note that similar *d*-spacing values are determined during SAED analysis (inset in Figure 3.11). A schematic representation of the lime structure and the intermediate phase along with simulated SAED patterns (along the $[1\bar{1}0]$ zone axis) are presented in Figure 3.13.

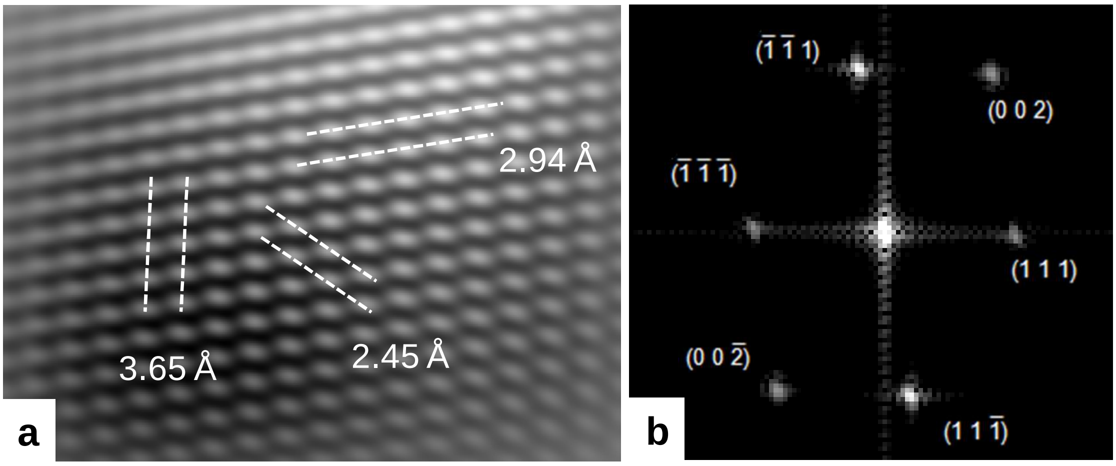

Figure 3.12. HRTEM image of intermediate phase between lime and portlandite formed during hydration of lime (a) and corresponding FFT image.

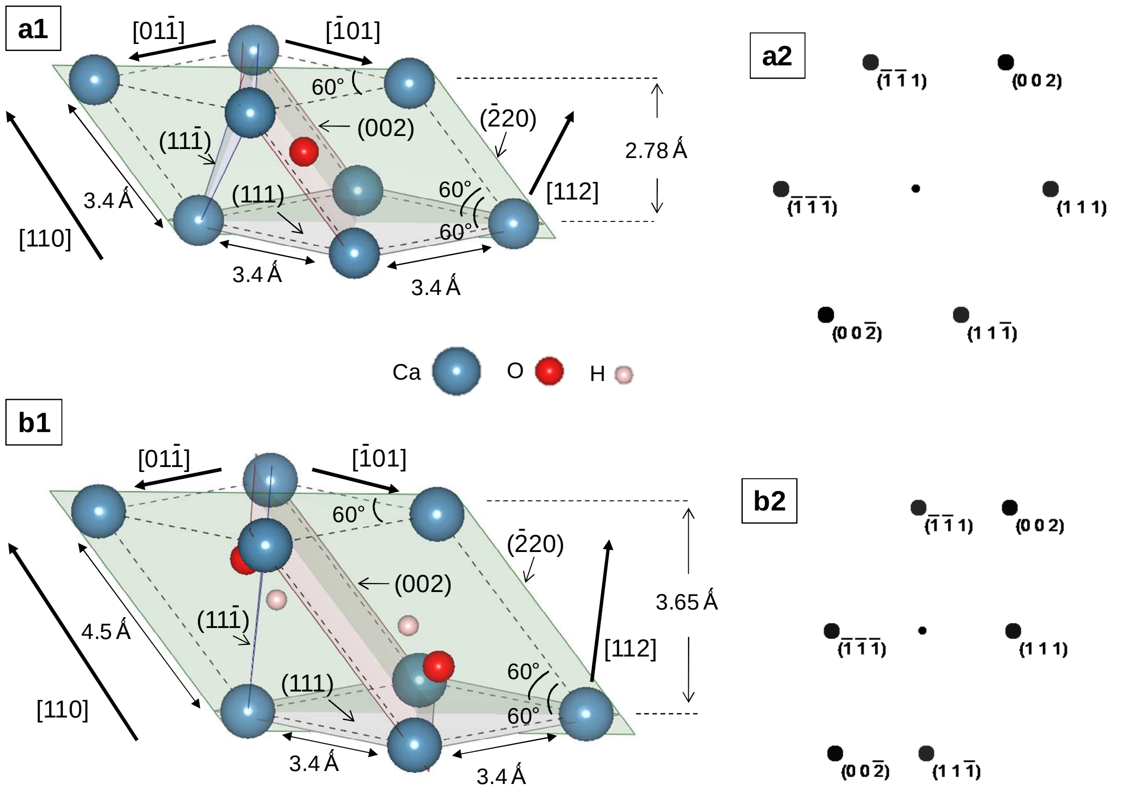

Figure 3.13. Schematic representation of structures and simulated SAED patterns: lime (a1 and a2) and the intermediate phase (b1 and b2).

The intermediate phase (i.e. the lime structure expanded along the [110] direction) requires further changes in order to form portlandite. Such a transition is shown by the HRTEM and FFT images in Figure 3.14. The intermediate phase is viewed along the [112] zone axis (Figure 3.14b1 and Figure 3.14b2), while portlandite along the [001] zone axis (i.e., parallel to the c axis) (Figure 3.14c1 and Figure 3.14c2). It could be argued, that the structure in Figure 3.14b1 corresponds to lime (viewed along the [112] zone axis) rather than to the intermediate phase. Moreover, *d*-spacing values ~3.62 Å in Figure 3.14c1 could suggest the intermediate phase, not portlandite. Regarding the latter, the formation of the intermediate phase from lime is the result of the increase of the d_{111} spacing along the [110] direction. This increase occurs only for one set of parallel (111) planes out of four possible combinations (due to the symmetry of CaO lattice there are four sets of non-parallel symmetrically equivalent (111) planes). In Figure 3.14c1 there are two sets of non-parallel planes with *d*-spacing ~3.62 Å. Based on that observation, the possibility of the formation of the intermediate phase in Figure 3.14c1 can be rejected. Interestingly, portlandite in Figure 3.14c1 shows a strong degree of distortion. The origin of this phenomena will be discussed below.

The intermediate phase and lime give very similar SAED patterns (and therefore HRTEM images) if their [112] zone axis is parallel to the electron beam as is depicted in Figure 3.15. Theoretical *d*-spacing for lime and the intermediate phase are: lime $d_{\bar{2}20}$ = 1.7 Å, the intermediate phase $d_{\bar{2}20}$= 1.7 Å, lime $d_{11\bar{1}}$ = 2.78 Å, the intermediate phase $d_{11\bar{1}}$ = 2.94 Å. The measurement of $d_{11\bar{1}}$ spacing could unambiguously point at a particular phase. However, deviations from the theoretical values due to the lattice distortions, preclude that possibility. The identification of a phase in Figure 3.14b1 as the intermediate phase can be based on the crystallographic relationship between lime and portlandite derived from the pole figure analysis. Pole figures clearly show parallelism between lime (111) and portlandite (0001) planes, what means that $[111]_{lime}//[0001]_{portlandite}$. If the observed phase in Figure 3.14b1 was lime it would imply that $[112]_{lime}//[0001]_{portlandite}$. This discrepancy can be explained taking into account the distortion of the lime structure (Figure 3.12). If lime structure expanded along [110] direction up to ~5.1 Å, the [112] direction is perpendicular to the (111) plane (Figure 3.13). Therefore the (111) plane of distorted lime structure, i.e., lime structure forming the intermediated phase, which initially was the (111) plane of lime, is parallel to the (0001) plane of portlandite. Based on these observations it could be concluded that the structure observed in Figure 3.14b1 is the intermediate phase transforming into (distorted) portlandite.

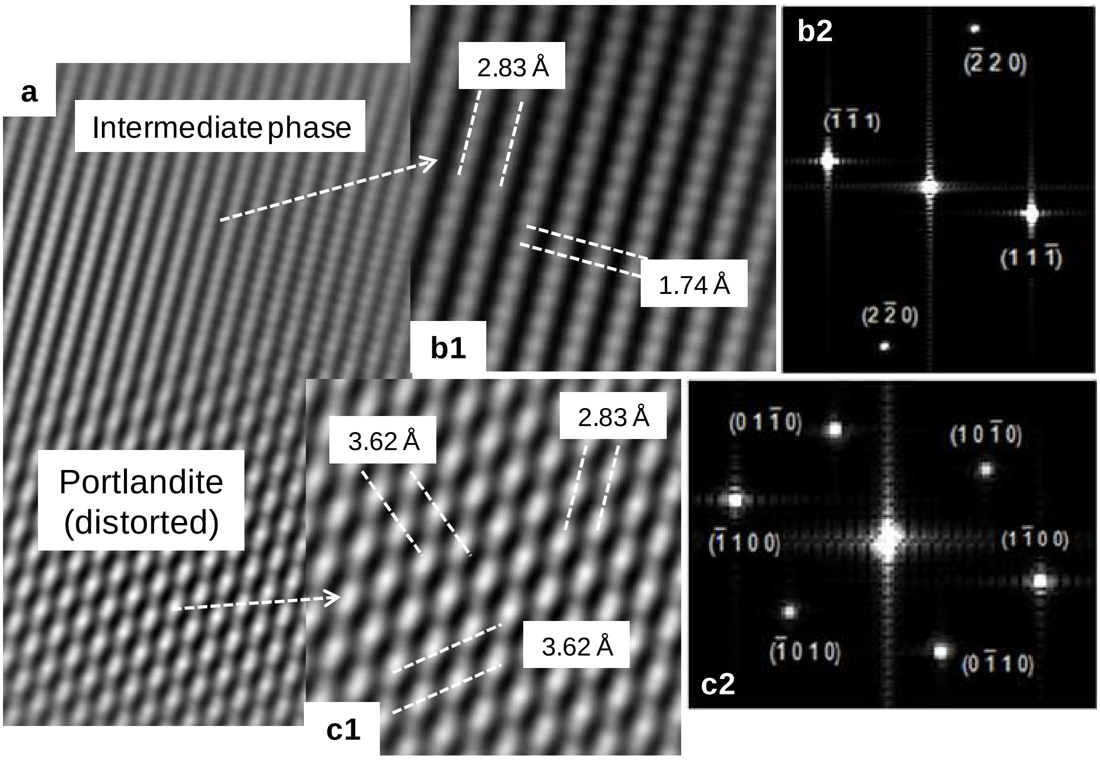

Figure 3.14. (a) HRTEM image of the partially hydrated zone. Enlarged of (a) with corresponding FFT images: lime (b1 and b2) and portlandite (c1 and c2).

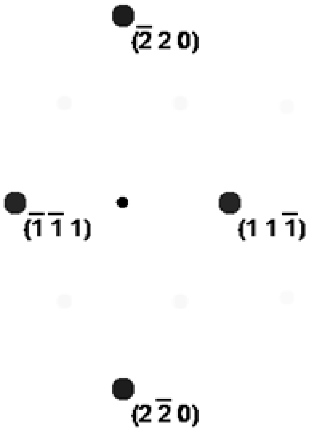

Figure 3.15. Simulated SAED along the [112] zone axis corresponding to both lime and intermediate phase. Theoretical *d*-spacing for lime and the intermediate are: lime $d_{\bar{2}20}$ = 1.7 Å, the intermediate phase $d_{\bar{2}20}$ = 1.7 Å, lime $d_{11\bar{1}}$ = 2.78 Å, the intermediate phase $d_{11\bar{1}}$ = 2.94 Å.

As mentioned earlier, portlandite structure shown in Figure 3.14c1 displays a strong degree of distortion. Measured d_{100} and d_{010} spacing equal ~3.62 Å, whereas their theoretical value is ~3.11 Å. Also the angle between $(10\bar{1}0)_{portlandite}$ and $(01\bar{1}0)_{portlandite}$ planes is ~75° instead of 60°, what corresponds to an angle of ~105° between the *a*-axis and the *b*-axis. Portlandite $d_{1\bar{1}0}$ spacing instead of ~3.11 Å equals 2.83 Å. This value is the same as the interplanar distance of $(11\bar{1})$ planes of the intermediate phase and is responsible for the observed distortion of its structure. The data also show that the transition from the intermediate structure to portlandite preserves the parallelism between (111) and $(11\bar{1})$ planes of the intermediate phase and (0001) and $(1\bar{1}00)$ planes of portlandite respectively. This fact imposes that the transformation from the intermediate phase into portlandite occurs via shifting of two consecutive (111) planes of the intermediate phase parallel to its $[1\bar{1}0]$ direction.

Figure 3.16a1 shows the intergrowth of lime and portlandite. Since the analysis of such a complicated image is difficult the following procedure was applied. The corresponding FFT image (Figure 3.16a2) was digitally separated into two images corresponding to lime and portlandite respectively. For each FFT image, inverse fast Fourier transform (IFFT) was applied in order to recreate HRTEM. The results of these operations are presented in Figure 3.16.

The results show that $(0001)_{portlandite}//(111)_{lime}$. This is in agreement with previous observations. Measured portlandite $d_{1\bar{1}0}$ (~2.86 Å) and $d_{1\bar{1}1}$ (~2.4 Å) spacing are lower than theoretical values (~3.11 Å and 2.62 Å respectively). Moreover, portlandite $(1\bar{1}01)$ plane is parallel to lime (002) plane. The lower *d*-spacing values are consistent with results presented in Figure 3.14 and are explained by the distortion of portlandite lattice where the angle between the *a*-axis and the *b*-axis is ~105°. The parallelism between portlandite $(1\bar{1}01)$ plane and lime (002) plane is in agreement with shifting of (111) planes of the intermediate structure along its $[1\bar{1}0]$ direction. The distorted structure of portlandite should transform into un-distorted portlandite structure with time via a stress release. The mechanistic model of the vapor phase hydration of lime is described in the following section.

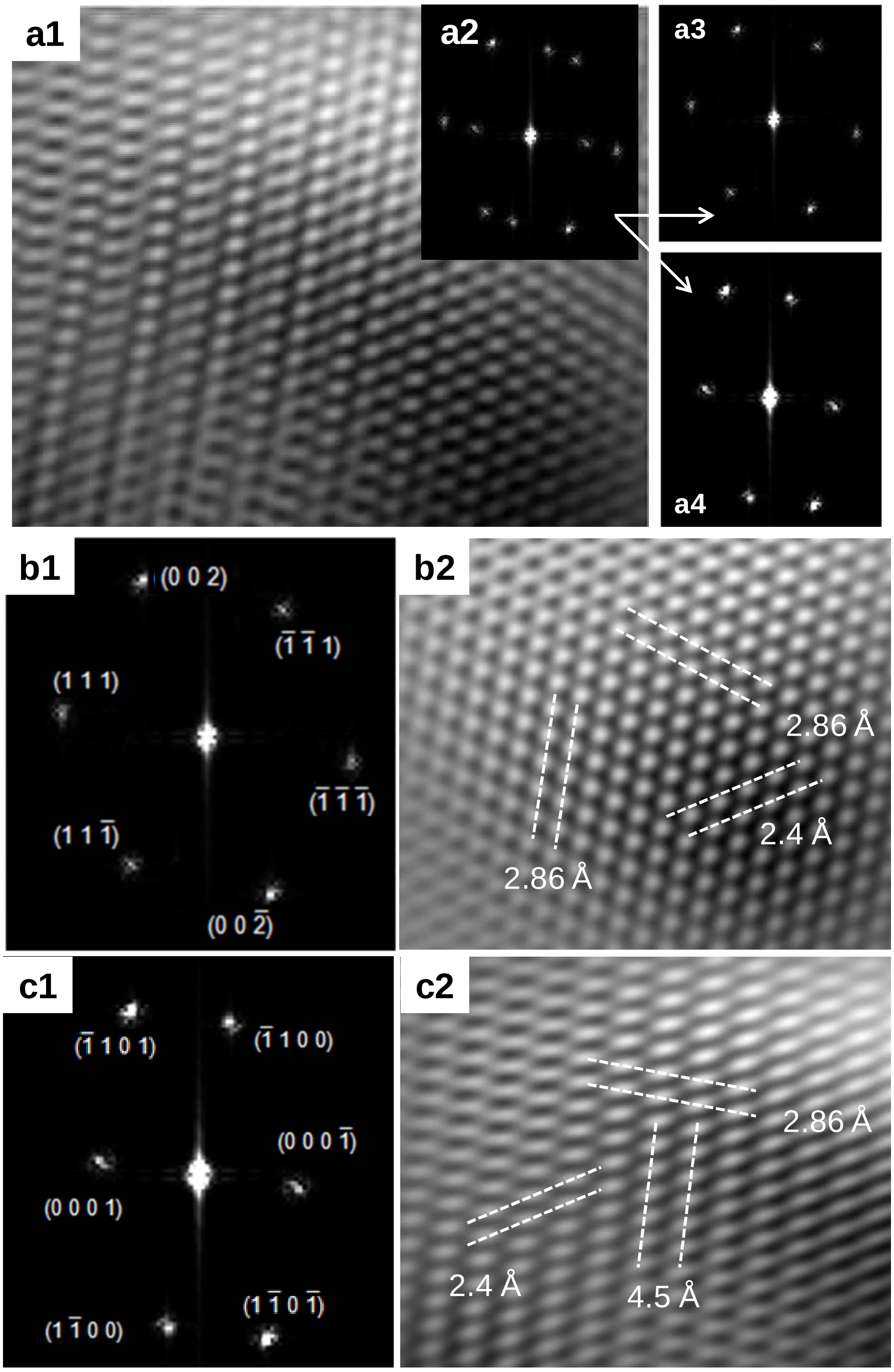

Figure 3.16. HRTEM image of mixture of lime and portlandite (a1) and corresponding FFT image (a2). Separation of a2 into two FFT images for each phase: lime (a3 and b1) and portlandite (a4 and c1). HRTEM images obtained by IFFT of corresponding FFT images: b2 –lime (IFFT of b1), c2 – portlandite (IFFT of c1).

3.4. Discussion

A limited number of studies on vapor phase hydration of lime proposed different reaction models based on the solid-gas reaction between lime and vaporized water (Beruto et al., 1981; Serris et al., 2011). One has to take into account that in traditionally slaked quicklime, in which initial hydration occurs by reaction with liquid water, it could be expected, that at some point of the reaction solid calcium oxide will be in contact with water vapor. Water vapor is produced due to the heat released during the reaction which is a highly exothermal one (Wolter, 2004).

It appears that the selection of the hydration mechanisms for solid calcium oxide hydration in contact with a humid atmosphere is mainly dependent on the RH value (Beruto et al. 1981). The other important factor influencing the mechanisms of hydration appears to be related with the microstructural characteristics of calcium oxide (Beruto et al. 1981, Wolter 2004). These include features like porosity or crystal size distribution, which are established during the calcination process (Rodriguez-Navarro 2009) and depend strongly on the calcination conditions (e.g., calcination *T*, soaking time).

If the RH value is sufficiently low, it could be hypothesized that hydration should occur by adsorption of water molecules onto CaO crystals without disintegration (dissolution) of the lime structure (Beruto et al., 1981, Serris et al., 2011). When the humidity is above a certain threshold value, water may condensate on the surface and/or in the pores of the sample. In this latter situation, the solid state hydration is not expected to be the ruling mechanism. Most probably, hydration will occur via the dissolution of lime followed by the precipitation of portlandite.

The measurements of portlandite crystallite size show approximately equal values regardless of calcination *T* of precursor carbonate. This seems to be rather improbable if a solid state hydration mechanism would be at work. Considering the significant differences in the initial size of CaO crystals, one should expect that a solid state mechanism would led to $Ca(OH)_2$ crystals of increasing size for precursor oxides of increasing size (due to sintering at high *T*). Therefore, the dissolution of lime followed by the precipitation of portlandite appears to be the main mechanism for lime hydration also in the core of vapor phase hydration. FESEM observations of hydrated calcite pseudomorphs showing preservation of the external rhombohedral shape, along with 2D-

XRD analyses indicating a strong crystallographic control in the progress of the reaction, indicate that dissolution and precipitation have to be tightly coupled in space and time (i.e., coupled dissolution/precipitation reaction, Putnis 2009). However, a solid state hydration cannot be ruled out, at least in the deeper parts of the sample, where transport of a liquid phase would be hampered by the formation of an impervious product shell. The formation of such a shell is related with the reduction in porosity and takes place when portlandite replaces lime (i.e., the molar volume of portlandite is higher than the molar volume of lime). The pore structure of the sample, which evolves as the hydration progresses, is responsible for controlling the diffusion of water vapor within the sample and is expected to play a key role in the selection of the hydration mechanism. Therefore, at a low RH the solid state hydration would be more probable, whereas at a high RH the coupled dissolution/precipitation mechanism is expected to be at work. On the other hand, as indicated by Wolter et al. (2004), the differences in molar volume between CaO and replacing $Ca(OH)_2$ may facilitating the breaking and peeling off the hydrated shell. This phenomenon would enable the progress of the coupled dissolution/precipitation reaction towards the core of the sample and the full conversion of CaO particles into portlandite without the need of solid state hydration.

Pole figures of parent (lime) and product (portlandite) phases along with HRTEM analyses, gave insights into the progress of the hydration process from a crystallographic point of view. Regardless the mechanism of reaction (coupled dissolution/precipitation reaction or solid state reaction), the structures of lime and portlandite appear to play an important role in the advancement of the hydration process. Figure 3.17 presents the structure of lime (a) and the unit cell of portlandite (b). Comparison of these structures demonstrates that there are strong similarities between $(111)_{lime}$ and $(0001)_{portlandite}$ planes, i.e., similar distribution of Ca ions on these planes. Basically, the hydration of lime requires the expansion of d_{111} spacing of lime from 2.78 Ǻ up to 4.91 Ǻ coupled with a parallel shifting of $(111)_{lime}$ planes. HRTEM analyses show that this is achieved by the expansion of the lime structure along the $[110]_{lime}$ direction followed by a shifting along the $[\bar{1}10]_{lime}$ direction. Structural rearrangements also require the expansion along the $[01\bar{1}]_{lime}$ and $[\bar{1}01]_{lime}$ directions from 3.4 Ǻ up to 3.59 Ǻ in order to form the *a*-axis and the *b*-axis of portlandite lattice. These operations are the result of the replacement of the oxygen atom by two hydroxyl groups, and are responsible for the increase in molar volume and reduction in porosity observed during FESEM analyses. It also appears that if hydration occurs via a coupled dissolution/precipitation reaction, water should penetrate the lime parallel to its (111) planes, which leads to the conclusion that dissolution of lime is highly anisotropic. Such a dissolution of lime and subsequent precipitation of portlandite has to be coupled in space and time, i.e., has to take place within a sufficiently thin reaction interface as to preserve the crystallographic information regarding the relative orientation between lime and portlandite (Putnis, 2009). If hydration takes place via adsorption of water molecules without disintegration (dissolution) of the lime structure (i.e., solid state reaction) the formation of portlandite has to be preceded by the adsorption of water molecule (physisorption). Subsequently the adsorbed H_2O molecule has to dissociate in the presence of the remaining oxygen ion in the CaO structure forming two hydroxyl groups which are incorporated into the structure (chemisorptions) of the newly-forming portlandite (Manzano et al., 2012).

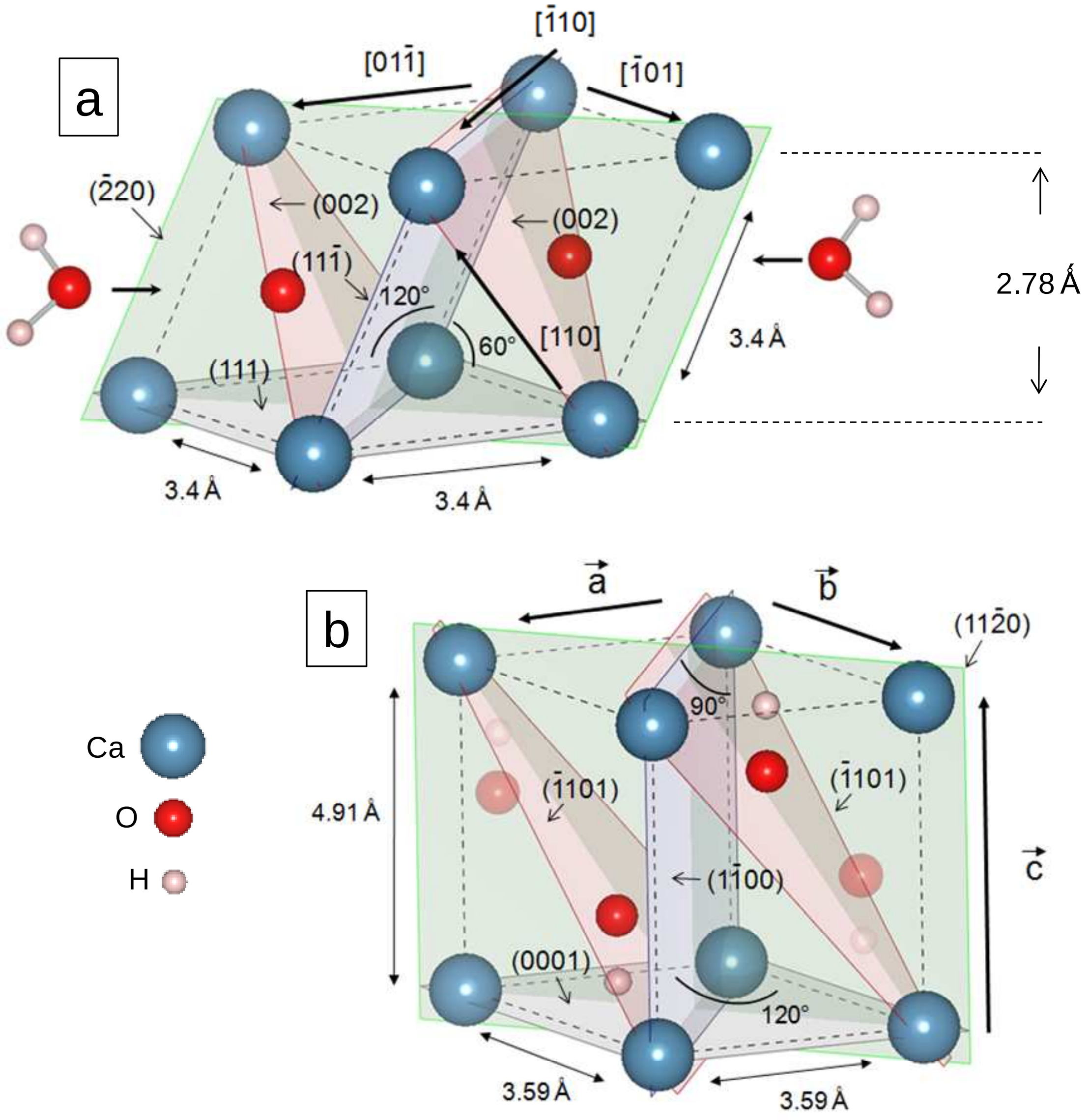

Figure 3.17. Lime structure (a) and portlandite unit cell (b). Note good matching between $(111)_{lime}$ and $(0001)_{portlandite}$ planes. Each water molecule and oxygen atom in lime structure (a) produces two hydroxyl groups. Semi transparent OH^- groups (b) belong to adjoining portlandite unit cells.

4. CARBONATION OF CALCIUM HYDROXIDE

4.1. Introduction

As it has been stated in sec. 1.3 carbonation has received less attention than other processes within the lime cycle (i.e., calcination and hydration). Up until now most studies on carbonation have concentrated on the tailoring of size and properties of industrially produced calcium carbonate, as well as on the analyses of the deterious effects of carbonation in Portland cement. However, these studies are not directly applicable in the field of heritage conservation.

In order to shed some light on the carbonation phenomenon taking place in lime pastes, mortars or nanolimes applied in conservation interventions, including the mechanism(s) of such a reaction, phase evolution and morphology changes, a series of experiments was designed and performed. These experiments are grouped in four major types: (1) precipitation from lime water, (2) carbonation of portlandite single crystal, (3) carbonation of hydrated calcite pseudomorphs and (4) observation of carbonation in lime pastes. Various types of analyses (including in-situ and ex-situ observations) which cover a wide range of observation scales were performed. Moreover, the problem of the crystallographic nature of the carbonation process (topotactic/epitactic) was investigated by the analysis of the crystallographic orientation relationship between parent and product phases.

In addition to experimental methods, theoretical investigations were also performed. The evolution of lime water chemistry was simulated with the aid of PHREEQC software. Simulations of diffraction patterns of stable prenucleation clusters and short range order in amorphous precursors in the context of the so-called non-classical nucleation were also performed and compared with experimental results.

4.2. Materials and Methods

Prior to analyses, two types of $Ca(OH)_2$ pastes were obtained by slaking of one industrially produced quicklime (AC – Andaluza de Cales, Seville, Spain) and one traditionally produced quicklime (FG – Francisco Gordillo Lime, Seville, Spain). Details of the textural and physical properties of both quicklimes can be found elsewhere (Ruiz-Agudo and Rodriguez-Navarro, 2010). Slaked lime putties were prepared in the laboratory by mixing CaO pebbles (1-2cm in size) and deionized water under vigorous stirring. The water/oxide weight ratio was 1:4. The suspensions, covered by a supernatant solution were kept in air-tight plastic containers to avoid carbonation (after Ruiz-Agudo and Rodriguez-Navarro, 2010). Details of the physical properties of both limes are presented in Appendix 1. Additional details on the physical and rheological properties of these slaked limes can be found in Ruiz-Agudo and Rodriguez-Navarro (2010).

4.2.1. Carbonation in solution

Two types of experiments regarding precipitation of calcium carbonate from solution (i.e., lime water, the supernatant above the slaked lime) were performed, here denoted as Run A and Run B. Carbonation took place at the solution/air interface following lime water exposure to air at room *T*. Run A involved precipitation of calcium carbonate from a solution saturated with respect to calcium hydroxide, placed in a container (crystallization dish). In contrast, Run B involved the precipitation of calcium carbonate at the solution/air interface in a crystallization dish where excess solid $Ca(OH)_2$ was present at its bottom. Run A represents a general situation, which occurs at the very initial stages of carbonation, as well as the very end of carbonation within pore solution of lime mortars. Run B reflects a situation occurring between the initial and final stages of carbonation. In other words, it represents a situation, when carbonation follows partial dissolution of the calcium hydroxide binder. A schematic representation of the main features of Run A and Run B are presented in Figure 4.1.

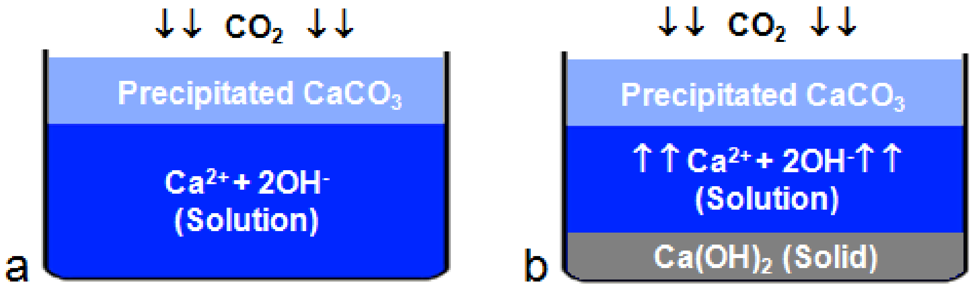

Figure 4.1. Schematic representation of Run A (a) Run B (b).

Various analyses of Run A and Run B precipitates were performed, including the use of both in-situ and ex-situ techniques. In the following section details of such analyses will be described.

4.2.2. In-situ analyses

The temporal evolution of the formation of precipitates (amorphous and crystalline) was analyzed in-situ by the use of X-ray diffraction. In the case of in-situ XRD analysis, a few milliliters of lime water solution formed upon dissolution of slaked lime (FG) were placed in a zero-background silicon sample holder. Carbonation took place at the solution/air interface following exposure to air, at room *T* and $p\text{CO}_2 = 10^{-3.5}$ atm. Analyses were performed both using a solution saturated with respect to $Ca(OH)_2$ (Run A sample) and lime water with excess of $Ca(OH)_2$ (continuous supply of Ca^{2+} and OH^{-}), i.e., FG slaked lime particles deposited at the bottom of the holder (Run B sample). Subsequently, sample holders were placed in the chamber of a Philips X'Pert Pro x-ray diffractometer (XRD) and analyzed with Cu Kα radiation, $\lambda = 1.5405$ Å at the °2θ range 10-50 ° and at a ~0.11 °2θ/s goniometer scan rate. Precipitation of calcium carbonate was monitored over a 3 h period of time, following continuous acquisition of XRD patterns. Collection of each individual pattern took ~6 min.

The precipitation of $CaCO_3$ was also followed in-situ by using micro-Raman spectroscopy. Prior to the observations with the aid of Raman Spectroscopy coupled with optical microscopy (JASCO 6200, laser wavelength: 532.14 nm), a few milliliters of FG lime water were placed on an ultraclean silicon slide using a pipette. Subsequently, the sample was placed inside the device chamber and exposed to air at room *T* and $p\text{CO}_2$ for ~1 h. Measurements involved collection of images (using a built-in optical microscope) and recording of Raman spectra of precipitates. In order to complete the study on crystal morphology and its evolution during carbonation, independent observations by polarized light optical microscopy (Olympus BX60) were performed. Sample and carbonation conditions were similar as in the previous case, with the difference, that in this later case, a glass slide was used. During observation photographs were collected. Both analyses corresponded to a run A-type test. No attempt to perform a run B test using this set up was done because the excess solid below the supernatant precluded the observation under transmitted light of the precipitates formed at the air-solution interface.

Using environmental scanning electron microscope (ESEM), evaporation and condensation of water on a sample holder (a Peltier stage) was obtained by decreasing and increasing of the pH_2O, respectively, at constant T (3 ºC) inside the ESEM chamber. The first step of precipitation, here denoted as the 1st crystallization (or carbonation) cycle, involved the evaporation of water from a sample after placing it in the ESEM chamber. Subsequent condensation (leading to dissolution of previously formed precipitate) and evaporation (associated with re-precipitation of the previously not fully or fully dissolved precipitate) of water will be referred as to the 2nd crystallization (carbonation) cycle. Analyses performed here have involved only a run A-type test, with no further cycles than 2nd. Two different situations were examined. In the first one (Experiment 1), a drop of FG lime water was placed on a sample holder and equilibrated with air at standard room temperature and pressure for 2 min prior to analysis. Once placed in the ESEM chamber, the temperature was decreased to 3 ºC within one minute. The formation of precipitates was observed within two successive crystallization cycles. The second examination (Experiment 2) involved equilibration of the solution at room temperature and pressure for 7 min, after which it was subjected to analysis in the ESEM chamber. Like in the case of Experiment 1, T was decreased to 3 ºC, at the same rate. In this latter case, the formation of precipitated calcium carbonate was observed only within the 1st crystallization cycle.

4.2.3. Ex-situ analyses

In the case of Run A, precipitated calcium carbonate (PCC) was allowed to grow for 2 min or 2 h. Additionally, in a set of experiments, the solution was air bubbled for about 10 min in order to accelerate carbonation. In the case of Run B, carbonation took place for 2 min or 2 h. All precipitates were collected with a spatula, rinsed in ethanol and dried in an oven at 100 °C during 30 min prior to analysis.

Precipitated calcium carbonate was analyzed by Fourier transform infrared spectroscopy (FTIR) and by XRD (Philips PW-1710 diffractometer with Cu Kα radiation, λ = 1.5405 Å) in order to identify calcium carbonate phases. For FTIR analysis, powdered samples were mixed with KBr and pressed into pellets. The analysis was carried out using a Perkin Elmer 1725x spectrometer in the frequency range 400-4000 cm^{-1} with 128 scans/sample and 4.0 cm^{-1} resolution. The morphology of precipitates was analyzed using a LEO Carl Zeiss GEMINI-1530 Field Emission Scanning Electron Microscope (FESEM) after coating the samples with carbon. In order to determine any structural changes taking place during carbonation, as well as microstructural features of parent and product phases, precipitates were analyzed with the aid of a Philips CM20 transmission electron microscopy (TEM), operated at a 200 kV acceleration voltage. Prior to TEM observations samples were dispersed in ethanol, sonicated 2 min, and deposited on carbon-coated copper grids.

4.2.4. Carbonation of portlandite single crystals

Millimeter-sized portlandite single crystals were obtained by mixing (homogenous synthesis) 0.2M NaOH solution with 0.1M $CaCl_2$ solution (Johnston, 1914). Solid reactants were placed in separate beakers (50 ml vol., 20g of NaOH and 27.72g of $CaCl_2$), and subsequently placed in a large plastic container (2.5 l), filled out with de-ionized water and covered with plastic tape to separate the system from the atmosphere in order to avoid carbonation while portlandite crystals were growing. A schematic representation of the setup in which crystallization of portlandite single crystals was performed is shown in Figure 4.2.. Upon dissolution of the reactants and counter diffusion of ions in solution, portlandite crystals formed after one week. Crystals, with typical prism-shaped morphology (Figure 4.2), were kept growing in the container until their size reached about 4 mm length and 2 mm width. Crystals were collected, rinsed thoroughly in ethanol, and oven dried for 30 min at 100 ºC. Portlandite crystals were placed in an air-ventilated plastic container with high RH (~93%) at 20 ºC in order to achieve carbonation.

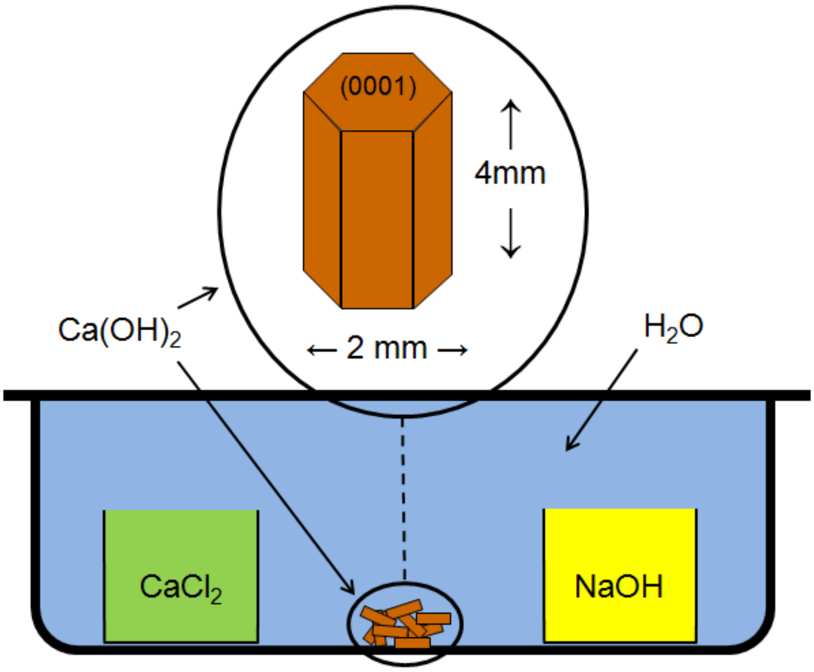

Figure 4.2. Schematic representation of the setup used for the homogenous synthesis of portlandite single crystals.

Purity and phase of newly synthesized portlandite crystals was confirmed by XRD analysis (Philips PW-1710 diffractometer with Cu Kα radiation, $\lambda = 1.5405$ Å). Pole figures describing the 3D orientation relationships between portlandite pseudomorphs and PCC (calcite) were determined using an X-ray single crystal diffractometer equipped with an area detector (D8 SMART APEX, Bruker). To determine parent/product crystallographic orientation relationship(s) samples were collected at different time intervals during a 4 months carbonation time and analyzed with 2D-XRD. For these 2D-XRD experiments, the working conditions were: Mo Kα ($\lambda = 0.7093$ Å), 50 kV and 30 mA, a pin-hole collimator of 0.5 mm in diameter, and an exposure time of 20 s per frame. Portlandite pseudomorphs were analyzed resting flat either on (0001) or on $(11\bar{2}0)$ faces (diffractometer ω and 2θ angles were set at 10 and 20 degrees, respectively). A set of frames (2D diffraction patterns) was registered while rotating the sample around φ angle (a frame every 5 degrees; a total of 72 frames). Pole figures were calculated and displayed in stereographic projection using the XRD2DScan software (Rodriguez-Navarro 2006). The morphology of portlandite single crystals, as well as pseudomorphs formed following carbonation, was analyzed with the aid of a LEO Carl Zeiss GEMINI-1530 field emission scanning electron microscope (FESEM) after coating the samples with carbon.

4.2.5. Carbonation of hydrated calcite pseudomorphs (HCP)

Single crystal calcite pseudomorphs calcined at different *T* (700, 800 and 900 ºC for 30 min) which were previously hydrated for 24 h (in air de-voided of CO_2 at RH~50%) were subjected to carbonation in an air-ventilated plastic container with high RH (~93%) at 20 ºC for four days. The degree of carbonation was determined based on 2D-XRD 2-theta scans analysis (XRD quantification, see sec. 4.2.7.2). Pole figures of precipitated calcite were calculated and displayed in stereographic projection using the XRD2DScan software (Rodriguez-Navarro 2006). The morphology of calcite precipitated on the surface and within the bulk pseudomorph was analyzed using a LEO Carl Zeiss GEMINI-1530 field emission scanning electron microscope (FESEM). Prior to FESEM analysis samples were carbon coated.

4.2.6. Carbonation of hydrated lime pastes (HLP)

Lime putties (AC and FG) were collected from containers, dried in an oven for 24 hours at 100 ºC and grinded to obtain a fine powder. Powders were passed through a mesh in order to eliminate particles with size bigger that 60 µm. Hydrated lime pastes were prepared by mixing dried hydrated lime powders (~1g) with de-ionized water, with ~0.5 mass ratio. Each type of lime paste was thinly (~ 0.5mm) spreaded over sample cups with the aid of a spatula. A flat sample geometry was selected in order to ensure the one-dimensional advancement of the carbonation reaction front (from the upper exposed surface, down through the sample depth), and to maximize the diffusion of CO_2 through the sample thickness (Cizer, 2009). Subsequently, samples were placed in an air-ventilated plastic container with high RH (~93%) at 20 ºC. Samples undergoing carbonation were collected at different time intervals during a 2 months period and subsequently analyzed with TG, XRD, FESEM and TEM-SAED. Additionally, after completion of analyses, samples were kept for two months more to achieve full carbonation, and once again analyzed with TG and XRD.

The degree of HLP carbonation was determined by thermogravimetric (TG) analysis in flowing (100 $cm^3 \cdot min^{-1}$) air atmosphere on a Shimadzu TGA-50H analyzer equipped with a Mettler-Toledo AX26 Delta Range microbalance. For each TG run, the temperature was risen from 20 ºC up to 1000 ºC at a controlled heating rate of 10°C/min. In each measurement a sample of ~30 mg was placed into a platinum crucible, and weight loss data were collected at regular time intervals. For comparison purposes, the degree of carbonation was also determined from XRD data (see sec. 4.2.7.2).

All X-ray diffraction analyses (phase evolution with carbonation, determination of portlandite/calcite intensity ratio for calibration) were performed using a Philips PW-1710 diffractometer with Cu Kα radiation (λ = 1.5405 Å). Data were collected between 15 and 40 º2θ at a 0.03 º2θ/s scan rate. Prior to XRD analysis, samples were weighted, grinded in an agate mortar and placed in zero-background silicon sample holders. XRD patterns were analyzed with the aid of the XPowder software package (Martin-Ramos 2004). Additionally, in some cases (e.g., problems associated with XRD peak separation) the XRDFit software, written by the author (Appendix 2), was used. Morphological investigations of calcium carbonate precipitated on the exposed surfaces and along the freshly-broken cross sections (i.e., depth profiles) were performed using a LEO Carl Zeiss GEMINI-1530 Field Emission Scanning Electron Microscope (FESEM) after coating the samples with carbon. Shape, size, microstructure and crystallographic relationship(s) of parent (portlandite) and product (calcite) phases were analyzed using a Philips CM20 TEM, operated at a 200 kV acceleration voltage. Prior to TEM observations samples were grinded in an agate mortar and dispersed in ethanol, sonicated 2 min, and deposited on carbon-coated copper grids.

4.2.7. Quantification of carbonation degree

4.2.7.1. TG quantification

TG traces as a function of temperature of carbonated HLP samples contain two slopes which correspond to the mass lost in two steps. The first step occurred at around

400 ºC and corresponded to the thermal decomposition of portlandite to lime (CaO) and water, as expressed by the following dehydroxylation equation:

$$Ca(OH)_2 \rightarrow CaO + H_2O \uparrow \quad (4.1)$$

The second step (thermal decomposition of calcite) appears near 700 ºC and leads to lime formation plus release of CO_2:

$$CaCO_3 \rightarrow CaO + CO_2 \uparrow \quad (4.2)$$

The final products of portlandite and calcite thermal decomposition with their weight percent are listed in Table 4.1.

Table 4.1. Product phases of the thermal decomposition of portlandite and calcite, and their weight percent (after www.webmineral.com)

	Portlandite	***Calcite***
Products of thermal decomposition	CaO (75.69 wt %) H_2O (24.31 wt %)	CaO (56.03 wt %) CO_2 (43.97 wt %)

Mass loss in the first step (Δm_1) is caused by the release of water which constitutes 24.31 wt % of portlandite mass (m_p). Having Δm_1, the mass of portlandite is calculated from equation(s):

$$\Delta m_1 = 0.2431 m_p \quad (4.3)$$

$$m_p = 4.1135 \Delta m_1 \quad (4.4)$$

During the second step (calcite thermal decomposition at ~700 °C), the mass lost (Δm_2) corresponds to the release of carbon dioxide, constituting 43.97% of the calcite mass. The mass of calcite (m_c) is calculated from equation(s):

$$\Delta m_2 = 0.4397\ m_c \quad (4.5)$$

$$m_c = 2.2743\ \Delta m_2 \quad (4.6)$$

The degree of carbonation (in percent) is equal to the calcite weight percent in the sample and is expressed by the equation:

$$W_c = \frac{m_c}{m_c + m_p} 100 \quad (4.7)$$

4.2.7.2. *XRD quantification*

The other method of determining the carbonation degree applied in this work involved the comparison of the XRD peak intensity ratio of parent (portlandite) and the product (calcite) phases. Prior to this type of quantification, a model carbonation curve was experimentally determined. The following procedure was applied. First, known amounts of portlandite and calcite were mixed at different ratios, (calcite weight fraction ranging from ~0.1 up to ~0.9). Mixtures were analyzed with XRD. By means of peak profile analysis (using XPowder) the intensity ratios of $(10\bar{1}4)_{calcite}$ /$(10\bar{1}1)_{portlandite}$ were determined for each mixture. Selection of these peaks was dictated by their highest intensities. Subsequently $(10\bar{1}4)_{calcite}$ /$(10\bar{1}1)_{portlandite}$ ratios were plotted as a function of calcite weight percent. To these experimental points a curve was fitted (using gnuplot (http://www.gnuplot.info)). The fitting equation was derived as follows:

The simplified X-ray diffraction peak intensity ($I_{\alpha}^{(hkl)}$) for a particular phase (α) in a multiphase powder sample can be expressed by the following equation (Connolly, 2010):

$$I_{\alpha}^{(hkl)} = \frac{K_e K_{\alpha}^{(hkl)} W_{\alpha}}{\rho_{\alpha} (\mu / \rho)_s} \quad (4.8)$$

where:

- K_e – experimental constant, which depends on the experimental setup (e.g., X-ray wavelength, incident beam intensity)
- $K_{\alpha}^{(hkl)}$ - constant effectively equal to the structure factor for α phase and (*hkl*) plane
- W_{α} – weight fraction of α phase
- ρ_{α} – density of α phase
- $(\mu / \rho)_s$ – mass absorption coefficient of the specimen, defined as:

$$(\mu/\rho)_s = \sum_{i=1}^{n} W_i (\mu/\rho)_i \quad (4.9)$$

where:

- $(\mu/\rho)_i$ – mass absorption coefficient of the ith phase
- W_i - weight fraction of ith phase

In our case we considered the sample composed of two phases: portlandite and calcite. Thus, the intensity ratio of two X-ray diffraction peaks corresponding to the two different phases (C - calcite and P - portlandite) in the sample can be expressed as:

$$\frac{I_C^{(h_1k_1l_1)}}{I_P^{(h_2k_2l_2)}} = A\frac{W_C}{W_P} \quad (4.10)$$

where A is a constant:

$$A = \frac{K_C^{(h_1k_1l_1)}}{\rho_C}\frac{\rho_P}{K_P^{(h_2k_2l_2)}} \quad (4.11)$$

W_C and W_P are weight percent of calcite and portlandite respectively. Since our sample contains only two phases, the sum of weight percent of calcite and portlandite equals 100%, thus

$$W_P = 100 - W_C \quad (4.12)$$

Therefore the intensity ratio can be expressed as a function of calcite weight percent:

$$\frac{I_C^{(h_1k_1l_1)}}{I_P^{(h_2k_2l_2)}} = A\frac{W_C}{100 - W_C} \quad (4.13)$$

The A value was determined by fitting Eq. 4.13 to experimental points (using gnuplot). Figure 4.3 presents the results of this fitting.

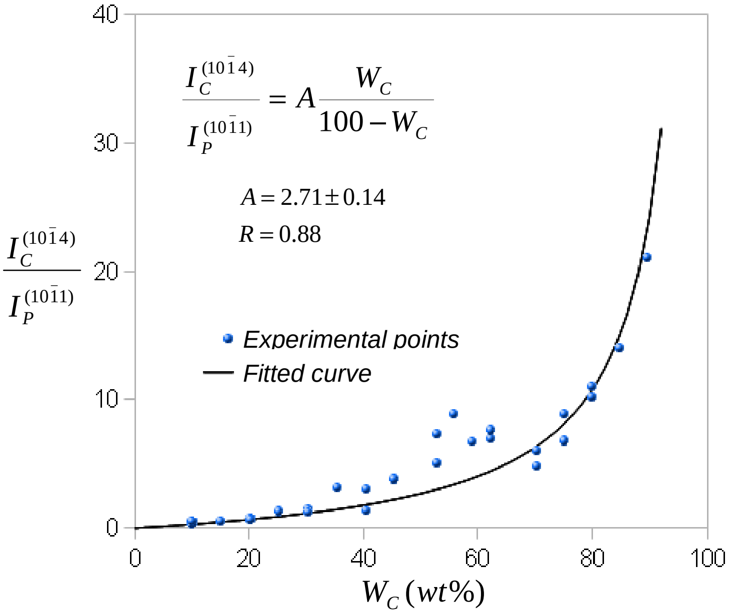

Figure 4.3. Relative $(10\bar{1}4)_{calcite}$ / $(10\bar{1}1)_{portlandite}$ peaks intensity ratio (blue dots) as a function of calcite weight percent, and fitted carbonation curve (black solid line).

After transformation of Eq. 4.13, having A constant and knowing the intensity ratio, the expression for weight percent of calcite (degree of carbonation) is as follows:

$$W_c = \frac{\dfrac{I_C^{(h_1k_1l_1)}}{I_P^{(h_2k_2l_2)}}}{A + \dfrac{I_C^{(h_1k_1l_1)}}{I_P^{(h_2k_2l_2)}}}100 \quad (4.14)$$

4.2.8. Evolution of pore water chemistry (PHREEQC simulation)

In order to gain an insight into the evolution of pore water solution chemistry (changes of pH, saturation index, $[Ca^{2+}]/[CO_3^{2-}]$ ratio) as carbonation progresses, simulation of carbonation in lime water was performed. It was achieved with the aid of PHREEQC software (Parkhurst and Appelo, 1999).

The saturation index (SI) is defined as:

$$SI = \log(\Omega) = \log(\frac{IAP}{Ks}) \quad (4.15)$$

where:

- Ω - is the saturation state of the system,
- IAP - is the ion activity product
- Ks - is the thermodynamic solubility product of the relevant phase (i.e., calcium carbonate polymorphs and ACC)

Phases considered and their thermodynamic solubility product (log(Ks)) at standard temperature and pressure (STP) are presented in Table 2 (Brečević and Nielsen, 1989).

The simulation covered the very initial stage of carbonation at the solution/air interface, i.e., carbonation in lime water during Run A, when no additional supply of $Ca(OH)_2$ occurs. Initial values of the simulation also represents the final stage of carbonation during run B, once full dissolution of excess solid $Ca(OH)_2$ occurs.

The PHREEQC simulation was performed as follows. First, lime water ($Ca(OH)_2$ saturated solution) was equilibrated with air at room temperature. The whole equilibration reaction was divided into 100 steps. At each step, saturation indexes with respect to calcium carbonate polymorph, $[Ca^{2+}]/[CO_3^{2-}]$ ratio and pH were calculated.

Table 4.2. Different phases (first column) considered in PHREEQC simulation and their thermodynamic solubility product (log(Ks)) at standard temperature and pressure (STP) (Brečević and Nielsen, 1989).

Phase	***log(Ks) at STP***
Portlandite	-5.19
Calcite	-8.48
Vaterite	-7.91
Aragonite	-8.33
ACC	-6.4

4.3. Results

4.3.1. In-situ XRD

Figure 4.4 presents three dimensional time resolved XRD patterns collected in-situ, corresponding to the evolution of two types of lime water (i.e., lime water with and without excess of $Ca(OH)_2$), air-exposed for three hours at standard room *T* and pressure. Figure 4.4a shows the evolution of the sample without additional calcium hydroxide (Run A), whereas Figure 4.4b. depicts the evolution of the sample with addition of solid $Ca(OH)_2$ (Run B). The patterns reveal that independently of the sample considered, the only precipitated calcium carbonate polymorph was calcite. Furthermore, in the case of Run B, portlandite Bragg peaks were recorded throughout the experiment. Their presence in XRD patterns was associated with excess solid $Ca(OH)_2$ in the solution. The intensity of portlandite peaks was however reduced as carbonation progressed with time, while the corresponding intensity of calcite peaks increased over time in both cases (Run A and Run B).

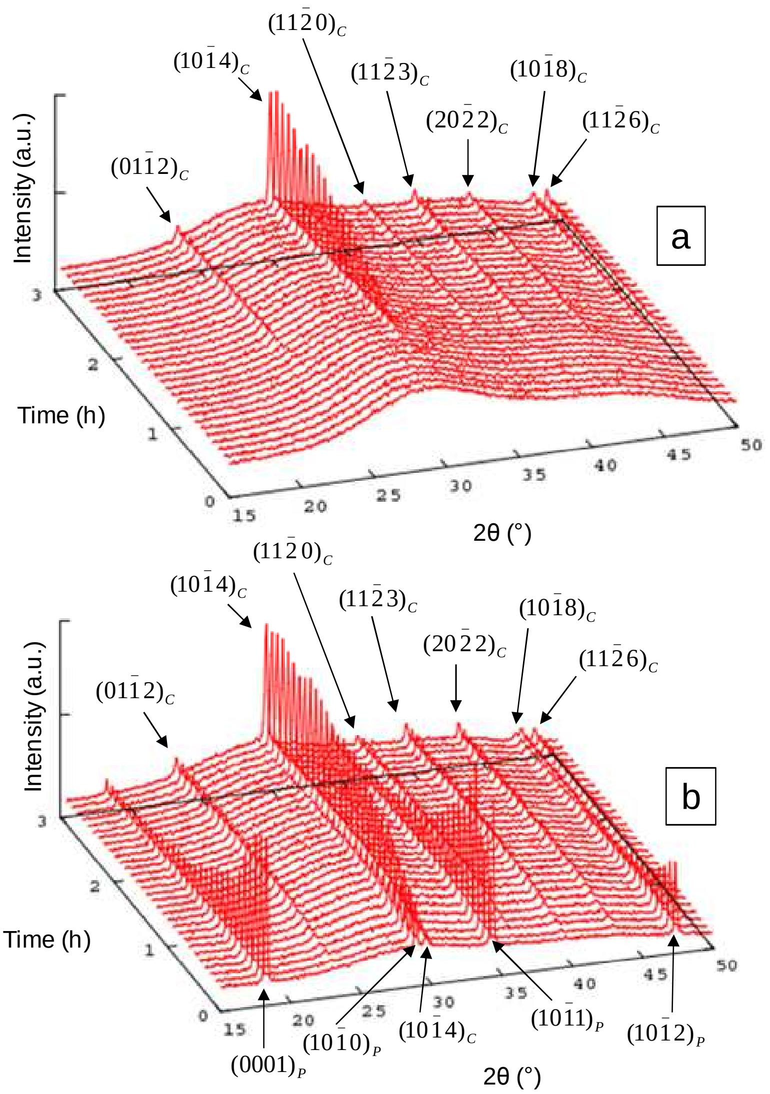

Figure 4.4. Three-dimensional, time resolved XRD patterns showing the evolution of calcite precipitated from solution saturated with respect to portlandite, Run A (a) and with continuous supply of $Ca(OH)_2$, Run B (b) at standard room *T* and *P*. In both cases calcite is the only calcium carbonate polymorph observed.

The presence of a broad bump between ~20 and ~35 °2θ range was observed at each recorded stage of carbonation, in both runs. Figure 4.5a1 presents two XRD patterns corresponding to the initial (brown line) and final (blue line) stage of carbonation evolution of Run A sample. Figure 4.5b1 depicts the bump intensities at the beginning and at the end of run B. Such a broadening is more vivid on the XRD pattern corresponding to run A (Figure 4.5a1). Bernal and Fowler (1933) showed that water at room *T* is responsible for the presence of such a broadened bump. However the intensity of the bump tends to either decrease (run A) or increase (run B) with time. Thus, the intensity of the bump must correspond to the sum of the intensity of water plus an amorphous phase. Figure 4.5a2 shows the evolution of the bump intensity (water plus amorphous phase) compared with the intensity of calcite 104 Bragg peak recorded in run A. Note, that calcite was observed after ~1h. The changes of the intensities with time suggest, that calcium carbonate initially forms as an amorphous phase (amorphous calcium carbonate – ACC), and that the formation of calcite is associated with subsequent transformation of ACC into crystalline $CaCO_3$ (Rodriguez-Blanco et al., 2010). Conversely, the intensity of the bump observed during the evolution of run B was higher at the end of the experiment. Figure 4.5b2 presents the intensity changes of the bump along with the intensity evolution of calcite 104 and portlandite 101 Bragg peaks. It can be seen that the amount of ACC initially increased, and reached a plateau after ~1 h maintaining a constant value until the end of the analysis. Calcite showed a logarithmic increase in intensity. The portlandite intensity decreased with time, suggesting its progressive dissolution during analysis. Like in the previous case, it appears that calcium carbonate precipitates initially as ACC and then transforms into calcite. The fact that the amount of ACC does not decrease in this sample (once a plateau was reached), can be related with the constant supply of Ca^{2+} ions, following dissolution of excess solid $Ca(OH)_2$. This in turn compensates for the continuous transformation of ACC into calcite.

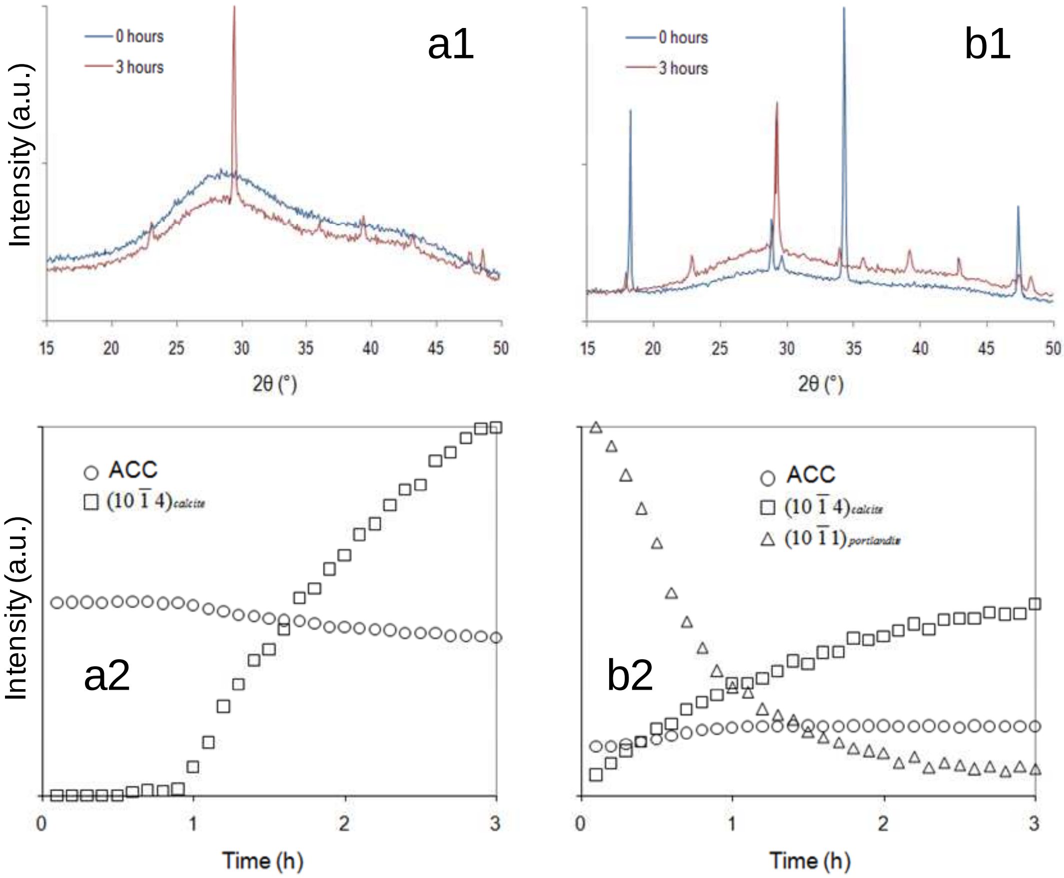

Figure 4.5. XRD patterns corresponding to the initial (blue line) and the final (brown line) stages of carbonation in Run A (a1) and Run B (b1). Notice the presence of a broad bump between ~20 and ~35 º2θ in both stages (corresponding to ACC plus water) and its smaller (Run A) and higher (Run B) intensity after 3 h carbonation. Intensity evolution of Bragg peaks in run A (a2) and B (b2) sample.

Crystallite size evolution of calcite, precipitated in saturated lime water (i.e., in run A sample) is presented in Figure 4.6a1, Figure 4.6b1 and Figure 4.6c1. Its development under continuous supply of Ca^{2+} ions OH$^-$ (run B sample) is depicted in Figure 4.6a2, Figure 4.6b2 and Figure 4.6c2. The most characteristic difference in calcite crystallite size evolution between run A and run B samples, is that in the case of carbonation in saturated lime water slightly higher values were reached. The first reliable (i.e. solved by the software, either by XPowder or XRDFit) calcite $(10\bar{1}4)$ Bragg peak in run A was recorded after ~1 h with an initial crystallite size ~16 nm. Conversely, in run B at the very beginning of the reaction, calcite crystallite size was approximately 27 nm. Moreover, the rate of calcite growth in run A was higher than under excess $Ca(OH)_2$. This phenomenon can be explained taking into account the (super)saturation differences in both samples and the presence of foreign particles (portlandite) that can favor heterogeneous nucleation. The time from the beginning of the reaction to the first appearance of the Bragg peak (i.e., waiting time) is longer (~1 h) in the case of run A, comparing to run B sample, where calcite peaks were recorded from the beginning of the process. According to the classical nucleation theory, the waiting time is inversely proportional to saturation index (SI) whereas the nucleation density is directly proportional to SI (Nielsen, 1964). Following that model, in run B a continuous supply of Ca^{2+} and OH^- ions results in higher SI in turn leading to a higher nucleation density. A higher nucleation density, however, would result in a larger number of crystals competing for the incorporation of Ca^{2+} an CO_3^{2-} ions available in the solution, thus finally growing with a smaller size. However, we do not see this. Despite the higher nucleation density in run B, the crystallite size is higher, but nearly constant throughout the experiment because in this case heterogeneous nucleation onto existing portlandite nanoparticles is favored. This explains the near absence of a “waiting time” in run B. In run A, the absence of any particles at the beginning of the experiment, favors the attainment of a higher supersaturation, leading to nucleation (homogenous) after a long waiting time. Such a high supersaturation results in a high nucleation density, and smaller crystals which eventually continue to grow up to a maximum size of ca. 60 nm. In run B, nucleation is more important driving the whole precipitation, thereby, particles do not tend to keep growing.

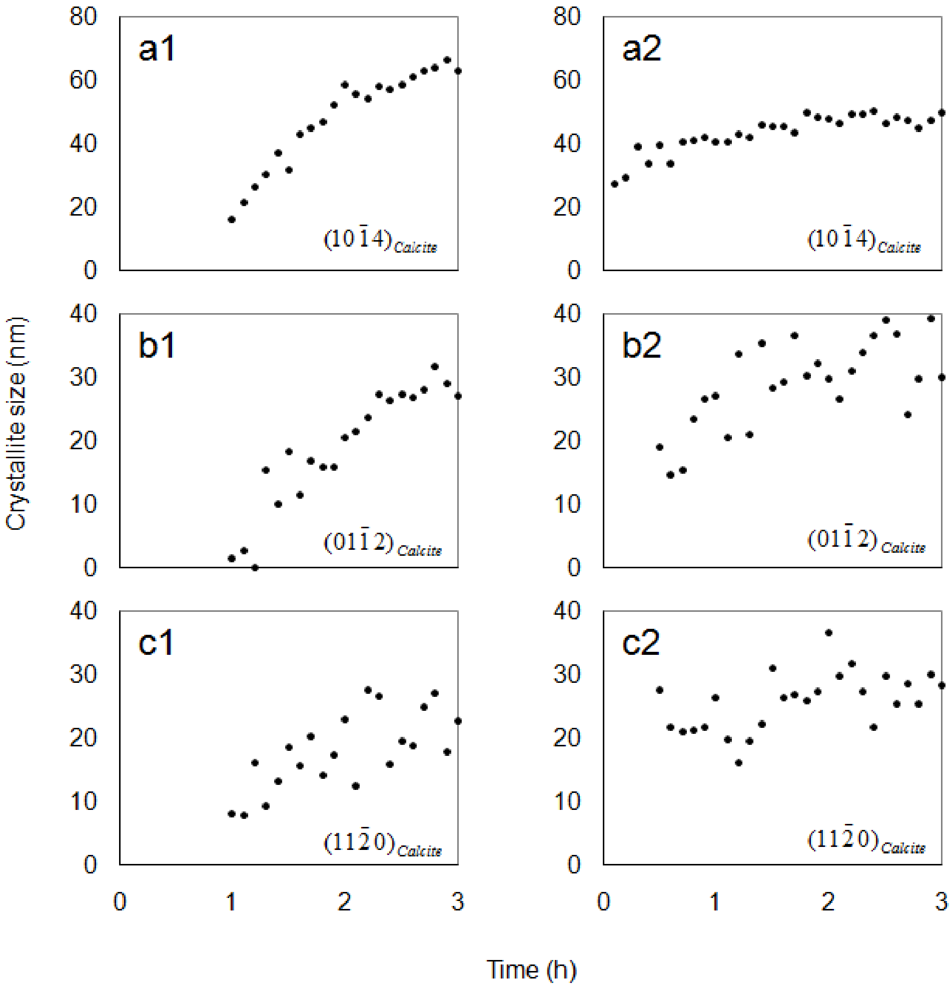

Figure 4.6. Calcite crystallite size evolution from XRD in-situ precipitation, where a1, b1, c1 correspond to $(10\bar{1}4)_{calcite}$, $(01\bar{1}2)_{calcite}$, $(11\bar{2}0)_{calcite}$ of Run A sample (saturated lime water) and a2, b2, c2 correspond to $(10\bar{1}4)_{calcite}$, $(01\bar{1}2)_{calcite}$, $(10\bar{2}0)_{calcite}$ of Run B sample (saturated lime water with excess portlandite).

As shown in Figure 4.4b, apart from calcite, Bragg peaks corresponding to portlandite were also recorded in run B. The presence of such peaks is related to excess solid calcium hydroxide dispersed in solution. Their intensities decrease with time (Figure 4.4b), which indicates that portlandite dissolved during the experiment. The evolution of portlandite crystal size during its dissolution is presented in Figure 4.7. Interestingly, portlandite size tends to decrease in directions normal to the prism faces, while the size along the [001] direction (i.e., perpendicular to the basal plane) remains almost constant during the dissolution/carbonation experiment. In particular, portlandite size in a direction normal to $(10\bar{1}0)$ plane decreases from ~70 nm to ~30 nm, while remained ~70 nm in a direction normal to basal plane ((0001)). These results indicate that portlandite dissolution is strongly anisotropic, and are in agreement with results obtained from carbonation of portlandite single crystals showing that carbonation progresses along basal planes, rather than perpendicular to them (see sec. 4.3.7).

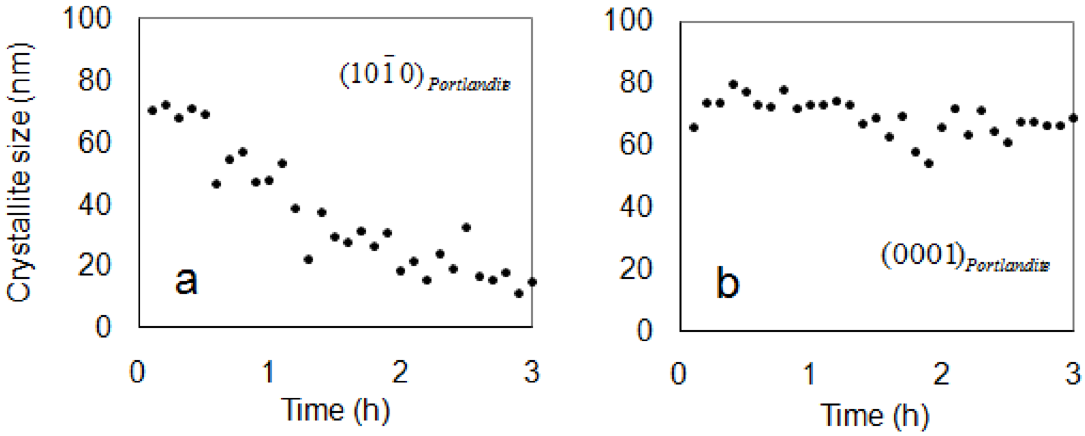

Figure 4.7. Portlandite crystallite size evolution during carbonation: $(10\bar{1}0)$ (a) and (0001) (b). Note almost constant value of (0001) crystallite size.

4.3.2. In-situ Raman spectroscopy and optical microscopy

Within the considered Raman shift range (100-1200 cm^{-1}) calcite exhibits four vibration modes. Two of them are lattice modes (translation mode at 154 cm^{-1} and a higher frequency libration mode at 281 cm^{-1}), and two are internal modes: carbonate ion internal symmetric C-O stretch mode (ν_1, at 1085 cm^{-1}) and in-plane bend mode (ν_4 at 711 cm^{-1}). Only two modes are observable in the case of ACC (e.g., Wang et al., 2011). These are: ν_1 mode at ~1080 cm^{-1} and ν_4 at ~714 cm^{-1}. However, the first one tends to be very weak and broad, and the second can be absent (Brečević and Nielsen 1989).

The results of in-situ Raman Spectroscopy analysis of run A sample coupled with optical microscopy observations are consistent with those obtained from in-situ XRD experiments. Precipitation of calcium carbonate initiated with the formation of micrometer-size spheres at the solution surface (Figure 4.8a1 and Figure 4.9a1). Observation in cross polarized light (Figure 4.9b1) confirmed the amorphous nature of the initial precipitates. Recorded Raman spectra showed only one broad peak of calcium carbonate at ~1076 cm^{-1} (Figure 4.8a2). Its position corresponds to the theoretical value of the ν_1 mode observed in the case of ACC. The peak at ~714 cm^{-1}, corresponding to the ν_4 mode was not observed.

Observation with an optical microscope revealed interesting features regarding the formation of calcium carbonate. Despite being much denser than water, calcium carbonate precipitated at the air/water interface and did not sink. Hashmi et. al., (2005) proposed that the origin of this phenomenon is the nucleation of calcium carbonate on CO_2 bubbles, produced when calcium reacts with bicarbonate and releases CO_2 from the solution.

$$\mathrm{Ca^{2+}} + 2\mathrm{HCO_3^-} \rightarrow \mathrm{CaCO_3} \downarrow + \mathrm{CO_2} \uparrow + \mathrm{H_2O} \qquad (4.16)$$

That way carbon dioxide provides buoyancy to the nucleating calcium carbonate particles, bringing them towards the surface.

As shown by XRD analysis, ACC is a metastable phase which undergoes a fast transformation into calcite. During the initial stages of ACC to calcite transformation, the formation of fractals was observed (Figure 4.9a2 and Figure 4.9b2). Hashmi et. al. (2005) stated that this phenomenon occurs as a result of the competition between attractive and repulsive forces among precipitates.

After ~1 hour, calcite crystals with rhombohedral morphology were observed (Figure 4.8b1). The final size of calcite crystals ranged from a few micrometers up to ~20 µm. Collected Raman spectra confirm the calcite structure of final precipitates, showing all four vibration modes (Figure 4.8b2). The ν_1 position is slightly shifted from ~1076 cm^{-1} in ACC up to ~1080 cm^{-1} in calcite. Furthermore, this peak underwent sharpening. Its FWHM decreased from 26 down to 4.34 cm^{-1}. When the process of calcite precipitation was completed, some crystals were found not only on the surface of the solution, but at the bottom of the glass slide as well (unfocused crystals in Figure 4.9a3).

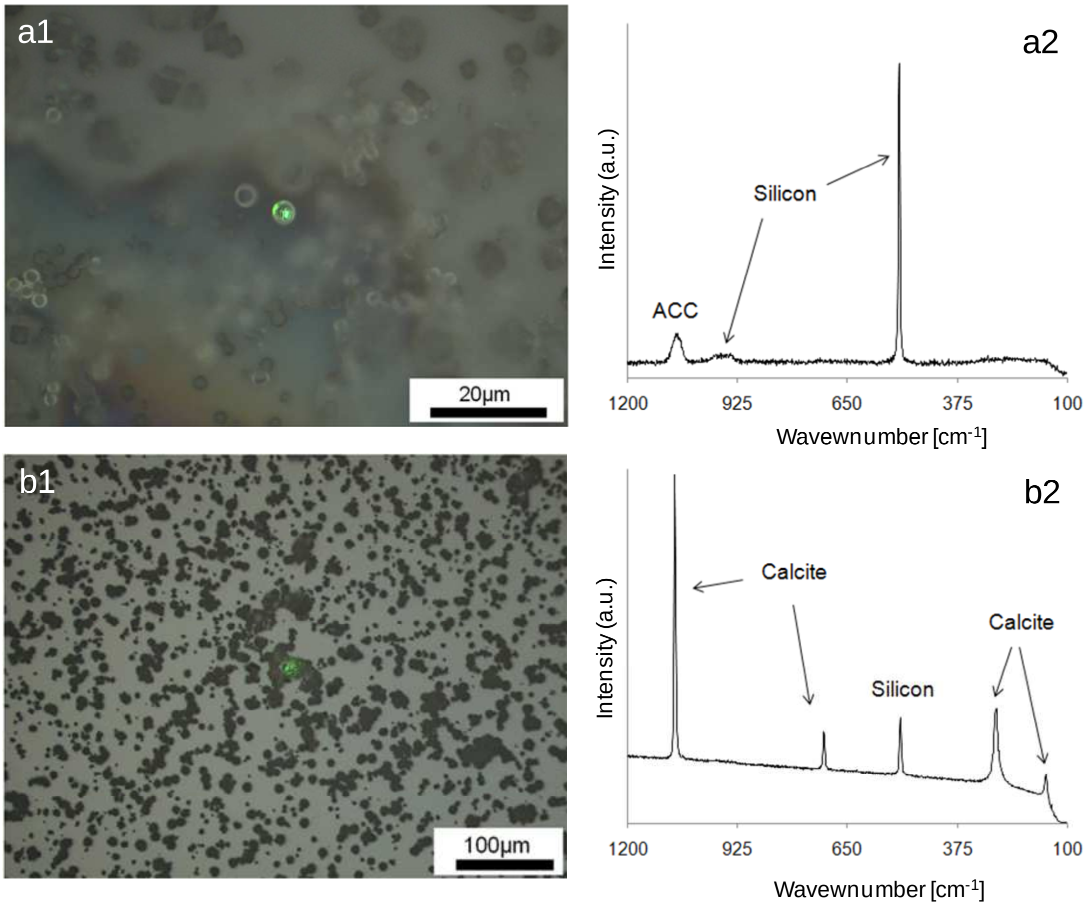

Figure 4.8. Optical microscopy photomicrographs and Raman spectra of calcium carbonate precipitated during Run A recorded in-situ. Initial amorphous calcium carbonate (a1) and final rhombohedral calcite (b1). Corresponding Raman spectrum of ACC (a2) and calcite (b2). Note the presence of the silicon peaks corresponding to the sample holder.

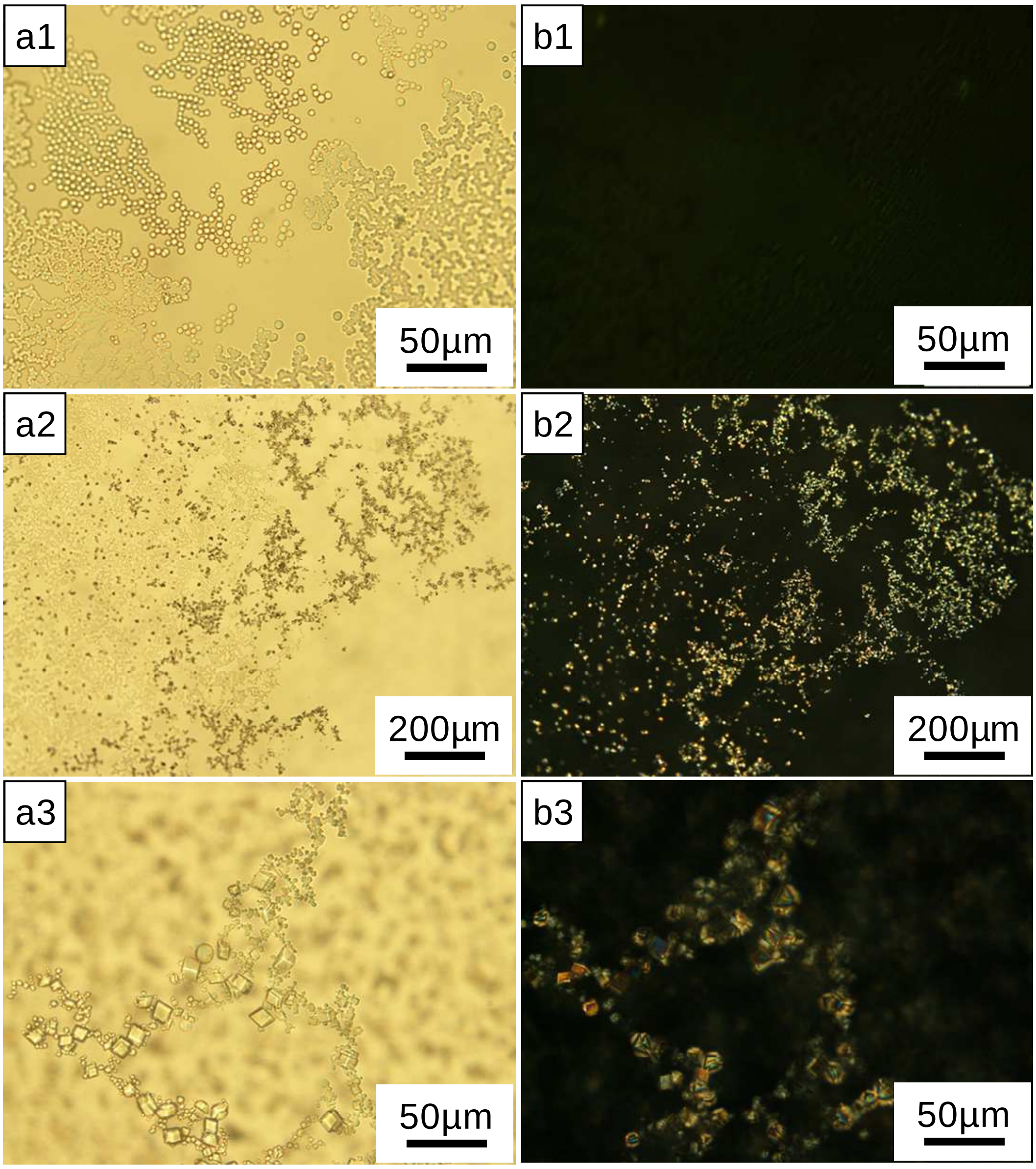

Figure 4.9. Optical microscopy photomicrographs of calcium carbonate precipitation observed in-situ (Run A), using plane light (a1, a2, a3) and under cross polarized light (b1, b2, b3). Initial formation of amorphous calcium carbonate (a1), initial transformation into calcite aggregates with a fractal morphology (a2) and final precipitate – rhombohedral calcite (a3). The crossed Nicol image confirms the amorphous nature of early PCC (b1).

4.3.3. Ex-situ XRD

XRD examinations of precipitates formed after 2 min air-exposure (Figure 4.10a) in the saturated solution without portlandite excess (Run A) are in good agreement with in-situ XRD results. Like in the case of previous analyses, the broad bump between ~20 and ~35 º2θ range, indicates the formation of ACC. Interestingly, along with the formation of ACC, calcite Bragg peaks were recorded. Such a transformation took place much faster than in the case of in-situ XRD experiments. The source of such a discrepancy is not clear, but most probably could be related with different history of the samples. Nevertheless, the fact that ACC to calcite transition took place after such a short time clearly shows how unstable this phase is. The simultaneous coexistence of these two phases, and the fact that no other Bragg peaks corresponding either to aragonite or vaterite were recorded, indicates that ACC to calcite transformation occurs directly, without formation of any other calcium carbonate metastable phase.

The measured calcite $(10\bar{1}4)$ crystallite size was ~50 nm, which is smaller than the corresponding value of calcite crystallite size at the end of in-situ XRD experiment (~65 nm). However, $(01\bar{1}2)$ and $(11\bar{2}0)$ calcite crystallite sizes showed ~72 and ~58 nm respectively. These values significantly exceed the values of equivalent crystallite size measured at any stage of in-situ experiments. The width of the broad bump correspond to a crystallite size of ~1 nm. Note that a reliable measurement could not be performed on the bump from in-situ XRD experiment, since in that case, the bump was the result of the overlapping of calcium carbonate and water reflections. Moreover, the center of the bump observed here, was shifted towards smaller 2θ values (23.62º) if compared to the bump observed during in-situ XRD analysis (28.17º). The center of the bump in the former case corresponds to a *d*-spacing value ~3.76 Å. Gebauer et al. (2008) reported on the formation of the so-called stable prenuclation clusters, with size reaching up to ~2 nm, which later tend to aggregate forming ACC (~30 nm). Following their conclusions, and taking into account the size of the amorphous structure observed here, it might be assumed that the bump corresponds to prenucleation clusters (with a proto-calcite structure) which eventually transforms into “proper” ACC. The formation of a proto-calcite structure was also observed in TEM (see below).

Figure 4.10b shows XRD pattern of the precipitate formed after 10 min air exposure in run A. The only calcium carbonate phase observed in the sample was calcite. The lack of a broad bump observed in Figure 4.10a suggests that the full transformation of the initial amorphous phase took place. The final calcite $(01\bar{1}2)$ and $(11\bar{2}0)$ crystallite size were ~72 and ~59 nm, respectively. These values are similar to the values at the initial stages of ACC to calcite transformation shown in Figure 4.10a. The main difference is observed in the case of calcite $(10\bar{1}4)$ crystallite size, which increased from ~50 nm up to ~62 nm.

The XRD pattern of the precipitate formed after 10 min air bubbling in run A is presented in Figure 4.10c. The only calcium carbonate phase recorded was calcite. Since no other crystalline form of calcium carbonate was recorded, it appears that forced air injection do not affect the phase selection and do not change the transition sequence. The final calcite $(01\bar{1}2)$, $(11\bar{2}0)$ and $(10\bar{1}4)$ crystallite size were ~44, ~42 and ~35 nm respectively. These values are significantly smaller than crystallite sizes observed in the case of 10 min air exposure in run A. One of the possible explanations could be related with the formation of pre-nucleation clusters and their aggregation coupled with dehydration of ACC particles, which result in the formation of calcite crystals (Radha et al. 2010). Forced air injection could increase the dehydration rate leading to clusters aggregation on a smaller scale, thus resulting in the formation of crystals with smaller sizes. Moreover, the pseudomorphic formation of calcite crystals (~30-40 nm in size) during forced air injection was also observed under TEM (see below).

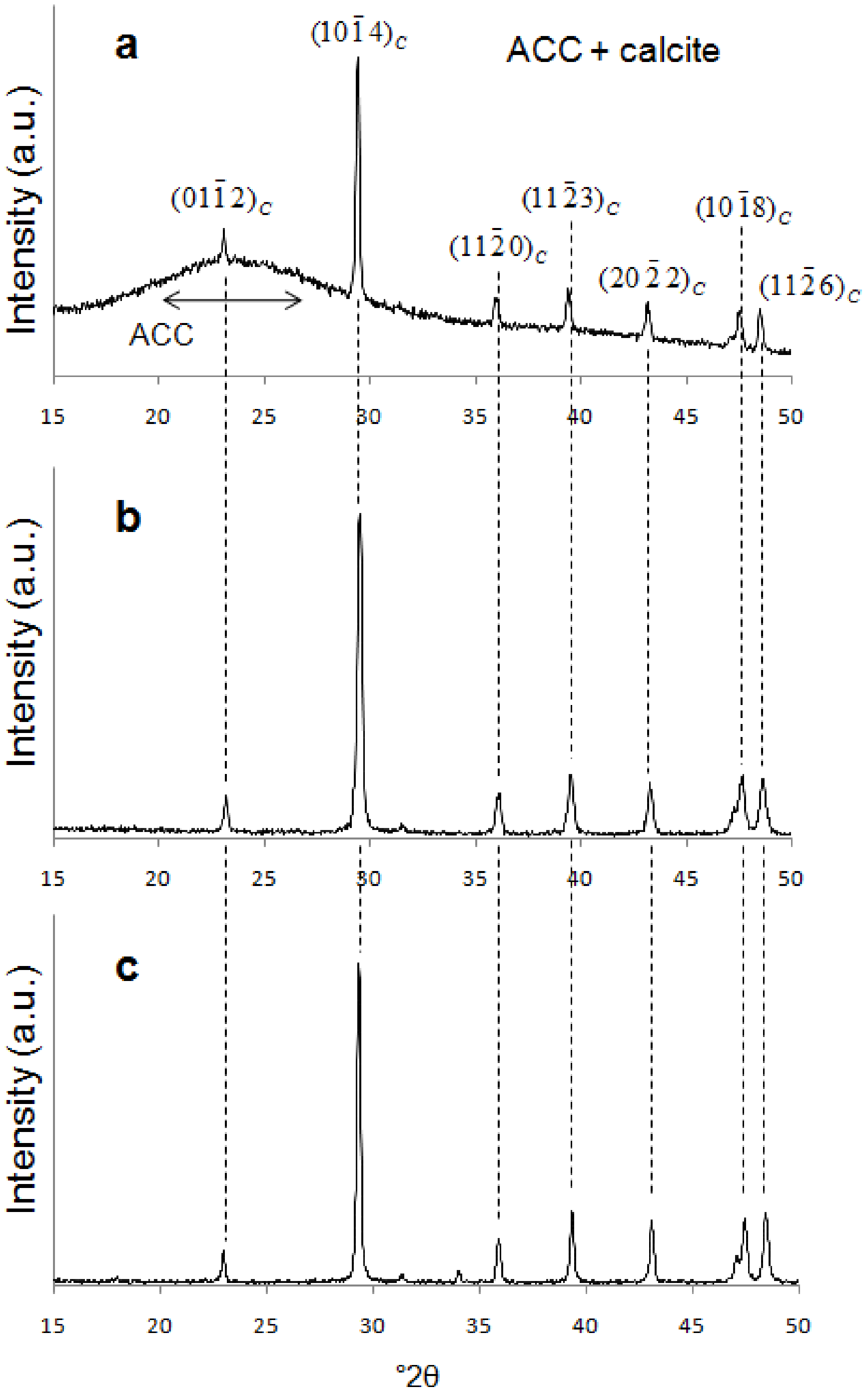

Figure 4.10. XRD patterns corresponding to the precipitate formed in Run A sample after 2 min (a) and 10 min (b) air exposure, and after 10 min air bubbling (c). The characteristic broad bump between ~20 and ~35 º2θ (a) indicates the presence of ACC.

4.3.4. Ex-situ TEM

TEM and SAED analyses of the precipitates formed in Run A after 2 min air exposure revealed interesting features of ACC and its further transformation into calcite. Figure 4.11a shows the initial formation of ACC as a shapeless aggregate of spheroidal nanoparticles (ca. 50-100 nm in size), with corresponding SAED pattern (inset) confirming its amorphous nature. Subsequently, micrometer sized spheres were produced out of the initial aggregates (Figure 4.11b). In this case, however, instead of typical diffuse diffraction image, corresponding to a fully amorphous phase, rings indicating the formation of a short range order were observed (inset in Figure 4.11b). Furthermore, after 10 min of forced air bubbling in Run A samples, these spheres, with similar diameter as in the previous case were found (Figure 4.11c), yet with the internal structure of calcite, what is depicted in Figure 4.11d. Their SAED pattern indicates the following crystallographic orientation: <100>$_{calcite}$ normal to the image plane. A closer examination of such a pseudomorph shows that it developed an internal texture made of perfectly oriented nanocrystalline calcite grains (Figure 4.11e andFigure 4.11f).

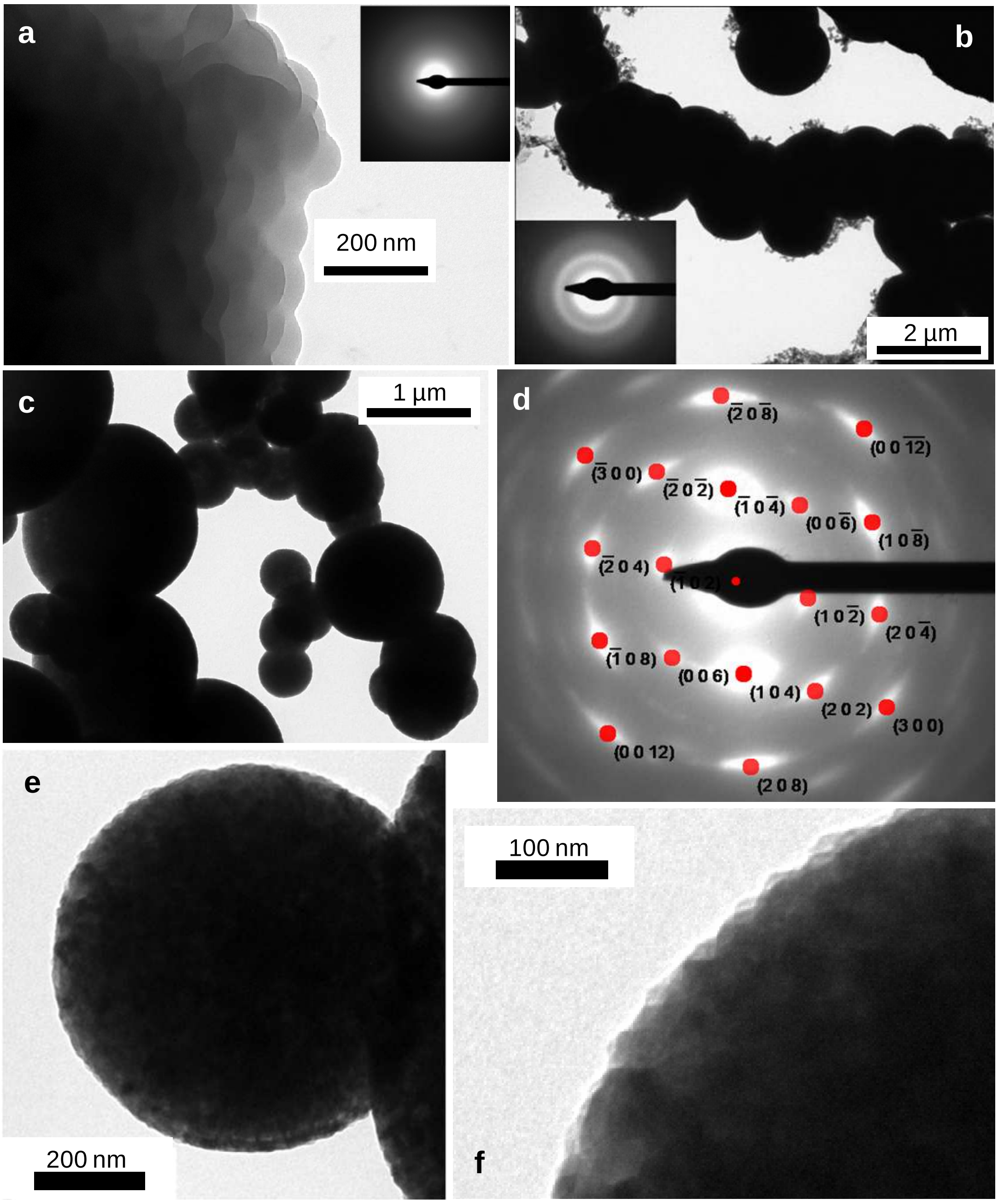

Figure 4.11. Initial shapeless aggregate of ACC nanospheres (a) in Run A sample after 2 min carbonation in air (SAED pattern in inset), turning afterwards into micrometer sized spheres (b) with short range order (SAED patterns inset). Pseudomorphs of ACC micrometer sized spheres forming aggregates (c) (after 10 min forced air injection). These aggregates are highly oriented calcite pseudomorphs as shown by the SAED pattern (d). A closer examination of spheres shows that they are made of calcite crystal of nanometer size (e and f)

Lime water mixed with ethyl alcohol, in 1:2 proportion, showed a different evolution during carbonation if compared with the pure aqueous solution. After mixing, the first phenomenon observed was that the solution became milky-like. TEM observations revealed, that this was due to the precipitation of portlandite. Addition of ethyl alcohol into solution caused a sudden increase of SI, i.e., the solution became supersaturated with respect to portlandite and resulted in its precipitation, because ethanol strongly reduces the water activity. Figure 4.12a shows precipitated portlandite crystals with hexagonal plate-like morphology, ~100-500 nm in size. SAED (inset in Figure 4.12a) confirmed the portlandite structure of precipitates. Precipitates formed after forced air-bubbling displayed interesting features. In some cases, residual rims of hexagonal shape were observed (Figure 4.12b). SEAD patterns of these rims gave diffraction rings, similar to those observed in the case of ACC spheres formed in run A sample after 2 min air-exposure (inset in Figure 4.12b). Additionally, spherically shaped amorphous particles were also observed (ACC with size ~30-100 nm). SAED patterns of ACC spheres were similar to those produced by residual rims. However, in some cases the formation of diffraction spots was observed suggesting the onset of the formation of crystallites within ACC spheres (Figure 4.13).

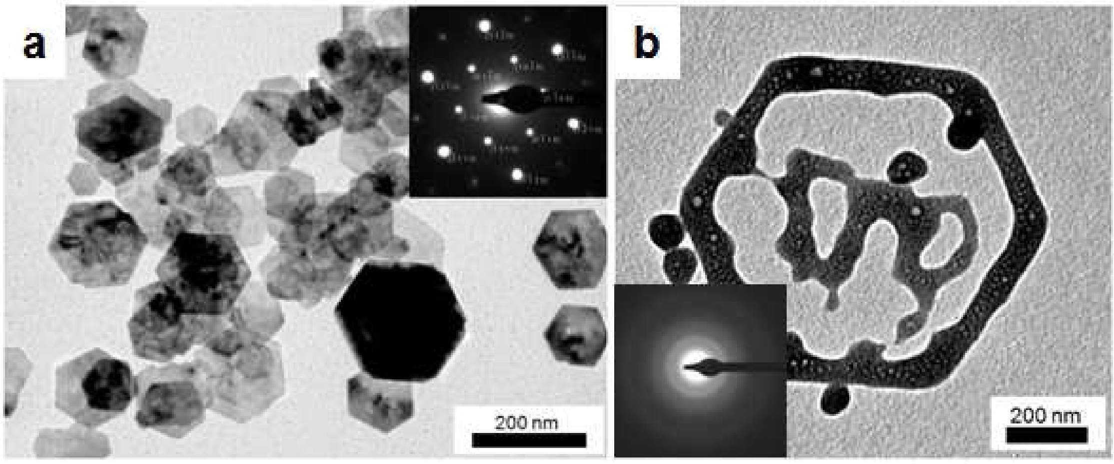

Figure 4.12. Initial precipitation of hexagonal portlandite (a) formed in lime water mixed with alcohol and its subsequent dissolution during forced air injection resulting in hexagonal rims (b).

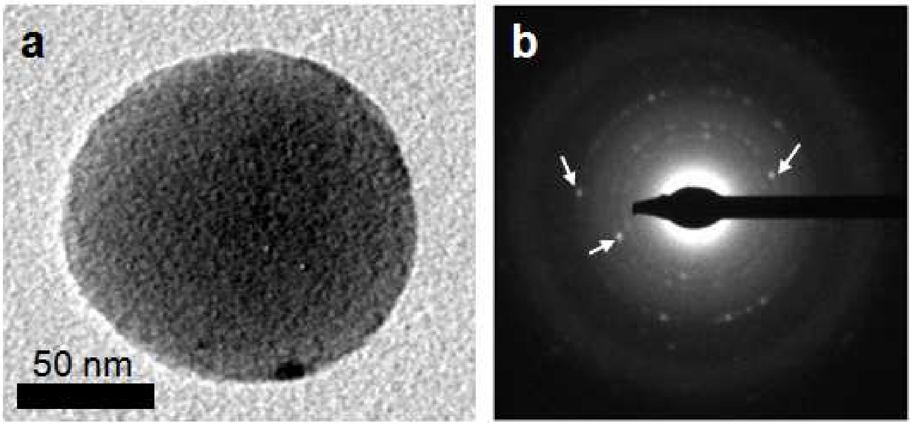

Figure 4.13. ACC spheres formed in lime water mixed with alcohol after forced air injection (a) and corresponding SAED pattern (b). The presence of diffraction spots in SAED pattern indicates the formation of crystallites within its volume.

In order to get insights into structural short range order characteristics of early carbonate precipitates formed in pure lime water and in its mixture with alcohol, as well as to identify and characterize the crystallites within ACC spheres formed in lime water mixed with alcohol, the intensity of pixels in corresponding SAED patterns were radially integrated (using SAEDP software). This operation allows to plot the diffraction intensity as a function of scattering vector length, *k* (i.e., distance form (0,0,0) point in reciprocal lattice), and can be consider as an equivalent of electron powder diffraction pattern (EPDP) (Czigany and Hultman, 2010). Figure 4.14b shows the EPDP corresponding to precipitates formed in lime water, whereas Figure 4.15b depicts the EPDP of precipitates (i.e., residual rims) formed in lime water mixed with alcohol. Figure 4.16 shows the EPDP corresponding to crystallites formed within an ACC sphere in lime water mixed with alcohol. To these plots a series of three Pearson VII functions were fitted including a polynomial function representing the background baseline, in order to estimate the peak profiles (i.e., its center – *k* and full width at half medium (FWHM)). The result of fitting are presented in Tab. 4.1 (lime water), Tab. 4.2 (mixture with alcohol) and Tab. 4.3 (crystallites in ACC formed in lime water mixed with alcohol).

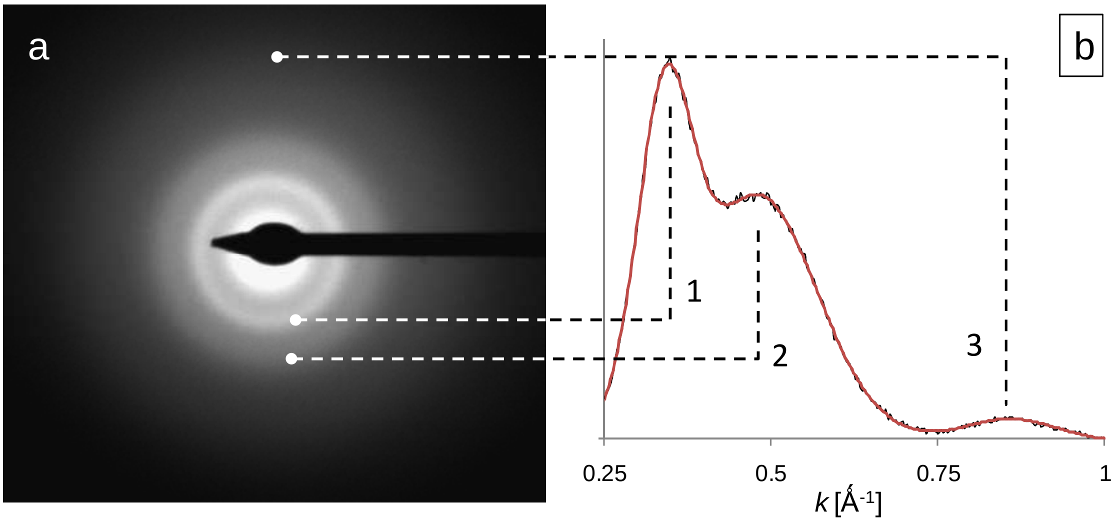

Figure 4.14. SAED pattern of $CaCO_3$ spheres formed in run A sample after 2 min (a) and corresponding EPDP (b). The black pattern represents the results of the integration while the red line corresponds to the fitted functions (*k* is scattering vector length).

Table 4.1. Results of EPDP fitting from the precipitate formed in lime water after 2 min air exposure

Nº	**k** [$Å^{-1}$]	**FWHM** [$Å^{-1}$]	**k^{-1}** [Å]	**$FWHM^{-1}$** [Å]
1	0.341	0.096	2.936	10.406
2	0.488	0.200	2.050	5.003
3	0.860	0.163	1.163	6.143

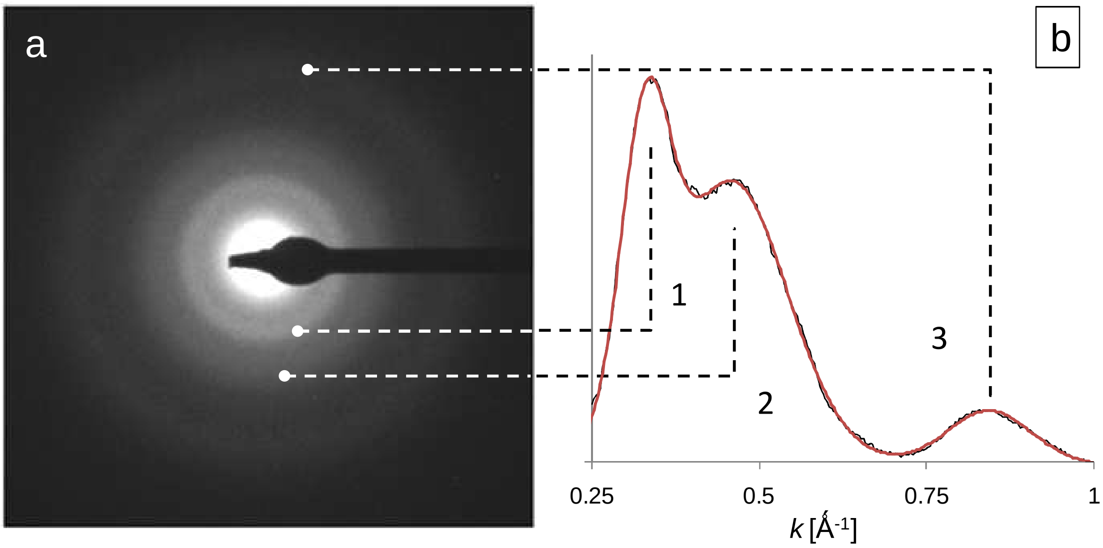

Figure 4.15. SAED pattern of residual rims with hexagonal shape formed in lime water mixed with alcohol after forced air injection (a) and corresponding EPDP (b). The black pattern represents the results of the integration while the red line corresponds to the fitted functions.

Table 4.2. Results of EPDP fitting from residual rims formed in lime water mixed with alcohol after forced air injection.

Nº	**k** [Å^{-1}]	**FWHM** [Å^{-1}]	**k^{-1}** [Å]	**FWHM^{-1}** [Å]
1	0.331	0.088	3.023	11.338
2	0.461	0.196	2.169	5.107
3	0.844	0.149	1.185	6.729

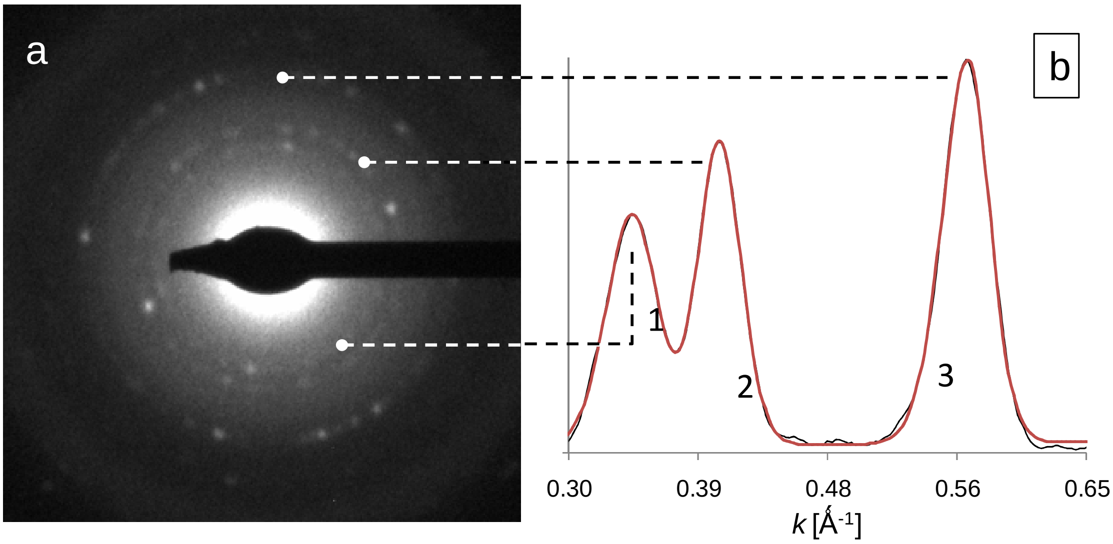

Figure 4.16. SAED pattern of ACC nanosphere formed in lime water mixed with alcohol after forced air injection showing the formation of crystallites within ACC (a) and EPDP corresponding to these crystallites (b). The black pattern represents the results of the integration while the red line corresponds to the fitted functions.

Table 4.3. Results of EPDP fitting of crystallites within an ACC sphere formed in lime water mixed with alcohol after forced air injection.

Nº	**k** [Å^{-1}]	**FWHM** [Å^{-1}]	**k^{-1}** [Å]	**FWHM^{-1}** [Å]
1	0.343	0.041	2.915	24.570
2	0.402	0.034	2.489	29.240
3	0.570	0.038	1.755	26.525

EPDPs of ACC spheres formed in lime water after 2 min air exposure and residual rims with hexagonal shape formed in lime water mixed with alcohol after forced air injection show very similar profiles, with three, clearly distinguished peaks. The position and broadness of these peaks, estimated by fitting, also show similar values in each case. Peak positions of ACC formed in lime water were slightly shifted towards smaller *k* values, and the peaks were slightly sharper. However, the differences were minor. The FWHM parameter obtained by fitting can give certain information on the range of short order (and crystallite size). Using the simplest approximation, it can be stated that the extend of short range order (and crystallite size) are equal to the reciprocal value of FWHM (Ciupina et al. 2007). For the first peak in Figure 4.14b and Figure 4.15b the reciprocal FWHM is ~10 Ǻ.

In an attempt to evaluate the structural characteristics of the short range order of ACC the peak positions were compared with the theoretical positions of four calcium carbonate crystalline phases, i.e., aragonite, vaterite, calcite and monohydrocalcite. It could be argued that these peaks may be the product of overlapping of other peaks. However, comparison of the position of the peaks estimated by fitting, in particular the first one, with the theoretical peak positions of the four calcium carbonate polymorphs, shows that the first matches with calcite 104 Bragg peak (3.036 Ǻ) and monohydrocalcite 102 Bragg peak (3.069 Ǻ). This is more evident in the case of lime water mixed with alcohol, where the position of the first ACC peak (~3.023 Ǻ) is closer to the value of calcite 104 peak and monohydrocalcite 102 peak if compared with the case of pure lime water (~2.94 Ǻ). The comparison of the other peaks positions with theoretical positions of calcium carbonate crystalline phases is more complex due to possible overlapping, and cannot be easily estimated.

In the case of crystallites within ACC spheres formed in lime water mixed with alcohol after forced air injection, the position of the first peak (~2.915 Ǻ) shows very similar value to that of the first peak of ACC spheres formed in lime water after 2 min air exposure. The position of the first peak is closest to the theoretical positions of calcite 104 Bragg peak (3.036 Ǻ) and monohydrocalcite 102 Bragg peak (3.069 Ǻ). The position of the second peak (~2.489 Ǻ) shows good matching with aragonite 200 Brag peak (~2.48 Ǻ), calcite 110 Bragg peak (~2.495 Ǻ) and monohydrocalcite $20\bar{1}$ Bragg peak (~2.491 Ǻ). The position of the last peak (~1.755 Ǻ) matches the theoretical positions of aragonite 113 Bragg peak (~1.742 Ǻ), vaterite 104 Bragg peak (~1.825 Ǻ), calcite 116 Bragg peak (~1.875 Ǻ) and monohydrocalcite 104 Bragg peak (~ 1.776 Ǻ). For all considered phases only calcite and monohydrocalcite can be assigned to all peaks. It appears that the structure of crystallites is intermediate between calcite and monohydrocalcite. Apparently, the observed short range order in the ACC precursor, which presents structural similarities to the calcite and monohydrocalcite structures, predetermines the formation (i.e., phase selection) of crystallites. The origin of the short range order could be associated with the formation of stable prenucleation clusters with proto-calcite or proto-monohydrocalcite structure. The formation of crystallites (FWHM^{-1} ~25 Ǻ for the first peak, see Tab. 4.3) could be the result of the oriented aggregation of these clusters (Figure 4.17). Moreover, the preservation of the external shape of a sphere in the case of ACC formed in pure lime water, suggests that the ACC to calcite transformation involves either a solid state transformation, i.e., ACC dehydration (Radha et al. 2010) or a coupled dissolution/precipitation pseudomorphic replacement mechanism (Rieger et al. 2007). These two different possibilities are discussed in sec. 4.5.2.

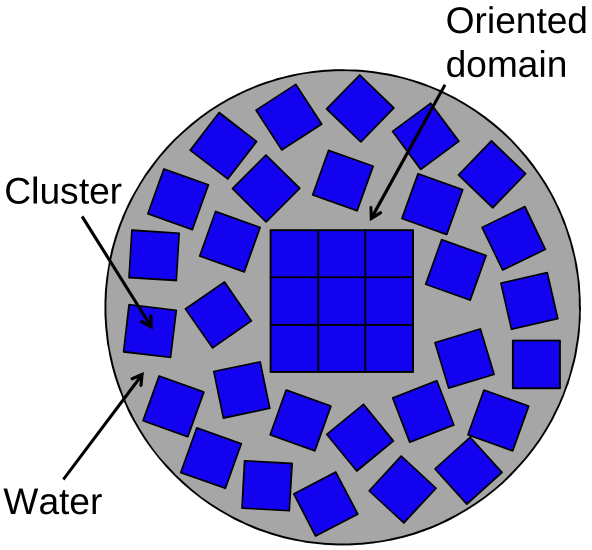

Figure 4.17. Schematic representation of ACC and its transformation into a crystalline phase via oriented aggregation of the stable pre-nucleation clusters.

4.3.5. Cluster diffraction simulation

As shown in the previous section, the estimated FWHM of the first EPDP peak corresponds to a size ~10 Ǻ. This value, which can be interpreted as a cluster size, was used in simulations. The shape of the clusters was assumed to be a sphere of 10 Ǻ in diameter. Four different arrangements of atoms within the cluster volume were considered. They correspond to vaterite, aragonite, calcite and monohydrocalcite. Two sets of simulations were performed, corresponding to the case of a randomly oriented clusters, as well as to the case where a possible preferred orientation develops.

The first set of data simulation was performed using the Debye function:

$$I(\theta) = \sum_{i=1}^{N} \sum_{j=1}^{N} f_i \, f_j \frac{\sin\left(4\pi \frac{\sin(\theta)}{\lambda} r_{ij}\right)}{4\pi \frac{\sin(\theta)}{\lambda} r_{ij}} \quad (4.16)$$

where:

I - intensity

f_i - scaterring amplitude of the i-th atom

θ - scattering angle (2θ is the Bragg angle)

λ - wavelength

r_{ij} - separation vector of i-th and j-th atoms in a cluster

The results of the simulation for randomly oriented clusters and their comparison with experimental results (i.e., EPDPs) are presented in Figure 4.18. Simulated EPDPs corresponding to clusters with vaterite, aragonite and calcite structure (Figure 4.18a, Figure 4.18b and Figure 4.18c) do not show a good matching with experimental EPDPs (Figure 4.18e and Figure 4.18f).

The positions of the first and second peak (at ~0.34 Å^{-1} and ~0.5 Å^{-1} respectively) of simulated EPDP for a cluster with monohydrocalcite structure (Figure 4.18d) match the positions of the two first peaks of experimental EPDPs (Figure 4.18e and Figure 4.18f). The matching is better in the case of calculated EPDP corresponding to lime water (Figure 4.18e) if compared with the experimental EPDP of lime water mixed with alcohol after forced air injection (Figure 4.18f). Note that both EPDPs show the peak at ~0.85 Å^{-1}, however, in the case of lime water mixed with alcohol its intensity is higher. One of the explanations for the differences in intensities may be the oriented aggregation of clusters within the ACC volume.

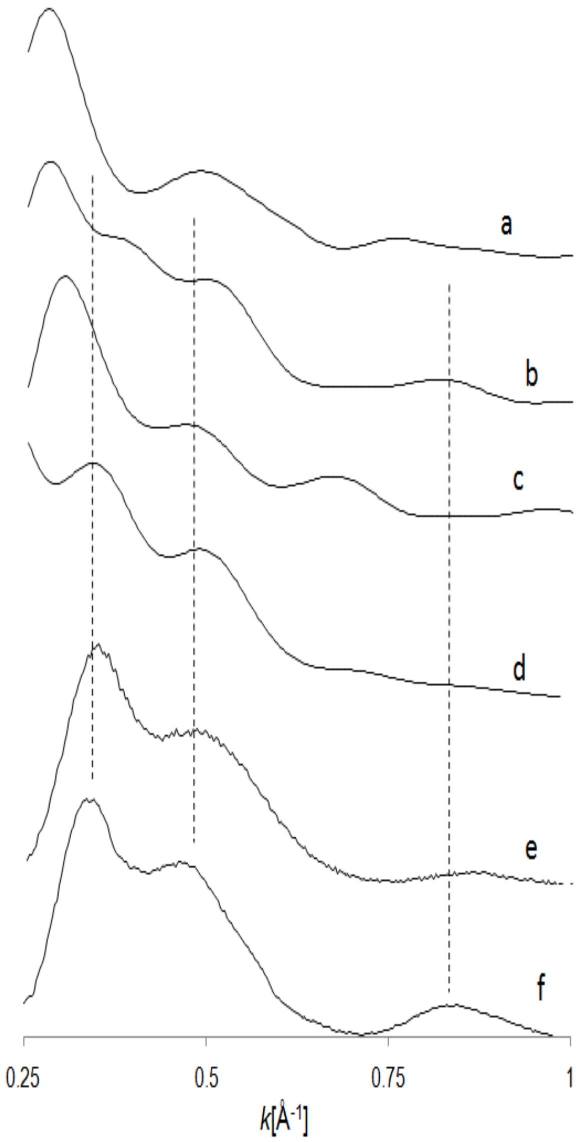

Figure 4.18. Comparison between simulated EPDPs for clusters with 10 Å crystallite size and different internal structures: vaterite (a), aragonite (b), calcite (c), monohydrocalcite (d) and experimental EPDPs corresponding to ACC formed in lime water after 2 min air exposure (e) and after dissolution of portlandite in lime water mixed with alcohol (f).

In the case of forced air injection in run A sample, the initial amorphous structure was pseudomorphically replaced by highly oriented calcite. It could be hypothesized that oriented aggregation of pre-nucleation clusters preceded the formation of calcite with a well developed texture. Therefore, other equation, taking into account the development of a preferred cluster orientation was used (Hudson and Hofstadter, 1952):

$$I(\theta) = \sum_{i=1}^{N} \sum_{j=1}^{N} f_i \, f_j \cos\left[2\pi S_{ij}(1 - \cos{(2\theta)})/\lambda\right] \; x \, J_0(2\pi D_{ij} \frac{\sin(2\theta)}{\lambda}) \quad (4.17)$$

where:

S_{ij} - separation vector of i-th and j-th atom in a cluster along the direction of electron beam

D_{ij} - separation vector of i-th and j-th atom projected on the plane perpendicular to the electron beam direction

2θ - scattering (Bragg) angle

J_0 - Bessel function of zero order

The orientation between two Cartesian coordinate systems can be described using Euler angles (φ_1, ϕ, φ_2) (Morawiec 2004). In order to transform one coordinate system into another it is necessary to perform a set of orientation transformations corresponding to each of the Euler angles according to the equation:

$$(x', y', z') = O(\varphi_1, \phi, \varphi_2)\,(x, y, z) \quad (4.18)$$

where:

(x, y, z) – initial coordinate system

(x', y', z') – (x, y, z) after transformation

$O(\varphi_1, \phi, \varphi_2)$ – transformation operator (set of orientations)

There are a few different conventions regarding the sequence and the direction of the rotations. Here, one of the most popular was used, which involves the consecutive rotations around the z, x and z axis of the coordinate system subjected to rotation at an angle φ_1, ϕ, φ_2 respectively:

$$O(\varphi_1, \phi, \varphi_2) = O(z, \varphi_2)O(x, \phi)O(z, \varphi_1) \quad (4.19)$$

where $0 \le \varphi_1 < 360°$, $0 \le \phi \le 180°$ and $0 \le \varphi_2 < 360°$. The angular range for each rotation allows to reach any possible orientation.

As mentioned earlier different types of internal structure of the cluster were considered. In order to calculate different orientations of the cluster according to equation 4.19, its lattice (which is non-Cartesian in each case) has to be associated with a Cartesian coordinate system. The applied relationship between lattice vectors (a, b, c) of the considered structure and Cartesian axes (x, y, z) is the following: i) vaterite: a//x and c//z ii) aragonite a//x, b//y and c//z iii) calcite: a//x and c//z iv) monohydrocalcite: a//x and c//z.

It can be seen that the first rotation (i.e., $O(z, \varphi_1)$) does not change S_{ij} and D_{ij} values (used in the equation 4.17) when the z-axis of the cluster is parallel to the electron beam. Therefore selection of the initial orientation of the cluster with its z-axis parallel to the electron beam limits the EPDP calculation to the two consecutive rotations around the x and z-axis of the cluster at angles ϕ and φ_2 respectively. Therefore the simulation of EPDP according to equation 4.17 is performed for all orientation described by the equation:

$$(x', y', z') = O(z, \beta)O(x, \alpha)(x, y, z) \quad (4.20)$$

where:

(x, y, z) – initial cluster coordinate system with its z-axis parallel to the electron beam

(x', y', z') – (x, y, z) after transformation

$O(x, \alpha)$ – orientation around the cluster x-axis at α angle ($0 \le \alpha \le 180°$)

$O(z, \beta)$ – orientation around the cluster z-axis at β angle ($0 \le \beta < 360°$)

The procedure for EPDP simulation was the following. Initially the structure (i.e., vaterite, aragonite or calcite) was oriented with its z-axis parallel to the electron beam. Subsequently, the structure was oriented in space according to equation 4.20, where α and β were changed every 5°. Finally, the cluster shape (sphere with 10 Å in diameter) was “cut” from the oriented structure and the EPDP was simulated according to the equation 4.17. The theoretical (simulated) EPDPs were compared with experimental data (EPDPs obtained by the integration of SAED patterns) according to the equation:

$$R = \sqrt[2]{\sum_{i=1}^{n}(S(k_i) - E(k_i))^2} \quad (4.21)$$

where:

R – matching coefficient between simulated (from equation 4.17) and experimental EPDPs

S – simulated EPDP intensity at k_i (wavelength) point

E – experimental EPDP intensity at k_i point

Figure 4.19 presents simulated EPDPs with the best matching to experimental EPDPs (i.e., with the smallest R value) for the considered types of internal structure. From all three considered types of internal structure of the cluster the best matching was obtained for clusters with calcite (Figure 4.19c) and monohydrocalcite (Figure 4.19d) structure. Their orientations correspond to $[\bar{4}\bar{2}1]$ and $[1\bar{1}0]$ zone axis parallel to the electron beam direction for clusters with calcite and monohydrocalcite structure respectively. Both simulated EPDPs show peaks at very similar positions to experimental EPDPs. This second type of simulation shows that clusters must have a preferred orientation, because, the previous simulation showing non-oriented clusters never achieved such a good matching between simulated and experimental results.

Theoretical findings combined with experimental data point to the existence of short range order in ACC with characteristics of monohydrocalcite and/or calcite. However, the reliability of simulated data may be questionable. It has to be taken into account that theoretical considerations are based on two assumptions: equal size distribution and lack of misorientation among aggregating clusters.

Despite the differences between the two examined systems (pure lime water exposed to air and lime water with addition of alcohol subjected to forced air injection) short range order in ACC is very similar in both cases. The fact that in both cases (pure system and with alcohol) ACC always transformed directly into calcite indicates that the observed short range order may have an important role in crystalline phase selection. Its origin could be related to the formation of stable pre-nucleation clusters with a proto-calcite structure (short-range order) which forms ACC spheres, and transforms into calcite following an oriented aggregation.

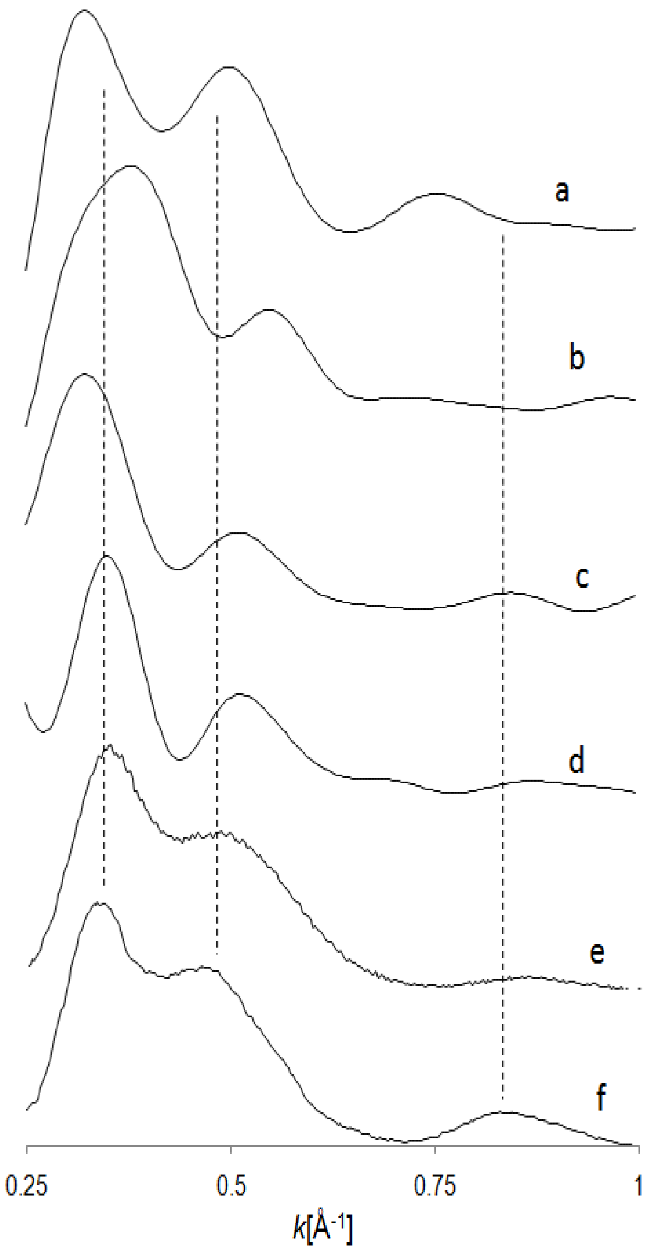

Figure 4.19. Simulated EPDPs for clusters (with spherical shape and 10 Å in diameter) with internal structure of vaterite (a), aragonite (b), calcite (c) and monohydrocalcite (d) displaying a preferred cluster orientation, in comparison with experimental EPDPs of ACC formed in lime water after 2 min air exposure (e) and after dissolution of portlandite in lime water mixed with alcohol (f).

4.3.6. Morphology evolution: ESEM and FESEM observation

The initial stages of the 1st crystallization cycle (at *p*H_2O 6.5 Torr) during Experiment 1 performed in the ESEM resulted in the formation of spherical precipitates with ~1 µm in diameter. By comparison with previous results (optical microscopy, TEM analysis) this early formed precipitate can be associated with ACC (Figure 4.20a and Figure 4.20b). A further decrease of *p*H_2O down to 5 Torr resulted in the formation of calcite with typical rhombohedral and rhombo-scalenohedral morphology (Figure 4.20c and Figure 4.20d). These crystals were observed along with spherical ACC. The sample subjected to a 2nd crystallization cycle, showed interesting features. Once *p*H_2O was reduced to 5 Torr, ACC, previously exhibiting a spherical morphology, transformed into particles with a disk-like shape (Figure 4.21a), showing dissolution features (Figure 4.21b and Figure 4.21c), while calcite crystals with rhombohedral and rhombo-scalenohedral morphology transformed into aggregates of crystals with scalenohedral morphology (Figure 4.21d).

In the case of Experiment 2, results of the 1st crystallization cycle, which was performed under *p*H_2O of 5 Torr, were similar to those obtained at the beginning of Experiment 1. The initial formation of ACC spheres was observed (Figure 4.22a and Figure 4.22b). The subsequent decrease in *p*H_2O down to 3 Torr led to the transformation of ACC into agglomerates of calcite crystals with two types of morphology. The first type involved the formation of rhombohedral calcite aggregates made up of randomly oriented crystals (Figure 4.22c). The other type revealed a “staircase” morphology formed by intergrowth of rhombohedral calcite crystals (Figure 4.22d).

Such a difference in morphology development should be related with the different time of equilibration (air exposure) of the sample prior to observation in the ESEM. During this process samples in Experiments 1 and 2 reached different degrees of carbonation, which were reflected by the differences observed in the ESEM.

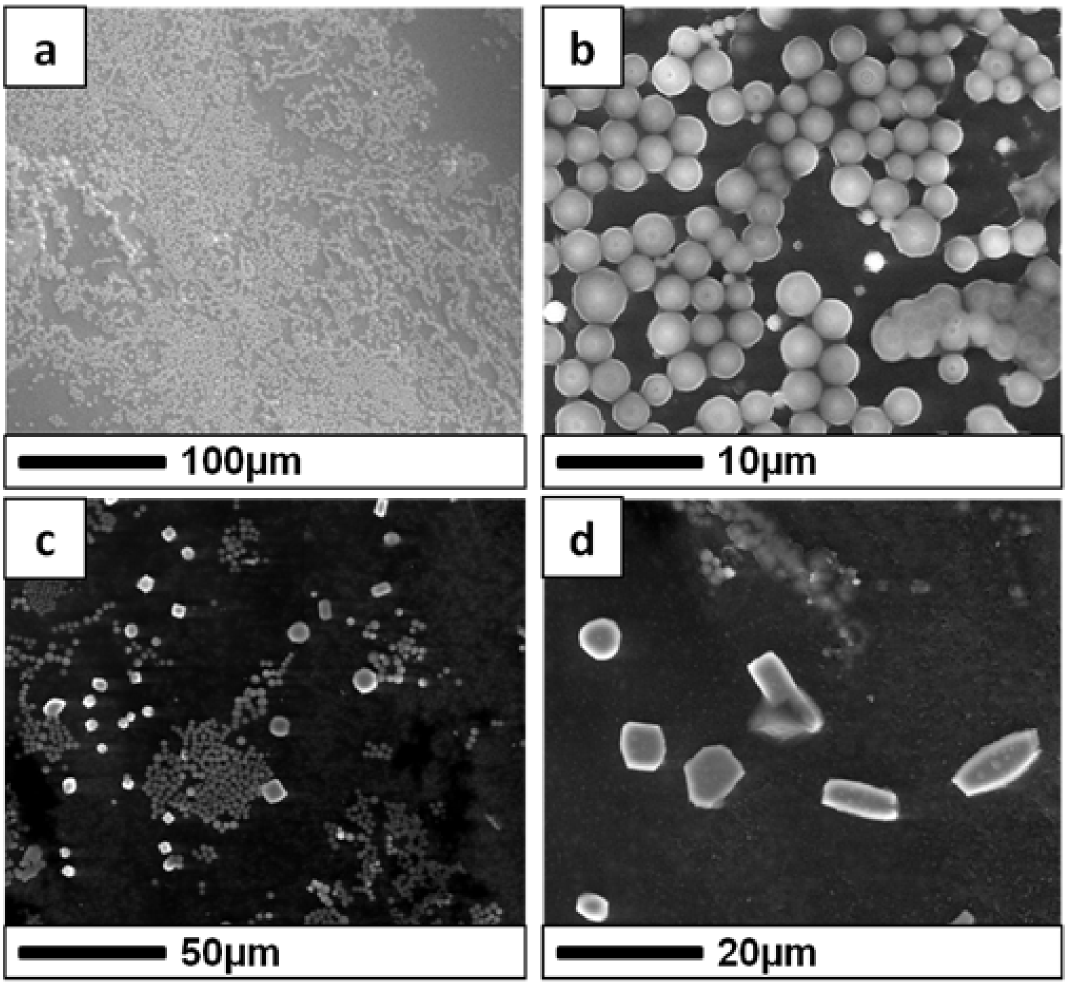

Figure 4.20. Images of calcium carbonate precipitation observed in-situ, in the ESEM, during the first crystallization cycle (Experiment 1). General view of initial ACC (a) and detailed view (b). Final precipitates: general (c) and detailed view (d)

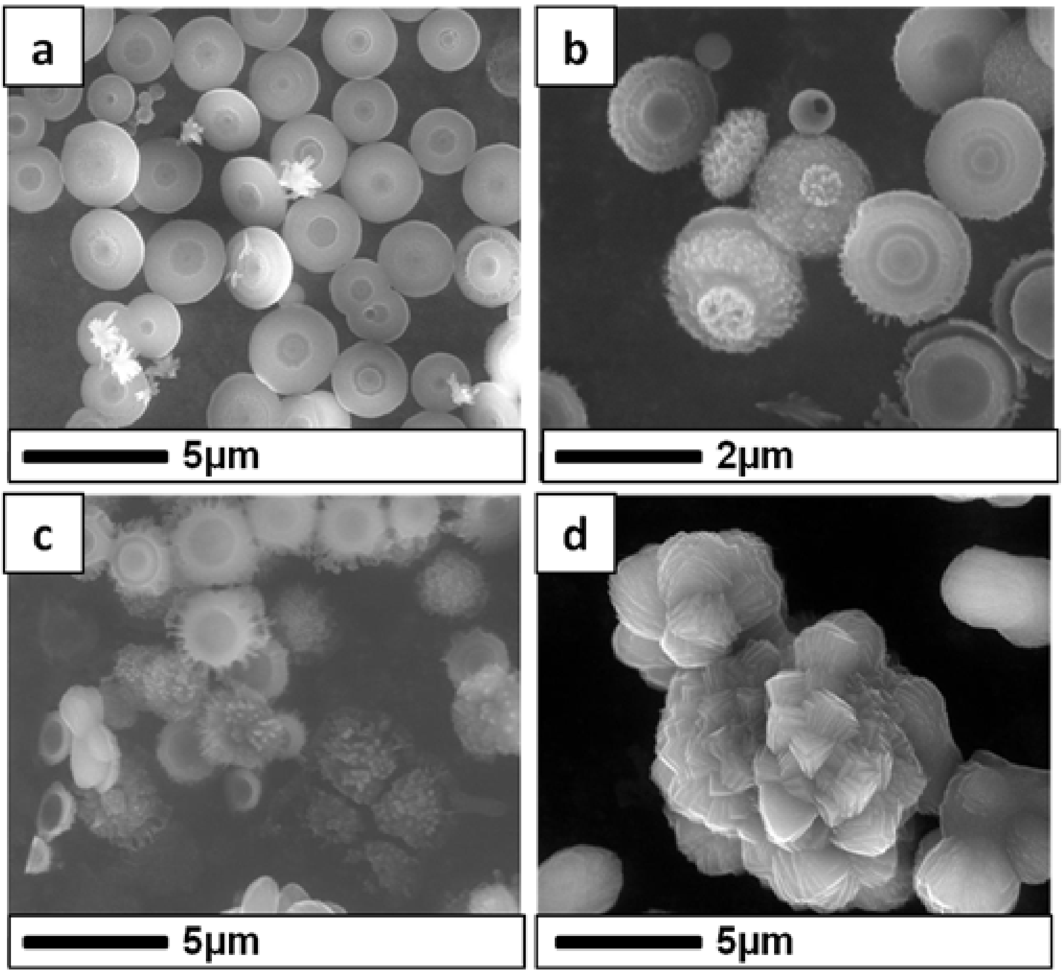

Figure 4.21. Sequence of calcium carbonate precipitation in the ESEM during the second cycle (Experiment 1). Initial precipitation of ACC (a) leading to scalenohedral calcite (d) via "corrosion" (dissolution) of initial ACC spheres (b, c). Finally, after a new cycle of evaporation and condensation of water, precipitation and aggregation of calcite crystals with scalenohedral morphology occurs (d).

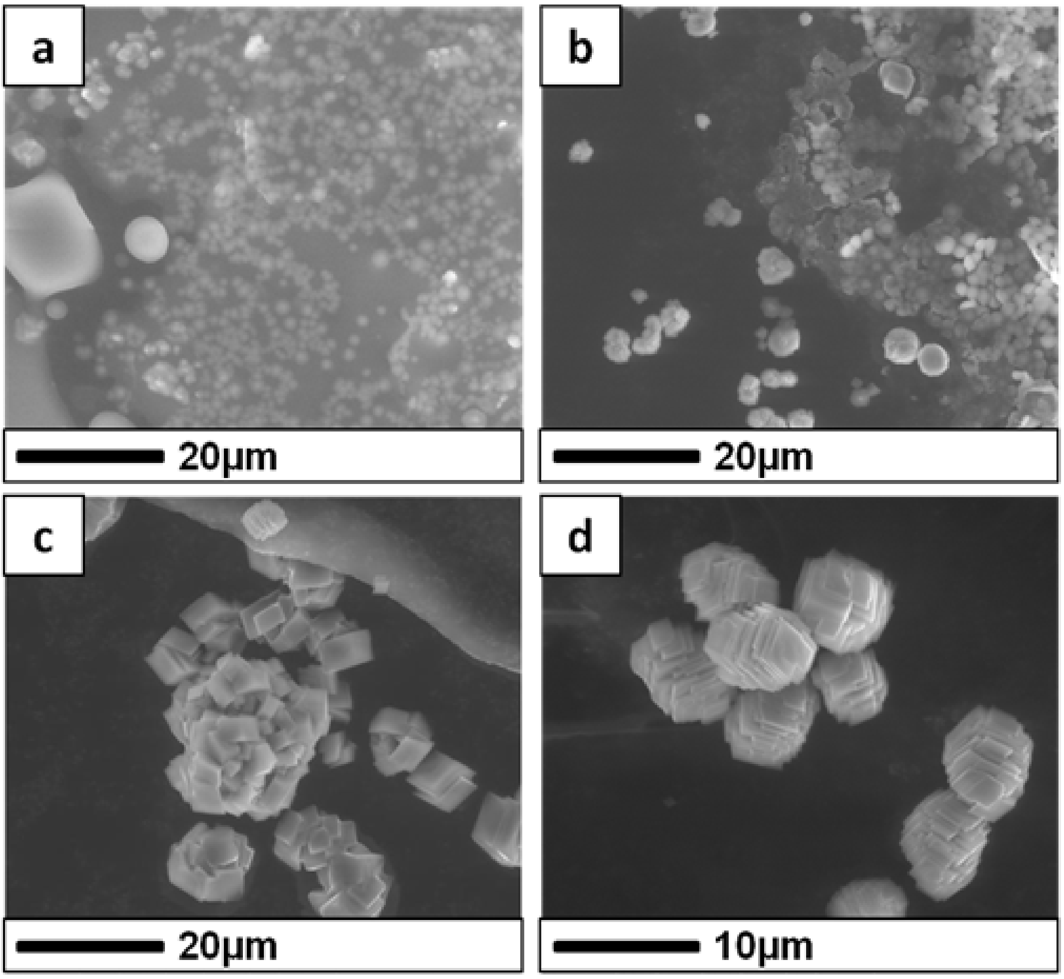

Figure 4.22. Sequence of ESEM images in Experiment 2: ACC (a), beginning of transition to calcite (b), rhombohedral calcite crystals (c) and calcite aggregates with “staircase” morphology (d).

Ex-situ FESEM analyses of precipitates formed in run A and B revealed a simpler sequence of morphology evolution. After 2 min air exposure in run A sample, the precipitation of ACC in the form of spheres with ~0.5 µm diameter was observed (Figure 4.23). This morphology is similar to that observed in-situ in the ESEM, during the 1st crystallization cycle. After 2 h exposure, calcite developed in run A and run B samples displayed significantly different morphologies. In the case of run A, calcite developed with typical rhombohedral morphology (Figure 4.24a). This is in agreement with the observation made with the aid of optical microscopy. In the case of run B, calcite precipitated with scalenohedral morphology (Figure 4.24b). These significant differences in morphology development should be related to the fact that, in the case of Run B, a continuous supply of $Ca(OH)_2$ was provided, resulting in a different $[Ca^{2+}]/[CO_3^{2-}]$ ratio and SI, which are two of the main factors that influence calcite morphology, as will be discussed latter on.

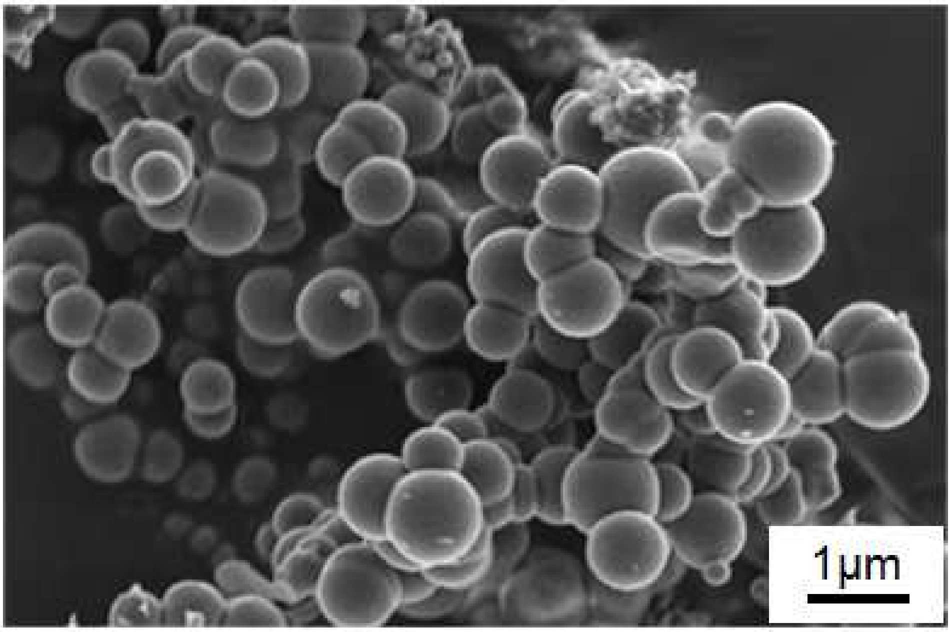

Figure 4.23. FESEM image of ACC precipitated from lime water (Run A).

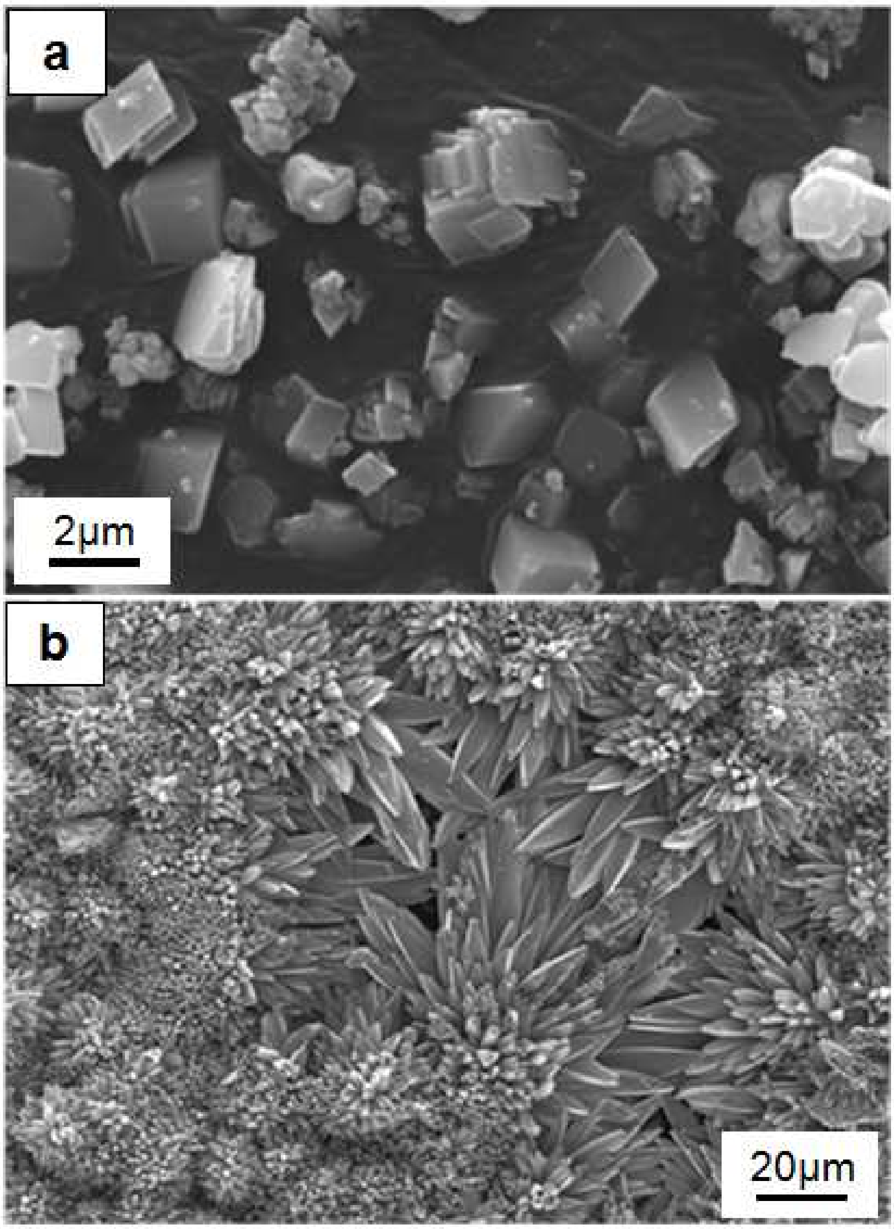

Figure 4.24. Rhombohedral (a) and scalenohedral (b) calcite precipitated after 2 h air exposure in Run A and Run B respectively.

4.3.7. Carbonation of portlandite single crystals

Figure 4.25 shows the carbonation degree of portlandite single crystals kept in air under high RH (~93%) for different periods of time. Within the observed 20 days carbonation period, the degree of transformation was ~1.5%. This is a relatively low value, especially if compared with results from carbonation of hydrated calcite pseudomorphs (sec. 4.3.8) or carbonation of hydrated lime pastes (sec. 4.3.9). Such differences can be explained by considering the differences in porosity of the above mentioned systems and portlandite single crystals (no porosity). Note that porosity is one of the crucial factors controlling the kinetics of carbonation reaction. The rate of the reaction tends to slow down as carbonation progresses, showing an exponential decay with time.

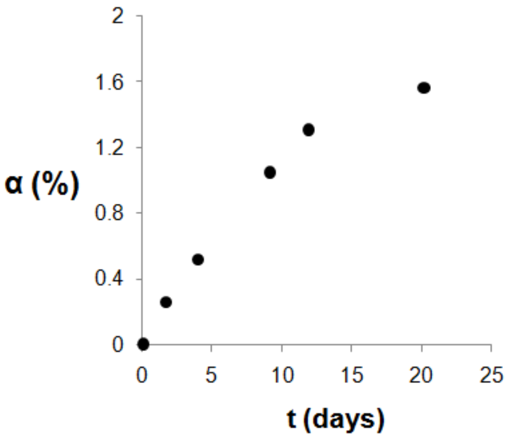

Figure 4.25. Degree of portlandite single crystals carbonation α (%) as a function of time. Note the exponential decay vs. time.

FESEM observations of partially reacted portlandite single crystals subjected to carbonation under high relative humidity atmosphere, showed that they resulted in pseudomorphs that fully preserved the external hexagonal prism-shape, bounded by $\{11\bar{2}0\}$ and $\{0001\}$ faces (Figure 4.26a). A closer examination of the surface of pseudomorphs showed the degradation of both prismatic and basal faces (Figure 4.26b). In some cases, the formation of randomly oriented rhombohedral calcite crystal aggregates, ~0.1-0.5 μm in size, forming on the prismatic faces, was observed (Figure 4.26b). Interestingly, dissolution features along with formation of cracks were observed first and foremost on prismatic faces, and they were parallel to the basal plane. Such a phenomenon is in agreement with measurements of portlandite crystallite size evolution during carbonation performed in run B sample. They show that dissolution of portlandite progresses in directions parallel to the basal plane, rather than parallel to the c-axis.

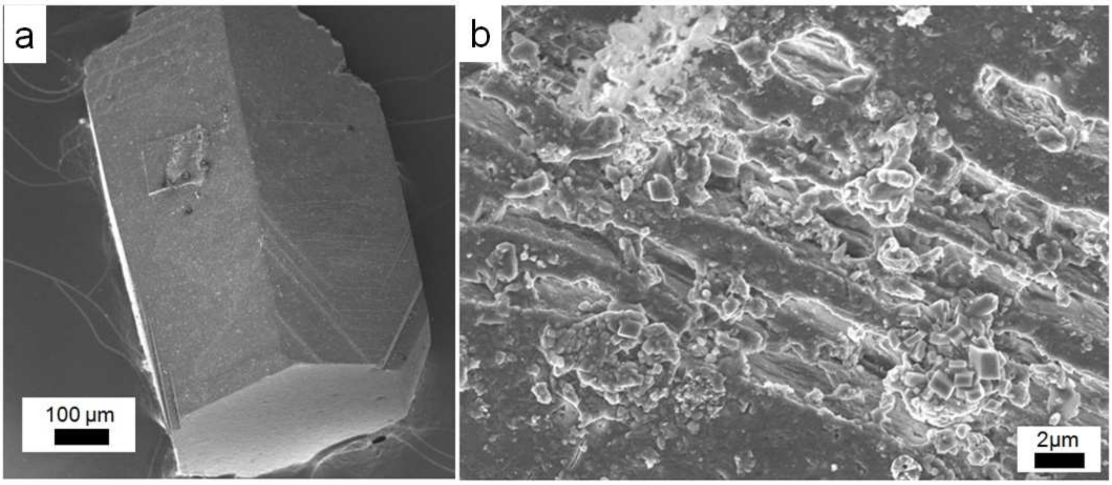

Figure 4.26. Preservation of hexagonal shape (a) and dissolution features (b) parallel to basal planes observed on the prismatic face of a portlandite crystal subjected to carbonation under high RH (~93%) for two weeks.

Figure 4.27 shows the calcite $(10\bar{1}4)$ pole figure of the partially carbonated portlandite single crystal pseudomorph, oriented with the basal plane parallel to the projection plane. The $(10\bar{1}4)_{calcite}$ pole figure indicates a strong preferred (epitactic) crystallographic orientation. Characteristic rings occur due to the lack of axis symmetry along calcite <0001> axis. The pseudomorphic replacement of portlandite by calcite and the epitactic nature of the process suggests that the carbonation of portlandite is a coupled dissolution/precipitation process (Putnis, 2009). Details of the mechanisms of carbonation via such a process are discussed in sec. 4.5.4.

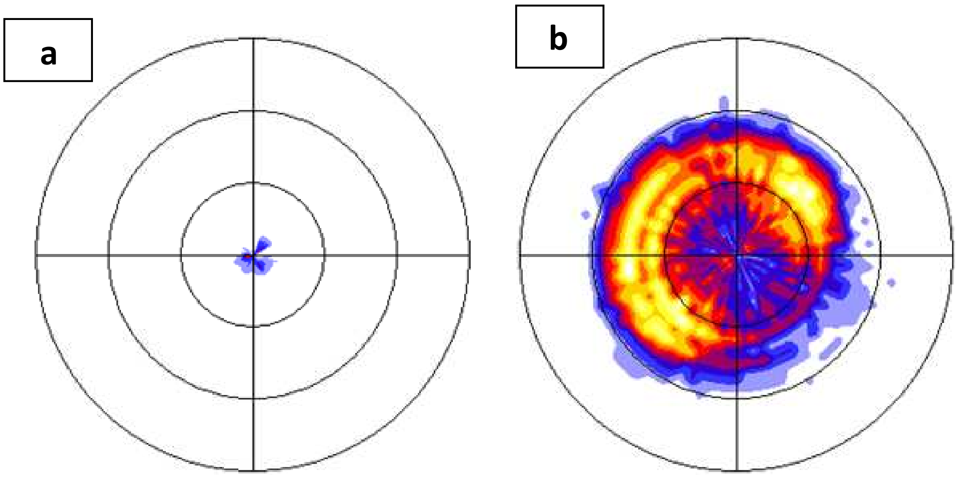

Figure 4.27. Pole figures: (a) single crystal of portlandite oriented with the basal plane parallel to the projection plane, i.e., $(0001)_{portlandite}$ and (b) $(10\bar{1}4)_{calcite}$ after 4 months carbonation in air at 93% RH.

4.3.8. Carbonation of hydrated calcite pseudomorphs (HCP)

On a global scale, carbonation of HCP resulted in the formation of small crystals that preserved the external shape of the original rhombohedra corresponding to the calcite pseudomorph. Figure 4.28 shows the degree of HCP carbonation as a function of calcination *T*. The degree of conversion was calculated from Eq. 4.14 using intensities from 2-theta scans. The carbonation degree corresponding to samples calcined at 800 and 900 ºC equals ~44 % and ~50 % respectively. However, the carbonation degree of HPC calcined at 700 ºC is ~79 %, a value significantly higher than that of samples calcined at higher *T*. As shown in sec. 3.3.2, the relatively low degree of calcination obtained at 700 ºC results in the preservation of the original calcite. This residual calcite contributes to the overall calcite content in HCP thus resulting in such a high (apparent) degree of carbonation. Nevertheless, the degree of carbonation of HCP calcined 800 and 900 ºC revealed a fast kinetics of the process, especially if compared with HLP carbonation results (see sec. 4.3.9).

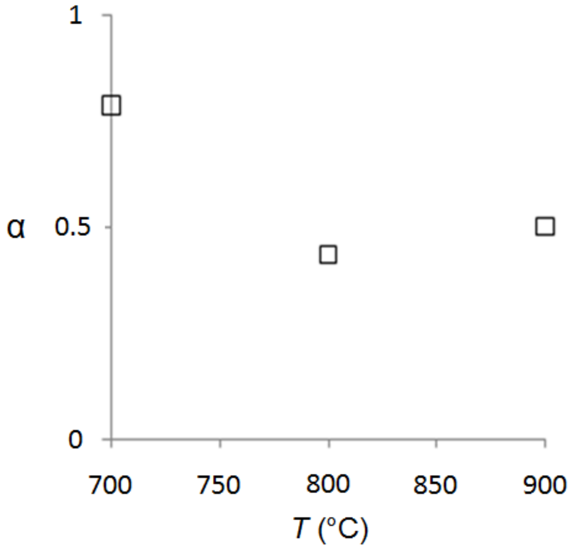

Figure 4.28. The fractional degree of carbonation (α) as a function of calcination *T*.

FESEM observations of carbonated HCP show the formation of cracks which might be responsible for their disintegration. As in the case of the hydration process, that phenomenon was most probably a result of differences in molar volume between growing calcite and portlandite precursor. A closer examination of the surface shows that carbonated HCP present very limited degree of porosity, which appears to be independent of calcination *T*. The morphology of the crystals showed variations depending on the sample depth. Crystals developed on the surface of the pseudomorphs presented scalenohedral morphology (Figure 4.29a). In deeper parts of the pseudomorph, calcite crystals showed variations in both morphology and size (Figure 4.29b). The bigger ones presented similar size and shape to those on the surface, i.e., scalenohedral shape and micrometer size. Along with them, crystals with sizes of approximately one order of magnitude smaller, and no well defined morphology were observed. These features did not show much variation with calcination *T*.

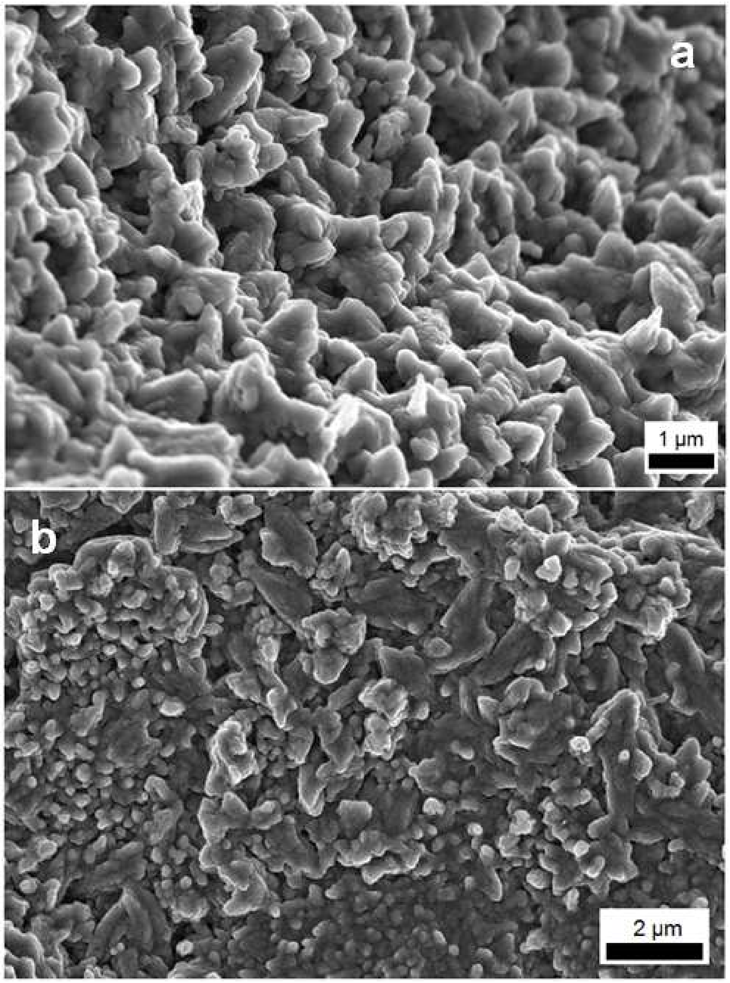

Figure 4.29. Morphology of calcite developed on the surface (a) and in deeper parts (b) of carbonated HCP (calcined at 900 °C).

2D-XRD analysis performed in order to determine the crystallographic orientation relationships between parent and product phases did not reveal the formation of any preferred orientation (epitactic or topotactic). The results showed fully random orientation of precipitated calcite crystals. On the other hand, measurements of orientation distribution function (ODF) using electron backscattered diffraction analysis (EBSD) were performed to examine the possibility of the formation of a crystallographic texture at a smaller scale. Calculated pole figures (with the aid of PFS software, see Appendix 1), showed the formation of oriented calcite, but separated into oriented domains with random orientation (Figure 4.30). Such a high degree of scattering made it impossible the reliable identification of any possible texture. Moreover, the reliability of these data is questionable. As indicated by FESEM observations, irregularities on the carbonated HCP surface may cause problems during electron diffraction, which requires homogenous, well polished sample surfaces. In any case, both results contradict the results from 2D-XRD analyses of portlandite single crystals showing the epitactic nature of the carbonation. The lack of epitaxy in 2D-XRD analyses of carbonated HCP may be related with the increase in molar volume of the product phase (calcite) compared to the parent phase (portlandite). This volume change results in the disintegration of the sample and may introduce a certain degree of misorientation among nascent calcite crystals, masking any possible preferred orientation.

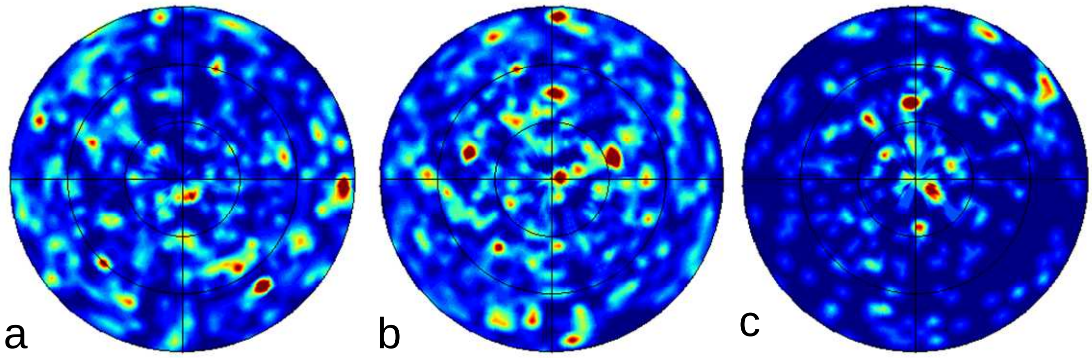

Figure 4.30. Calcite pole figures calculated from EBSD data from carbonated HCP: (a) $(11\bar{2}0)$, (b) $(10\bar{1}4)$ and (c) (0001). Note that $(10\bar{1}4)_{calcite}$ of the original calcite pseudomorph is the projection plane.

4.3.9. Carbonation of hydrated lime pastes (HLP)

4.3.9.1. General characteristic

The carbonation degree of FG and AC samples as a function of time, and determined from XRD and TG analyses is presented in Figure 4.31. Despite small differences during the initial stages of carbonation (e.g., the TG analysis of AC sample showed a slightly higher degree of carbonation after one week if compared with XRD results), the carbonation rate seemed to be independent of sample type, showing similar, exponential transformation with time.

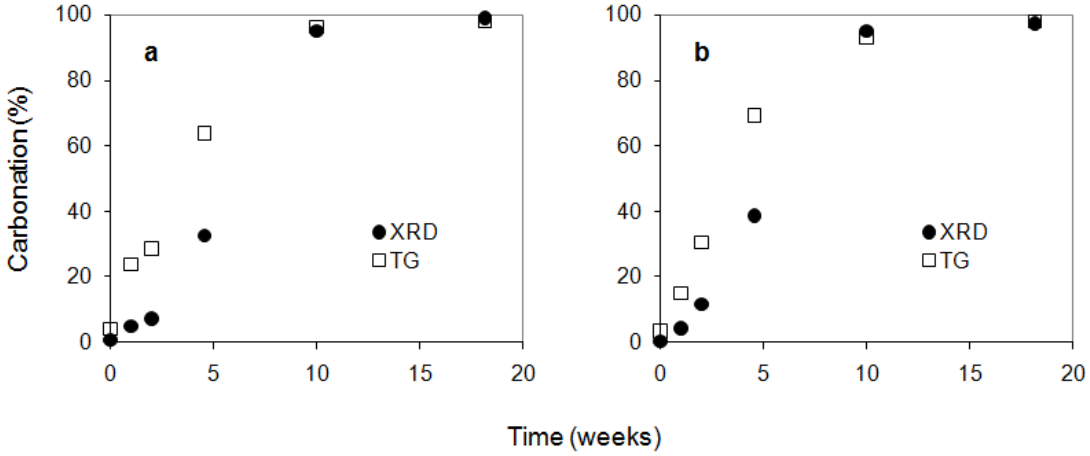

Figure 4.31. Degree of carbonation vs. time determined from TG and XRD. Analyses were performed for AC (a) and FG (b) samples.

However, XRD and TG results were not fully in agreement. The error of TG is estimated to be below 1 wt%, whereas the reliability of XRD data is questionable. This is related to two main problems. The first one is associated with the degree of heterogeneity of the sample. Even well-grinded and well-mixed samples, locally can exhibit differences in calcite/portlandite ratio, which do not reflect the average phase concentration in the bulk sample. The other problem of XRD data reliability is related with preferred orientation. Portlandite crystals, with their common hexagonal plate-like morphology (Figure 4.32) tend to orient with their basal plane parallel to the bottom of the sample holder. This in turn leads to an increase in the intensity of some diffraction peaks (e.g. 001 and 101 peaks), which would not take place if all crystals were randomly oriented. Thus, the relative intensity ratio of portlandite/calcite peaks does not give accurate information on the real phase content, typically overestimating the amount of portlandite in the sample. It could be expected that this effect would be stronger at the initial stages of carbonation, when portlandite is more abundant than newly-formed calcite.

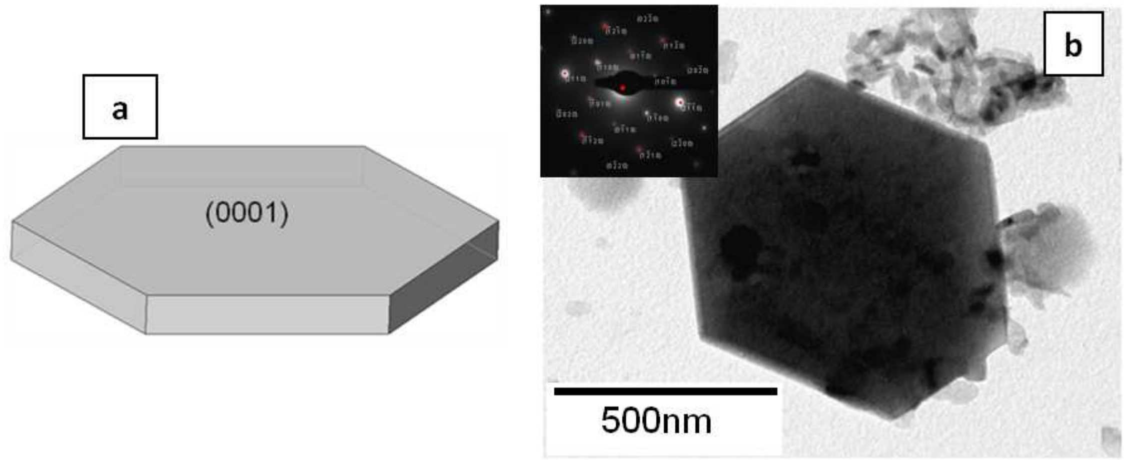

Figure 4.32. Schematic representation of portlandite crystal with plate-like morphology (a), and as observed in the TEM (FG sample) (b). The SEAD pattern confirms that the crystal is portlandite, oriented with its (0001) plane parallel to the image plane.

Figure 4.33 shows calcite crystallite size evolution determined from XRD analysis of both HLP types (FG and AC). The size of calcite crystals tends to increase continuously as carbonation progresses. This tendency was more clear in the case of AC samples. In the case of FG samples, this trend showed a sudden break after 5 and 18 weeks of carbonation. This discontinuity in crystallite size evolution could be due to sampling of a lime paste portion less carbonated than the sample as a whole. Each type of lime also showed significant differences in carbonation rate. For instance, after 10 weeks of carbonation in 93% RH atmosphere the size of $(01\bar{1}2)_{calcite}$ reached values of ~40 and ~90 nm for AC and FG samples respectively. Such a high size difference must be related with differences in particle size, degree of agglomeration and, first and foremost, with surface area of the samples which was equal to 19.8 m^2g^{-1} for AC, and 7.9 m^2g^{-1} in the case of FG (Ruiz-Agudo and Rodriguez-Navarro, 2010) (Appendix 1). Also, the larger scattering of calcite crystallite size values observed in FG sample if compared to AC sample, may suggest a change in the morphology of precipitating calcite.

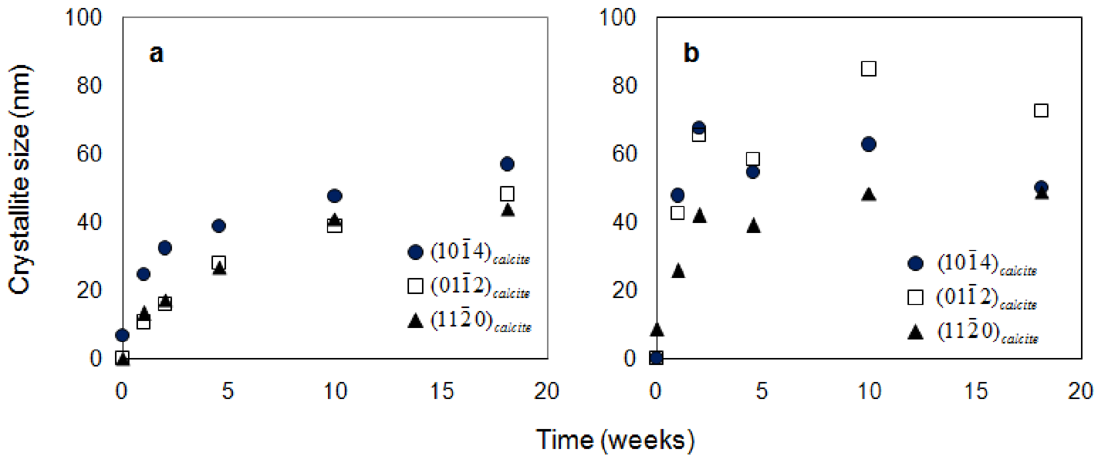

Figure 4.33. Calcite crystal size evolution with time for AC (a) and FG (b) samples.

4.3.9.2. Morphology of $CaCO_3$

Exposure of AC and FG samples to air at 93% RH for 2 months resulted in the formation of calcite crystals with similar morphologies and size on the surface of each sample. Figure 4.34a1 presents scaleno-rhombohedral calcite crystals of nanometer size formed on the surface of AC sample. The morphology of calcite developed on the surface of FG sample is shown in Figure 4.34a2. However, significant differences were observed during depth profile analyses. AC samples showed the transformation of scaleno-rhombohedra formed on the carbonated surface into scalenohedral crystals with cracked surfaces in deeper parts of the sample (Figure 4.34b1). These features were not observed in the case of FG samples, where calcite did not reveal any changes in morphology along the depth profile (Figure 4.34b2). Due to the moist condition during carbonation, almost full transformation of portlandite into calcite (≤95 %) was achieved within 2 months. In both samples subjected to carbonation, the matrix was made up of shapeless, interlocked nanocrystals of calcite with a compact microstructure. This nanocrystalline matrix was most evident in the depth profile of carbonated FG lime paste (Figure 4.34b2).

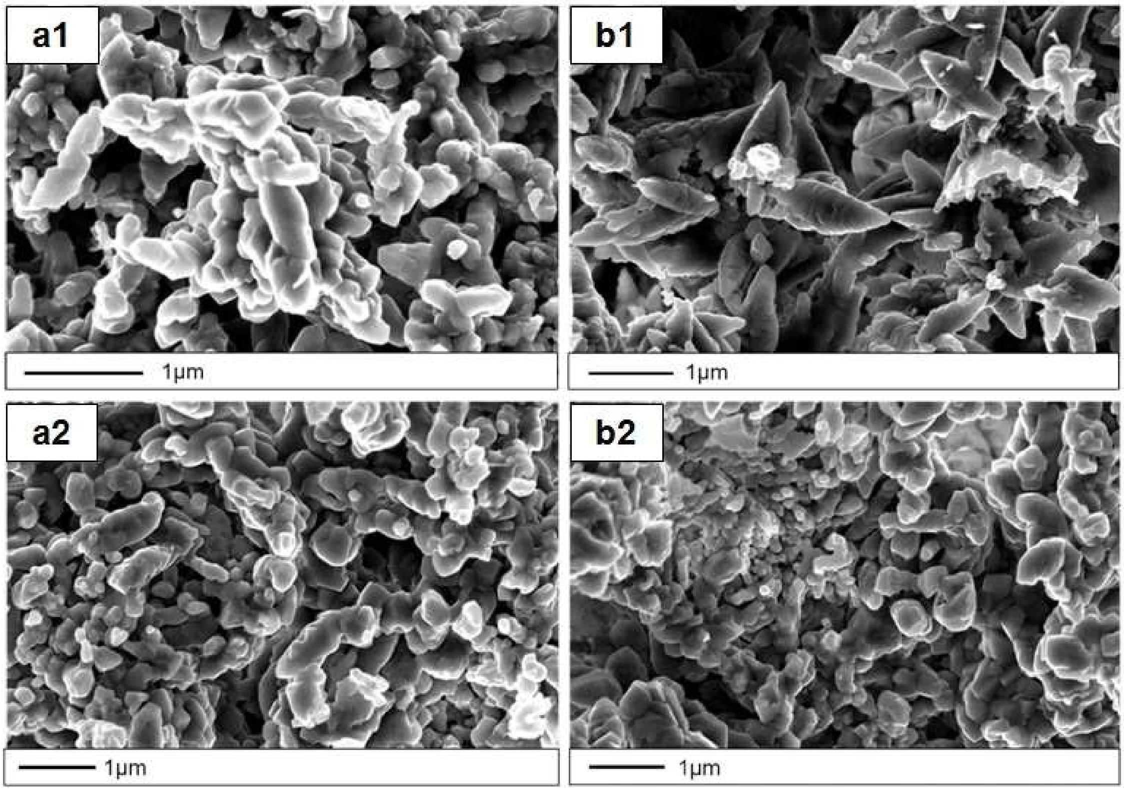

Figure 4.34. Calcium carbonate morphology in lime pastes subjected to two months carbonation in air at 93% RH. Surface (a1) and depth-profile (b1) of AC sample, and FG surface (a2) and sub-surface (b2) image.

4.3.9.3. TEM observations

One of the aims of the TEM study was to determine the possible crystallographic control (epitactic/topotactic) in the carbonation of portlandite crystals. The attempts to find a portlandite pseudomorph that could conclusively confirm the existence of such a control in the advancement of the process failed. Moreover, the poor quality and/or high complexity of the diffraction patterns of carbonated samples prevented the unambiguous identification of any possible crystallographic orientation in the observed crystals. This is exemplified in Figure 4.35. Figure 4.35a shows randomly orientated portlandite nanoparticles along with a bigger portlandite single crystal found in uncarbonated AC sample. Figure 4.35b shows randomly oriented calcite crystals forming aggregates after carbonation in air at 93% RH of this sample for two months. Interestingly, these randomly oriented calcite crystals showed a scalenohedral morphology, in agreement with FESEM observations.

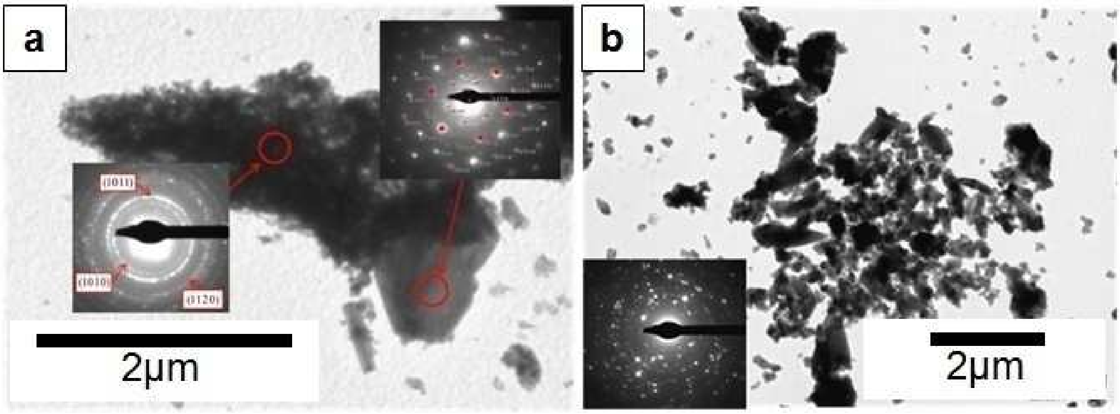

Figure 4.35. Portlandite single crystal in uncarbonated AC sample, surrounded by randomly oriented portlandite aggregates (a) and scalenohedral calcite crystals after two months carbonation in air at 93% RH (b)

4.4. PHREEQC simulation

Figure 4.36 shows the pH evolution in pure lime water (Run A) and lime water with additional supply of $Ca(OH)_2$ (Run B) exposed to air (T = 25 ºC, $pCO_2 = 10^{-3.5}$ atm) as a function of time (arbitrary units). During consumption of calcium hydroxide, in run A, the pH of the solution drops from ~12.46 (lime water) down to ~9.39. The initial pH of lime water will be maintained constant (or slightly below this value) at the air/water interface during $CaCO_3$ precipitation from lime water as long as a continuous supply of $Ca(OH)_2$ is provided. This is observed in the case of run B, which reflects the situation of the initial stages of carbonation taking place in lime pastes (or in lime mortars). The final stage of carbonation starts when excess of solid $Ca(OH)_2$ is fully consumed, so the evolution of the solution chemistry corresponds to the situation of run A.

The evolution of $[Ca^{2+}]/[CO_3^{2-}]$ ratio as a function of carbonation time (arbitrary units) is presented in Figure 4.37. Values range from ~$4x10^2$ (initial stage of Run A) down to ~3.54 once full carbonation has occurred (final stage of Run A). During run B, when a constant supply of $Ca(OH)_2$ is provided, the $[Ca^{2+}]/[CO_3^{2-}]$ ratio maintains a value ~$4x10^2$, which is equal to that corresponding to the initial stage of Run A.

SI values of all calcium carbonate phases in Run A, i.e., ACC, vaterite, aragonite and calcite, are presented as a function of time (arbitrary units) in Figure 4.38. At the final stage of carbonation (reflected by the end of Run A) the solution is supersaturated with respect to all calcium carbonate phases: ACC ~1.21, vaterite ~2.72, aragonite ~ 3.14 and calcite ~ 3.29.

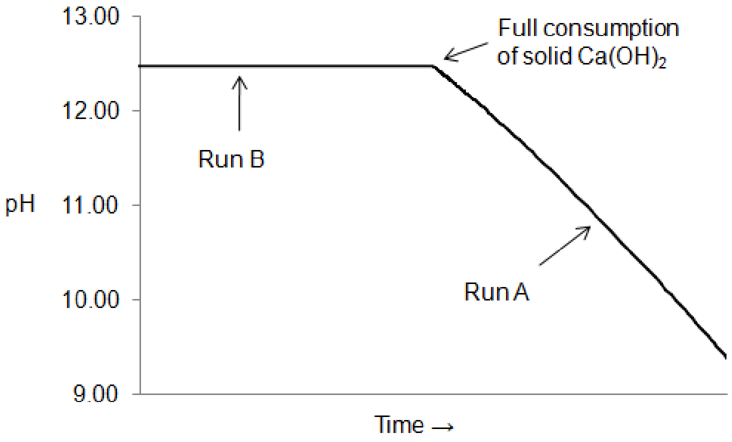

Figure 4.36. pH as a function of time (arbitrary units) in run A and run B.

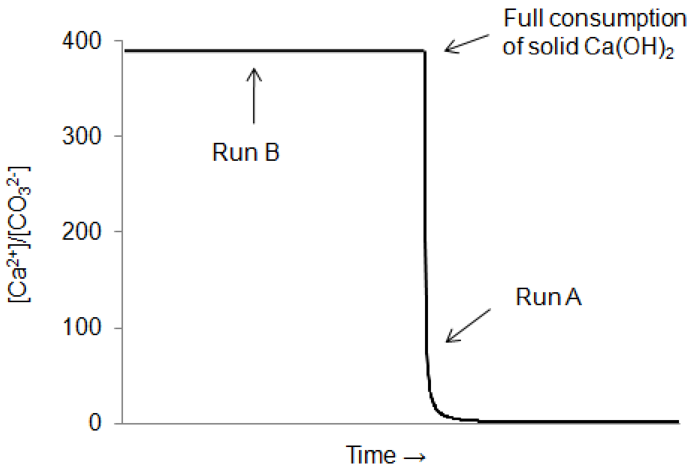

Figure 4.37. Evolution of $[Ca^{2+}]/[CO_3^{2-}]$ ratio as a function of time (arbitrary units) in run A and run B.

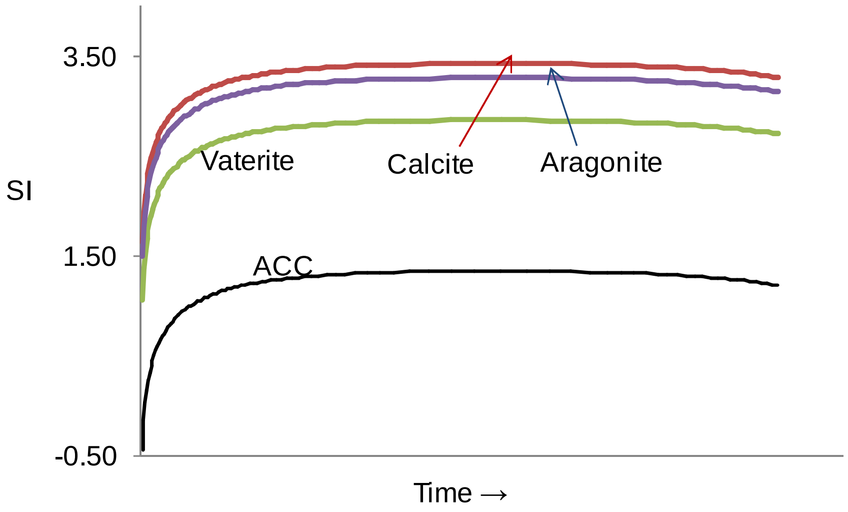

Figure 4.38. Saturation index of all calcium carbonate polymorphs (vaterite, aragonite and calcite) and ACC as a function of time (arbitrary units).

4.5. Discussion

4.5.1. Carbonation in solution vs. carbonation of solid $Ca(OH)_2$

It has been stated that water plays a crucial role in the carbonation process (Moorehead 1989; Yang, 2003), and its presence is necessary for such a reaction to proceed. Carbonation of hydrated pastes, exposed to air for 2 months at 93 % RH, resulted in ~95 wt % transformation of initial portlandite precursor into calcite. In the case of carbonation of hydrated calcite pseudomorphs performed under the same conditions, the achieved degree of transformation was ~50 % within four days. As it has been shown by Beruto and Botter (2000), carbonation of $Ca(OH)_2$ significantly speeds up upon adsorption of up to four H_2O monolayers that catalyze $Ca(OH)_2/CO_2$ solid/gas reaction. In consequence, the kinetics of carbonation show a strong correlation with RH value. The authors have shown that there is a significant increase in the rate of carbonation at RH $\geq$ 70 % when at least 4 monolayers of water are adsorbed into $Ca(OH)_2$ crystals.

The initial water/solid ratio in the hydrated lime pastes, tends to decrease as their carbonation progresses due to drying. Depending on the actual amount of water in the pores, carbonation can occur via two different reaction pathways. The first one involves direct precipitation of calcium carbonate from solution (reflected by both Run A and Run B). This situation is observed when solid $Ca(OH)_2$ (portlandite) dissolves in the pore water and calcium carbonate nucleates and grows from solution. During the evolution of lime pastes form a saturated system to an unsaturated one upon drying, the amount of pore water is reduced to a degree when crystallization of $CaCO_3$ from solution stops being the ruling mechanism for carbonation. At this point, dissolution of portlandite in adsorbed water and precipitation of calcite can be coupled in space and time at the thin interface between parent (portlandite) and product (calcite) phases. In this case carbonation can occur via a coupled dissolution/precipitation reaction (Putnis, 2009). As it was observed here, such a process results in a pseudomorph and is characterized by epitactic control in its progress (Putnis and Mezger, 2004). Direct precipitation of calcium carbonate from solution will be favored at the initial stages of carbonation when excess pore water is present in the system. The other mechanism of carbonation, i.e., coupled dissolution/precipitation reaction, will dominate later on when condensation of H_2O monolayers inside the pores occurs in an unsaturated porous media. The later situation is reflected by portlandite single crystal carbonation. It has to be taken into account, that the change of the calcium carbonate formation mechanisms is expected to have a strong effect on the kinetics of the process. Such an effect is related with the fact that the kinetics of precipitation from solution are many orders of magnitude faster than coupled dissolution/precipitation reactions (Putnis, 2009). This also can explain why the carbonation rate of hydrated lime pastes displayed an exponential decay vs. time. On the other hand, based on the exponential decay in the reaction rate, it could be argued that the carbonation of hydrated lime pastes is a diffusion controlled process. Nevertheless, the fact that the carbonation is kinetically described as a diffusion controlled reaction does not invalidate the fact that from the mechanistic point of view this process is driven by a coupled dissolution/precipitation reaction. Another possibility for the second stage of carbonation could be a solid state replacement mechanism as suggested by Moorehead (1986). However, it has been shown that in the absence H_2O, no carbonation occurs (at room *T*) when $Ca(OH)_2$ is exposed to CO_2. Thus a solid state carbonation mechanism is ruled out. Although it could be argued that such a mechanism could operate at high *T*, due to the fact that the diffusion coefficient of CO_2 could be higher.

4.5.2. $CaCO_3$ phase evolution

The results obtained from run A and run B samples, including XRD, Raman spectroscopy coupled with optical microscope observations, and TEM-SAED analyses, show that ACC always precipitates from solution as a first calcium carbonate phase. These results also clearly indicate that ACC is a highly metastable phase which transforms directly into calcite, without any intermediate phase, i.e., vaterite and/or aragonite. Such an observation contradicts the so-called Ostwald rule of stages (Van Santen, 1984). This empirical rule states that final precipitation of calcite, as the most stable calcium carbonate polymorph, should be preceded by the formation of the less stable phase (i.e., ACC) via metastable vaterite and/or aragonite. Such a phenomenon has been observed by several authors. Ogino et al. (1987) for instance, reported that calcium carbonate precipitation in solution typically follows the Ostwald step rule. Simulation of lime water evolution (run A) performed with the aid of PHREEQC software, indicates that after certain amount of time, counting from the beginning of the carbonation, the solution will be supersaturated with respect to all four calcium carbonate phases. These theoretical findings clearly contradict experimental results, showing that the Ostwald rule is fulfilled only partially, with initial formation of ACC and subsequent transformation into calcite without intermediate stages. Not following the Ostwald rule in the studied system, is a key issue discussed below.

The study on calcium carbonate precipitation in stochiometric Na_2CO_3 and $CaCl_2$ solution at T range 7.5 – 25 ºC performed by Rodriguez-Blanco et al., (2010) shows that the crystallization of calcite starts with the formation of ACC, which subsequently transforms to calcite via intermediate vaterite. This crystallization pathway only partially agrees with the results presented here, which do not show the formation of vaterite at any stage of carbonation. The lack of metastable vaterite formation in the systems analyzed here, can be associated with their high pH. The PHREEQC simulation predicts that the initial pH of saturated lime water equals ~12.4. This pH value remains constant while $Ca(OH)_2$ is supplied to the solution (run B). Once the supply of calcium hydroxide was consumed, the pH tends to drop down to ~9.6 with time. The initial pH of lime water (at the early stage of carbonation) is significantly higher than typical alkaline pH (8.5 – 10.5) reported in most of the experiments on calcium carbonate precipitation (Tai and Chen, 1998). It could be argued that the high pH in our system may favor the direct transformation of ACC into calcite. On the other hand, the crystallization path may be modified by the presence of additives or impurities in the solution. Lime water can be viewed as a chemically pure system, whereas the formation of calcium carbonate from Na_2CO_3 and $CaCl_2$ solution involves the release of Na and Cl ions during reaction, that may influence the formation of calcium carbonate (Kowacz and Putnis, 2008; Ruiz-Agudo et al., 2011). So, it could be argued that the absence of a background electrolyte in the studied system may favor direct calcite formation after ACC (Colfen and Meldrum, 2008).

Formation of ACC and its subsequent transformation into crystalline phases is a poorly understand process (Radha, et al. 2010; Rodriguez-Blanco et al., 2010). Some authors attempted to propose models based on classical nucleation theory. Navrotsky (2004) proposed an explanation regarding the initial formation of metastable precursors. She stated that the surface energy of a precipitating phase becomes smaller when it becomes more metastable (i.e., ACC compared to crystalline forms). This phenomenon is limited to crystals with nanometer-size range. When the size of crystals is bigger than a threshold value, this energetic tendency reverses, so that the stable phase is energetically favored (i.e., the stable phase has a lower Gibbs free energy than the metastable ones). Therefore, a lower energetic barrier at the initial stages of crystallization favors the formation of a metastable phase. Nevertheless, research published within the last few years present a very different approach to this problem. Some authors have reported on the formation of so-called stable prenucleation clusters, with size below the critical size, prior to the formation of amorphous calcium carbonate and crystalline phases (Rieger et al., 2007; Pouget et al., 2009; Gebauer, et al., 2008; Rodriguez-Blanco et al., 2008; Gebauer et al., 2010). Gebauer et al. (2008) showed that their size reach up to ~2 nm, and they tend to aggregate forming ACC (~30 nm). Gebauer et al. (2010) also showed that the type of short range order in the amorphous precursor may vary depending on pH of the solution. They reported the formation of two types of pre-nucleation clusters and ACC precursors: proto-vaterite, formed at pH~9.5 and proto-calcite formed at pH~8.75. They concluded that the type of short-range order is established at the prenucleation stage and inherited by ACC, which subsequently transforms into a specific crystalline form.

Their research, however, did not included observation of short-range order of ACC formed at high supersaturation levels. Conversely, the results involving such conditions are presented here. XRD analysis of precipitates, both in-situ and ex-situ, along with SAED studies point to the existence of short-range order in ACC precipitates formed during carbonation of $Ca(OH)_2$ in solution. The extent of short-range order established by the analyses of calculated electron powder diffraction patterns (EPDPs) is ~1 nm. This value is the same as the one corresponding to broadness of the bump in the ex-situ XRD patterns. The size of ACC spheres, however, reached up to a few micrometers in diamater, a value larger than any previously reported. The simulation of EPDPs produced by clusters with monohydrocalcite and calcite structure points to a non-oriented aggregation of the first ones and/or an oriented aggregation of both types of clusters forming ACC. An oriented aggregation would be in agreement with forced-air injection experiments showing the formation of oriented calcite pseudomorphs. The theoretical findings suggest that the structure of the clusters appears to have some similarities with both monohydrocalcite and calcite. This leads to the conclusion, that the precipitating calcium carbonate phase is established at the prenucleation assembly level, also at high supersaturation. Comparison of published results (Rieger et al. 2007; Rodriguez-Blanco et al. 2010; Gebauer et al. 2010) with those presented here, suggests a strong correlation between pH, SI and phase predetermination. It may be concluded that calcite, as opposed to vaterite, tends to precipitate at high pH and under high supersaturation conditions.

The most common mechanism of ACC to calcite transformation appears to be the full dissolution of the first one followed by the crystallization of the later (Rieger et al., 2007; Rodriguez-Blanco et al., 2010). This is in agreement with optical microscopy and ESEM experiments performed here. On the other hand, TEM observations showed that in some cases, the ACC to calcite transformation preserves the external shape of ACC spheres, thus it is pseudomorphic. Such a type of transformation is often associated with a coupled dissolution/precipitation reaction (Putnis, 2009). This type of transformation was proposed by Pouget et al. (2009) in the case of ACC to vaterite transition. Another ACC to calcite transformation pathway involves a solid state reaction, i.e., dehydration of ACC, as proposed by Radha et al. (2010). They observed the initial formation of pre-nucleation clusters 0.6 – 1 nm in size, predetermining the short range order in ACC.

Subsequently, ACC transformed into calcite via a sequence of endothermal dehydration steps, followed by exothermal reorganization in its internal structure (i.e., solid state mechanism). The structural rearrangement is sufficiently exothermal to compensate the endothermic effect associated with the release of water from ACC. Finally, anhydrous ACC transforms into more stable crystalline forms. However, this type of transition requires a low pH_2O. That condition is not fulfilled here, since the reaction takes place in solution. However, due to the high pH of lime water (~12.4) precipitating ACC is expected to be a less hydrated form due to the lower water activity, which according to PHREEQC simulations is established at the level of $\sim 10^{-2}$ as opposed to that value at pH ~7 of ~1. This in turn directly affects the hydration of ions, enabling a closer packing of prenucleation clusters. Nevertheless, EPDPs show some similarities of the clusters with both hydrated (monohydrocalcite) and anhydrous (calcite) forms of calcium carbonate. It could be hypothesized that pre-nucleation clusters initially precipitates as an hydrated form of $CaCO_3$ and as they aggregate in an oriented manner, dehydration of the initial cluster structure would be at work. This dehydration would work at the level of clusters, leading to their change towards calcite structure. On the other hand, prenucleation clusters could precipitate already with calcite structure. Similarities to monohydrocalcite may be related with the presence of water, which is “trapped” between the clusters within ACC volume. In that case dehydration would involve the removal of water present among the clusters, followed by their oriented aggregation forming calcite. The de-hydration process could be triggered once ACC exceeds a critical diameter or by forced air injection.

4.5.3. Morphology of calcite crystals

FESEM analysis of precipitates formed within 2 h in Run A and Run B samples coupled with PHREEQC simulations indicate that the $[Ca^{2+}]/[CO_3^{2-}]$ ratio in the solution appears to have a strong influence on the morphology of PCC. According to Laham (1978) the formation of calcite crystals elongated along the *c*-axis, i.e., with scalenohedral morphology, should be favored under excess of Ca^{2+} ions in solution. PHREEQC predictions show that in Run B sample, carbonation takes place under

$[Ca^{2+}]/[CO_3^{2-}]$ ratio >> 1 (~$4x10^2$). As FESEM analysis shows, under such conditions calcite develops with scalenohedral morphology. Conversely, conditions close to stoichiometry between Ca^{2+} and CO_3^{2-}, which according to PHREEQC predictions are approached in the case of pure lime water (i.e., Run A sample) , with a $[Ca^{2+}]/[CO_3^{2-}]$ ratio ~3.58, typically result in precipitation of calcite with rhombohedral morphology. These predictions are also confirmed by experimental observations (FESEM results). Other authors also reported on the formation of rhombohedral calcite in nearly stochiometric $[Ca^{2+}]/[CO_3^{2-}]$ ratios (Jung et al. 2000). The above mentioned results may explain the calcite morphology evolution along depth profiles observed in HLP samples carbonated in air at 93% RH (e.g., AC). These variations indicate that the conditions under which carbonation takes place are different inside the sample from those at the exposed surface.

Calcite crystals developed in deeper parts of AC sample, carbonated in air at 93% RH for two months show scalenohedral morphology. Carbonation of lime pastes is a process involving interrelated steps of setting, drying and chemical reactions. The pore water is rich in Ca^{2+} and OH^- ions due to dissolution of solid $Ca(OH)_2$ within the matrix. As the setting of lime pastes in air progresses, water evaporates from the outer surface, leaving space for CO_2 diffusion through the sample thickness. Under these conditions the concentration of CO_2 is very low, approximately 0.03% by volume (Cizer et al., 2011). This in turn has a strong influence on the concentration of ions in pore water, where Ca^{2+} concentration will outweigh CO_3^{2-} concentration. Such a proportion between Ca^{2+} and CO_3^{2-} ions induces the formation of calcite with scalenohedral morphology (Tai and Chen, 1998; Jung et al. 2000). The surface of the sample is directly exposed to the atmosphere where water vapor and carbon dioxide are present. These conditions guarantee the supply of water for dissolution of portlandite as well as the supply of CO_2. The concentration of CO_3^{2-} ions within the sample depends also on drying rate and diffusion rate of CO_2 through the pores, whose volume decreases with time. The cracked and corrode features observed in scalenohedral calcite crystals within the bulk sample suggest changes towards stoichiometry between Ca^{2+} and CO_3^{2-} ions in the pore water solution as carbonation progresses. Once full consumption of $Ca(OH)_2$ was reached, scalenohedral calcite may be subjected to dissolution (Cizer et al., 2011) followed by precipitation of energetically stable calcite rhombohedra under these conditions (i.e., $[Ca^{2+}]/[CO_3^{2-}] \cong 1$).

Precipitation of calcite with scalenohedral morphology in the ESEM was observed only in Experiment 1. The analysis involved air exposure of the sample for 2 min prior to observation of crystallization. No scalenohedral calcite formation was observed in Experiment 2, where prior to observation the sample was exposed to air for 7 min. Different times of exposure are directly responsible for differences in Ca^{2+} and CO_3^{2-} ion concentration. As far as pH of solution (lime water) remains sufficiently high, the amount of CO_2 dissolved in solution depends on exposure time. In other words, a longer exposure results in a higher amount of dissolved CO_2. Thus the different results regarding the morphology of precipitated calcite can be explained considering the differences Ca^{2+} and CO_3^{2-} ions ratio. A ratio closer to stoichiometry in the case of Experiment 2 leaded to the formation of rhombohedral calcite.

Both experimental results and theoretical consideration (PHREEQC simulation) performed in this work suggest that the main factor controlling the morphology of precipitating calcite is the $[Ca^{2+}]/[CO_3^{2-}]$ ratio. On the other hand, parameters like surface area and particle size distribution of $Ca(OH)_2$ in FG and AC lime putties (Appendix 2) seem to have a strong influence on the crystallite size evolution and carbonation rate. These factors along with the amount of pore water in turn control the $[Ca^{2+}]/[CO_3^{2-}]$ ratio. This may explain the observed differences in crystal morphology and size along the depth profiles in AC and FG samples. It also indicates how the previous steps of the lime cycle (e.g., calcination T and retention time as well as hydration conditions/dominant hydration mechanism) may affect the following ones.

4.5.4. Carbonation of portlandite single crystals

In spite of the numerous studies on the carbonation of calcium hydroxide in both Portland cement (Huet et al., 2011) and lime mortars (Rodriguez-Navarro et al., 2002; Cultrone et al., 2005), in high temperature capture of CO_2 (Materic and Smedley, 2001) as well as in industrial applications for PCC production (Uebo et al., 1992; Jung et al., 2000; García-Carmona et al., 2003; Dominguez et al., 2006 Montes-Hernandez et al., 2008), there is a gap regarding research on this process taking into account a possible crystallographic control in its advancement (i.e., epitaxy/topotaxy). Gillott (1967) suggested that the carbonation of portlandite single crystals may be a topotactic process. However, this conclusion was derived from powder XRD and thermal analysis, which precluded the possibility of an exact determination of the crystallographic relationship between parent and product phases supporting that statement. A solid state carbonation via substitution of OH^- by CO_3^{2-} followed by a change of d_{001} spacing of portlandite has been proposed by Stepkowska (2005). Unfortunately, these findings do not highlight the nature of the replacement process. The carbonation mechanism could be the result of a solid state reaction (topotaxy) as well as a coupled dissolution/precipitation reaction (epitaxy), and both of these mechanisms were proposed in the past. For instance, Johnston and Glasser (1992) suggested a dissolution/precipitation reaction path for portlandite carbonation. Montes-Hernandez et al. (2010) report direct (solid state reaction) carbonation of nanometer size portlandite crystals resulting in the formation of calcite crystals of nanometer size. However, they concluded that non zero water activity was required for carbonation to proceed. It should be mentioned, that once the carbonation reaction is triggered, what always takes place in the presence of water, water produced as a byproduct of calcium hydroxide carbonation, catalyzes the progress of the reaction. The presence of water is not required during solid-state carbonation. In contrast water is critical during coupled dissolution/precipitation reactions. Findings presented here indicate that the most possible mechanism for portlandite carbonation is a coupled dissolution/precipitation reaction consistent with the fact that water is necessary for the triggering of this reaction. Other evidence supporting this idea will be discussed below.

It has been stated that the $\{10\bar{1}0\}$ faces of portlandite pseudomorphs are always more corroded than the {0001} faces. This is in agreement with the results from in-situ XRD carbonation (Run B sample) which show that portlandite dissolution rate along [001] direction is much slower than along <100> (Figure 4.39). The solution penetrates the portlandite structure parallel to the basal planes, which are occupied by OH^- groups. These OH^- groups are totally replaced (dehydration) by CO_3^- ions (carbonation). From an energetic point of view this seems to be a favorable replacement process. However, such a direct replacement would led to a pseudomorph with a topotactic relationship between parent and product phase. This is not what our 2D-XRD results show. The relationship is in fact epitactic. It seems that the solution penetrates the $Ca(OH)_2$ structure parallel to (0001) plane and fully dissolves it (locally). After the $Ca(OH)_2$ dissolution calcite forms epitaxially on the remaining portlandite.

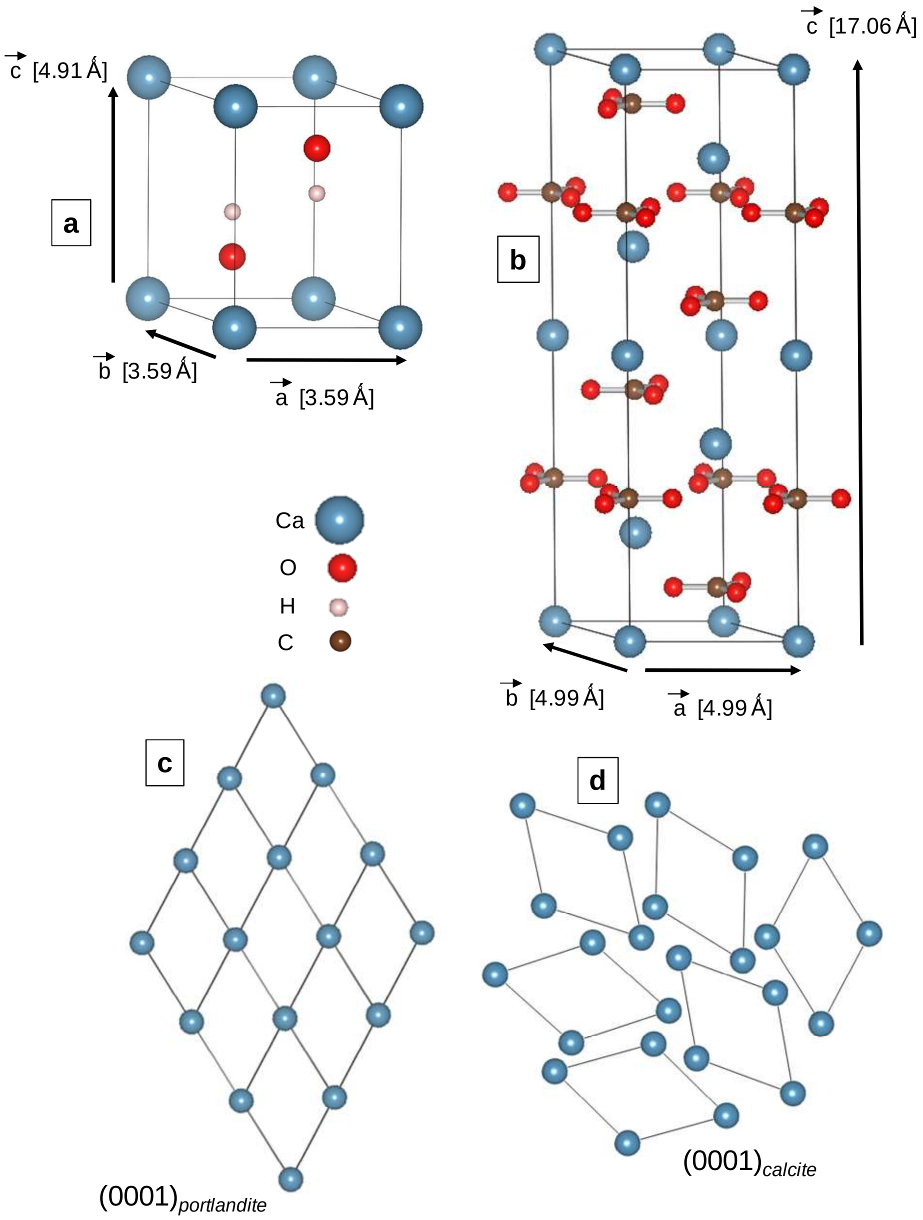

Figure 4.39. Portlandite (a) and calcite (b) unit cells. (c-d) schematic representation of an epitaxial replacement of portlandite by calcite via coupled dissolution/precipitation carbonation progressing parallel to the basal plane and resulting in an epitaxial relationship between parent and product phases.

FESEM observations show that carbonation of portlandite single crystal preserves its external shape, i.e., resulting in portlandite pseudomorphs. This suggests, along with the observed epitactic relationship, that carbonation of portlandite crystals occurs in fact in the presence of a solution and via a coupled dissolution/precipitation process, which typically results in the formation of pseudomorphs. One of the issues regarding the pseudomorphic replacement of portlandite by calcite is the higher molar volume of the product phase (calcite) compared to the parent phase (portlandite), which may result in the halt of the replacement progress (Montes-Hernandes et. al., 2010). This seems to be in agreement with the results presented here, which show that the rate of carbonation of portlandite tends to decrease with time, and is expected to stop at a certain point due to an increase of molar volume and a reduction of porosity. A model for the replacement of one phase (A) with smaller molar volume by another phase (B) with higher one was proposed by Jamtveit et al. (2008). Such a replacement of phase A by phase B results in accumulation of stress, which finally results in fracturing. Fractures produced in this process provide pathways for fluid penetrating the bulk sample. The transported fluid will react with phase A once again causing fracturing, but this time at smaller scale. Repetition of this process will yield a hierarchical sequence of fracturing, smaller in terms of volume at each step and finally resulting in diffusion control of the reaction. Moreover, differences in solubility between parent and product phases (i.e., the parent phase being more soluble than the product phase, what is observed in the case of portlandite and calcite) may facilitate the generation of porosity and the progress of coupled dissolution/precipitation reaction front in systems where the molar volume of the product phase is higher than that of the parent phase (i.e., the system here studied) (Putnis, 2009).

The model proposed here involving a coupled dissolution/precipitation reaction for the carbonation of portlandite crystals, explains all the observed features of the parent and product phases, as well as the kinetics of such a replacement process. This also shows that despite the reduction in carbonation rate as the reaction progresses, does not necessary end up with the halting of the process. Eventually, the whole portlandite crystal will be carbonated, either due to the generation of porosity or fractures, or both. These results have important implications in understanding the setting of lime mortars used for conservation purposes.

5. CONCLUSIONS

In this thesis, a methodology combining the use of advanced analytical techniques (i.e., SEM, HRTEM, SAED, 2D-XRD, FTIR) and simulation tools has been developed. Using this methodology, it has been possible to fully characterized the complex transformation mechanisms in the most relevant mineral reactions of the lime cycle and determine the crystallographic control and textural evolution during the transformation between parent and product phases.

In this section the conclusions of the studies performed in this thesis regarding three processes within the lime cycle (i.e., dolomite thermal decomposition, hydration of lime and carbonation of calcium hydroxide) are presented. Finally, the implications of these results and conclusions are outlined, emphasizing their significance and importance in heritage conservation.

5.1. Thermal decomposition of dolomite

1) The thermal decomposition of dolomite involves its direct transformation into a mixed oxide phase ($Ca_{0.5}Mg_{0.5}O$) with FCC structure (at low *T*). With increasing *T*, the mixed oxide structure separates into CaO and MgO via spinodal demixing.

2) The reaction is independent of pCO_2. The formation of calcite during the so-called “half-decomposition” is a result of solid state recarbonation of highly reactive CaO crystals.

3) The thermal decomposition of dolomite is a topotactic reaction with the following orientation relationships between parent (dolomite) and product phases (Ca and Mg oxides): $[001]_{dolomite}//\langle 111\rangle_{oxide}$, $\langle \bar{4}41\rangle_{dolomite}//\langle 100\rangle_{oxide}$, $\{11\bar{2}0\}_{dolomite}//\{110\}_{oxide}$, $\{11\bar{2}8\}_{dolomite}//\{110\}_{oxide}$.

5.2. *Hydration of lime*

1) Vapor phase hydration of lime is a pseudomorphic replacement reaction with a strong crystallographic control in its progress. Pole figures indicate the following (topotactic) orientation relationships between lime and portlandite: $\{11\bar{2}0\}_{portlandite}//\{110\}_{lime}$ and $\{0001\}_{portlandite}//\{111\}_{lime}$.

2) The two most probable mechanisms for vapor phase hydration are: i) a coupled dissolution/precipitation reaction and ii) a solid state replacement reaction.

3) Microstructural features of CaO pseudomorphs, which strongly depends on the calcination conditions (e.g., calcination *T*, retention time) have a strong influence on the hydration of lime. In particular these features, which change during hydration, may be responsible for the selection of the ruling mechanism of hydration, i.e., coupled dissolution/precipitation reaction or solid state hydration.

4) In addition to these processes, direct hydration of CaO dissolved in slaking water, also plays a key role during lime slaking.

5.3. *Carbonation of calcium hydroxide*

1) Calcium carbonate in lime water (pH ~12.4) always precipitates first as ACC and then transforms into calcite without any intermediate phase. Probably, the high pH in the system has a strong influence in determining the precipitating phase. Two routes for ACC to calcite transformation have been identified: (i) dissolution of ACC followed by crystallization of calcite from solution; and (ii) pseudomorphic ACC-to-calcite replacement via either a coupled dissolution/precipitation reaction or a solid state dehydration.

2) ACC is characterized by a short-range order (proto-calcite), which is inherited by subsequent calcite pseudomorphs. The origin of such a short range order could be related to the formation and aggregation of stable pre-nucleation clusters with structure similar to calcite and/or monohydrocalcite.

3) The Ca^{2+} and CO_3^{2-} ions ratio has a strong influence on calcite morphology. $[Ca^{2+}]/[CO_3^{2}]$ close to stoichiometry (precipitation in lime water, Run A) favors the formation of a rhombohedral morphology, while $[Ca^{2+}]/[CO_3^{2}] >> 1$ (precipitation in lime water with excess of $Ca(OH)_2$, Run B) renders the formation of scalenohedral calcite.

4) Portlandite is characterized by strong anisotropic dissolution features. Prism faces dissolve easier than basal planes. This in turn predetermines how (in what direction) the replacement of portlandite by calcite progresses.

5) Portlandite carbonation is a pseudomorphic, coupled dissolution/precipitation reaction involving strong epitactic control with the following relationship: $<001>_{calcite}//<001>_{portlandite}$.

6) $[Ca^{2+}]/[CO_3^{2}]$ ratio, relative humidity conditions and properties of lime pastes have a significant effect on the morphology, habit and size of precipitated calcite formed during carbonation of lime pastes.

7) Carbonation of lime pastes involves two processes: (i) precipitation of calcite (via intermediate ACC) in solution, and (ii) replacement of portlandite crystals by calcite via coupled dissolution/precipitation reaction.

5.4. Implications of the results

Extrapolation of the conclusions derived from the experiments presented in this work could shed some light on different problems and aspects regarding studied processes mainly in the field of the conservation of cultural heritage. Nevertheless, the importance and possible applications of the studied reactions extend to many different areas: geological, industrial and technological.

Dolomite limes, despite being less popular than those based on calcium carbonate, were used for building purposes since ancient times. Such materials are also gaining interest in the field of cultural heritage conservation. Dolomite has found numerous technical applications, including its use in ceramics, glass, iron and steel industry, in pharmacy, and as a source of important chemicals such as CaO and MgO. In all these cases, the thermal decomposition of dolomite is a first step leading to a product with desirable properties. The understanding of the nature of the thermal decomposition of dolomite appears to be a key factor in designing and controlling all these properties. From the point of view of the lime cycle, it should be expected that hydration and carbonation will be strongly affected by the properties of the quicklime produced during calcination of dolomite. Therefore, designing of new methods of conservation using dolomite based products seems difficult without a good understanding of the thermally induced decomposition of dolomite. On the other hand, this study, along with those performed recently on the calcination of calcite, show that both processes are topotactic and the mechanism is independent of T or pCO_2. Ultimately they show that calcination of both dolomite and calcite results in nanocrystalline oxide products whose properties are strongly controlled by the crystallographic features of the parent carbonates, carbonation T and retention time. Those features in turn will control the properties of the oxides and the performance of lime (both dolomitic and calcitic) during conservation applications.

The conclusions derived from the results of this thesis regarding hydration of lime can provide a better understanding of the lime slaking process, which is crucial in the production of lime based products like mortars. The understanding of the mechanisms of such a reaction can contribute to the development of new materials and methods of conservation where the properties of $Ca(OH)_2$ crystals can be controlled and/or tailored for specific application, like the production of nanolimes. Apart from the field of cultural heritage conservation, the results regarding the hydration of lime may have different implications in its production for a specific use. Calcium hydroxide is commonly used for neutralization of exhaust gases from factories, like nitrogen or sulfur oxides, which are the main cause of acid rain. It is also a popular and cheap neutralizing agent used for the reduction of soil acidity. The specific use of the product requires well defined properties, which are difficult to achieve without the good understanding of the scientific aspects of its manufacturing. The gained knowledge may help in the optimization of industrial vapor phase hydration of CaO or traditional lime slaking process. The properties of the final product may be controlled by the selection of the ruling mechanism which strongly depends on water content or pH_2O (solid state hydration vs. coupled dissolution/precipitation reaction, or hydration via solution-mediated reaction). Nevertheless, the properties of calcium hydroxide product are influenced by the properties of CaO (e.g., microstructural features, like crystallite size or porosity, which in turn control its reactivity (hard/soft burnt lime)). Such properties are established during calcination of $CaCO_3$, and depend on factors like calcination T or retention time.

The conclusions regarding carbonation of calcium hydroxide can help to understand carbonation in traditional lime based mortars, which is the only process responsible for their setting and hardening. In particular this is related to the studies of HLP carbonation, which provide an accurate picture of the behavior of the lime mortars and their evolution during carbonation. They also exemplify how important the previous steps of the lime cycle are (i.e., calcination and hydration), when it comes to the determination of the properties of the final product. The information presented here may also shed some light on the influence of different factors, like T or RH, on the above mentioned processes, as well as their role in the selection of the ruling mechanism (e.g., solution mediated carbonation vs. coupled dissolution/precipitation reaction). The results may help in the better understanding of the performance of lime based products and contribute to the existing knowledge. This knowledge, in turn, can be used and applied in the field of the conservation of cultural heritage, and help in designing and applying new conservation treatments. The gained knowledge from portlandite single crystal carbonation as well as carbonation in $Ca(OH)_2$ solutions can be directly transferred to the area of Portland cement carbonation. Carbonation itself is also a process of great importance in other fields. PCC plays a vital role in the production of food, paper, plastic, cosmetics and pharmaceutical products. In each of these fields controlling the properties of PCC, like phase and morphology, is a key factor. The simplicity, relatively low cost, and potentially easy control over the carbonation process of the method, may result in a more effective way of calcium carbonate production. For example, the morphology of precipitating calcite crystals can be easily control by adjusting the calcium to carbonate ion ratio. Moreover, the lack of metastable phases (vaterite and aragonite) observed in all experiments, simplifies the crystallization process. This is crucial in fulfilling the demand for stable (calcite) product of high quality. Carbonation also can have interesting implication in CO_2 sequestration, helping to reduce the greenhouse effect. For instance, production of acetylene results in the production of carbide lime slurry, which normally is treated as a waste, but may be used for CO_2 sequestration by carbonation processes.

The analysis of the precipitation of calcium carbonate from lime water, is linked with the area of nanotechnology. The implications of these research may have an impact on many different areas. This stems from the fact that calcium carbonate is one of the most often synthesized and used substances. In the fast evolving area of conservation treatments, based on the design and application of novel nanotechnological methods, the results here presented and discussed may help in the better understanding, developing and use of consolidation methods for stones based on dispersion of $Ca(OH)_2$ nanoparticles (nanolimes) generating $CaCO_3$ cement. Nanolimes use, however, is not an easily controlled process and shows limited effectiveness. A better understanding of the mechanisms of $Ca(OH)_2$ carbonation will help in the design and application of modified nanolimes dispersions where either a solution-mediated, or a coupled dissolution/precipitation carbonation is promoted for specific applications. Another possibility for the development of novel consolidation methods may be based on the use of ACC dispersions. In this approach to the conservation of cultural heritage the main problem is related to the stabilization of ACC, and its controlled transformation into the crystalline form (calcite). The investigation on the mechanisms of ACC to calcite transformation sheds some light on this problem and could contribute to the development of such a novel consolidation method. The formation of calcium carbonate crystals in a submicrometer range, preceded by the formation of ACC, may occur in lime pastes influencing their properties and performance. These results may also have possible applications in the production of calcium carbonate where crystals with nanometer size and well defined properties are gaining interest. This includes applications of crystals as filler in food or ink. There is also a potential use of calcium carbonate crystals in the production of new drugs, where the active substance is attached to the crystals. The rate of its release to the system will depend on the crystal properties (e.g., crystallite size and dissolution rate). The advantage of the calcium carbonate use is related to its biocompatibility.

6. REFERENCES

Addadi, L., Raz, S. and Weiner, S. (2003) Taking advantage of disorder: amorphous calcium carbonate and its roles in biomineralization. Advanced Materials 15 , 959 970.

Agrinier, P., Deutsch, A., Schärer, V. and Martinez, I. (2001) Fast back-reactions of shock-released CO_2 from carbonates: An experimental approach. Geochimica et Cosmochimica Acta 65, 2615-2632.

Aizenberg, J., Lambert, G., Weiner, S. and Addadi, L. (2002) Factors involved in the formation of amorphous and crystalline calcium carbonate: A study of an Ascidian skeleton. Journal of the American Chemical Society 124 , 32-39.

Aizenberg, J., Muller, D. A., Grazul, J. L. and Hamann, D. R. (2003) Direct fabrication of large micropatterned single crystals. Science 299 , 1205-1208.

Allen, E. and Thallon, R. (2011) Fundamentals of Residential Construction. Wiley, Hoboken, N.J.

Bandi, W.R. and Krapf, G. (1976) The effect of CO_2 pressure and alkali salt on the mechanism of decomposition of dolomite. Thermochimica Acta 14, 221 - 243.

Barber, D.J, Wenk, H.R. (1979) Deformation twinning in calcite, dolomite and other rhombohedral carbonates. Physics and Chemistry of Minerals 5, 141-165.

Barber, D.J., Heard, H.C. and Wenk, H.R. (1981) Deformation of dolomite single crystals from 20-800 ºC. Physics and Chemistry of Minerals 7, 27l-286.

Bernal, J. D. and Fowler, R. H. (1933) A theory of water and ionic solution, with particular reference to hydrogen and hydroxyl ions. The Journal of Chemical Physics 1, 515-548.

Bertrand, G. (1978) Comments on “Kinetics of endothermic decomposition reactions. 2. Effect of the solid and gaseous product.” Journal of Physical Chemistry 82, 2536–2537.

Beruto, D. and Searcy, A.W. (1974) Use of the Langmuir Method for kinetic studies of decomposition reactions: Calcite ($CaCO_3$). Journal of the Chemical Society, Faraday Transactions I 70, 2145-2153.

Beruto, D. T. and Botter, R. (2000) Liquid-like H_2O adsorption layers to catalyze the $Ca(OH)_2/CO_2$ solid–gas reaction and to form a non-protective solid product layer at 20 °C . Journal of the European Ceramic Society 20 , 497-503.

Beruto, D., Barco, L., Belleri, G. and Searcy, A. W. (1981) Vapor-Phase Hydration of Submicrometer CaO Particles. Journal of the American Ceramic Society, 64, 74–80.

Beruto, D., Searcy, A.W. and Kim, M.G. (2004) Microstructure, kinetic, structure, thermodynamic analysis for calcite decomposition: Free-surface and powder bed experiments. Thermochimica Acta 424, 99-109.

Beruto, D.T., Veccchiattini, R. and Giordani, M. (2003) Solid products and rate-limiting step in the thermal half decomposition of natural dolomite in a CO_2 (g) atmosphere. Thermochimica Acta, 405, 183-194.

Best, M.G. (1982) Igneous and Metamorphic Petrology. Freeman, New York.

Boynton, R.S. (1980) Chemistry and Technology of Lime and Limestone (2nd edition). Wiley-Interscience, New York.

Brečević, L. and Nielsen, A. (1989) Solubility of amorphous calcium carbonate. Journal of Crystal Growth 98 , 504-510.

Britton, H.T.S., Gregg, S.J. and Winsor, G.W. (1951) The calcinations of dolomite. Part II.-The Thermal decomposition of dolomite. Transactions of the Faraday Society, 48, 70 - 75.

Britton, H.T.S., Gregg, S.J., Winsor, G.W., and Willing, E.G.J. (1952) The heat treatment of dolomite. II. The “activity” of dolime in relation to its temperature of preparation of dolomite. Journal of Applied Chemistry, 2, 698-700.

Cater, E.D., and Buseck, P.E. (1985) Mechanism of decomposition of dolomite, $Ca0.5Mg0.5CO_3$, in the electron microscope. Ultramicroscopy, 18, 241-252.

Cazalla, O., Rodriguez-Navarro, C., Sebastian, E. and Cultrone, G. (2000) Aging of lime putty: Effects on traditional lime mortar carbonation. Journal of American Ceramic Society 83 , 1070-1076.

Chen, P. C., Tai, C. Y. and Lee, K. C. (1997) Morphology and growth rate of calcium carbonate crystals in a gas-liquid-solid reactive crystallizer. Chemical Engineering Science 52 , 4171-4177.

Ciupina V., Zamfirescu, S. and Prodan G. (2007) Evaluation of Mean Diameter values using Scherrer Equation Applied to Electron Diffraction Images. Nanotechnology – Toxicological Issues and Environmental Safety and Environmental Safety. 231-237.

Cizer, O. (2009) Competition between Carbonation and Hydration on the Hardening of Calcium Hydroxide and Calcium Silicate Binders. PhD Thesis. K.U.Leuven.

Cizer, O., Rodriguez-Navarro, C., Ruiz-Agudo, E., Elsen, J., Van Gemert, D. and Van Balen, K. (2012) Phase and morphology evolution of calcium carbonate precipitated by carbonation of hydrated lime. Journal of Materials Science 47, 6151-6165.

Cizer, Ö., Van Balen, K., Rodriguez-Navarro, C., Elsen, J. and Van Gemert, D., (2011) Evolution of calcium carbonate phase and morphology during carbonation of hydrated lime pastes.. Submitted to Cement and Concrete Reaearch.

Connolly, J. R. (2010) EPS400 - Intro to XRD. Retrieved May 26, 2011, from Introduction to X-Ray Powder Diffraction: http://epswww.unm.edu/xrd/xrd-course-info.htm.

Cultrone, G., Arizzi A., Sebastián E. and Rodriguez-Navarro C. (2008) Sulfation of calcitic and dolomitic lime mortars in the presence of diesel particulate matter. Environmental Geology, 56, 741-752.

Cultrone, G., Sebastian, E. and Ortega, H. M. (2005) Forced and natural carbonation of lime-based mortars with and without additives: Mineralogical and textural changes. Cement and Concrete Research 35 , 2278-2289.

Czigany, Z. and Hultman, L. (2010) Interpretation of electron diffraction patterns from amorphous and fullerene-like carbon allotropes. Ultramicroscopy 110, 815-819.

Danilatos, G. D. (1994) Environmental Scanning Electron Microscopy and Microanalysis. Microchimica Acta 114 , 143-155.

Dasgupta, D.R. (1961) Topotactic transformations in iron oxides and oxyhydroxides. Indian Journal of Physics 35, 401-419.

Dasgupta, D.R. (1964) Oriented transformation of magnesite. Indian Journal of Physics 38, 623-626.

Dasgupta, D.R. (1967) Thermal decomposition of dolomite and ankerite. Mineralogical Magazine, 36, 138-141.

De Aza, A.H., Rodríguez, M.A., Rodríguez, J.L., De Aza, S., Pena, P., Convert, P., Hansen, T. and Turrillas, X. (2002) Decomposition of dolomite monitored by neutron thermodiffractometry. Journal of the American Ceramic Society, 85, 881–888.

Dennis, J.S. and Hayhurst, A.N. (1987) The effect of CO_2 on the kinetics and extent of calcination of limestone and dolomite particles in fluidized beds Chemical Engineering Science 42, 2361 - 2372.

Dollimore, D., Dunn, J.G., Lee, Y.F. and Penrod, B.M. (1994) The decrepitation of dolomite and limestone. Thermochimica Acta, 237, 125 - 131.

Domingo, C., Loste, E., Gomez-Morales, J., Garcia-Carmona, J. and Fraile, J. (2006) Calcite precipitation by a high-pressure CO_2 carbonation route. The Journal of Supercritical Fluids 36 , 202-215.

Egerton, R.F. and Malac, P.L.M. (2004) Radiation damage in the TEM and SEM. Micron, 35, 399-409.

Elert, K., Rodriguez-Navarro, C., Pardo, E. S., Hansen, E. and Cazalla, O. (2002) Lime mortars for the conservation of historic buildings. Studies in Conservation 47 , 62-75.

Elsen J. (2006) Microscopy of historic mortars—a review. Cement and Concrete Research 36, 1416–1424.

Engler, P., Santana, M.W., Mittleman, M.L. and Balazs, D., (1989) Non-isothermal, in situ XRD analysis of dolomite decomposition. Thermochimica Acta, 140, 67-76.

Fazeli, A. R. and Tareen, J.A.K (1992) Thermal decomposition of rhombohedral double carbonates of dolomite type. Journal of Thermal Analysis and Calorimetry, 38, 2459-2465.

Fisler, D. K. and Cygan, R, T. (1999) Diffusion of Ca and Mg in calcite. American Mineralogist, 84, 1392-1399.

Floquet, N. and Niepce, J.C. (1978) Three-fold transformation twin in the topotactic decomposition of cadmium carbonate crystals. Journal of Materials Science, 13, 766-776.

Fonseca, A.T., Vieira, J.M. and Baptista, J.L. (1998) Grain growth in synthetic and natural dolomas. Ceramics International, 24, 163-173.

Galai, H., Pijolat, M., Nahdi, K. and Trabelsi-Ayadi, M. (2007) Mechanism of growth of MgO and $CaCO_3$ during a dolomite partial decomposition. Solid State Ionics, 178, 1039-1047.

Galwey, A. K. and Brown, M.E., (1999) Thermal Decomposition of Ionic Solids. Elsevier, Amsterdam.

Gárate Rojas, I. (1994) Las Artes de la Cal (2ª Edición). Ministerio de Cultura-ICBRBC, Madrid.

Garcia-Carmona, J., Gomez Morales, J. and Rodriguez Clemente, R. (2003) Rhombohedral–scalenohedral calcite transition produced by adjusting the solution electrical conductivity in the system $Ca(OH)_2–CO_2–H_2O$. Journal of Colloid and Interface Science 261 , 434-440.

Gebauer, D., Gunawidjaja, P. N., Ko, J. Y., Bacsik, Z., Aziz, B., Liu, L., et al. (2010) Proto-calcite and proto-vaterite in amorphous calcium carbonates. Angewandte Chemie International Edition 49 , 8889-8891.

Gebauer, D., Völkel, A. and Cölfen, H. (2008) Stable prenucleation calcium carbonate clusters. Science 322 , 1819-1822.

Gillott, J. E. (1967) Carbonation of $Ca(OH)_2$ investigated by thermal and XRD methods of analysis. Journal of Applied Chemistry 17 , 185-189.

Glasser, F. P. and Matschei, T. (2007) Interactions between portland cement and carbon dioxide. 12th International Congress on the Chemistry of Cement.

Gnuplt. (2010, March 13) Retrieved 2011, from gnuplot.info.

Goldsmith, J.R. and Graf, D.L. (1958) Relation between lattice constant and composition of the Ca-Mg carbonates. American Mineralogist 43, 84-101.

Goldsmith, J.R. and Heard, H.C. (1961) Subsolidus phase relations in the system $CaCO_3$-$MgCO_3$. Journal of Geology, 69, 45-74.

Graf, D.L., and Goldsmith, J.R. (1955) Dolomite magnesian-calcite relations at elevated temperatures and CO_2 pressure. Geochimica et Cosmochimica Acta, 7, 109-128.

Grapes, R. (2006) Pyrometamorphism. Springer, Berlin.

Hansen, E. F., Rodriguez-Navarro, C. and Van Balen, K. (2008) Lime Putties and Mortars: Insights into fundamental properties. Studies in Conservation 53 , 9-23.

Hartman, M., Trnka, O., Veselý, V. and Svoboda, K. (1996) Predicting the rate of thermal decomposition of dolomite. Chemical Engineering Science, 51, 5229-5232.

Hashimoto, H., Komaki, E., Hayashi, F. and Uematsu, T. (1980) Partial decomposition of dolomite in CO_2. Journal of Solid State Chemistry, 33, 181-188.

Hashmi, S. M., Wickman, H. H. and Weitz, D. A. (2005) Tetrahedral calcite crystals facilitate self-assembly at the air-water interface. Physical Review E 72 , 041605.

Haul, R.A.W. and Heystek, H. (1952) Differential thermal analysis of the dolomite decomposition, American Mineralogist, 37, 166-179.

Haul, R.A.W. and Markus, J. (1952) On the thermal decomposition of dolomite. IV. Thermogravimetric investigation of the dolomite decomposition, Journal of Applied Chemistry, 2, 298-306.

Haul, R.A.W. and Raal, F.A. (1955) Zur thermischen Zersetzung von Dolomit. VI. Adsorptionsuntersuchungen an thermisch zersetzten Dolomitkristallen. Zeitschrift für Anorganische und Allgemeine Chemie, 281, 199-211.

Haul, R.A.W. and Wilsdorf, H. (1952) Röntgenographische Untersuchung der thermischen Zersetzung von Dolomitkristallen. Acta Crystallographica, 5, 250–255.

Haul, R.A.W., Stein, L.H. and Louw, J.D. (1951) Exchange of carbon-13 dioxide between solid carbonates and gaseous carbon dioxide. Nature, 167, 241 - 242.

Hedvall, J.A. (1925) Om det kemiska sonderfallet hos jarnspat, manganspat och dolomit. Geologiska Föreningens i Stockholm Förhandlingar, 47, 73-80.

Houben, H. and Guillaud, H. (1994) Earth Construction: A Comprehensive Guide. CRATerre-EAG, Intermediate Technology Publications, London.

Hudson, A. and Hofstadter R. (1952) Electron Diffraction from Small Crystals. Physical Review 88, 596-599.

Huet, B., Tasoti, V. and Khalfallah, I. (2011) A review of Portland cement carbonation mechanisms in CO_2 rich environment. Energy Procedia 4 , 5275-5282.

Iwafuchi, K.D. (1982) Eng. Thesis, Waseda University, Tokyo, Japan.

Jacobs, H. and Low, M.J.D (1974) Infrared spectroscopic study of the thermal decomposition of dolomite in vacuum. Journal of Colloid and Interface Science, 46, 165-176.

Jamtveit, B., Putnis, C. V. and Malthe-Sørenssen, A. (2009) Reaction induced fracturing during replacement processes. Contributions to Mineralogy and Petrology 157 , 127-133.

Johnston, J. (1914) The utilization of diffusion processes in the preparation of pure substances. Journal of the American Chemical Society 36 , 16-19.

Johnstone, J. R. and Glasser, F. P. (1992) Carbonation of portlandite single crystals and portlandite in cement paste. 9th International Congress on the Chemistry of Cement 5 , 370-376).

Jung, W. M., Kang, S. H., Kim, W. S. and Choi, C. K. (2000) Particle morphology of calcium carbonate precipitated by gas–liquid reaction in a Couette–Taylor reactor. Chemical Engineering Science 55 , 733-747.

Kim, M.G., Dahmen, U., and Searcy, A.W. (1987) Structural transformations in the decomposition of $Mg(OH)_2$ and $MgCO_3$. Journal of the American Ceramic Society, 70, 146-154.

Kingery, W.D., Vandiver, P.B. and Prickett, M. (1988) The beginnings of pyrotechnology, part II: production and use of lime and gypsum plaster in the pre-pottery neolithic Near East. Journal of Field Archaeology 15, 219-244.

Kowacz, M. and Putnis, A. (2008) The effect of specific background electrolytes on water structure and solute hydration: Consequences for crystal dissolution and growth. Geochimica et Cosmochimica Acta 72 , 4476–4487.

Lackner, K. S. (2002) Carbonate chemistry for sequestering fossil carbon. Annual Review of Energy and the Environment 27, 193-232.

Lahann, R. W. (1978) A chemical model for calcite crystal growth and morphology control. Journal of Sedimentary Petrology 48 , 337-347.

Lam, R.S.K., Charnock, J.M., Lennie, A. and Meldrum, F.C. (2007) Synthesis-dependent structural variations in amorphous calcium carbonate. Crystal Engineering Communications, 9, 1226-1236.

Lange, P.A. and Roesky, H. (1964) Untersuchungen zur thermischen Dissoziation von Dolomit. Berichte Deutsche Keramik Gesellschaft, 41, 497-499.

Lea, F.M. (1970) The Chemistry of Cement and Concrete, 3rd edn. Edward Arnold Ltd., London.

Lippman, F. (1973) Sedimentary Carbonate Minerals. Springer-Verlag, Berlin.

MacKenzie, K.J.D. and Meinhold, RH. (1993) Thermal decomposition of dolomite (calcium magnesium carbonate) studied by 25Mg solid-state nuclear magnetic resonance. Thermochimica Acta, 230, 331 - 337.

Maitra, S., Choudhury, A., Das, H. S. and Pramanik, MS. J. (2005) Effect of compaction on the kinetics of thermal decomposition of dolomite under non-isothermal condition. Journal of Materials Science, 40, 4749-4751.

Manzano H, Pellenq RJ, Ulm FJ, Buehler MJ, van Duin AC. (2012) Hydration of calcium oxide surface predicted by reactive force field molecular dynamics. Langmuir 28, 4187-4197.

Martin-Ramos, J.D. (2004) XPowder: A Software Package for Powder X-Ray Diffraction Analysis, Version 2004.03, [www.xpowder.com].

Materic, V. and Smedley, S., I., (2010) High temperature carbonation of $Ca(OH)_2$. Industrial and Engineering Chemistry Research 50 , 5927-5932.

McCauley, R.A. and Johnson, L.A. (1991) Decrepitation and thermal decomposition of dolomite. Thermochimica Acta, 185, 271- 282.

McIntosh, R.M., Sharp, J.H. and Wilburn, F.W. (1990) The thermal decomposition of dolomite. Thermochimica Acta, 165, 281 - 296.

Meldrum, F. and Cölfen, H. (2008) Controlling mineral morphologies and structures in biological and synthetic systems. Chemical Reviews 108, 4332–4432.

Mellaart, J. (1967) Çatal Hüyük: A Neolithic town in Anatolia. Thames & Hudson, London.

Meybeck, M. (1987) Global chemical weathering of surficial rocks estimated from river dissolved loads. American Journal of Science, 287, 401–428.

Milodowski, A.E. and Morgan, D.J. (1989) The thermal analysis of the dolomite-ferroan dolomite-ankerite series. II. Decomposition mechanisms in flowing CO_2 atmosphere. Thermochimica Acta, 152, 279-297.

Montes-Hernandez, G., Fernandez-Martinez, A., Charlet, L., Tisserand, D. and Renard, F. (2008) Textural properties of synthetic nano-calcite produced by hydrothermal carbonation of calcium hydroxide. Journal of Crystal Growth 310 , 2946-2953.

Montes-Hernandez, G., Pommerol, A., Renard, F., Beck, P., Quirico, E. and Brissaud, O. (2010) In situ kinetic measurements of gas-solid carbonation of $Ca(OH)_2$ by using an infrared microscope coupled to a reaction cell. Chemical Engineering Journal 161 , 250-256.

Moorehead, D. R. (1986) Cementation by the carbonation of hydrated lime. Cement and Concrete Research 16 , 700-708.

Morawiec, A. (2004) Orientations and Rotations: Computations in Crystallographic Textures. Springer.

Navrotsky, A. (2004) Energetic clues to pathways to biomineralization: Precursors, clusters, and nanoparticles. PNAS 101 , 12096-12101.

Nielsen, A.E. (1964) Kinetics of Precipitation. Macmillan Co, New York.

O'Keefe, J.D. and Ahrens, T.J. (1989) Impact production of CO_2 by the Cretaceous/Tertiary extinction bolide and the resultant heating of the Earth. Nature, 338, 247–249.

Ogino, T., Suzuki, T. and Sawada, K. (1987) The formation and transformation mechanism of calcium carbonate in water. Geochimica et Cosmochimica Acta 51, 2757-2767.

Otsuka, R. (1986) Recent studies on the decomposition of the dolomite group by thermal analysis. Thermochimica Acta, 100, 69-80.

Papadakis, V. G., Vayenas, C. G. and Fardis, M. N. (1991) Fundamental modeling and experimental investigation of concrete carbonation. ACI Materials Journal 88 , 363-373.

Paquette, J. and Reeder, R.J. (1995) Relationship between surface structure, growth mechanism, and trace element incorporation in calcite. Geochimica et Cosmochimica Acta, 59, 735-749.

Parkhurst, D. L. and Appelo, C. A. (1999) User's guide to PHREEQC (version 2)--A computer program for speciation, batch-reaction, one-dimensional transport, and inverse geochemical calculations. U.S. Geological Survey Water-Resources Investigations Report.

Penn, R.L. and Banfield, J.F. (1998) Imperfect oriented attachment: Dislocation generation in defect-free nanocrystals. Science, 281, 969-971.

Pouget, E. M., Bomans, B. H., Goos, J. A., Frederik, P. M., de With, G. and Sommerdijk, N. A. (2009) The initial stages of template-controlled $CaCO_3$ formation revealed by cryo-TEM. Science 13 , 1455-1458.

Powell, E.K. and Searcy, A.W. (1978) Kinetics and thermodynamics of decomposition of dolomite to a metastable solid product. Journal of the American Ceramic Society, 61, 216-221.

Putnis, A. (2009) Mineral Replacement Reactions. Reviews in Mineralogy and Geochemistry 70 , 87-124.

Putnis, C. V. and Mezger, K. (2004) A mechanism of mineral replacement: Isotope tracing in the model system KCl-KBr-H_2O. Geochimica et Cosmochimica Acta 68 , 2839–2848.

Radha, A. V., Forbes, T. Z., Killian, C. E., Gilbert, P. U. and Navrotsky, A. (2010) Transformation and crystallization energetics of synthetic and biogenic amorphous calcium carbonate. PNAS 107 , 16438–16443.

Ralph L. Carr, R. L. (1976) Wet-Slaking Speeds Lime Reactivity. Water & Sewage Works 8, 82-85.

Ramachandran, V. S.; Sereda, P. J.; Feldman, R. F. (1964) Mechanism of Hydration of Calcium Oxide. Nature 201, 288-289.

Readman, J.E. and Blom, R. (2005) The use of in-situ powder X-Ray diffraction in the investigation of dolomite as a potential reversible high-temperature CO_2 adsorbent. Physical Chemistry Chemical Physics, 7, 1214-1219.

Reeder, R.J., and Markgraf, S. (1986) High-temperature crystal chemistry of dolomite. American Mineralogist, 71, 794-804.

Reeder, R.J., and Nakajima, Y. (1982) The nature of ordering and ordering defects in dolomite. Physics and Chemistry of Minerals, 8 .29-35.

Reeder, R.J. (1983) Carbonates: Mineralogy and Chemistry. Review in Mineralogy 11, Mineneralogical Society of America, Washington, D.C.

Regnault, O., Lagneau, V. and Schneider, H. (2009) Experimental measurement of portlandite carbonation kinetics with supercritical CO_2. Chemical Geology 265 , 113-121.

Rieger, J., Frechen, T., Cox, G., Heckmann, W., Schmidt, C. and Thieme, J. (2007) Precursor structures in the crystallization/precipitation processes of $CaCO_3$ and control of particle formation by polyelectrolytes. Faraday Discussions, 136 , 265-277.

Rodriguez-Blanco, J. D. and Shaw, S. B. (2008) How to make 'stable' ACC: protocol and preliminary structural characterization. Mineralogical Magazine 72 , 283-286.

Rodriguez-Blanco, J. D., Shaw, S. and Benning, L. G. (2010) The kinetics and mechanisms of amorphous calcium carbonate (ACC) crystallization to calcite, via vaterite. Nanoscale 3 , 265-271.

Rodriguez-Navarro, A. B. (2006) XRD2DScan : new software for polycrystalline materials characterization using two-dimensional X-ray diffraction. Journal of Applied Crystallography, 39 , 905-909.

Rodriguez-Navarro, C. Hansen, E. and Ginell, W.S. (1998) Calcium hydroxide crystal evolution upon aging of lime putty. Journal of the American Ceramic Society 81, 3032–3034.

Rodriguez-Navarro, C., Cazalla, O., Elert, K. and Sebastian, E. (2002) Liesegang pattern development in carbonating traditional lime mortars. Proceedings of the Royal Society of London A 458, 2261-2273.

Rodriguez-Navarro, C., Ruiz-Agudo, E., Luque, A., Rodriguez-Navarro, A. B. and Ortega-Huertas, M. (2009) Thermal decomposition of calcite: Mechanisms of formation and textural evolution of CaO nanocrystals. American Mineralogist 94 , 578-593.

Rodriguez-Navarro, C., Ruiz-Agudo, E., Ortega-Huertas, M. and Hansen, E. (2005) Nanostructure and irreversible colloidal behavior of $Ca(OH)_2$: implications in cultural heritage conservation. Langmuir 21 , 10948–10957.

Ruiz-Agudo, E. and Rodriguez-Navarro, C. (2010) Microstructure and rheology of lime putty. Langmuir 26 , 3868-3877.

Ruiz-Agudo, E., Putnis, C. V., Wang, L. J. and Putnis, A. (2011) Specific effects of background electrolytes on step propagation during calcite growth. Geochimica et Cosmochimica Acta 75 , 3803-3814.

Samtani, M., Dollimore, D., Wilburn, F.W. and Alexander, K. (2001) Isolation and identification of the intermediate and final products in the decomposition of dolomite in an atmosphere of carbon dioxide. Thermochimica Acta, 367-368, 285-295.

Sato, T., Beaudoin, J.J., Ramachandran, V.S., Mitchell, L.D. and Tumidajski, P.J. (2007) Thermal decomposition of nanoparticulate $Ca(OH)_2$ – Anomalous effects. Advances in Cement Research 19, 1-7.

Schwob, Y. (1947) Sur la dissociation thermique de la dolomite. Influence de faibles quantités de fondants. Comptes Rendus Academie Sciences, Paris, 224, 47-49.

Serris, E., Favergeon, L., Pijolat, M., Soustelle, M., Nortier, P., Gärtner, R.S., Chopin, T., Habib Z. (2011) Study of the hydration of CaO powder by gas–solid reaction. Cement and Concrete Research 41, 1078-1084.

Siegel, S., Fuchs, L. H., Hubble, B. R. and Nielsen, E. K. (1978) Relationship between the morphological properties of half-calcined dolomite and the kinetics of the sulfation reaction. Environmental Science and Technology, 12, 1411-1416.

Singh Dev, R. (1972) Topotaktische Phänomene bei der Calcinierung, Sulfatisierung und Chloridisierung einiger Karbonat-Einkristalle. Neues Jahrbuch für Mineralogie Monatshefte, 1, 12-22.

Singh, A., Dash, S., Kamruddin, M., Ajikumar, P.K., Tyagi, A.K., Raghunathan, V.S. and Raj, B. (2002) Formation of nanocrystalline calcia by the decomposition of calcite. Journal of the America Ceramic Society, 85, 927-932.

Spinolo, G. and Anselmi-Tamburini, U. (1984a) Dolomite decomposition to (Ca,Mg)O solid solutions: An X-ray diffraction study, Part I. Zeitschrift für Naturforschung A, 39a, 975 – 980.

Spinolo, G. and Anselmi-Tamburini, U. (1984b) Dolomite decomposition to (Ca,Mg)O solid solutions: An X-ray diffraction study, Part II. Zeitschrift für Naturforschung A, 39a, 981- 985.

Spinolo, G. and Anselmi-Tamburini, U. (1989) Nonequillibrium (Ca,Mg)O solid solutions produced by chemical decomposition. Journal of Physical Chemistry, 93, 6837 - 6843.

Spinolo, G. and Beruto, D. (1982) Thermodynamic analysis of the thermal decomposition of dolomite. Journal of the Chemical Society, Faraday Transactions I, 78, 2631 – 2642.

Stanmore, B.R., and Gilot, P. (2005) Review – Calcination and carbonation of limestone during thermal cycling for CO_2 sequestration. Fuel Processing Technology, 86, 1707-1743.

Steen, C. L., Li, K. and Heiskell Rogan, F. (1980) Half-calcination of dolomite at high pressures. Kinetics and structural changes. Environmental Science and Technology, 14, 588-593.

Stepkowska, E. T. (2005) Hypothetical transformation of $Ca(OH)_2$ into $CaCO_3$ in solid-state reactions of Portland cement. Journal of Thermal Analysis and Calorimetry 80 , 727-733.

Tai, C., and Chen, F.B. (1998) Polymorphism of $CaCO_3$ precipitated in a constant-composition Environment. AIChE Journal 44 , 1790-1798.

Tlili, M. M., Ben Amor, M., Gabrielli, C., Joiret, S., Maurin, G. and Rousseau P. (2002) Characterization of $CaCO_3$ hydrates by micro-Raman spectroscopy. Journal of Raman Spectroscopy, 33, 10-16.

Uebo, K., Yamazaki, R. and Yoshida, K. (1992) Precipitation mechanism of calcium carbonate fine particles in a three-phase reactor. Advanced Powder Technology 3 , 71-76.

University of Maryland. (2011) Environmental Scanning Electron Microscpe. Retrieved July 2011, from Center for Advanced Life Cycle Engeneering: http://www.calce.umd.edu/.

Van Balen, K. and Van Gemert, D. (1994) Modeling Lime Mortar Carbonation. Materials and Structures 27 , 393-398.

Van Balen, K., Van Den Brande, C., Toumbakari, E. E. and Van Gemert, D. (1997) Influence of Moisture Content on the Effective Diffusion Coefficient in Lime Mortars with Different Porosities. In Proceedings of the 10th International Congress on The Chemistry of Cement, Amarkai AB and Congrex Goteborg AB, Gothenburg (Sweden), p. 4IV010.

Van Santen, R. A. (1984) The Ostwald step rule . The Journal of Physical Chemistry 88 , 5768-5769.

Von Landsberg, D. (1992) The history of lime production and use from early times to the Industrial Revolution. ZKG 45, 199-203.

Wenk, H. R., Barber, D. J. and Reeder, R. J. (1983) Microstructures in carbonates. In: Carbonates. Mineralogy and Chemistry. Reviews in Mineralogy vol. 11, 301-367.

Wiedemann, H.G. and Bayer, G. (1987) Note on the thermal decomposition of dolomite. Thermochimica Acta, 121, 479 - 485.

Wilsdorf, H.G.F. and Haul, R.A.W. (1951) X-ray study of the thermal decomposition of dolomite. Nature, 167, 945-946.

Wolter, A. (2004) The kinetics of the hydration of quicklime. ZKG International 8, 60-68.

Yang, T., Keller, B., Magyari, E., Hatmetner, K. and Günther, D. (2003) Direct observation of the carbonation process on the surface of calcium hydroxide crystals in hardened cement paste using atomic force microscope. Journal of Materials Science 38 , 1909-1916.

7. Appendix 1

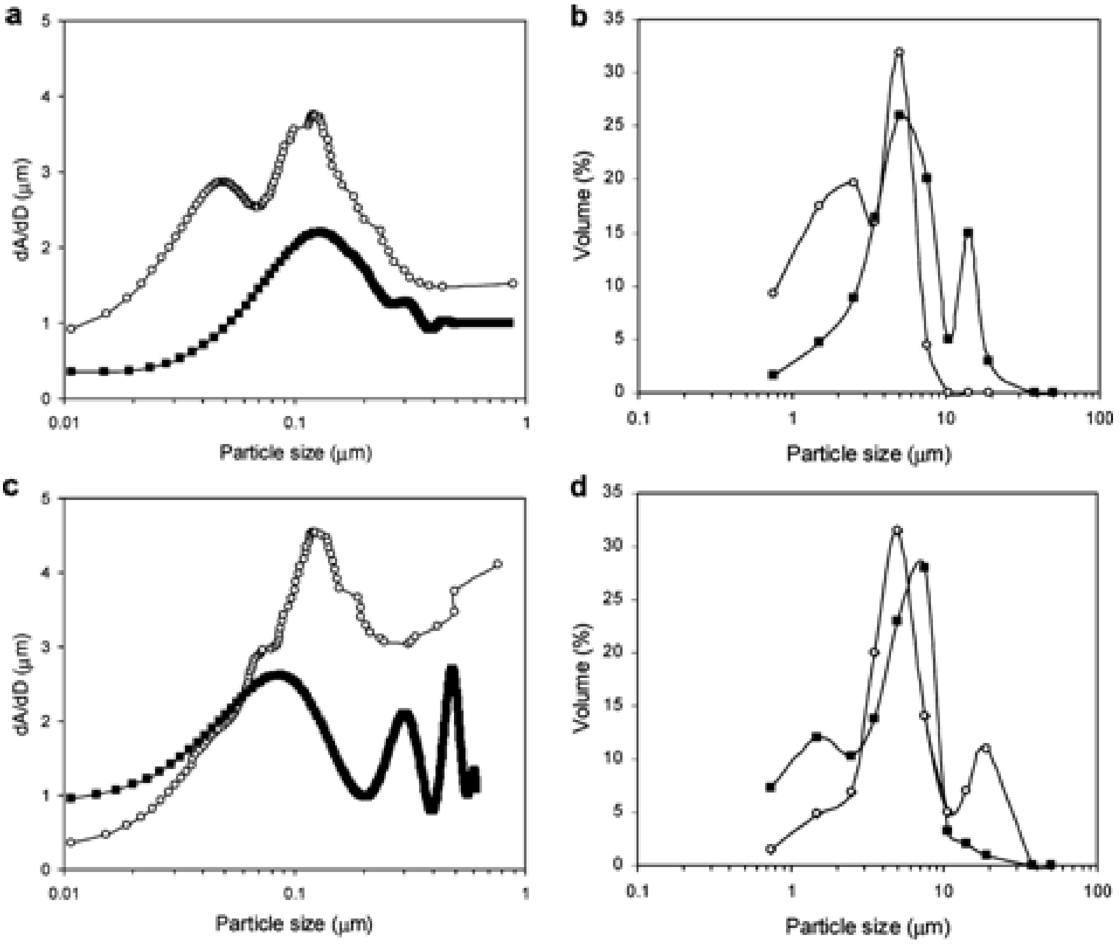

Figure 7.1. Particle size distribution of FG (a, b) and AC (c, d) obtained from digital image analysis of TEM images (a and c) and laser scattering granulometry (b and d). Legend: ○, fresh lime putty (6 h after slaking); ▪ , aged lime putty (3 years after slaking) (after Ruiz-Agudo and Rodriguez-Navarro, 2010).

Table 5.1. Surface area of lime putty samples (FG and AC) (after Ruiz-Agudo and Rodriguez-Navarro, 2010).

FG	7.9 m^2g^1
AC	19.8 m^2g^{-1}

8. *Appendix 2*

Within the frame of this work three programs used for the analysis of the data have been developed by the author. These are:

- **XRDFit** – software for XRD profile analysis
- **SAEDP** - software for kinematical simulation of selected area electron diffraction patterns
- **PFS** – software for analysis of the pole figures, and their recalculation from orientation distribution function (ODF)

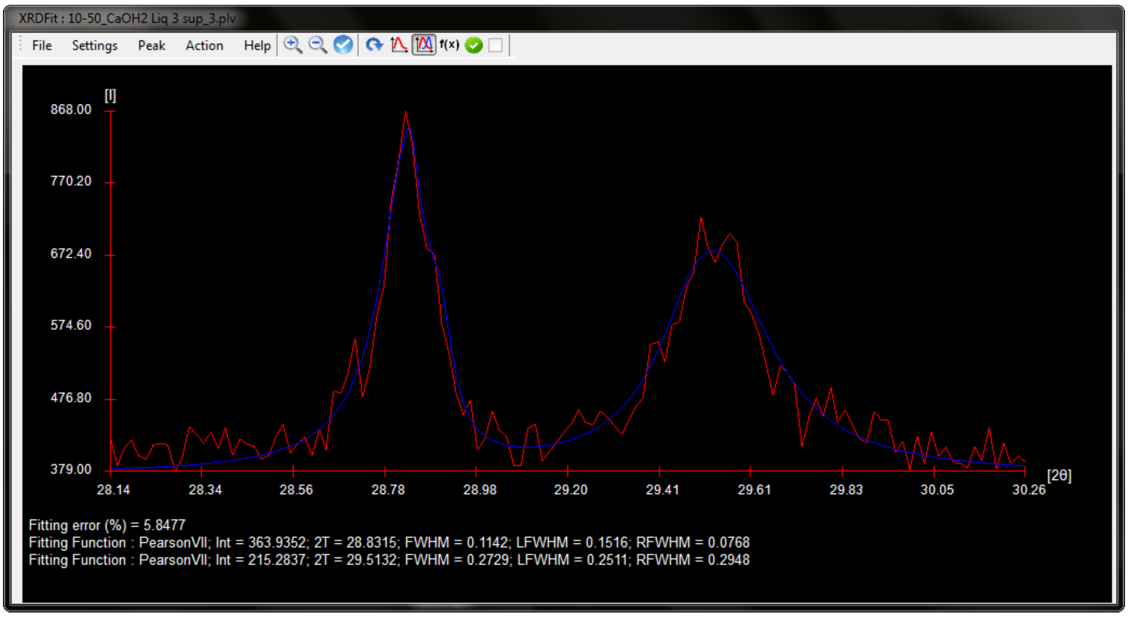

```
Fitting error (%) = 5.8477
Fitting Function : PearsonVII; Int = 363.9352; 2T = 28.8315; FWHM = 0.1142; LFWHM = 0.1516; RFWHM = 0.0768
Fitting Function : PearsonVII; Int = 215.2837; 2T = 29.5132; FWHM = 0.2729; LFWHM = 0.2511; RFWHM = 0.2948
```

Figure 8.1. XRDFit user interface.

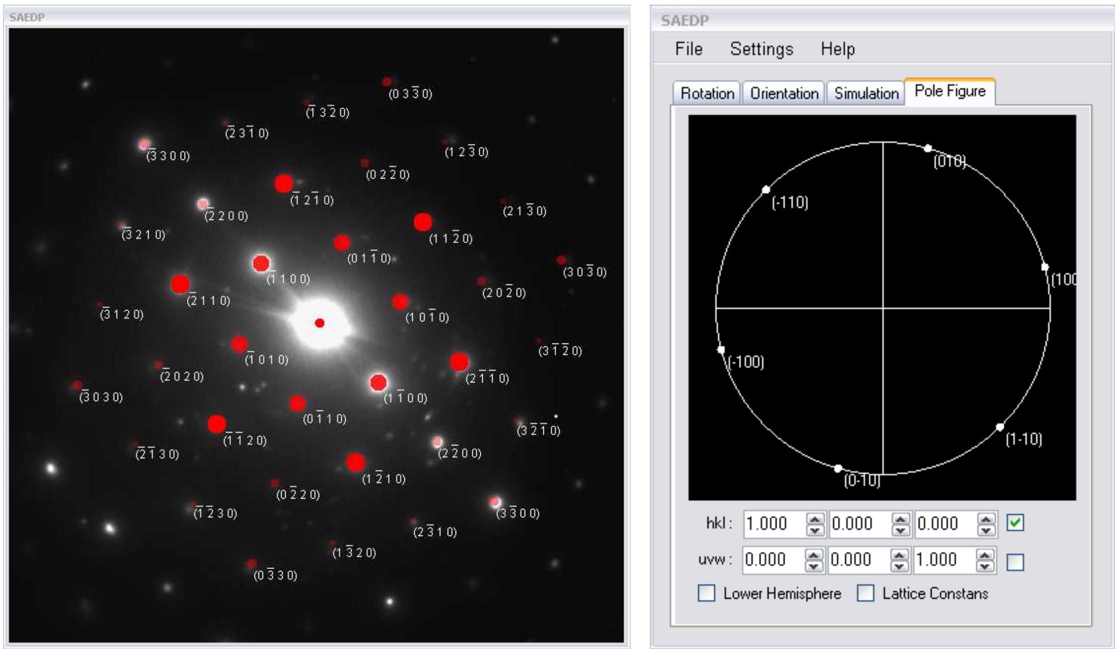

hkl : 1.000 0.000 0.000 ☑

uvw : 0.000 0.000 1.000 ☐

☐ Lower Hemisphere ☐ Lattice Constans

Figure 8.2. SADP user interface

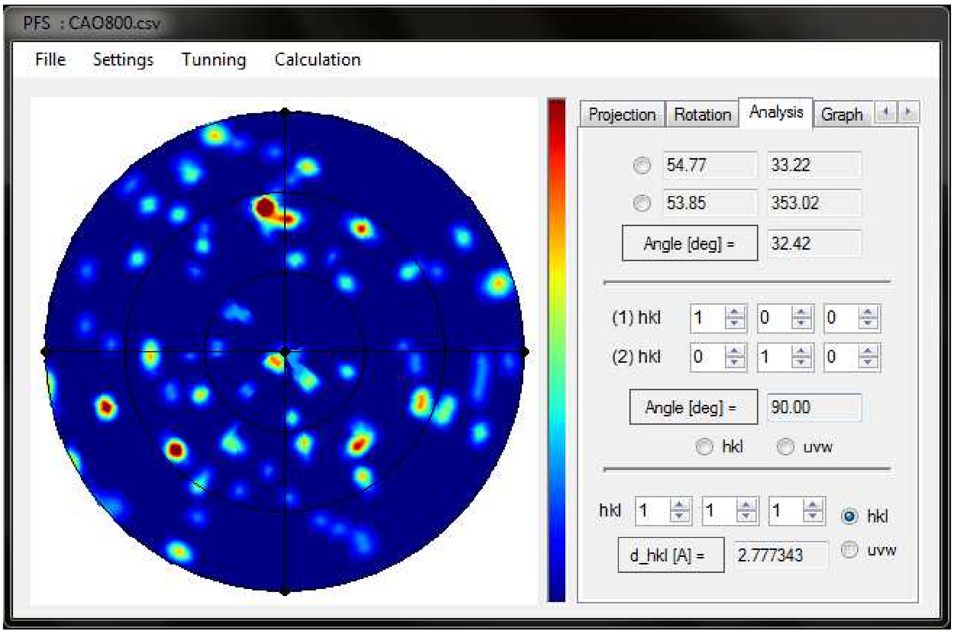

○ 54.77 33.22

○ 53.85 353.02

Angle [deg] = 32.42

(1) hkl 1 0 0

(2) hkl 0 1 0

Angle [deg] = 90.00

○ hkl ○ uvw

hkl 1 1 1 ● hkl ○ uvw

d_hkl [A] = 2.777343

Figure 8.3. PFS user interface